# Submarine landslides offshore Vancouver Island, British Columbia and the possible role of gas hydrates in slope stability

by

Nastasja Anaïs Scholz

M.Sc, Victoria University of Wellington, 2007
Diplom, Technische Hochschule Karlsruhe, 2008

A Dissertation Submitted in Partial Fulfillment of the
Requirements for the Degree of

DOCTOR OF PHILOSOPHY

in the School of Earth and Ocean Sciences

# Supervisory Committee

Submarine landslides offshore Vancouver Island, British Columbia and the possible role of gas hydrates in slope stability

by

Nastasja Anaïs Scholz

M.Sc, Victoria University of Wellington, 2007
Diplom, Technische Hochschule Karlsruhe, 2008

**Supervisory Committee**

---

Dr. Michael Riedel, (Natural Resources Canada, Geological Survey of Canada)

**Co-Supervisor**

---

Dr. George Spence, (School of Earth and Ocean Sciences, University of Victoria)

**Co-Supervisor**

---

Dr. Roy Hyndman, (Natural Resources Canada, Geological Survey of Canada)

**Departmental Member**

---

Dr. Joanne Wegner, (Department of Mechanical Engineering, University of Victoria)

**Outside Member**

# ABSTRACT

**Supervisory Committee**

Dr. Michael Riedel, (Natural Resources Canada, Geological Survey of Canada)
**Co-Supervisor**
Dr. George Spence, (School of Earth and Ocean Sciences, University of Victoria)
**Co-Supervisor**
Dr. Roy Hyndman, (Natural Resources Canada, Geological Survey of Canada)
**Departmental Member**
Dr. Joanne Wegner, (Department of Mechanical Engineering, University of Victoria)
**Outside Member**

This dissertation investigates the nature of submarine landslides along the deformation front of the northern Cascadia subduction zone. As the first slope stability analysis on the west coast of Vancouver Island, this study covers a variety of large-scale tectonic to small-scale, site-specific factors to investigate the nature of slope failure. Slope failure occurred mainly on the steep slopes of frontal ridges that were formed by compressive forces due to the subduction of the Juan de Fuca plate. Multi-beam swath bathymetry data are used to study the morphology of the whole margin and the geometry of two Holocene landslides that serve as representative examples. The overall margin stability is estimated using the critical taper theory, and a first-order limit equilibrium slope stability analysis provides threshold values for external forces to cause slope failure. The present-day pore pressure regime at different sites of the Cascadia margin is estimated from log-density data and expected ground accelerations are calculated via ground motion attenuation relationships. A comparison to threshold values derived from the limit equilibrium analysis suggests that, at present, slope stability is more sensitive to overpressure than to earthquake shaking. Differences in power spectral density derived from OBS-velocity data imply a slightly amplified ground response at the ridge crest compared to sites along the continental shelf and abyssal plain. Apart from estimating the trigger mechanisms of submarine landslides offshore Vancouver Island, a particular consideration is given to the potential link between slope failure and methane hydrate occurrence. The history of the gas hydrate stability zone (GHSZ) boundaries is investigated using information on regional sea-level history. Assuming colder ocean-bottom temperatures during the Holocene, a gradual shoaling of the BSR is inferred, which potentially could have caused hydrate melting. Pore pressure due to hydrate

dissociation, as estimated by a previously developed method, varies over several orders of magnitude. Depending on sediment permeability, overpressure ratios can be comparable to threshold values. The two Holocene landslides are modeled numerically using a two-dimensional finite difference code in order to recreate the along-strike variability in ridge geometry and slide morphology observed along the northern Cascadia margin. Geometry and morphology correlate with the two prevalent slide mechanisms and model results suggest that sediment yield strength and average slide thickness are associated with the slide mechanism as well.

# Table of Contents

# List of Figures

# List of Tables

## Acknowledgments

I like to take this as my chance to thank the people without whom this thesis would not have been possible and those who kept me company along the way.

First of all, I would like to thank my co-advisers Michael Riedel and George Spence for giving me the chance to pursue a PhD at the University of Victoria, for giving me the freedom to explore different aspects of my topic, and for supporting me from the very start to the very end. I would also like to thank my committee members Roy Hyndman, Joanne Wegner, and Jeffrey Priest for their input.

I am grateful for the support I got from various people. In particular, I would like to thank Andreas Rosenberger who has shown a lot of patience and persistence with helping me to turn the slightly cryptic Xu & Germanovich paper into a functioning code. Furthermore, I would like to thank Camille Brillon for all those hours and hours of extracting squiggles for me, Thomas James and Kevin Belanger for providing me with the regional sea-level history and Brian Bornhold and Isaac Fine for sharing their knowledge of submarine landslides and tsunami generation. I am also thankful to Brandon Dugan for giving me the opportunity to visit Rice University and for his introduction to a topic which now has turned into a dissertation. Many, many thanks go out to Allison and Kimberly of the SEOS office for their invaluable help and support.

Over the past 4 ½ years I have met many people who came and went and some of them turned into very good friends. In particular, I would like to thank Ren, Leah, and Charlie for their continuous friendship and for being there when I needed it. Thank you, Rob and all of my dear CSers, for your great company, for enriching my life and making the past couple of years so much more joyful. You all have done a fabulous job in cheering me up. You will always feel close to me.

Finally, a big ‘thank you’ to my family and friends back in Germany, France, and Sweden for their continuous love and support.

# Chapter 1: INTRODUCTION

## 1.1 Objectives and motivation

Although slope failure is a ubiquitous feature on the northern Cascadia margin, there have been few studies examining slide processes in this region. On this margin submarine landslides are almost solely confined to the frontal ridges along the deformation front and alternate between debris flows and coherent block slides correlating with the direction in which the ridges are facing (Naegeli, 2010). Large earthquakes have occurred in this region in the past (e.g. Clague 1997; Hyndman and Rogers, 2010) some of which caused tsunamis such as the ~M9 event in the year 1700 that triggered a tsunami crossing the entire Pacific Ocean even reaching the Japanese islands (e.g. Satake et al., 1996). However, it is not known if the submarine landslides that occurred along the west coast of Vancouver Island have been tsunamigenic nor what has caused the slope failure in the first place. Earthquake shaking and overpressures are among the most likely trigger mechanisms along the northern Cascadia margin. This region is seismically very active and the subduction of the Juan de Fuca plate underneath the North America plate leads to horizontal compressive stresses and tectonic compaction. These are capable of producing high pore pressures and may potentially drive fluid flow (e.g. Hyndman et al., 1993). Another consequence of tectonically induced fluid flow is the occurrence of gas hydrate and it has been found that the distribution of the slope failure features generally matches the spatial distribution of gas hydrates (e.g. Riedel et al., 2006a, 2010). Additionally, failure planes have in the past been found to coincide with the base of the hydrate stability zone (Lopez

et al., 2010). This raises the question if gas hydrates are playing a significant role in slope stability along the northern Cascadia margin.

The submarine landslides identified along the northern Cascadia margin are concluded to have occurred during the Holocene at the end of the Last Glacial Maximum (LGM) and are small in size. However, Goldfinger et al. (2000) have found signs of three large-scale underwater landslides that occurred between 100 ka and 1 Ma ago off the coast of Southern Oregon comprising a total area of 7890 $km^2$. This proves that larger mass movements are indeed possible along the Cascadia subduction zone and that they have occurred at different times in the geologic history of the margin. This also underlines the importance of studing the general nature of regional slope failure and of including slope stability and tsunami research into future geohazard studies to assess the likelihood of catastrophic slope failure events and resulting tsunamis.

With Canada's vast coast-line this study represents an input for a future National Tsunami Hazard Assessment and the creation of a tsunami hazard map for Canada (e.g. Leonard et al., 2010; 2013). Understanding submarine landslide occurrence also provides additional information on regional paleoseismicity and climate patterns (Camerlenghi et al., 2007).

This dissertation aims to,

- Explore the nature of past slope failure along the northern Cascadia margin.
- Estimate general margin stability as well as local ridge stability, in order to evaluate the potential for future slides.
- Discuss prevalent slide trigger mechanisms.
- Identify potential trigger scenarios, especially for the landslides that occurred on the steep slopes of two frontal ridges situated along the deformation front.

- Estimate threshold values of pore pressure and earthquake shaking to induce slope failure on both ridges.
- Assess present pore pressure regimes.
- Estimate earthquake ground accelerations possible in this region as well as potential amplification effects due to topography.
- Study the role of gas hydrates either as a facilitator or initiator of slope failure by investigating the effect of past hydrate associated pressure and temperature changes on the stability conditions and by searching for spatial and temporal coincidence of slope failure and the boundaries of the gas hydrate stability zone (GHSZ).
- Quantify pore pressure generation from gas hydrate dissociation.
- Study the slide processes to identify differences between debris flow and blocky slide dynamics.
- Explain the correlation of slide morphology with ridge geometry and orientation as well as the zigzag alignment of the frontal ridges.

## 1.2 Introduction to global gas hydrates

Gas hydrates, also known as clathrates, are ice-like compounds of frozen water and gas. Unlike sea ice which has a hexagonal crystallographic system, water molecules are packed tightly into a cubic system (e.g. Sloan and Koh, 2007). Gas hydrates are mechanically stronger and possess different thermal properties and pressure-temperature stability conditions compared to sea ice (e.g. Nixon and Grozic, 2007).

During formation of hydrates, most salt molecules are excluded and lower molecular weight hydrocarbons are incorporated into a crystal lattice of water molecules through van der Waals forces, without any chemical bond. The ratio between water and gas molecules is variable

and limited by the number of available cages in the crystalline structure. The occupational rate is one of the determining factors of how much free gas is released during gas hydrate dissociation (e.g. Handa, 1990; Sloan, 1998). In a fully saturated structure I methane hydrate the ratio of methane molecules to water molecules is 1 to 5.75. Structure I hydrates differ from other hydrate structures in their crystallographic packing and in the type of gas molecules they can incorporate. About 90% of the naturally occurring gas hydrates are hosting principally methane gas (e.g. Riedel et al., 2010). This thesis focusses on methane hydrates. Other typical host gasses are carbon dioxide ($CO_2$), or hydrogen sulfide ($H_2S$), but also ethane, propane, butane, isobutene, and nitrogen.

Deep sea hydrate-forming methane is predominantly biogenic, but occasionally the methane source is thermogenic in its origin. Biogenic methane is either produced *in situ* via the bacterial break-down of organic matter or transported from greater depths via upward fluid migration (e.g. Hyndman and Spence, 1992b; Riedel et al., 2010). In contrast, thermogenic or fossil methane is formed at greater depths under higher temperature and pressure conditions. The nature of the methane source is discernible by the difference in their respective carbon isotopic ratios (e.g. Pohlman et al., 2005).

Marine gas hydrates are predominantly found in shallow sediments beneath the seafloor along the slopes of continental margins and islands or in the abyssal part of intra-continental and marginal seas where water depths exceed about 300 m. Gas hydrate stability is primarily controlled by local pressure and temperature conditions but also by gas composition and solubility. Fig. 1.1 shows a schematic of the relationship between phase-boundary, geothermal gradient, and the presence of gas hydrate and free gas in a marine environment. Typical values

for stability pressure and temperatures at the base of the GHSZ are between about 5 and 30 MPa and between 10° and 25°.

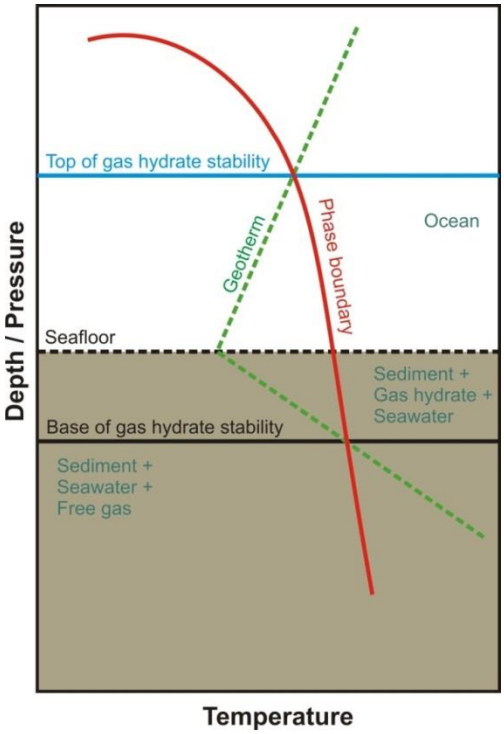


**Figure 1.1**: Schematic sketch of the stability conditions of gas hydrate in a marine environment

Fig. 1.1 also shows the definition of the bottom simulating reflector (BSR) that marks the lower limit of hydrate stability in seismic data. It is an important seismic indicator for possible gas hydrate occurrence, visible as a strong reflection that parallels the seafloor. It usually possesses a reversed polarity compared to the seafloor reflector due to a negative velocity gradient either caused by the gas hydrate-bearing sediments overlying gas hydrate-free sediment or by the free gas that underlies the gas hydrate stability zone (GHSZ), or a combination of both. As gas hydrate can only occur if the gas concentration exceeds solubility at a certain depth, the distinction between gas hydrate stability zone (GHSZ) and gas hydrate occurrence zone (GHOZ) is made (e.g. Malinverno, 2008).

Apart from the stability conditions, the amount and distribution of gas hydrate is also controlled by the salinity of the surrounding seawater and the lithology of the host sediment, especially by the pore-size distribution (e.g. Wright et al., 2005). Hydrates preferably occur disseminated within coarse-grained sediments but are also found in fine-grained sediments in a more concentrated form as nodules, lenses, veins, or as fracture fill (e.g. Kvenvolden, 1998; Sloan, 1998; Ginsburg and Soloviev, 1998; Clennel et al., 1999; Davie et al., 2004; Collett et al., 2008; Malinverno, 2008; Ryu et al., 2009).

Other than in the marine environment, gas hydrates are also present in areas of permafrost where they can be stable over a larger depth range due to the very low surface temperatures at higher latitudes. Fig. 1.2 shows the world-wide distribution of sites with recovered and inferred marine, as well as Arctic gas hydrates, as of 2007.

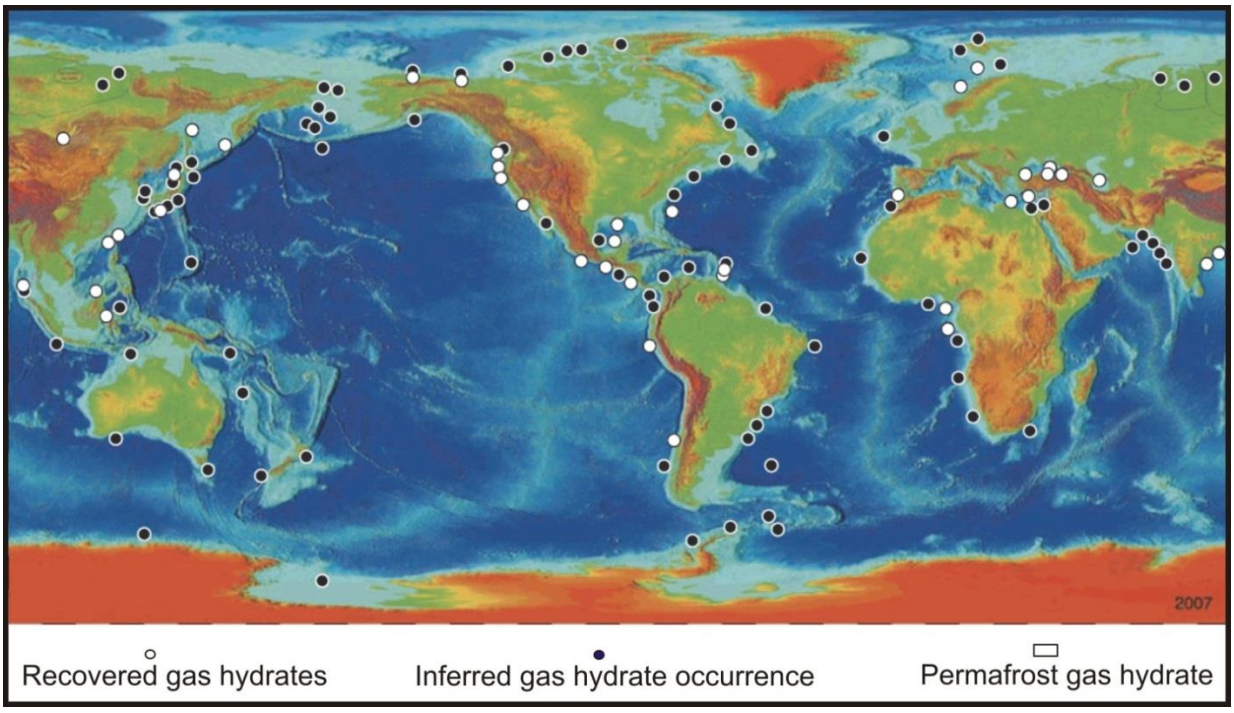


**Figure 1.2**: World-wide recovered and inferred occurrence of gas hydrates as of 2007 (after Kvenvolden in Paull et al. (2010))

### 1.2.1 Gas hydrates as a potential climate and geo-hazard

Gas hydrate research focuses on three main areas. The general aims are to assess the potential role of gas hydrates either as a future energy resource, a major climate hazard, or as a pre-conditioner or trigger of submarine slope failure. The influence of gas hydrates on submarine slope stability concerns both naturally-occurring slope failures as well as slope failure as a consequence of human activities. The latter is especially important in areas where gas hydrate production tests are planned or already underway such as in the Nankai Trough (REF) and at the northern slope of Alaska (Collett, 2004).

One related question is how much gas hydrate actually exists world-wide. Methane is stored in hydrates is tightly compacted and can expand its volume by a factor of up to 150. The area over which gas hydrates can potentially occur is vast but no attempt of quantification so far has led to a convincing result and has therefore been the object of debate (e.g. Milkov, 2004; Buffet and Archer, 2004). Global estimates differ over a range of magnitudes with the more recent numbers of the order of $10^{15}$ $m^3$ (Buffet and Archer, 2004). Canada is assumed to store between $10^{10}$ to $10^{12}$ $m^3$ of gas hydrates along its continental slopes and Arctic permafrost regions corresponding to a methane potential of $10^{12}$ to $10^{14}$ $m^3$ (Majorowicz and Osadetz, 2001).

McIver (1977, 1982) was the first to propose a link between gas hydrates and the triggering of submarine landslides. Examples of locations where possibly hydrate-related slumps and slides of varying sizes have occurred are the Norwegian continental margin (e.g. Bugge et al., 1988; Mienert et al., 2005), the British Columbia fjords (Bornhold and Prior, 1989), the slopes along the continental margin of SW Africa (Summerhayes et al., 1979), and the continental margin of the Alaskan Beaufort Sea (Kayen and Lee, 1991). Hance (2003) provided an overview of worldwide slope failure events attributed to gas hydrate dissociation (Fig. 1.3).

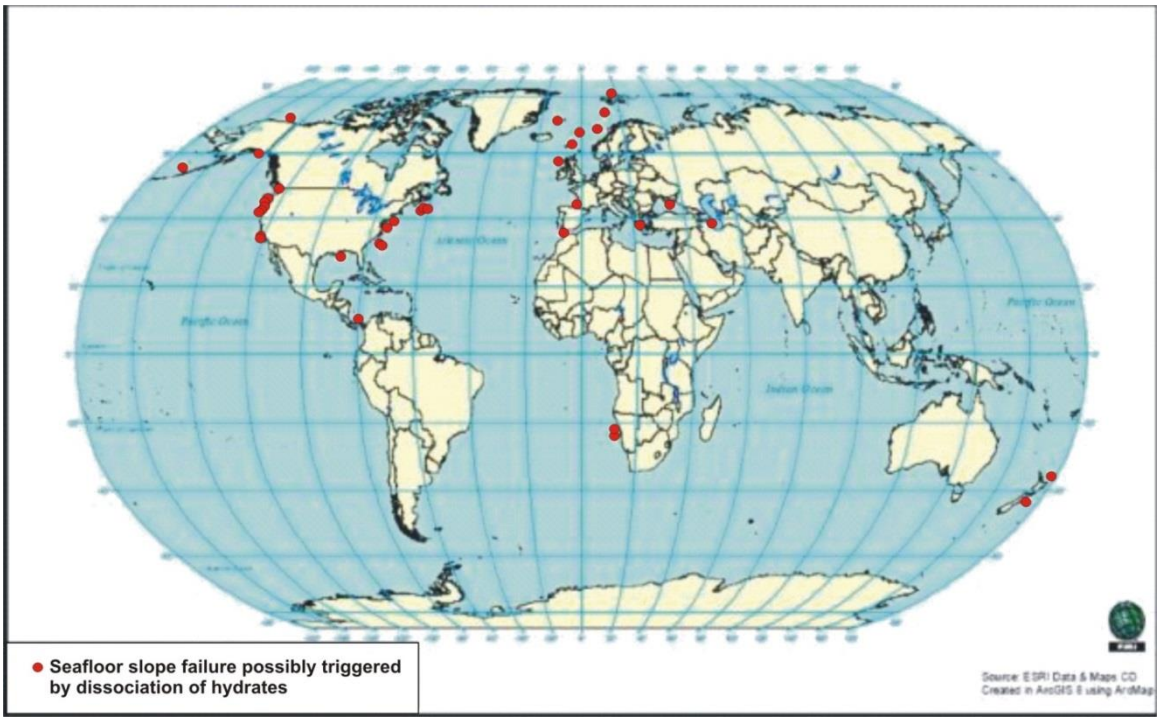


**Figure 1.3**: Global distribution of submarine landslides attributed to gas hydrate dissociation (taken from Hance (2003))

Methane is also a powerful climate agent greatly outperforming the effects of $CO_2$, potentially providing a positive feedback mechanism to both global warming and cooling trends (Shine et al., 1990). Dickens et al. (1995) previously suggested that methane had been released in significant amounts during the late Paleocene thermal maximum. During a warming period sea-level rises leading to an increase hydrostatic pressure. As increase in pressure shifts the GHSZ downward gas hydrates might remain stable. At the same time sea-bottom temperatures increase and lead to a warming pulse that could effectively move the GHSZ to shallower depths. Fig. 1.4a and b show the upward shift of the GHSZ due to a decrease in sea-level or an increase in ocean-bottom water temperature, a process that potentially leads to the dissociation of hydrate.

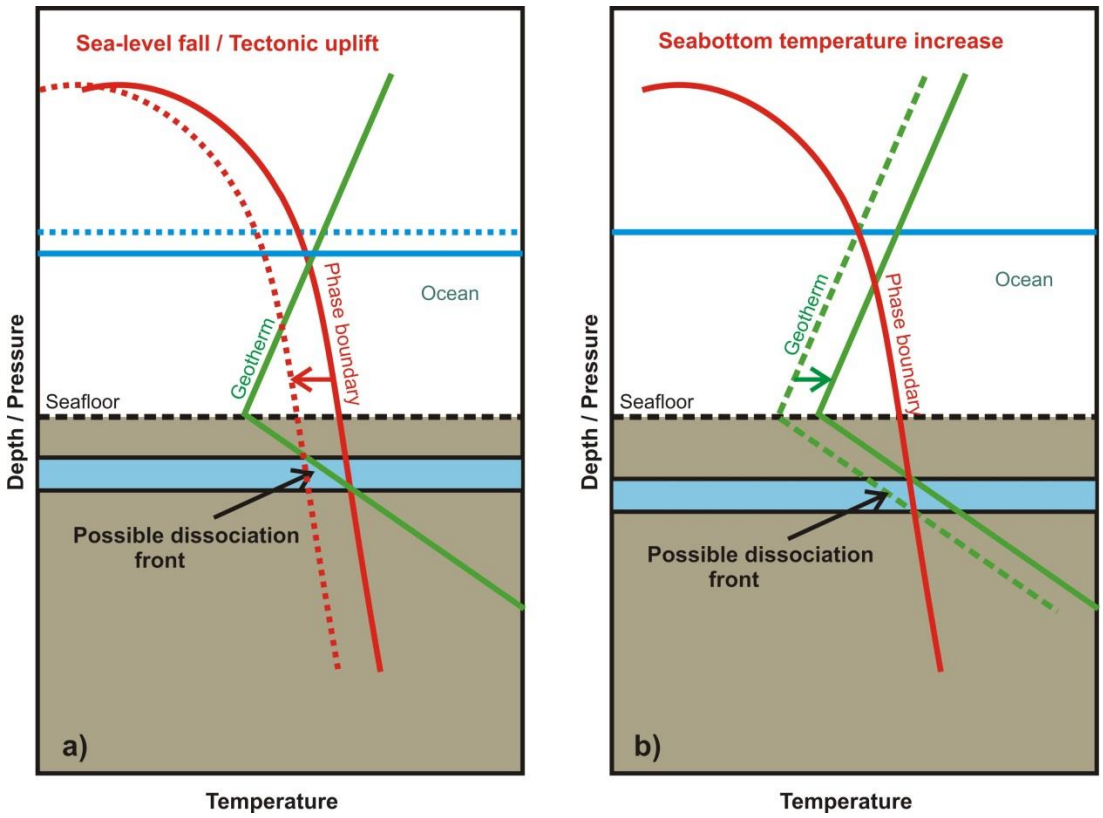


**Figure 1.4**: Schematic sketch of the influence of a) sea-level fall / tectonic uplift and b) ocean-bottom water warming on the gas hydrate stability conditions in a marine environment

There are several ways in which gas hydrates are thought to influence slope stability. Where gas hydrate occurs in large amounts, they are suggested to have a cementing effect since the mechanical strength of gas hydrate exceeds that of water ice by a factor up to 20 (e.g. Zhang et al., 1999; Sultan et al., 2004; Nixon and Grozic, 2007); however, the cementing effect has not been observed in nature yet. This might lead to a significant contrast in sediment strength at the base of hydrate stability that can pre-condition a future slide event. The dissociation of hydrate, either caused by geological processes or by petroleum drilling and production operations, in turn could lead to the loss of cementation and to a subsequent decrease in sediment strength. It has also been suggested that the presence of hydrate impedes the normal compaction of sediment within the GHSZ. The process of dissociation would then lead to under-consolidated, weakened soil, although this process has not been quantified so far (e.g. Sultan et al., 2004).

Gas hydrate dissociation could increase the bulk volume through the release of free gas and water and result in the generation of excess pore pressure possibly coupled with fluid flux. Furthermore, the free gas that is associated with gas hydrate could weaken the sediment. Free gas that is released during gas hydrate dissociation could generate significant overpressure when hydraulic permeability is sufficiently low. Overpressure in turn reduces effective stress, leading to a loss in shear strength and further promote destabilization via sediment deformation, hydraulic fracturing, the reactivation of faults and fluid flow channels, or even liquefaction, turning a slide event into a muddy debris flow (e.g. Xu and Germanovich, 2006; Kwon et al., 2008; Liu and Flemings, 2009).

As there is a complex interplay of gas hydrates and pore pressure with sediment permeability it has also been suggested that gas hydrates themselves can represent a fluid barrier which inhibits fluid flow from below leading to the build-up of high pore pressures and localized weakened zones (e.g. Sultan et al., 2004; Xu and Germanovich, 2006). Furthermore, sliding could be induced along the BSR due to the stratigraphic contrast between cementing gas hydrate above and free gas underneath. Hornbach et al. (2004) argued that the free gas beneath BSRs can act as a critically pressured layer. Although this has not been proven yet, the coincidence of the failure plane and pre-slide BSR has been observed in the past and taken as an indication that gas hydrates play an important part in slope failure (e.g. Dillon et al., 1998; Spence et al., 2010). Starting with Carpenter (1981), the coincidence of submarine landslide scars with the BSR has been reported in several studies.

Alternatively, gas hydrate dissociation can also be a consequence of submarine landslides (e.g. Delisle et al., 1998). Either the removal of a substantial part of the overburden pressure or the removal of gas-hydrate-bearing sediment can expose gas hydrate to P-T-conditions in which

it becomes unstable. Brewer et al. (2002) and Paull et al. (2003) have shown how easily sub-seafloor gas hydrate can be removed from its initial location and how the released methane subsequently has even been able to reach the atmosphere. The expulsion of methane into the atmosphere might then have further implications on global climate.

### 1.2.2 Detection and quantification of marine gas hydrates

The detection of gas hydrates is enabled mainly by their effects on the bulk properties of the host sediment. The presence of gas hydrate is known to increase sonic velocity and electrical resistivity of sediment and to decrease the effective porosity. Thus, the remote sensing of gas hydrate is possible.

Seismic methods used to study gas hydrates are single-channel seismic (SCS), multi-channel seismic (MCS), 3D-seismic, deep-towed acoustics geophysics (DTAGS), and ocean bottom seismometer data (OBS). These different systems vary in their source-receiver offsets, depth of penetration, and spatial resolution (depending mainly on dominant frequency) thereby resolving different aspects of gas hydrate systems. The presence of a small amount of free gas, as low as 1% of pore space, below the GHSZ can be sufficient to give rise to a strong impedance contrast. Thus, the existence of a BSR only proves the existence of a negative velocity contrast but does not guarantee the presence of significant gas hydrate.

Since the BSR is a velocity gradient that occurs over a range of ~4 m, the ideal frequency range for BSR identification lies between 20 and 650 Hz (Fink and Spence, 1999; Chapman et al., 2002). In cases where the identification of the BSR is hampered by stratigraphy or where a BSR is expected but missing, its depth can be calculated theoretically if local heat flow, thermal conductivity, geothermal gradient, and seafloor temperature are known. The BSR is much more

sensitive to temperature than to pressure and in cases where lateral heat flow is fairly constant, the BSR can be seen as an isotherm (e.g. Spence et al., 2010).

Gas hydrate cemented sediments have higher P- and S-wave velocities and hydrate concentration can therefore be estimated from the amount by which interval velocities increase relative to a no-hydrate reference velocity. P-wave velocity has been determined by the tomographic inversion of travel-times, 1D full-waveform inversion and acoustic impedance inversion, and the conversion of P-wave velocity into gas hydrate concentration has been attempted by the effective porosity-reduction method, the time-averaging and weighted equations methods, and from rock-physics and effective medium theory modeling (e.g. summary by Spence et al., 2010). The appropriate conversion relation for the increase in p- and S-wave velocities with hydrate concentration is also a function of gas hydrate distribution. This is a complex phenomenon; pore-filling gas hydrate has little effect on S-wave velocity but increases P-wave velocity, whereas grain-cementing gas hydrate increases both P- and S-wave velocities (e.g. Dvorkin and Nur, 1993; Lee et al., 1993; Yuan et al., 1996; Helgerud et al., 1999; Dvorkin et al., 2000; Chand et al., 2004; Spence et al., 2010). As P-wave velocity is mostly affected by the sediment's bulk modulus, methods to determine S-wave velocity, particularly OBS studies that allow estimations of shear velocities are the most effective tools to quantify the mode of gas hydrate occurrence and the shear strength of marine sediments.

Further seismic indicators for the presence of gas hydrates are seismic attenuation, amplitude blanking, and velocity pull-up. The strength of the attenuation depends on seismic frequency, the amount of gas hydrate present, and the way it is distributed within the sediment. The often observed heterogeneity of the gas hydrate distribution can lead to anisotropy in the

physical properties used to find and quantify hydrates (e.g. Pecher et al., 2003; Haacke and Westbrook, 2006; Spence et al., 2010).

Among other seismic and non-seismic techniques used to study gas hydrates are high-resolution 3.5–12 kHz sub-bottom profiling, 12 kHz SeaMARC acoustic imaging, piston coring, controlled-source electromagnetics (CSEM), seafloor compliance, and deep sea drilling (DSDP/ODP/IODP). High-resolution side-scan sonar acoustic imagery surveys focus on the hydrate-related seafloor expressions of methane flux, such as faults and pockmarks, as well as signs of gas-hydrate-related mass wasting (e.g. Kenyon, 1987; Masson et al., 1997). Deep sea drilling downhole measurements such as wireline logging and logging-while-drilling (LWD) measure neutron porosity, heat flow, magnetic susceptibility, electrical resistivity, chlorinity, or sonic velocity. Since gas hydrate dissociation is an endothermic reaction and leads to the release of fresh water, the decrease in ambient temperatures and the increase in pore water salinity in recovered cores can be used to detect and quantify gas hydrate. Furthermore, gas hydrate presence increases electric resistivity, an effect that can also be translated into gas hydrate concentration.

Sediment coring is used to study gas hydrate occurrence more directly. Apart from the possibility to retrieve actual samples of gas hydrate, infrared scanning of cores can reveal signs of coring-related gas hydrate dissociation expressed in the form of cold spots. Visual core observations can identify soupy or mousse-like sediment textures that have been associated with gas hydrate. Finally, X-ray computed tomography (CT) can be used to image gas hydrate distribution within the cores (e.g. Schultheiss et al., 2010).

## 1.3 Geologic setting of the northern Cascadia margin

The northern Cascadia margin is located along the coast of British Columbia and offshore of the northwestern corner of Washington State. Here, the Juan de Fuca plate is being subducted underneath the North American plate for the past ~180 Ma. Subduction related destructive thrust earthquakes with magnitudes of 8.0 and greater have occurred in the past, the most recent being the megathrust earthquake of 1700. Processes such as the expulsion and transportation of pore fluids that accompany subduction also form an important supply mechanism for the local gas hydrate system. A BSR is present over much of the continental shelf off Vancouver Island, covering an area of roughly 250 km x 30 km (Hyndman et al., 2001) (Fig. 1.5).

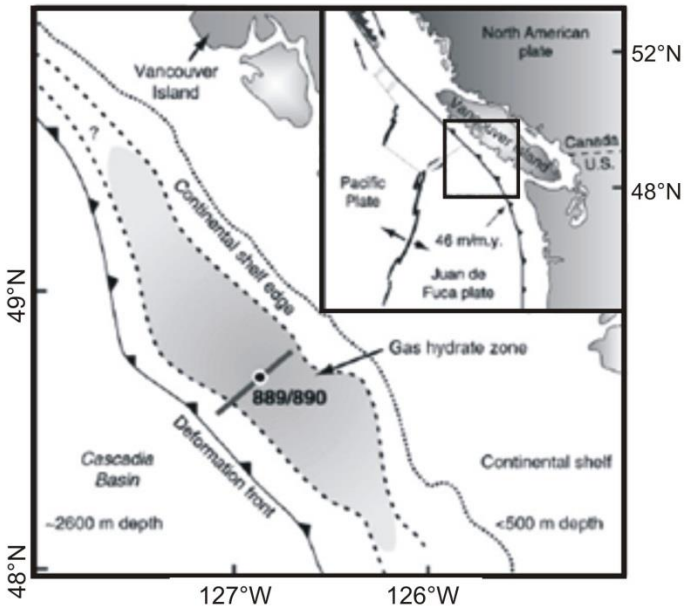


**Figure 1.5**: Area of BSR occurrence along the northern Cascadia margin. Sites 889/890 were drilled during ODP Leg 146. Black line indicates drilling transect for IODP Leg 311 (Hyndman et al., 1994)

For several decades, extensive research has been conducted to assess the potential of a future major thrust earthquake and to explore the nature of the gas hydrate system. This led to a wealth of information on the local tectonics and structural geology, as well as the physical, geochemical, and biological processes essential for the existence of fluids and gas hydrate in this

region. The following review of the studies conducted along the northern Cascadia margin gives an introduction to the tectonic setting and to local gas hydrate occurrence.

### 1.3.1 The Cascadia subduction zone

The Cascadia subduction zone stretches from the central part of Vancouver Island down to Cape Mendocino in California. It is the result of the relative motion between the Pacific and North America plates and the oblique subduction of the Juan de Fuca plate at a rate of ~40-46 mm/yr (Davis and Hyndman, 1989). The Juan de Fuca plate system is further fragmented into the Explorer and the Gorda plate in the north and south, respectively. Both plates are separated from the main plate via large faults and fracture zones which themselves are in the process of breaking up (Fig. 1.6).

Offshore Vancouver Island the oceanic plate is relatively young (2 to 6 Ma) and therefore warm and buoyant (Davis et al., 1990). The km-thick sedimentary section that lies on top of the oceanic plate near the deformation front consists of hemi-pelagic sediments and Pleistocene turbidites. At the deformation front, the sedimentary section is mainly off-scraped and accreted to the margin and ongoing sedimentation covers the already accreted sediments with pelagic material. Subduction is accompanied by sediment thickening and deformation, bulk shortening, folding, faulting, as well as fluid expulsion (e.g. Hyndman and Wang, 1993; Hyndman et al., 1993).

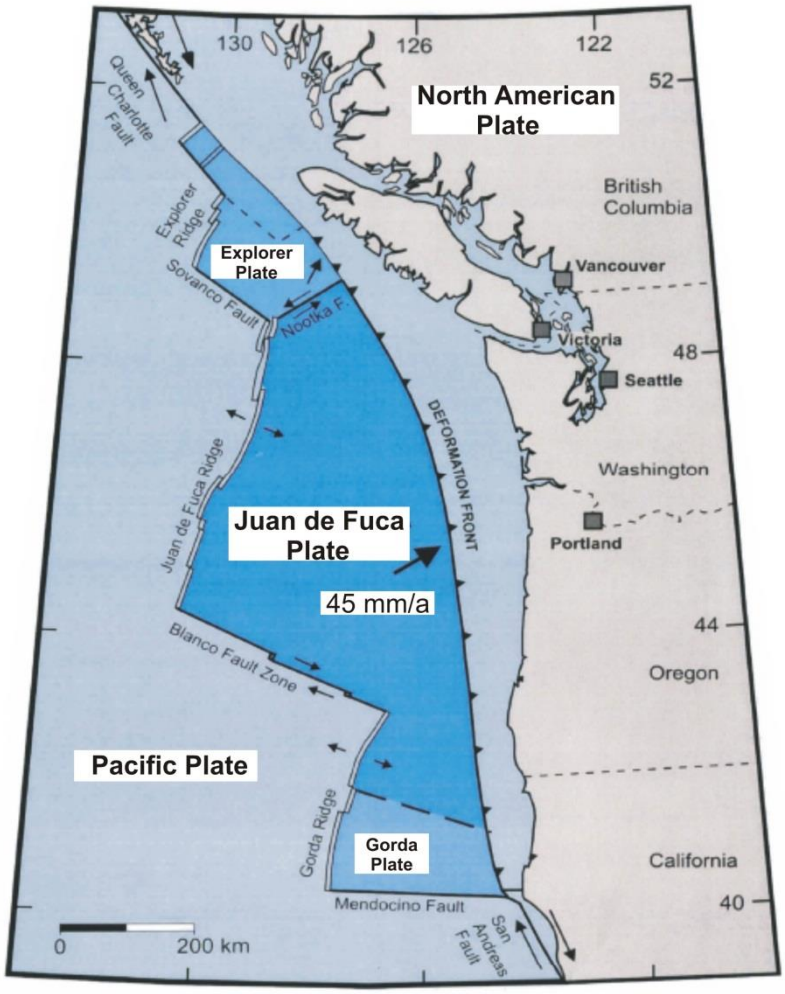


**Figure 1.6**: Overview of the Cascadia subduction zone plate system (modified after Hyndman, 1995)

At the northern Cascadia margin, earthquakes with magnitudes of $\leq 7$ are common. Additionally, there is now convincing evidence for past and the likelihood of future, very large, tsunamigenic 'megathrust' events of up to M9. There is strong proof for margin-wide events over the past 3000 to 7000 years with a recurrence rate of 400 to 600 years (e.g. Hyndman and Wang, 1995a; Clague and Bobrowsky, 1994; Atwater et al., 1995; Hyndman, 1995; Goldfinger et al., 2003; McAdoo et al., 2004). The ongoing shortening of the coastal region in the direction of plate convergence suggests that the majority of the shallow part of the subduction zone, extending from the continental shelf break to the base of the accretionary prism, might be locked

and thus accumulating elastic strain energy for a future major thrust earthquake (Dragert et al., 1994; Hyndman and Wang, 1995b; Hyndman, 2013; McCaffrey et al., 2013).

The incoming accreted sediment represents the building material for a series of anticlines situated along the deformation front at the toe of the continental shelf. Anticline formation is controlled by the occurrence of steeply landward-dipping thrust faults which penetrate down to near the décollement, acting as ramps on which sediments are pushed upwards. Here, the recession of the ice sheets following the LGM has led to the deposition of glacial material and ice-rafted debris on top of more porous, organic-rich sediments. This provided the necessary trap for natural gasses for gas hydrate formation.

### 1.3.2 Gas hydrate occurrence at the northern Cascadia margin

The first signs of gas hydrate within the accretionary prism off Vancouver Island were found in 1985 (as summarized by Riedel et al., 2010). Multi-channel seismic lines revealed the occurrence of a BSR underlying much of the continental slope (Fig. 1.5). Studies such as Hyndman and Spence (1992a) and Hyndman et al. (2001) have mapped the extent of the local BSR. The seaward limit was found to lie 5-10 km to the east of the deformation front at water depths between 800 and 2200 m. BSR depths are generally around 230 to 250 mbsf. At seismic frequencies between 20 and 650 Hz the velocity gradient that gives rise to the BSR covers a depth interval of 6 to 10 m (Chapman et al., 2002).

Core samples confirmed the existence of partly massive amounts of gas hydrate (Riedel et al., 2002; 2010). Gas hydrate in this region consists almost exclusively of microbial methane with the exception of a cold vent site at Site U1328, approximately 20 km landward of the frontal ridges where there is some thermogenic methane (e.g. Whiticar et al., 1995; Pohlman et al., 2009; Riedel et al., 2010). Infrared imagery of cores showed that the distribution is largely

controlled by lithology. Gas hydrate is found mostly within coarser sandy/silt turbidites as well as in coarse-grained sand layers and in fault-controlled fluid and gas migration conduits where it locally exceeds 80% of the pore space (e.g. Riedel et al., 2006c; Malinverno et al., 2008; Riedel et al., 2010). The explanation for the small-scale distribution is that in fine-grained muds methane stays in solution and diffuses into coarser grained sand or silt layers where it then forms concentrated gas hydrate leading to the highly heterogeneous gas hydrate distribution observed in this region (Malinverno, 2010).

## 1.4 Introduction to submarine landslides and landslide hazard assessment

Submarine mass movements are important sediment transport agents from the continental shelf to the deep ocean and play an active part in shaping the seafloor along continental margins (e.g. McAdoo et al., 2000). After the Grand Banks landslide of 1929 that generated a significant tsunami marked by the severing of several deep sea cables, international research focussed more on submarine landslides as a geo-hazard. Increasing interest stems from the potential destructive impact on the growing number of offshore installations such as sub-sea wells, pipelines, exploration and production platforms, and data transmission ocean cables. Submarine landslides also pose a threat onshore, triggering tsunami waves that can endanger harbors and settlements along the coast, thus representing enormous societal and economic threats.

### 1.4.1 Submarine landslides

Slope instability occurs when there is either a significant reduction in the shear strength of the slope material or an increase in the driving forces in the slope direction. The causes for slope failure are divided into long-term and short-term factors, also called ‘pre-conditioners’ and ‘triggers’. Pre-conditioning factors weaken the slope, making it prone to failure. High

sedimentation rates, steep slope angles, free gas occurrence, gas seepage, erosion, and gas hydrate occurrence are among the known pre-conditioning factors. An important pre-conditioner is high pore pressure resulting from rapid sedimentation. Trigger mechanisms are the ultimate causes for slope failure and include transient overpressures, seepage forces, tidal events, ocean storm waves, mud volcano activity, sediment creep, tsunamis, sea-level changes, and potentially gas hydrate dissociation. However, earthquake shaking is probably the most obvious and frequent trigger. Earthquake-induced forces decrease sediment strength and can generate a transient increase in pore pressure. In the most extreme cases, earthquake shaking can lead to sediment liquefaction.

In reality, slope failure is most likely the result of an interplay between pre-conditioning and triggering factors rather than resulting from one single cause. For example, the presence of free gas alone might not induce failure but provide the necessary reduction in shear strength for the next earthquake to destabilize the slope.

Once initiated, the sliding process involves a range of mechanisms. Submarine landslides can be purely gravity-driven, laminar, or turbulent depending on whether they remain cohesive slides and slumps or transform into flows and turbidity currents (e.g. Mulder and Cochonat, 1996). Submarine slope failures also vary in volume from less than one cubic kilometre to tens of thousands of cubic kilometres. For example, the Agulhas Slide offshore South Africa displaced 20,000 $km^3$ of material downslope (McAdoo et al., 2000). Seafloor slides often move at higher speeds than their onshore counterparts and can reach velocities of up to 19 m/s (e.g. Piper et al., 1999; Elverhøi et al., 2000; De Blasio et al., 2005) making them especially dangerous for offshore infrastructure. Debris flows are known for their potential to travel large distances even at slope angles as low as 0.1° (e.g. McAdoo et al., 2000; De Blasio et al., 2004).

Submarine landslides can occur anywhere between the equatorial and polar regions at passive or active margins, at rift and transform margins, as well as on the slopes of oceanic volcanoes. They are concentrated along the coasts of North America and Europe, including the Atlantic and Pacific coasts of both the US and Canada, the Gulf of Mexico and the Gulf of Alaska, in the region of the Aleutian Islands as well as United Kingdom, Norway, Greece, and France. The apparent scarcity of landslides along the coasts of Africa is probably due to the absence of detailed mapping. Hance (2003) and Meyer et al. (2010) have reported the signs of giant submarine landslides in NW Africa.

Along the US coast McAdoo et al. (2000) identified the offshore regions of California, Oregon, Texas and New Jersey as the most prone areas for submarine landslides. Amongst the significant slides which originated off the east coast are the well-known Cape Fear and the Currituck slides. The Cape Fear event was noteworthy as it produced a 50 km long slide scar directly above a region of gas hydrate occurrence (Paull et al., 1996; Locat et al., 2009).

The probably most well-known underwater landslide in Canada was triggered by the Grand Banks earthquake of 1929. It generated a tsunami that caused extensive damage along the coast of Newfoundland and killed 27 people in its wake. The debris flow traveled over a distance of >80 km and the subsequent turbidity current went as far as 1,000 km rupturing many seafloor trans-Atlantic cables. The total mass transported during this event amounted to 200 $km^3$ and the sequence of recorded successive cable breaks suggested that the slide moved at a velocity of ~5 m/s. This event was of great significance in landslide research since it was the first incident that provided ‘real-time’ data of the event and so it can be seen as the initiator for the modern study of submarine landslides (e.g. Locat et al., 1990; Jiang and LeBlond, 1992). A further example is the Kitimat Slide of 1995, in which parts of the sidewall of a narrow fjord in British Columbia

failed and generated water waves with amplitudes reaching heights up to 8.2 m. The Kitimat Slide mobilized a sediment volume of $2.6\times10^7$ $m^3$ within a time window of 0.5 to 2 mins (Murty, 1979; Prior et al., 1982a).

At passive margins the mass movements tend to be large following a prolonged time of sediment accumulation, but the frequency of submarine landslides is higher at active margins due to frequent earthquake-related triggering. Slide events worldwide seem to follow climatic patterns. Between 45 ka BP and 16 ka BP many events can be tied to a lowering in sea-level, and a reduction in the hydrostatic pressure destabilized gas hydrate deposits. Several authors (e.g. Nisbet and Piper, 1998; Rothwell et al., 1998) noted that between 25 ka BP and 15 ka BP giant masses of sediment were relocated. The bulk of slope failures studied by Maslin et al. (2004) occurred during two relatively short time periods between 15 and 13 ka BP and between 11 and 8 ka BP. The first interval is associated with the onset of sea-level increase as a response to rapid deglaciation, and mass wasting was mostly confined to low latitudes. The second period of slope failure falls into a time during which sea-levels rose especially rapidly. This time most of the failure events occurred at higher latitudes, including the Storegga Slide. Maslin et al. (2004) associated these slides with glacial isostatic rebound that decreased hydrostatic pressure, potentially triggering gas hydrate dissociation and increasing earthquake activity.

Submarine landslides may be classified via their sedimentology, morphology and slide mechanism (e.g. Mulder and Cochonat, 1996; Locat and Lee, 2002). Fig. 1.7a shows several approaches that have been used to study submarine landslides and Fig. 1.7b summarizes the different styles of failure that have been observed.

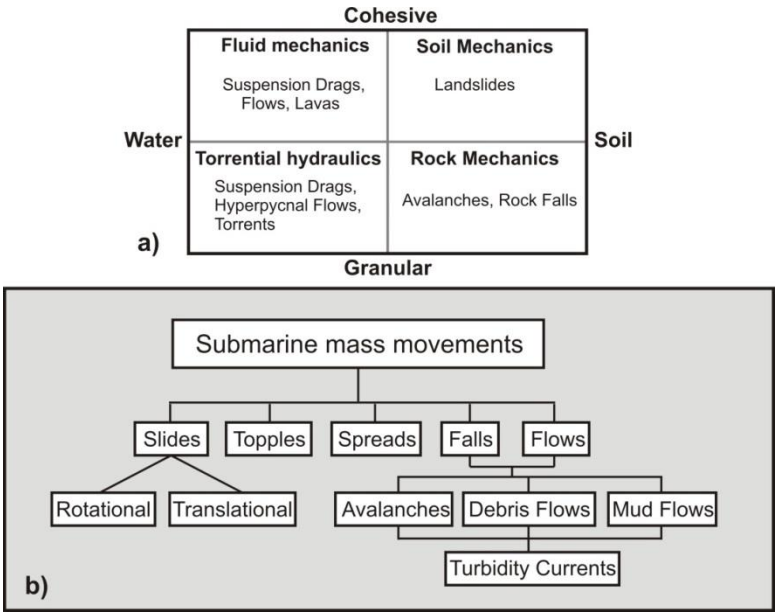


**Figure 1.7**: a) Subdivision of submarine mass movements according to their water and solid content and the physics involved in the phenomena; b) classification of submarine mass movements according to their geomorphology and style of failure (modified from Local and Lee, 2002)

Slides can be rotational, involving a rupture surface that is curved concavely and a movement of the material that is roughly rotational. Alternatively, slides can be translational, moving along a roughly planar surface with little rotation of the sliding material. Flows in turn, are subdivided into avalanches, mudflows, and debris flows which can further transform into turbidity currents (e.g. Mulder and Cochonat, 1996; Locat and Lee, 2002). This study focusses on the slides as well as debris flows.

Probably the most dangerous aspect of submarine landslides is their ability to generate tsunamis. The Storegga Slide is a well-known example of a slide-generated tsunami with waves reaching heights of 3 to 5 m along the coasts of Norway, Greenland, Iceland, and Scotland (Harbitz, 1992). In 1998, a tsunami in Papua New Guinea associated with a M7.1 earthquake killed around 2000 people. The tsunami was found to have been caused by an underwater slide triggered by the earthquake (Synolakis et al., 2002). Among the most well-known examples for landside-generated tsunamis along the coast of Canada are the 1929 Grand Banks slide linked to

the most catastrophic tsunami in Canada's history and the Kitimat Slide that produced a 6 to 13 m run-up in a British Columbia fjord (Murty, 1979) Fig. 1.8 summarizes known tsunamigenic submarine landslides along the west coast of Canada and Alaska, USA.

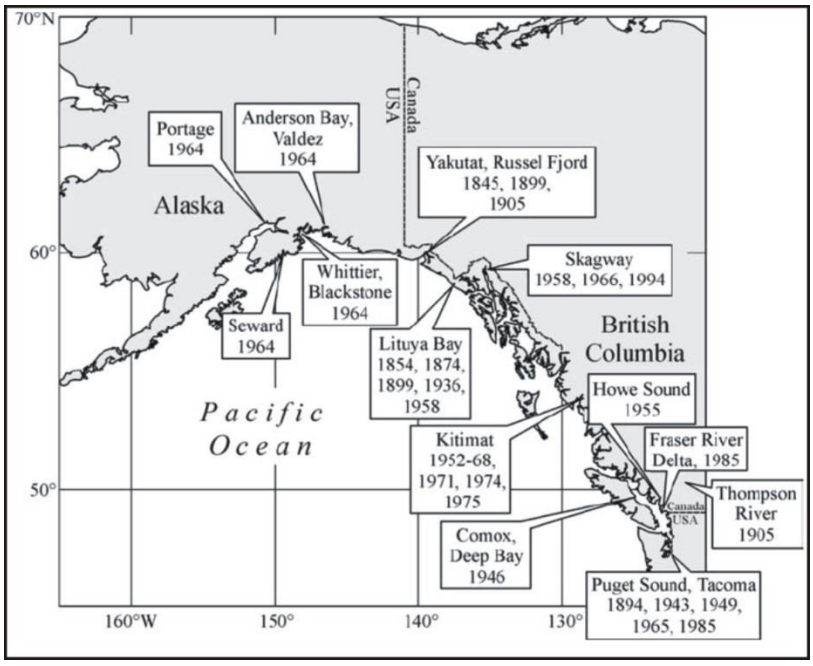


**Figure 1.8**: Landslide-generated tsunamis along the west coast of BC and Alaska, USA (taken from Rabinovich et al., 2003)

### 1.4.2 Assessment of the potential for offshore slope instability: methodology and examples of previous studies

Slope stability hazard assessments evaluate the areas that are prone to near-future failure and try to estimate the frequency of mass movements, previous and future triggers, the likelihood, extent and impact of a future event, and the possibility of a re-activation of previous slides. This information is also an important input for tsunami hazard estimation and the numerical calculation of expected run-up of tsunami waves (Locat and Lee, 2002; Leonard et al., 2010).

Important tools for the study of submarine landslides include detailed multi-beam swath bathymetry, side scan sonar, and 3D seismic profiling to get an image of the seafloor topography, the slide scar geometry, and sub-bottom stratigraphy (e.g. Piper et al., 1999). With a high-resolution bathymetry data set, powerful tools such as GIS can be used and a regional map of landslide susceptibility can be derived. Furthermore, the geomorphology of a mass deposit or of the whole margin can assist in the assessment of the possible triggers and prevalent failure. Margin geomorphology can also deliver important clues on local tectonics, especially since the subduction of slide material can act as future asperities or lead to 'slow earthquakes' (e.g. Kanamori and Kokuchi, 1993; McAdoo et al., 2000; McAdoo et al., 2004).

3D seismic reflection data in combination with seismic attributes are useful to detect faults and fractures that could represent areas of weakness and may be involved in the mechanics of previous failures. As an example, 3D seismic surveys were used to study slope failure and characterize mass transport deposits such as offshore Norway and helped to distinguish between the different slide mechanisms (Bull et al., 2008).

Further important information comes from the sediment's physical and geomechanical properties derived via downhole logging and coring, and by laboratory tests on sediment samples. The latter includes visual description (core disturbance, sedimentology, etc.), the derivation of sediment parameters, pore pressure quantification, and the testing of sediment strength properties. Strasser et al. (2010) highlight the importance of scientific drilling in slope failure studies using the example of the Nankai accretionary wedge. Furthermore, the knowledge of local and regional geologic processes assists in the estimation of trigger mechanisms. Historic landslides can provide information on regional recurrence rates, common triggers, and prevalent slide mechanisms. Lastly, numerical methods are an important tool to test hypotheses, to

estimate, quantify, simulate, understand, and visualize acting forces and geologic processes using a mathematical description of the underlying physical processes. For instance, Viesca and Rice (2010) employed finite element (FE) methods to model the slope instability as shear rupture propagation.

## 1.5 Previous gas hydrate and slope failure studies along the northern Cascadia margin

Previously, the main focus of research along the Cascadia subduction zone has been the assessment of local earthquake hazard and the characterization of the regional gas hydrate system. First descriptions of the geometry, internal structure, and deformation of the accretionary wedge were accomplished in the framework of the Lithoprobe surveys of 1984 and 1985 onshore (Yorath et al., 1985; Clowes et al., 1987) and the Frontier Geoscience Program of the Geological Survey of Canada (e.g. Hyndman et al., 1990). Later surveys along the Cascadia margin focused on seismic data acquisition and evaluation at smaller scales. Offshore Oregon, MCS and OBS data, vertical seismic profiles (VSP), and 3D seismic data were collected in 2000 (e.g. Tréhu and Flueh, 2001; Bangs et al., 2005; Kumar et al., 2006). Offshore Vancouver Island surveys included a second industry style MCS study conducted in 1989 (Hyndman and Spence, 1992a). Further studies included 2D and pseudo-3D SCS and MCS and high-resolution seismic studies (e.g. Yuan et al., 1996, 1999; Fink and Spence, 1999; Gettrust et al., 1999; Riedel et al., 2002; Chapman et al., 2002), VSP and (MacKay et al., 1994), OBS surveys (Spence et al., 1995; Hobro, 1999; Hobro et al., 2005), swath-bathymetry mapping, high-resolution sub-bottom profiling, and heat-flow studies (e.g. Davis et al., 1990; Ganguly et al., 2000).

Gas hydrates in particular have been studied using seismic reflection and refraction profiling. For multichannel data, common analysis methods that have been applied at the

northern Cascadia margin are Amplitude Versus Offset (AVO) (e.g. Hyndman and Spence, 1992; Chen et al., 2007) and full waveform inversion (FWI) (e.g. Yuan et al., 1999). Non-seismic methods include piston coring, geochemical and geophysical sediment analyses (e.g. Novosel, 2002; Solem et al., 2002; Riedel et al., 2006b), heat flow probe measurements (Davis et al., 1990; Hyndman et al., 1994; Riedel et al., 2006a), seafloor imaging using a remotely operating submersible (ROPOS) (e.g. Riedel et al., 2006a), magnetic susceptibility measurements (Novosel et al., 2005), swath bathymetry and acoustic imaging of the seafloor-topography (Zuehlsdorff and Spiess, 2004), electrical and electromagnetic studies (Edwards, 1997; Yuan and Edwards, 2000; Schwalenberg et al., 2005), seafloor compliance (e.g. Willoughby et al., 2005), and piston coring (Novosel, 2002; Riedel et al., 2002). In the course of these studies, gas hydrate concentrations were estimated using stacking velocity analyses, 1D full waveform inversion, and seismic refraction analyses of OBS data. Further estimates were made based on pore-water chlorinity excursions and on electrical resistivity-measurements combined with Archie's analyses (e.g. Yuan et al., 1996; Yuan et al., 1999; Hobro et al., 2005; Chen, 2006).

The most recent estimates of gas hydrate and free gas concentrations are based on the results of Expedition 311 of the Integrated Ocean Drilling Project (IODP) (Riedel et al, 2010). During earlier ODP Leg 146 in 1992 the drilling targeted the whole Cascadia margin. ODP Leg 204 and IODP Expedition 311 conducted in 2002 and 2005 focused specifically on the gas hydrate systems offshore Oregon and Vancouver Island. Fig. 1.9 shows the location of all three expeditions along the Cascadia margin.

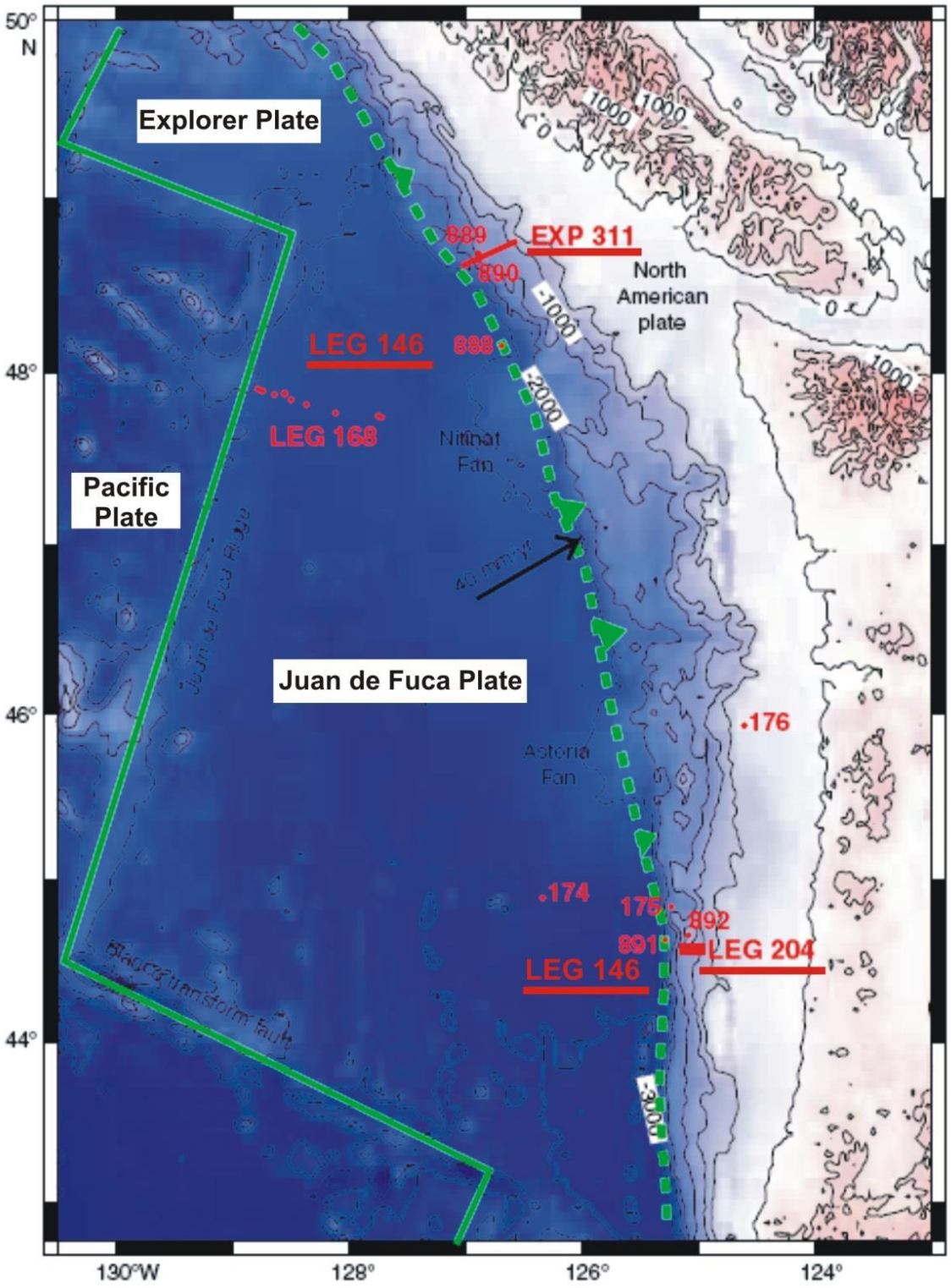


**Figure 1.9**: Locations of the IODP Expedition 311, ODP Leg 204, and ODP Leg 146 along the Cascadia margin; regional bathymetry is shown as well as plate boundaries and relative plate motion; ODP Legs 146, 204, and IODP Leg 311 are underlined in red (modified after Tréhu et al., 2006)

The main focus of ODP Leg 146 lay on the broader aspect of regional sediment consolidation and fluid expulsion with the link to the regional BSR-occurrence. ODP Leg 204 was carried out in order to help understand the process of gas hydrate occurrence within the framework of accretionary complexes. Nine closely spaced boreholes were drilled near the Sites 891 and 892 of ODP Leg 146 to study a system of gas hydrates and cold seeps discovered at an anticline close to the deformation front offshore the coast of Oregon (Tréhu et al., 2006).

IODP Expedition 311 aimed to study the nature of the gas hydrate formation and distribution along the northern Cascadia margin. Five sites were drilled, with four of them (U1325, U1326, U1327, U1329) positioned along a seismic transect coinciding with the MCS-line of a former survey (Fig. 1.10a). Site U1325 lies within a slope basin directly behind the first row of anticlines and Site U1326 is situated on the crest of Orca Ridge which is part of the research focus of this study. The location of Site U1327 approximately matches the ODP 146 Sites 889/890, and Site U1329 is situated near the landward limit of regional gas hydrate stability. The fifth site, U1328, is located at a cold vent field with active fluid and gas expulsion, drilled in order to compare focused fluid flow to the regional pervasive fluid regime (Fig. 1.10b).

Analysis of core and borehole P-wave velocity, electrical resistivity, and salinity measured during IODP Expedition 311 provided estimated average concentrations of gas hydrate of ~5%, much smaller than previous estimates based mainly on seismic data. Expedition 311 also revealed the strong influence of lithology on gas hydrate occurrence. The relatively shallow gas hydrate occurrence observed at depths <100 mbsf subsequently led to a revision of the pore fluid expulsion model of Hyndman and Davis (1992). This model had suggested that the highest gas hydrate concentrations should lie close to the base of the GHSZ. The drilling data showed that

shallow gas hydrate occurrence can only be explained by a significant locally focussed advective component of the fluid flow (Riedel et al., 2010) rather than just by regional upflow.

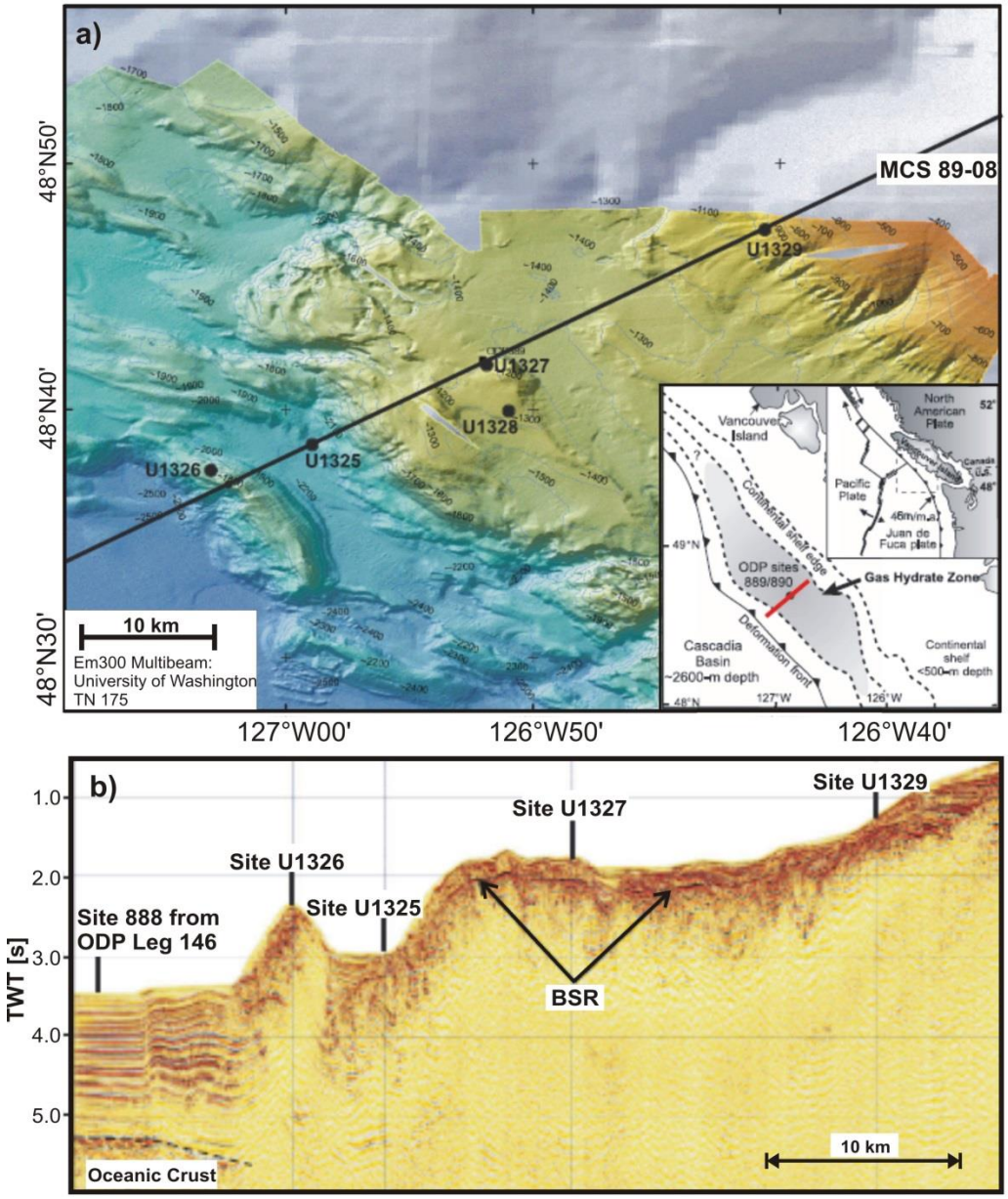


**Figure 1.10**: a) Locations of the IODP Expedition 311 drill sites along transect (location indicated as red line in inset); b) MCS line 89-08 with drill-sites (modified after Riedel et al., 2010)

The three most recent marine surveys along the northern Cascadia margin in 2004, 2008, and 2010 focused on the frontal ridges along the deformation front. Lopez (2007) performed the

first study at the northern Cascadia margin that focused on regional slope stability, using seismic data acquired during the 2004 survey. She was also the first to address the possible link between gas hydrate distribution, formation, and dissociation and the pervasive occurrence of landslides along the lower continental slope of the northern Cascadia margin.

The marine seismic survey and core sampling of 2008 on CSS John P. Tully that collected part of the data used in this studies was led by scientists from the Geological Survey of Canada, the University of Victoria, the US Geological Survey, McGill University, Florida State University, and the US Department of Energy. The aim was to add more information on the causal role of gas hydrate in ridge stability and the response of the gas hydrate system to regional slope failure. They investigated the nature of a set of normal faults first mentioned by Lopez (2007) and situated along the crest of Orca Ridge potentially acting as fluid pathways. The survey included high-resolution physical property, pore-water geochemistry, and biochemistry measurements, visual core descriptions, as well as seismic reflection and echo-sounder profiling. At three slumps, including the ones on Orca and Slipstream Ridge, seismic data were acquired and core samples taken, providing valuable information on the age of the slumps and of the local gas hydrate system.

The Seafloor Earthquake Array – Japan Canada Cascadia Experiment (SeaJade) of 2010 is the most recent study conducted along the northern Cascadia margin. In its course, 33 short-period OBS were deployed over a period of 3 months and 10 broadband OBS were placed on the seafloor for one whole year. The objectives included the acquisition of passive seismic data to assess the local earthquake hazard and the recording of active seismic data across Slipstream Ridge to further investigate landslide occurrence along the margin.

## 1.6 Thesis outline

The thesis has the following structure:

Chapter 1 gives a general introduction to gas hydrates, the tectonic setting, and submarine landslides as well as previous studies that were conducted along the northern Cascadia margin. Chapter 2 summarizes the observations based on regional multi-beam bathymetry, seismic, core and log data. Log-density data from both ODP Leg 204 and IODP Expedition 311 are used in Chapter 3 to estimate the present pore pressure. Chapter 4 calculates expected ground accelerations due to different earthquake scenarios and estimates possible amplification effects due to the local topography. Chapters 5 and 6 explore the history of the GHSZ boundaries resulting from sealevel and seafloor temperature changes, in relation to observed slope failure and estimate the pore pressure that could result from gas hydrate dissociation. In Chapter 7 a slope stability analysis is carried out, calculating the critical taper angle for the whole margin as well as the factor of safety along the slopes of Orca and Slipstream Ridge. Additionally, the critical values for pore pressure and horizontal ground acceleration are compared with the estimates from Chapters 3 to 6. Finally, Chapter 9 models the sliding process using a 2D-finite difference code to investigate the difference between debris flows and blocky slides along the deformation front of the northern Cascadia margin.

Appendix A contains additional pore pressure figures and Appendix B summarizes the coefficients used in the ground motion attenuation relationships. Lastly, Appendix C contains two published papers resulting from work done during this thesis program but outside the principle thesis area. The studies were conducted in the Ulleung Basin in South Korea and used seismic coherency as a tool to characterize mass transport deposit (MTD) features in a region of presumed gas hydrate occurrence.

# Chapter 2: SLOPE FAILURE ALONG THE NORTHERN CASCADIA MARGIN: DATA AND OBSERVATIONS

This study uses local bathymetry, active seismic and physical property data to study the slope failure of two frontal ridges along the northern Cascadia margin and to assess the role of gas hydrates in slope stability. High-resolution multi-beam swath-bathymetry provided the detailed depth information needed to analyze the ridge geometry and geomorphology. Together with information on the sediment's physical properties, the bathymetry represented an input for the slope stability analysis and slide characterization. In combination with the local sea-level history and the knowledge of local thermal characteristics, the bathymetry was also used to calculate changes in the depth of the gas hydrate stability boundaries over time. Physical property data were also used to estimate present-day pore pressure regimes and the response of the sediments to earthquake shaking. The following sections give an overview of the available data and the first observations.

## 2.1 Multi-beam swath bathymetry data

In 2004, a high-resolution EM 300 multi-beam swath bathymetry dataset was collected during a survey conducted by the University of Washington (Kelley and Delaney, 2005). Frequencies of 30 kHz were used for seafloor mapping with a horizontal resolution of 20 m by 20 m, and a vertical resolution of 0.2% to 0.5% of the water depth. The bathymetry covers a region between the abyssal plain and the edge of the continental shelf with water depths lying between 1500 and 2500 mbsf.

### 2.1.1 Entire margin

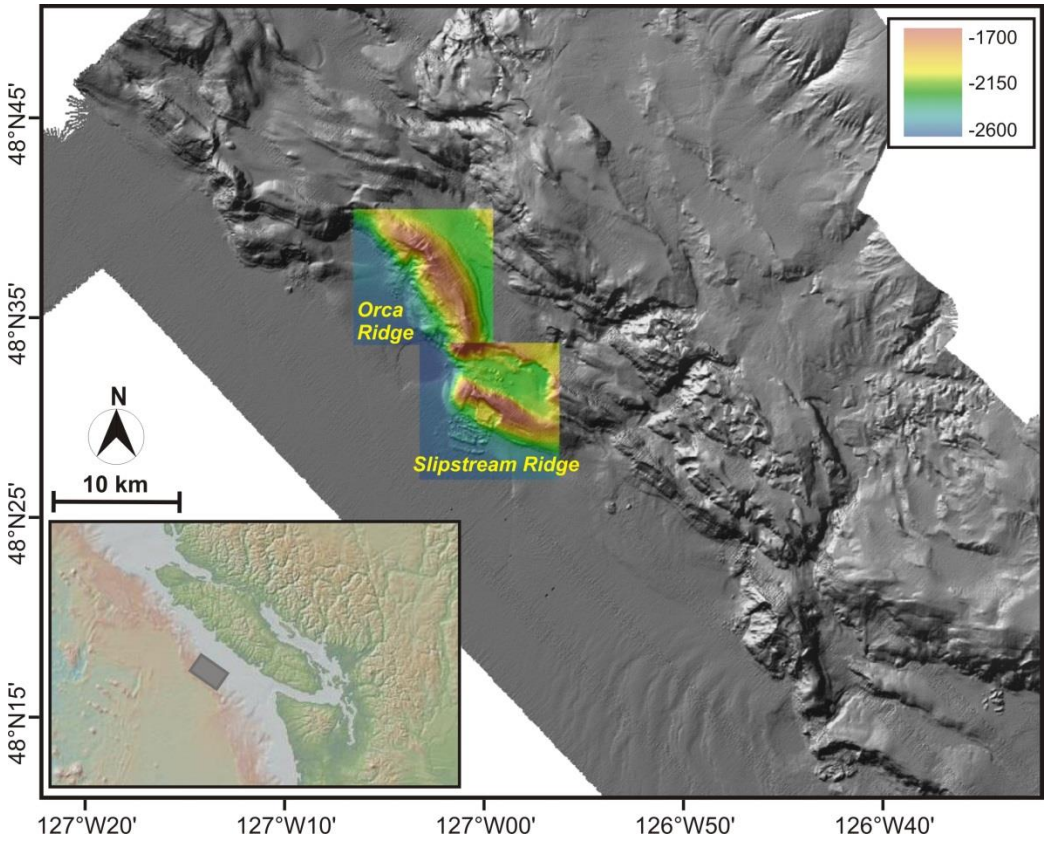


**Figure 2.1**: Side-lit multi-beam swath-bathymetry relief image of the northern Cascadia margin; inset (www.geomapp.org) shows location along the northern Cascadia margin

Fig. 2.1 shows the bathymetry of the deformation front along the northern Cascadia margin, a part of the margin that is relatively isolated from any recent sedimentary input. Also visible are canyons that might have played a role as sediment tributaries just after the last glaciation when the rate of sedimentation was much higher than at present. Several frontal ridges are aligned in a zigzag formation along the deformation front. The ridges, about 20 to 30 km in length (Davis and Hyndman, 1989), are seaward-verging and deviate from the average angle of convergence by $\leq 30°$ (2.12b).

The zigzag formation of the deformation front sets the northern Cascadia subduction zone apart from other active margins which mostly exhibit much more smoothly curved deformation

fronts such as the southern Cascadia margin, the Makran subduction zone, or the Nankai subduction zone (e.g. McAdoo et al., 2004).

***Morphology and style of failure along the northern Cascadia margin***

Along the northern Cascadia margin submarine landslides are mostly confined to the ridges along the deformation front and reveal a well-preserved morphology. Farther landward the seafloor shows less variation in topography and no significant signs of mass wasting (Fig. 2.1). Slope failure mainly occurs in the seaward direction. The exception is Slipstream Ridge where a significant steepening of the landward facing part indicates that this side of the ridge has failed in the past as well (Fig. 2.3b).

In a recent study, Naegeli (2010) focused on eight of the small-scale slumps and slides distributed over a distance of 75 km. There is a distinctive failure pattern along the northern Cascadia margin consisting of two different sliding mechanisms. Debris flows (DF) with small-scale sediment units alternate with blocky slides (BS) with large-scale sediment blocks, correlating with ridge orientation and geometry (Fig. 2.2).

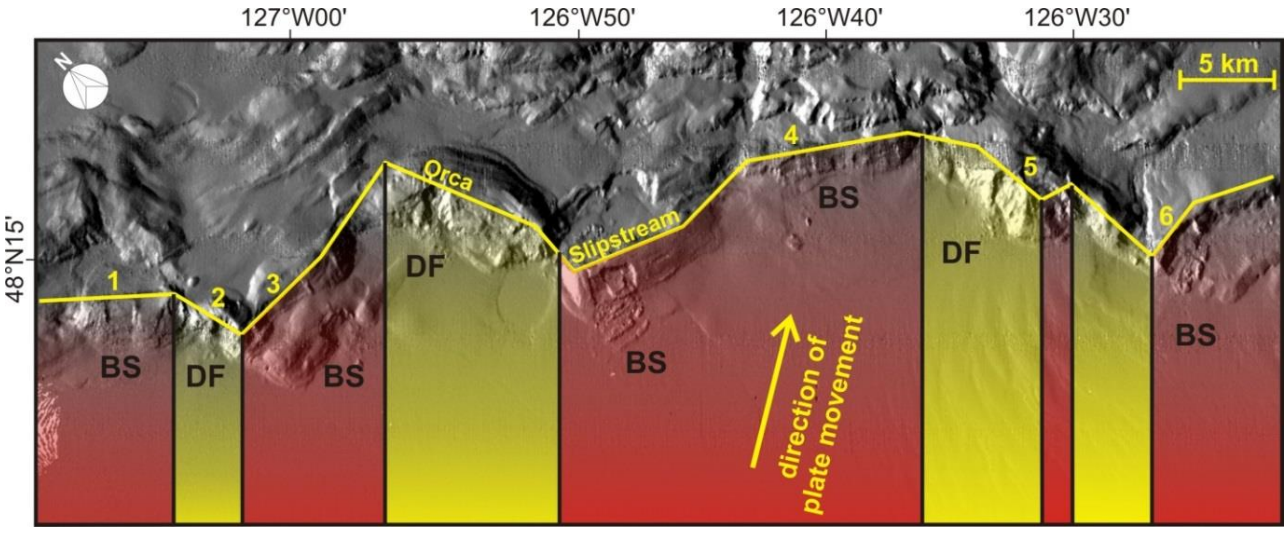


**Figure 2.2**: Detail of the ridges discussed by Naegeli (2010); red and yellow transparent boxes highlight the direction in which the failed frontal ridges are facing; BS=blocky slides, DF = debris flows; slide numbering is part of this thesis and given in Table 2.1

Fig. 2.2 shows that most debris flows are found on ridges facing approximately west, while the blockier slumps that failed as a more coherent mass occurred on ridges that face towards the south-southwest. Table 2.1 summarizes the results of the study by Naegeli (2010) with the numbering of the slides indicated in Fig. 2.2. Naegeli calculated the slide volumes by generating a virtual plane covering the failure area of each slide and subtracting the depth of the plane from the bathymetry underneath.

| Ridge | Direction | Height [m] | Slope angle (mean/max) [°] | Area [km$^2$] | Lost volume [km$^3$] | Length downslope* [km] | Morphology |
|---|---|---|---|---|---|---|---|
| **1** | SW | 540 | 13.0 / 15.7 | 3.2 | 0.019 | 2.0 | BS |
| **2** | NW | 790 | 20.0 / 24.0 | 2.0 | 0.151 | 1.4 | DF |
| **3** | SW | 370 | 11.5 / 15.9 | 2.3 | 0.128 | 1.2 | BS |
| **Orca** | NW | 880 | 17.3 / 26.8 | 3.8 | 0.409 | 2.4 | DF |
| **Slipstream** | SW | 500 | 16.1 / 25.7 | 5.0 | 0.237 | 2.0 | BS |
| **4** | SW | 550 | 14.4 / 16.4 | 1.5 | 0.049 | 0.7 | BS |
| **5** | NW | 985 | 18.0 / 24.0 | 4.6 | 0.629 | 2.2 | DF |
| **6** | SW | 470 | 18.9 / 29.4 | 4.1 | 0.338 | 1.3 | BS |

**Table 2.1**: Overview of results from a geometric characterization using ArcGIS® conducted by Naegeli (2010); BS = Blocky Slide, DF = Debris flow; the coloring highlights the correlation of sliding style with ridge-direction, ridge-height, and volume of lost material;
*: distance from the crest toe

Fig. 2.2 and Table 2.1 indicate that debris flows occur on the larger, slightly curved ridges that have been rotated and bent due to the local stress regime. Due to the bent shape of these ridges the head scarps are slightly rounded while blocky slides are rectangular in shape. As is characteristic for debris flows, no or little deposited fine-grained material can be identified in the bathymetry whereas some of the more coherent material of the blocky slides remained intact and is still visible at the toe of the ridges (Fig. 2.1).

According to Table 2.1, the amount of sediment that was removed during sliding is larger for debris flows than for blocky slides. The ratio of volume to area, which is the average depth of the failure plane, is lower for blocky slides than for debris flows. This seems to indicate that blocky slides generally have a shallower plane of failure than debris flows. The slide scars of debris flows seem to have higher maximum slope angles than blocky slides. This angle might have played a controlling factor in how deep the slide cut into the ridge and in the subsequent transformation of the slide into a debris flow.

Compared to some other margins the slides and slumps along the northern Cascadia margin are fairly small. McAdoo et al. (2000) has mapped slide features along all the US-American coasts (see Table 1 in McAdoo et al., 2000). Morphology, area, volume, and slope angles in Table 2.1 compare only moderately well to the observations along the southern Cascadia margin offshore Oregon. McAdoo et al. (2000) found that slope failure along the Oregon margin and the margin offshore New Jersey is more often disintegrative than blocky and some of the slides are considerably larger. Offshore California, where disintegrative slides are prevalent, the area and volume of slope failure exceeds that of the northern Cascadia margin by a factor of about 10.

### 2.1.2 Orca and Slipstream Ridge

Marked in color in Fig. 2.1 are Orca Ridge and Slipstream Ridge which are the focus of this study. The two ridges are only a few kilometers apart and their topographies reveal that they have experienced slope failure in the past. Orca Slide exhibits the visual characteristics of a debris flow with a disintegrative, incoherent morphology and no significant slide deposit (Lopez et al., 2010). Slipstream Slide is comprised of several cohesive blocks that remained intact throughout slope failure and have left an identifiable deposit on the present seafloor. Both ridges

probably failed progressively, exceeding peak material strength at different parts of the slope at different times. At its highest point, Orca Ridge stands 880 m above surrounding seafloor. The failed area extends over about 3.8 $km^2$, 1.5 km wide, and 2.5 km long (Table 2.1). The slide scar locally reaches the depth of the regional BSR (Lopez, 2007). Slipstream Ridge is lower in height, reaching about 500 m above the adjoining seafloor with a failure plane that extends over an area of ~5.0 $km^2$. The average net loss is 0.409 $km^3$ and 0.247 $km^3$ at Orca and Slipstream Slide, respectively (Naegeli, 2010).

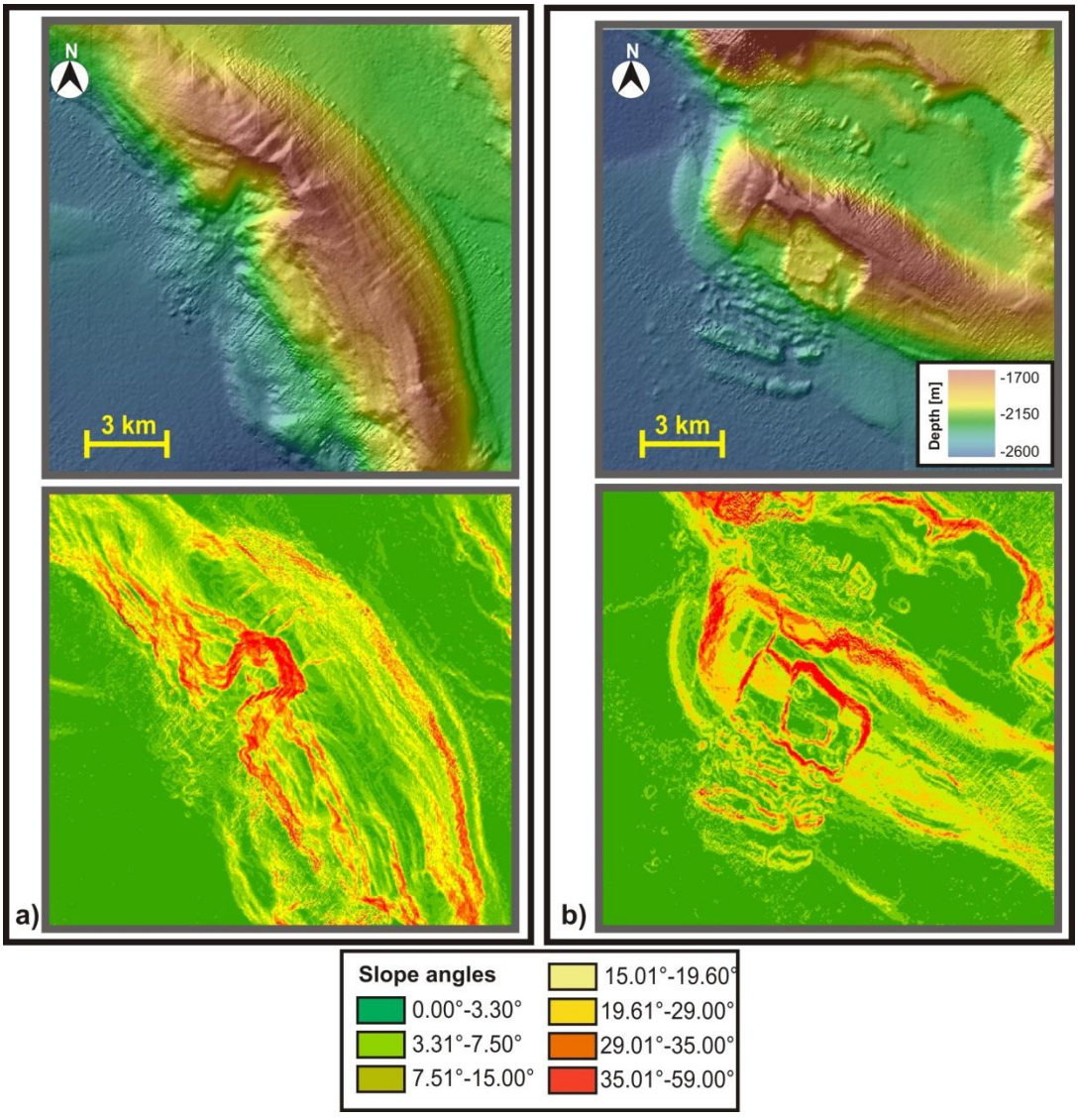


**Figure 2.3**: Bathymetry and slope angle distribution for a) Orca and b) Slipstream Ridge; for location of maps see Fig. 2.1

Fig. 2.3a and b suggest that the shape of the failed area at both ridges is controlled by the shape of the ridge. Similar to the other debris flows in Fig. 2.2, the head scar of Orca Slide is almost arcuate, paralleling the shape of the ridge, and the slide scar narrows in width from ~2 km at the crest to ~1 km at the ridge toe area (Fig. 2.3a). Slipstream Slide has fairly straight boundaries where the shape of the failed area is almost rectangular, which is characteristic of the blocky slides in Fig. 2.1. Furthermore, the landward side of the ridge shows a wide distribution of almost equally high slope angles as well as a square area that looks like a second but smaller failure area. Thus, the crest of Slipstream Ridge is very narrow.

Closer inspection of Orca Slide in Fig. 2.3a reveals some debris in the form of small blocks at the toe of the head-scar, as well as at the toe of the ridge. But it is not clear if Orca Slide failed in one big, or in several smaller episodes. Slipstream Slide initially failed along a listric normal fault as one or two coherent blocks but subsequently broke into about seven main rotational blocks while sliding along the failure plane (Expedition Scientists, 2008). The present slide scar is partitioned into one smaller and one bigger part with a big, square block that did not reach the toe of the ridge after breaking off. Overall, the deposits of Slipstream Slide seem to have barely changed from their initial configuration. The alignment of blocks along the seafloor suggests that the slide movement occurred in ‘surges’ (Fig. 2.3b) spreading the deposits over a distance of 2 to 5 km seaward of the toe.

The lower part of Fig. 2.3 depicts the slope angle distribution around both ridges. Large parts of slide walls at Orca Ridge have very steep slope angles of >35°. The crest reveals a few linear features dipping at high angles previously identified as seafloor scarps by Lopez et al. (2010). The intact part of the ridge still has some fairly high slope angles of around 15°. The whole seaward-directed side and parts of the landward-directed slope seem to have an almost step-like

geometry with present slope angles almost as steep as the side walls. The slide area at Slipstream Ridge is also bound by steep walls of >30°. The NW side of the ridge dips steeply while the SE part of the ridge slopes gently. The seafloor around both ridges has shallower angles between 0° and 3.3°.

Fig. 2.4 shows two profiles along Orca and Slipstream Ridge each, with one cutting through the intact (Fig. 2.4a and c) and one cutting through the failed part (Fig. 2.4b and d).

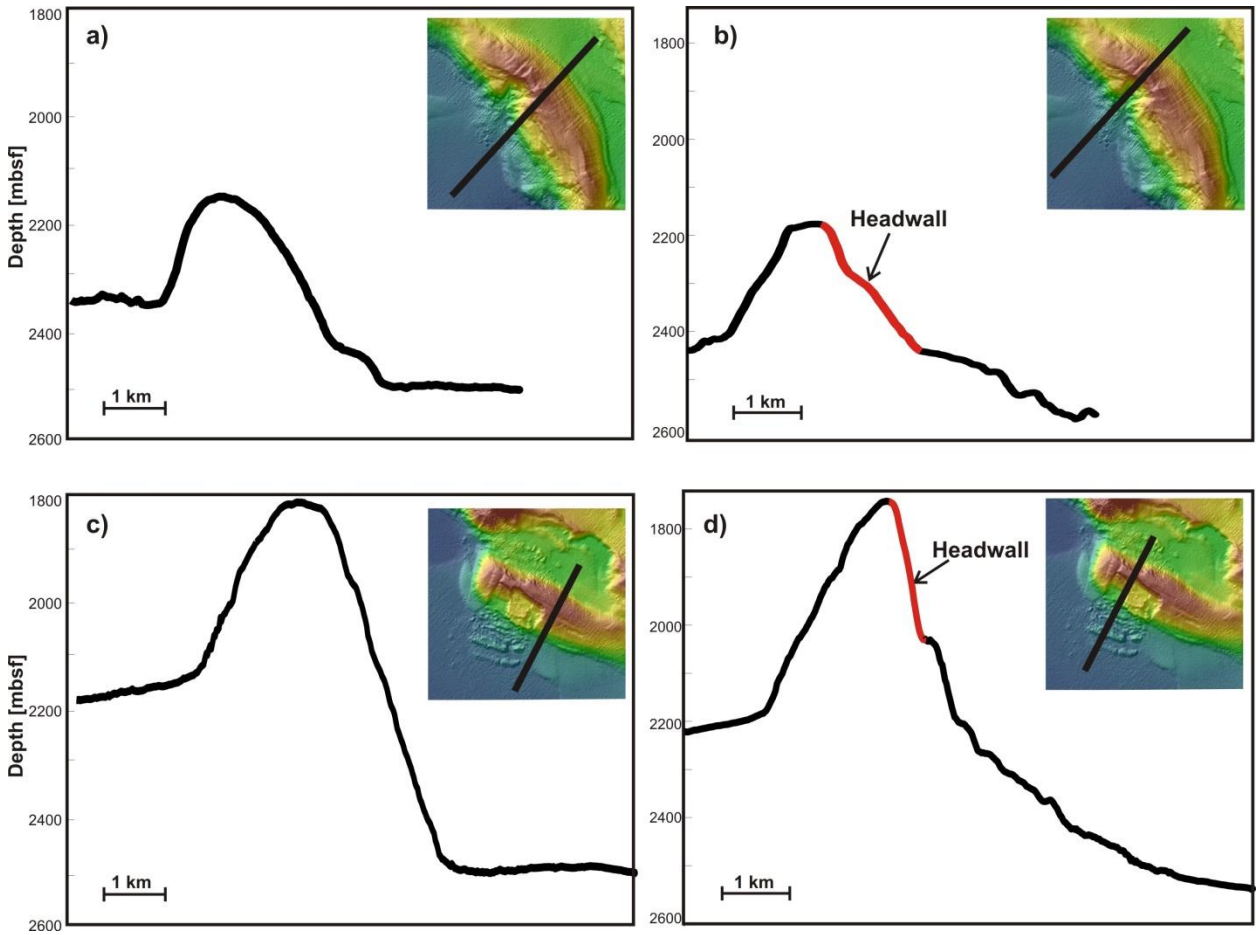


**Figure 2.4**: Slope profiles of a) intact part of Orca Ridge, b) failed part of Orca Ridge, c) intact part of Slipstream Ridge, d) failed part of Slipstream Ridge; insets show location in bathymetry; orange line shows where slope angle was measured

The headwalls of both slides in Fig. 2.4b and d are approximately 250 m high and dip with 15° and 33° at Orca and Slipstream Slide, respectively. Although measured angles change

between single profiles, the chosen profiles are representative of the present geometry. There are small deviations between slopes angles observed on the profiles (Fig. 2.4b and d) and those in Table 2.1 (Naegeli, 2010). This is likely due to differences in the horizontal scale over which the measurements were taken.

## 2.2 Overview and discussion of thesis-relevant previous work on available seismic data

The existing seismic data mainly consist of SCS and MCS lines that were collected mainly for the purposes of gas hydrate studies. Data processing was carried out as part of previous studies, aimed at the clear imaging of the BSR. However, previous analyses do not deliver sufficient information on the sub-seafloor structure needed for slope stability research which requires the analysis of 3D-seismic data. Furthermore, although slump-normal seismic lines are of special interest in the investigation of the causes of slope failure, sub-seafloor imaging is limited because of the steep slopes, and so very few such lines were recorded. The low signal to noise-ratios inherent in most of the data also prevent a thorough study of sub-seafloor structures. Therefore, only an overview of the seismic data acquisition and the results of the previous processing will be given.

### 2.2.1 SCS-data: acquisition and processing

In 2004, a grid of 18 ridge-parallel lines was collected crossing Orca Ridge (Fig. 2.5a). The lines were 7 to 10 km long and separated by 50 to 100 m. Additionally, ten ridge-normal lines were recorded, each 5 km in length and 500 m apart. The seismic source was a Bolt 1.97 L (120 $in^3$) air-gun (peak frequency ~12 Hz) that was deployed behind the ship at an initial distance of 12 m that was later in the survey increased to 25 m for a better source signal. Reflection data were recorded on a 25 m long Teledyne single channel hydrophone array at a

depth of 4 mbsl, with an internal low-cut filter of 30 Hz. An additional Kronhite band-pass filter between 30 Hz and 1 kHz was applied during recording. With a sampling rate of one millisecond the total record length was 6 s at water-depths <2200 m and 7 s for the deep ocean basin.

Processing of the 2004 SCS lines (Lopez, 2007; Lopez et al., 2010) included an initial gapped Wiener deconvolution on post-stack data with a gap of 10 ms and a filter length of 800 ms. This was followed by a phase-shift migration using interval velocities recorded at 311 Site U1326 that ranged from 1480 m/s at the seafloor to 2400 m/s at a depth of about 500 mbsf assuming a constant trace spacing of 10 m. The data were filtered with a zero-phase band-pass Butterworth filter with the low-cut frequency set to 20 Hz, a high-cut frequency of 95 Hz, and a slope to zero at 10 Hz and 115 Hz.

In 2005, the Geological Survey of Canada and the University of Victoria deployed eight OBS on the crest of Orca Ridge (see red dots in Fig 2.5b for locations) to gather detailed seismic structure and other geophysical information in support of the IODP Expedition 311 drilling proposal. The OBS had a nominal spacing of 650 m and were aligned with eight of the SCS lines collected as part of the same survey. Three lines were recorded parallel to Orca Ridge, two lines were recorded perpendicular to it, and three lines were at an angle, striking approximately NNE-SSW. The length of the lines ranged between 9 and 20 km. The location of OBS ‘D’ coincided with X311 Site U1326 (Fig. 2.5b).

A 1.7 L (105 $in^3$) airgun with a dominant signal frequency between 50 and 180 Hz and a peak at 120 Hz was used. The firing rate was initially 10 s and later increased to 11 s. OBS recordings and single channel seismic data were collected simultaneously using a 25 m long Teledyne single-channel array consisting of 50 hydrophones and a preamplifier filter with a low- cut frequency of 30 Hz. An additional Kronhite band-pass filter was applied with a frequency range

of 15 Hz to 2000 Hz. The record length was 4 to 6 s depending on the water depth (Lopez, 2007). Unfortunately bad weather conditions resulted in a low signal to noise-ratio of the SCS-data and resulting images of the SCS data processing were of poor quality (Lopez, 2007).

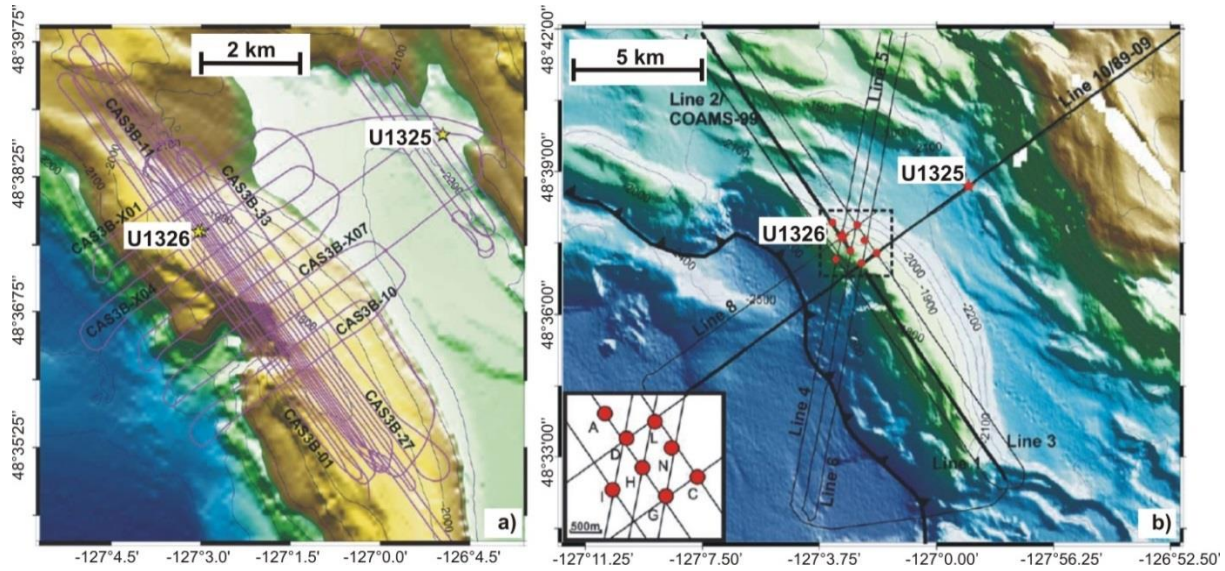


**Figure 2.5**: SCS-lines at Orca Ridge: a) 2004 survey; yellow stars show location of IODP 311 sites U1325 and U1326; b) 2005 survey; red dots are OBS locations; inset shows OBS labels (after Lopez, 2007)

In 2010, I participated in the SeaJade survey in which 33 short-period OBS and 10 broad-band OBS were deployed for three months and one year, respectively. A small active-seismic program, involving five of the 33 short-period OBS, was conducted across Slipstream Ridge (Fig. 2.6). Seismic data were acquired with a 1.97 L (120 $in^3$) air-gun towed 25 m behind the ship and a streamer consisting of 50 hydrophones with a 15.2 cm (6 inch) spacing. The firing interval was 7 s with a sampling rate of one millisecond. The total record length was 5 s. Three refraction lines perpendicular to Slipstream Ridge were recorded, each one 20 km in length, as well as one refraction line parallel to the ridge, with a length of 22 km. Among the recorded reflection lines were two lines that coincided with the refraction lines as well as three lines, each about 8 km long and perpendicular to the frontal ridge, with two of them cutting through different parts of slide area.

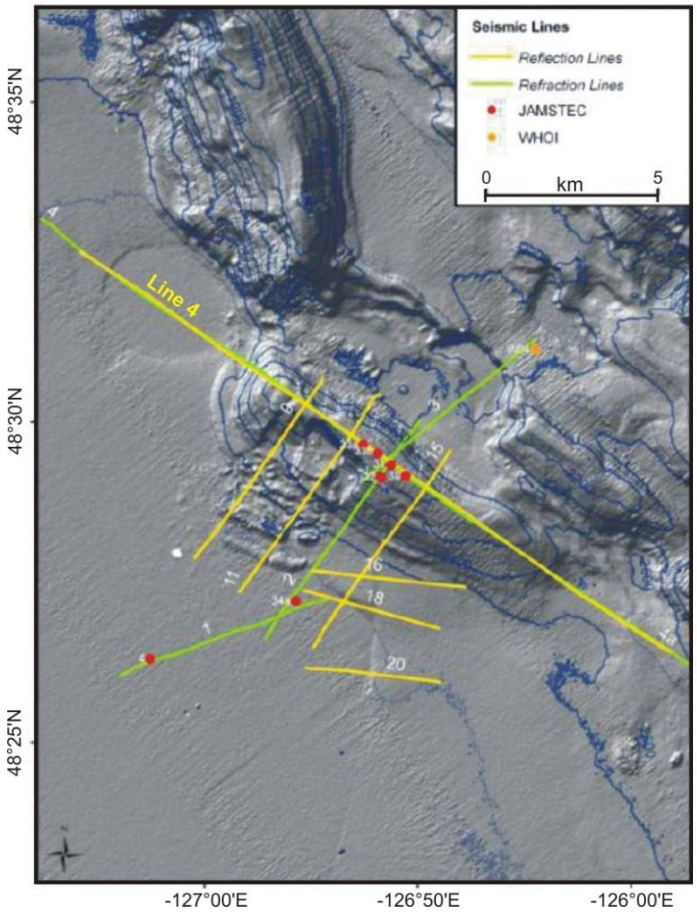


**Figure 2.6**: Seismic lines recorded at Slipstream Ridge (SeaJade cruise report); red dots indicate the location of the JAMSTEC OBS that were part of an active seismic program; grey-shaded seafloor relief image is overlain by bathymetry contour lines (every 100 m)

Only two of the recorded SCS-lines have proceeded past preliminary processing. Complete processing of the Line 4 (parallel to the ridge) included a Wiener deconvolution with a filter-length of 150 ms and no gap, followed by the application of a Butterworth band-pass filter (30-60-180-240 Hz). Migration consisted of a simple Stolt migration with a stretch of 1.0 assuming a sonic velocity of 1660 m/s. Line 1a, crossing Slipstream Ridge adjacent to the failure scar, was processed by S. Yelisetti (personal communication, 2013). First, a band-pass filter (15-25-160-230 Hz) and a Wiener deconvolution with a filter length of 600 ms and a gap length of

12 ms were applied. This was followed by a finite-difference time migration using seismic velocities derived from a previously conducted travel-time inversion.

### 2.2.2 Observations

***Orca ridge-parallel lines***

The margin-parallel lines at Orca Ridge constitute the bulk of the seismic data and also deliver the most information on sub-seafloor structures. The 2004 SCS data as processed and described by Lopez (2007) are the most suitable for the description of the BSR and sub-seafloor structures at Orca Ridge. All SCS-lines contain a faint BSR. Lopez' thesis work on local slope stability also focused on a set of near-vertical normal faults. In the multi-beam bathymetry these faults are expressed as a group of 13 seafloor scarps. Fault-strike is NE-SW and fault-offsets range from 22 m to as high as >75 m with some of the faults reaching down to the BSR. Noteworthy is the absence of a BSR underneath the failed part of the ridge, perhaps as a consequence of loss of the gas below the hydrate stability field. This matches observations at the Cape Fear Slide along the US Atlantic margin (Schmuck and Paul, 1993) where normal faults in the vicinity of the headwall were found to reach down to the BSR and where the BSR vanished beneath the center of the slide area. At Orca Ridge, the normal faults seem to have had control on the geometry of the slide area: Lopez (2007) found that some of the major faults coincide with the location of the side walls of the failure surface.

SCS-line CAS3B-01 (Fig. 2.7) cross-cuts the slide scar close to the toe of the headwall, CAS3B-11 (Fig. 2.8) crosses the slide close to the top of the headwall, and CAS3B-25 (Fig. 2.9) just landward of Orca Slide near the crest of the ridge (see also Fig. 2.5 for locations).

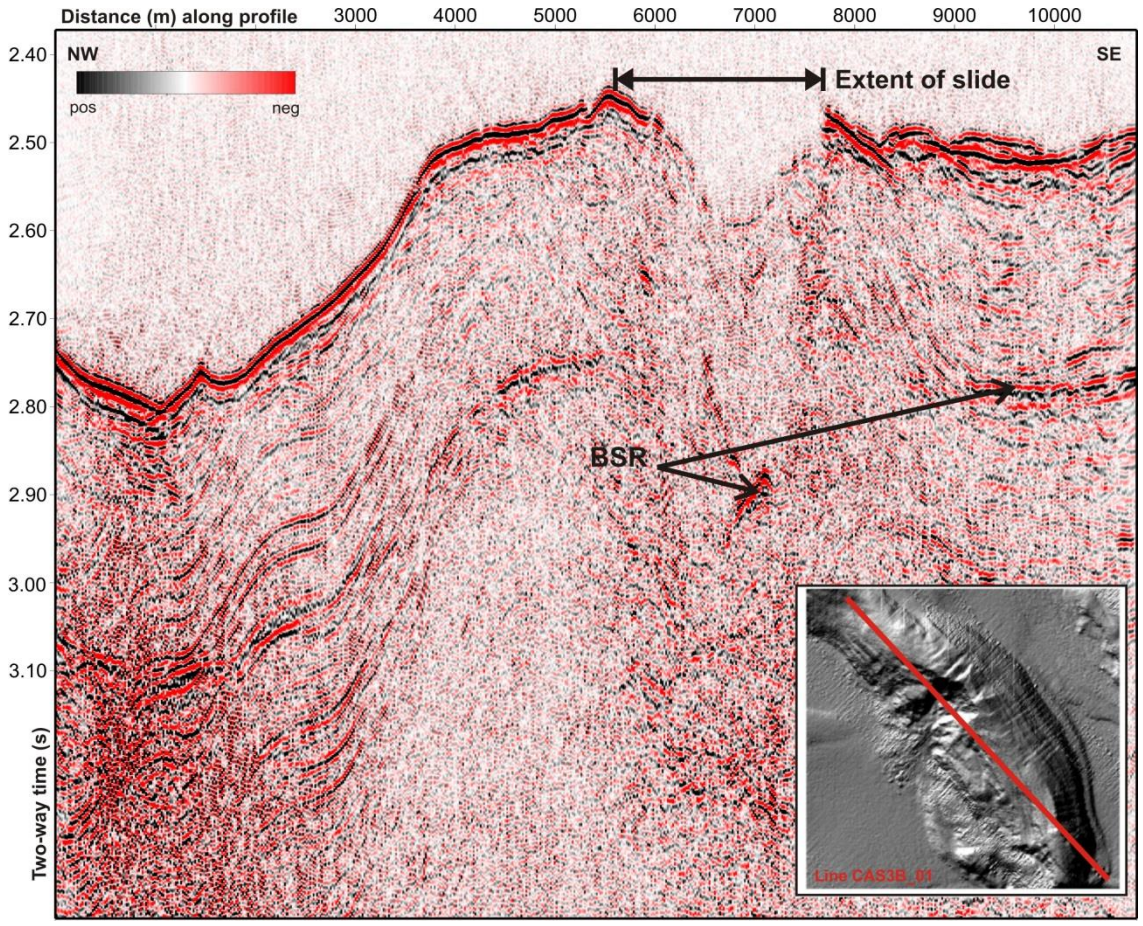


**Figure 2.7**: Seismic line CAS3B-01 parallel to Orca Ridge after processing according to Lopez (2007); inset shows location in bathymetry (modified from Naegeli (2010))

Line CAS3B-01 (Fig. 2.7), which is close to the toe of Orca Slide headwall, reveals an almost continuous BSR everywhere except below the slide scar. There is just one bright reflector-spot, possibly a re-initiated BSR, directly beneath the centre of the slide and the lower end of a ~200 ms long, steeply SE-dipping reflector while the reflectivity of the area above the BSR remains opaque. The faults mentioned by Lopez (2007) are not seen in line CAS3B-01 as this line is probably too far away from the area of slide initiation.

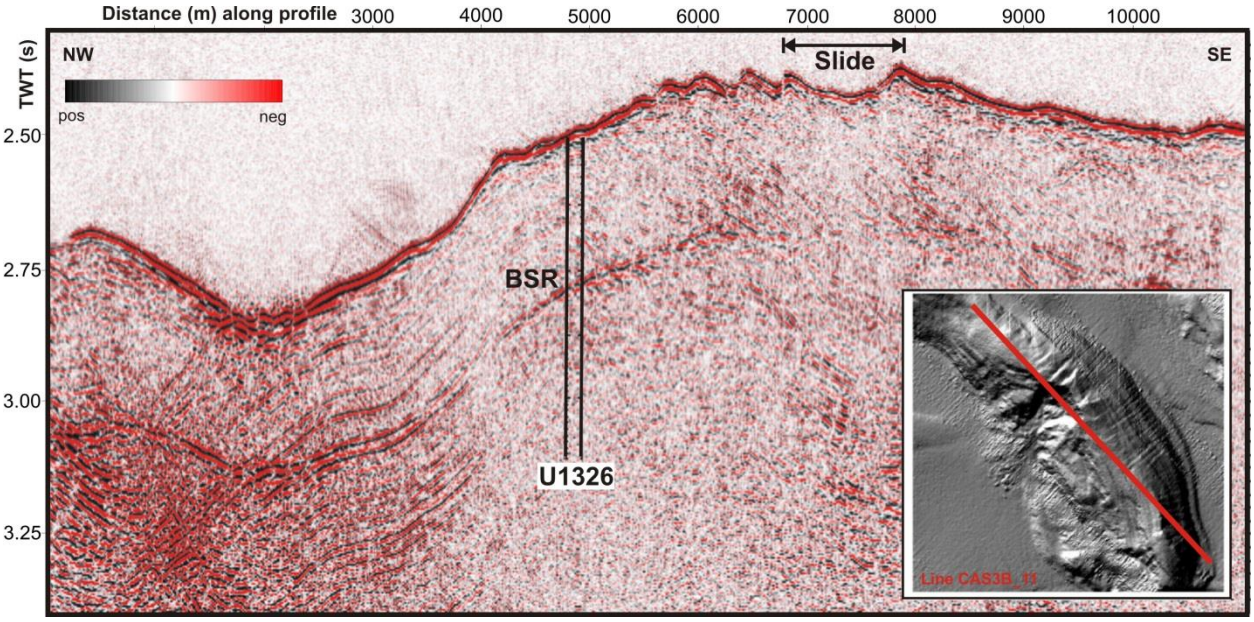


**Figure 2.8**: Seismic line CAS3B-11 parallel to Orca Ridge head scar processed according to Lopez (2007); inset shows location of the line across ridge (modified after Naegeli (2010); locations of two boreholes of Site U1326 are indicated as black lines

Similar features can be observed in CAS3B-11 (Fig. 2.8) which is located just below the top of the head-scar. The BSR is fairly clearly visible especially beneath the NW-flank of Orca Ridge where Site U1326 is located and again vanishes beneath the failed area. The internal structure of Orca is Ridge is fairly chaotic and reflectivity increases to the NW of the anticline. However, a few SE-dipping reflectors can be seen above the BSR to the sides of the failed area and the rugged seafloor topography adjacent to the head scar corresponds to the seafloor expression of the faults in the bathymetry as already noticed by Lopez (2007).

Line CAS3B-25 (Fig. 2.9), located approximately to the east of the head scar coincides with SCS Line 3 from 2005. In contrast to lines CAS3B-01 and CAS3B-11, there is an especially prominent BSR under the part of the ridge that corresponds to the failed part further to the west. However, the reflector is strongly disturbed by a set of normal faults. It is not clear if the enhanced reflectivity may be caused by the presence of free gas, but there is no direct evidence

of this. The offsets caused by these faults seem to be larger behind the failed part of the ridge (Fig. 2.9).

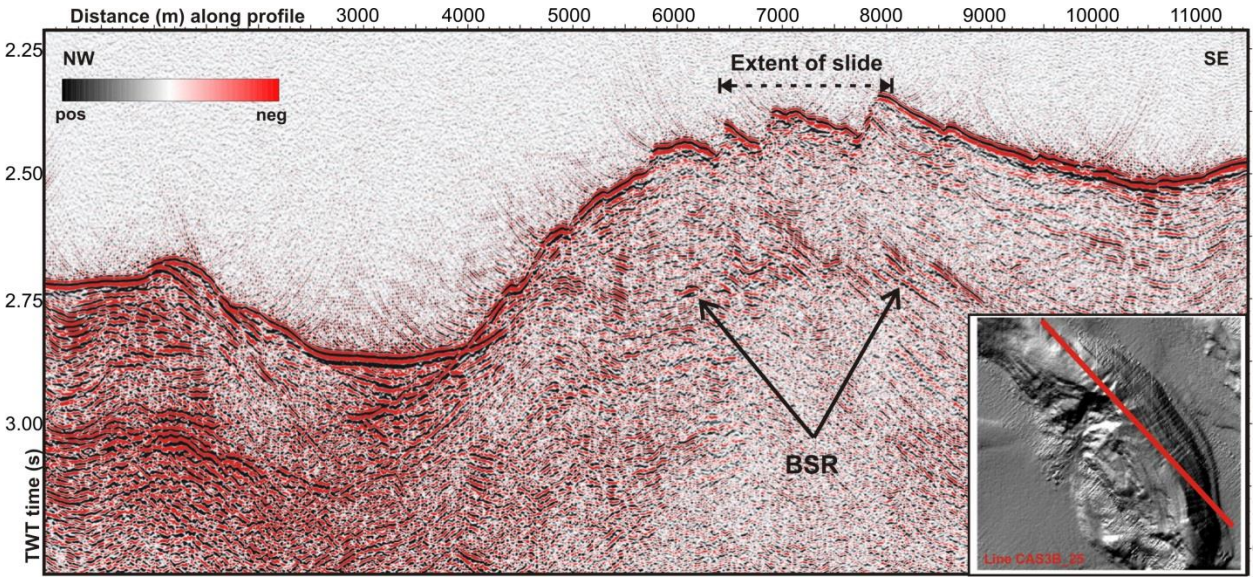


**Figure 2.9**: Seismic line CAS3B-25 parallel to Orca Ridge to the east of the failed area processed according to Lopez (2007); head scar dimensions indicated by dashed double-arrow; inset shows location of across ridge (modified from Naegeli, 2010)

### *Orca ridge-perpendicular lines*

Line 8 of the 2005 SCS data, MCS line 89-08, and CAS3B-X7 of the 2004 SCS-survey are the only ridge-perpendicular seismic lines available. Fig. 2.10 shows an image of line CAS3B-X7.

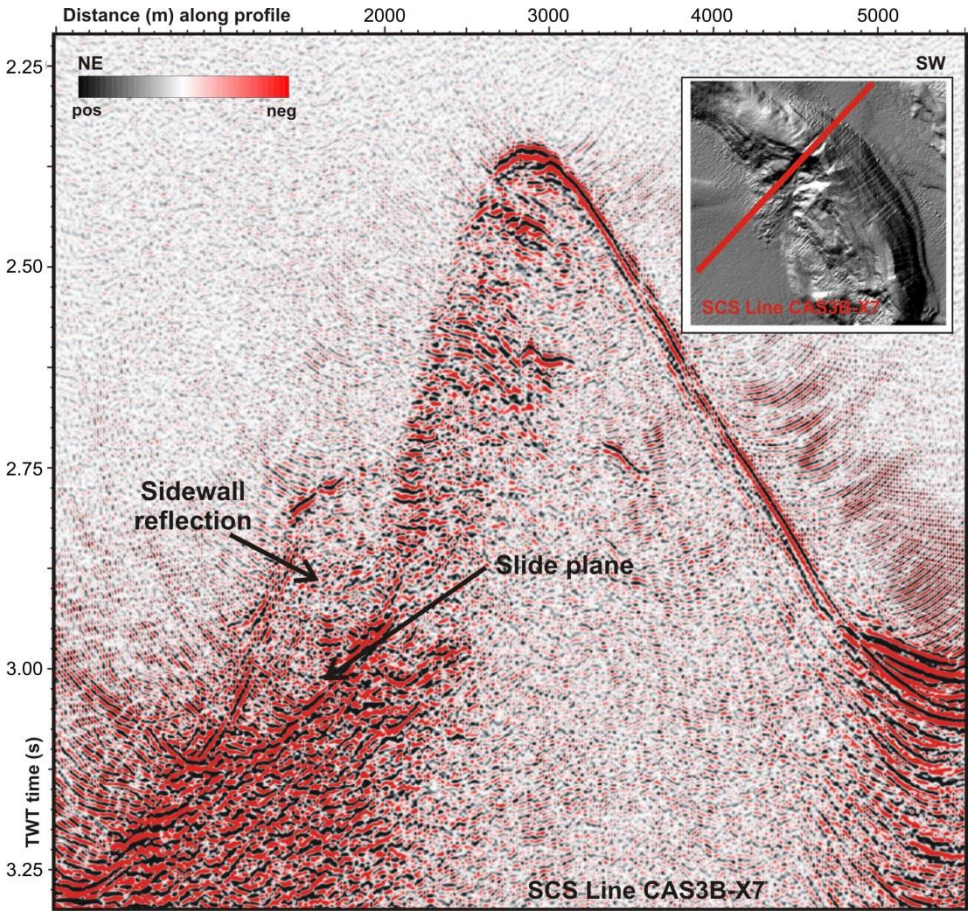


**Figure 2.10**: Seismic line CAS3B-X7 perpendicular to Orca Ridge processed according to Lopez (2007); inset shows location of the line across ridge (modified from Naegeli, 2010)

Line CAS3B-X7 cuts through the middle of the failed area. The angular feature above the gliding plane in Fig. 2.10 is a sidewall reflection rather than part of the sliding material. Reflectivity is substantially higher in the seaward part but in contrast to the other ridge-perpendicular lines (i.e. CAS3B-01, CAS3B-11, CAS3B-25) no BSR can be identified. This is in good agreement with the ridge-parallel lines that likewise do not show signs of a BSR underneath the slide scar. The two short but strong reflectors that are situated beneath the crest and slightly to the east have the same polarity as the seafloor and therefore might rather be signs of an existing fault.

The existence of a BSR at Orca Ridge has however been confirmed by seismic and physical property data acquired during IODP Expedition 311 (e.g. Riedel et al., 2006c; Lopez, 2007). Scherwath and Spence (2011) made use of the OBS-recorded refraction and wide-angle reflection data to perform a mirror imaging routine. The method images the subsurface using multiples in multi-component seismic data by separating the recorded wave-field into up- and down-going waves. Information that is carried by the each wave-field is therefore combined and the additional information is provided by the down-going wave (e.g. Ronen et al., 2005; Scherwath and Spence, 2011). Results showed that the BSR is only visible beneath the crest. Here, topographic effects could have led to an accumulation of free gas beneath the GHSZ leading to the strong BSR impedance contrast. Although several more reflectors can be seen to the west of the BSR, the eastern part of the ridge is seismically transparent (Scherwath and Spence, 2011).

***Slipstream ridge-parallel line***

SCS Line 4 (Fig. 2.11), located just east of the head-wall, is the only ridge-parallel line. It shows a clear contrast between the stratigraphy of the sediment adjacent to the ridge and the material within the anticline. The latter is almost seismically transparent with the exception of the BSR which can be seen in the middle part of the ridge as well as in the northwestern part directly beneath the slide initiation area. Furthermore, there is a second reflector paralleling the BSR underneath the failed area (see left inset in Fig. 2.11). The strength of the lower reflector is slightly lower than that of the upper reflector. The vertical distance between the reflectors is estimated to be about 32 m for a sonic velocity of 1660 m/s. This reflector will be further discussed in Chapter 5.

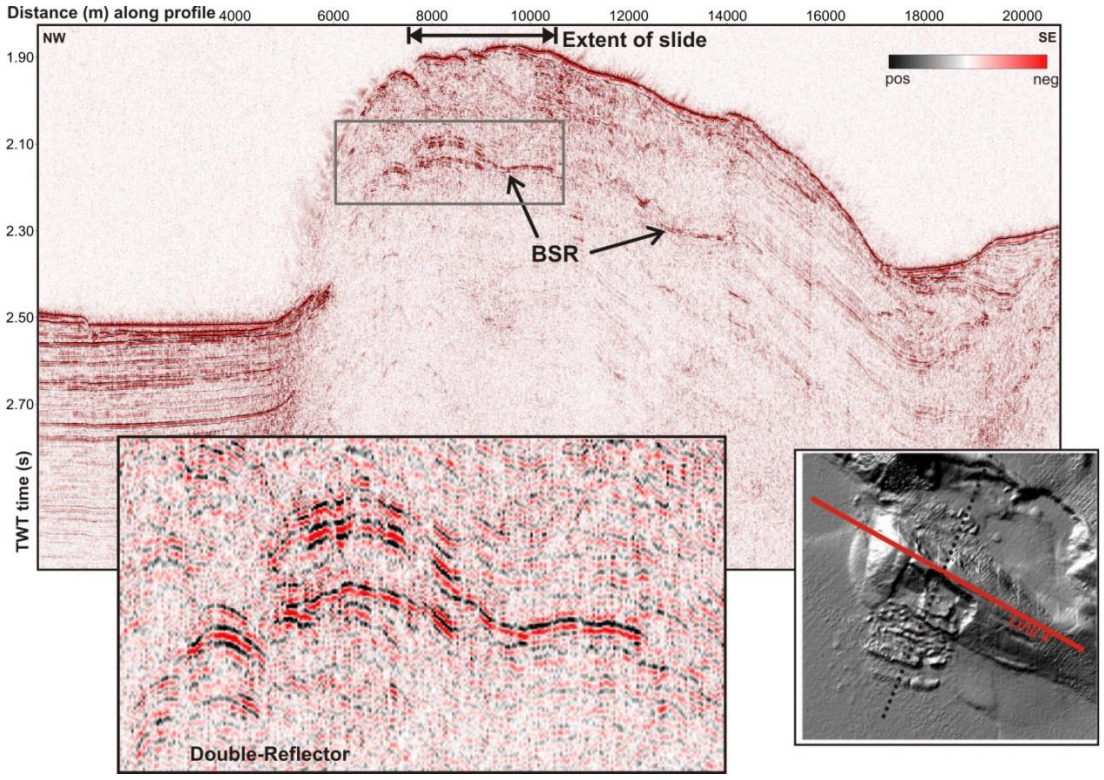


**Figure 2.11**: Processed SCS-line 4 parallel to Slipstream Ridge; left inset: close-up, indicated by grey rectangle shows the location of a possible double-BSR; right inset: location of line across ridge (modified from Naegeli, 2010)

In Fig. 2.11 it is not clear if Slipstream Slide is fault-controlled. The seafloor reflection next to the failed area shows a rugged topography that might be fault-controlled. More rigorous processing of SCS Line 4 is being conducted as part of another ongoing thesis. Results confirm the existence of faults along the crest of the ridge of Slipstream Slide (S. Yelisetti, personal communication, 2013). Furthermore, multi-beam bathymetry clearly indicates the existence of one or more ridge-parallel scarps that might be the seafloor expressions of faults similar to what is observed at Orca Ridge (Fig. 2.3a). Lastly, the BSR shows signs of being cut at several locations, which might be taken as an indicator for the existence of normal faults.

***Slipstream ridge-perpendicular line***

SCS Line 1a (Fig. 2.12), oriented perpendicular to Slipstream Ridge cross-cuts across the ridge just to the south of the failed area.

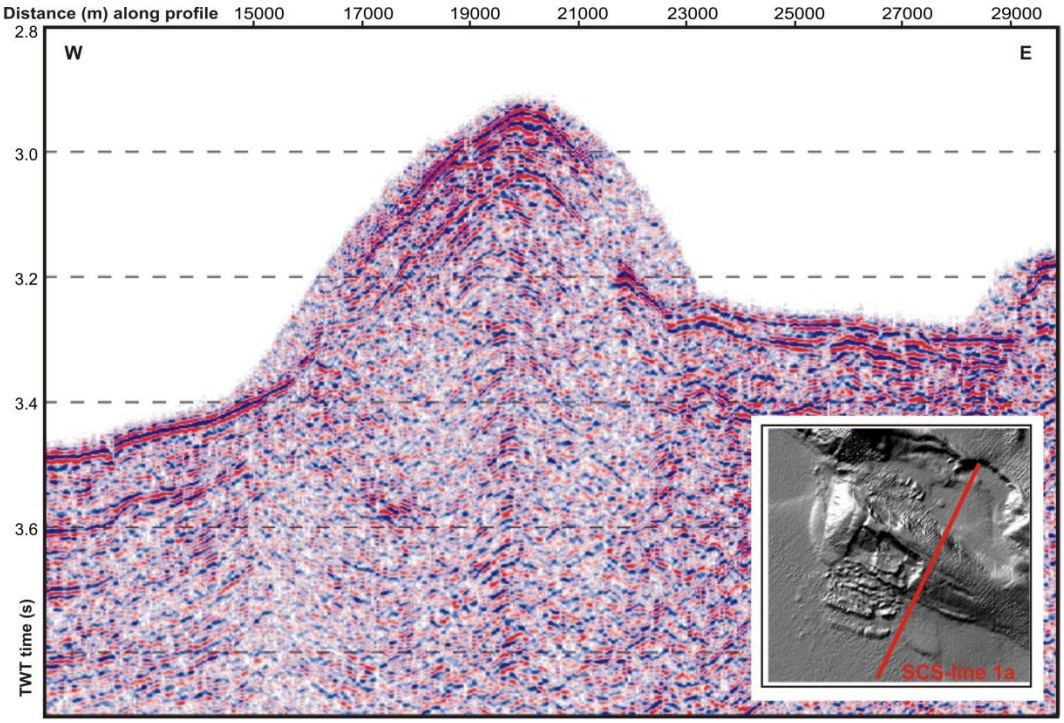


**Figure 2.12**: SCS line 1a perpendicular to Slipstream Ridge (processed by S. Yelisetti); blue = positive polarity; red = negative polarity; inset shows location of line in the bathymetry (modified from Naegeli, 2010)

In Fig. 2.12 the strong reflector paralleling the seafloor is likely a bubble pulse and not a BSR. Generally, the interior of the ridge is seismically almost transparent and there is barely any sign of internal structures. Although the line crosses a part of the ridge that is still intact, the bathymetry in Fig. 2.3b shows the existence of ridge-parallel seafloor scarps. These might match the location of the termination of the seafloor reflection just seaward of the crest (Fig. 2.12). Since the scarp approximately aligns with the head-wall of Slipstream Ridge this could be a zone of weakness and thus the location of a future sliding event.

## 2. 3 Core and log data

Most of the core, logging while drilling (LWD) and wireline data relevant to this study were acquired as part of IODP Expedition 311 in 2005. Logging- and coring operations were carried out at all five drilling sites, including Site U1326 at Orca Ridge. Pressure coring that retains *in situ* pressure of the core when returned to the surface, included the IODP Pressure Core Sampler (PCS) and the HYANCINTH Fugro Pressure Corer (FPC). At Site U1326 four holes were drilled but LWD operations were confined to U1326A. Samples for core description were taken at holes C and D. At U1326D additional wireline logging was conducted. One borehole served as a baseline and proxy for geochemical and microbiological methods. Shipboard analyses included visual core description, physical property measurements, interstitial water geochemistry, organic geochemistry, microbiology, X-Ray imaging, temperature measurements, and infrared analysis.

### 2.3.1 Log- and moisture and density (MAD)-derived bulk density

During IODP Expedition 311 LWD data were measured using the GeoVISION, the EcoScope, the SonicVISION MWD sonic tools, the ADNVISION, and the ProVision nuclear magnetic resonance tools, all mounted on one collar just above the drill-bit (Riedel et al., 2006e). At all 311 sites bulk density was derived with the EcoScope tool which was used for the first time during this IODP Expedition and is comparable to the ADN tool. Both tools use $^{127}$Cs that emits gamma rays which interact with the formation electrons via Compton scattering and photoelectric absorption. The bulk density can be accurately estimated since the number of scattered gamma rays is directly related to the number of electrons in the formation which in turn is closely related to the density of the formation.

The LWD measurements were carried out immediately after drilling to avoid the drilling-related long-time effects such as fluid infiltration. Measurements were taken at constant time intervals and were synchronized with a monitoring system on the drilling rig. During the logging procedure quality control of LWD data is done by tracking and compensating for the ship's motions. Furthermore, to detect washout zones and other kinds of borehole degradations, a caliper tool is used, measuring the diameter of the hole. A statistical method measures density variation during rotation, estimates the distance between tool and borehole wall, and then corrects the density measurement. Other sources of error lie in the gamma-ray count used as well as in the measured grain density. If standard deviations are below 1.0 the density log values are considered accurate within ±0.015 g/cm$^3$.

Bulk density $\rho_b$ can be used to calculate overburden pressure $\sigma_v$ as well as density-porosity $\Phi$ via

$$\sigma_v = g * \rho_w * h + g * \rho_b * d \tag{2.1}$$

and

$$\Phi = \frac{(\rho_b - \rho_w)}{(\rho_g - \rho_w)} \tag{2.2}$$

where $\rho_w$ is the density of seawater, $g$ is the gravitational acceleration, $h$ is water-depth, $d$ is depth below seafloor, and $\rho_g$ the grain density.

Laboratory work on push-cores included a moisture and density (MAD) analysis that was used as a ground-truth for a comparison with log-derived *in situ* physical properties. The method, as described e.g. by Riedel et al. (2006c), involves the derivation of the MAD parameters from the dry and wet mass as well as dry volume of the intact parts of the cores. The sample size of the push-cores was ~10 cm$^3$. Wet masses were measured right after core collection to avoid

moisture loss and dry masses were measured after the samples were heated up to 105° C for 24 hours and subsequently cooled using a vacuum desiccator. Measurements of the sample mass are accurate within 0.01 g and those of the sample volumes within 0.02 $cm^3$. Measuring was repeated to attain a standard deviation of less than 0.01% in these two parameters (Riedel et al., 2006c). With the MAD parameters, moisture content, bulk density, grain density, and porosity could then be calculated. Corrections for an increase in porosity, due to the drying process (Hamilton, 1976; Goldberg et al., 1986) and an excess of salt due to seawater evaporation (Blum, 1997), were made using a water density of 1.024 $g/cm^3$ and a seawater salt density of 2.2 $g/cm^3$. Fig. 2.13 shows LWD- and MAD-derived bulk densities for Site U1326.

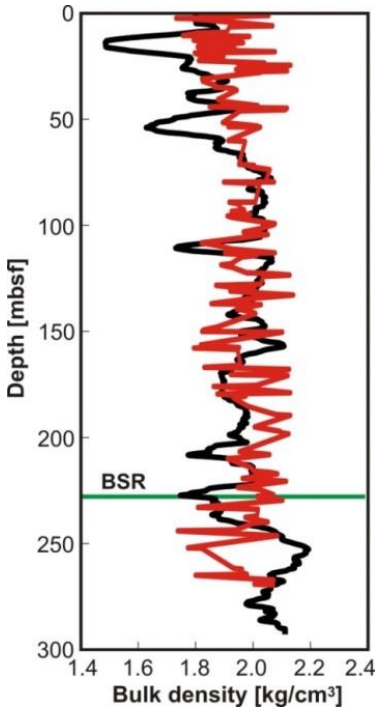


**Figure 2.13**: LWD (black line)- and MAD-derived (red line) bulk density; green line indicates seismically derived BSR depth

The LWD-density measured in the borehole has previously been separated into three distinct units (Riedel et al., 2006d). The first covers the uppermost 72 mbsf (Fig. 2.13a), showing a general increase in bulk density from 1.8 to 2.0 $g/cm^3$, with excursions to slightly lower values

between ~15 mbsf and 50 mbsf. Logging unit 2 reaches down to 240 mbsf and is marked by an almost uniform bulk density of ~2.0 g/cm$^3$. In contrast, the electrical resistivity and P-wave velocity values within this unit have been described as variable due to alternating layers of gas hydrate-free and gas hydrate-bearing sediments (Riedel et al., 2006c). This variability is not visible in the bulk density (Fig. 2.13a). Instead, there is only a slight increase in density around 155 mbsf as well as a minor decrease in bulk density just below 200 mbsf. The remaining 60 m of Hole U1326A were considered as log-unit 3 and are marked by an increased variability in bulk density. Around the depth of the seismically inferred BSR, bulk density values are perceptibly low, maybe due to the existence of free gas beneath the GHSZ. Density values then rise to 2.2 g/cm$^3$ at ~255 mbsf and subsequently decrease to 2.1 g/cm$^3$ for the remainder of the hole.

According to Riedel et al. (2006c) MAD- and LWD-derived porosities both have marked differences in the uppermost 25 mbsf at Site U1326, which was attributed to decreased logging-quality at shallow depths as well as to significant lateral heterogeneity at this site. MAD-derived porosity shows unusually low values at shallower depths (~53%). This was consistent with the observed high shear strength and high P-wave velocities, and tentatively attributed to mass wasting of previously buried and over-consolidated sediments. At Site U1326, seismic velocities at shallow depths were found to be unusually high, ranging between 1480 and 1580 m/s (Riedel et al., 2006c), probably the result of removal of a substantial upper sediment section.

In the following $\rho_g$ is held constant at 2.7 g/cm$^3$ and $\rho_w$ is assumed to be 1.04 g/cm$^3$.

### 2.3.2 Ridge sedimentology

Cores samples were taken at Orca Ridge in 2005 as part of the IODP Expedition 311 and at both ridges during the 2008 survey of the Geological Survey of Canada (GSC). A visual drill

core description revealed sediment in the vicinity of both ridges consisting mostly of deglacial clays, silts, and diamictons (Expedition Scientists, 2008). These are interspersed with layers of sand and cobble-sized, ice-rafted debris as well as finely laminated, stratified, hemipelagic material. Present sedimentation, consisting mainly of planktonic debris (foraminifera, diatoms, nannofossil ooze) occurred at rates less than 0.4 mm/a. The existence of a considerable amount of glacial deposits and ice-rafted debris derived from the Juan de Fuca Strait is unique to the northern Cascadia margin (Expedition Scientists, 2008). The visual core description on the IODP samples showed that the uppermost sediments contain turbidite-derived sand-layers (Riedel et al., 2006c). These are all tilted in the same direction at dip-angles between 45° and 85°. Biogenic components are abundant and include diatoms, foraminifers, as well as bivalve shells and sponge picules.

Slipstream Ridge failed along a stratigraphic boundary between denser, stronger, dewatered sediments and the more hydrous, glacial sediments. The Tertiary sediment, consisting of microfossil-rich ooze, is stiffer, drier, and more compacted compared to the overlying glaciomarine sediments giving rise to the observed strong stratigraphic contrast. The denser material might also have provided a cap for gas hydrate formation thought to date back to the last big deposition of sediment at the end of the last glaciation (Expedition Scientists, 2008). The failure of Orca Ridge has tentatively been attributed to the observed soft-sediment deformation (Riedel et al., 2006c). At greater depths abundant turbidite layers were identified stemming from a period of active prism tectonism.

Fig. 2.14 shows the results of several shear strength measurements on Orca Ridge sediments conducted during IODP Expedition 311. It should be noted that these measurements were made on conventionally cored samples, which can be significantly disturbed by the coring

technique used (piston coring or extendet rotary drilling) and processes related to the removal of sediments from their *in situ* conditions (e.g. exsolution of gas results in expansion of the sediments).

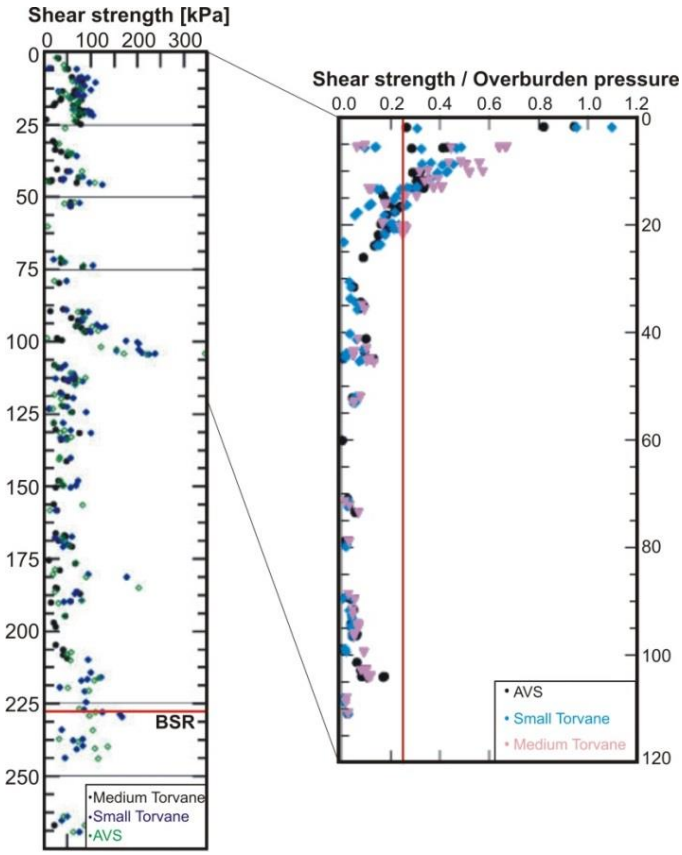


**Figure 2.14**: Measured shear strength at Site U1326; red line indicates location of BSR; large inset: ratio between shear strength and overburden pressure; red line indicating limit between under- and over-consolidation (modified after Riedel et al., 2006c)

Shear strength generally increases with depth with but varies strongly between different types of lithology. Values for sand were found to be of the order of 5 kPa, while clay is considerably stronger with values of ~300 kPa (Riedel et al., 2006c). The ratio between shear strength and overburden with a value of less than 0.25 at depths greater than 20 mbsf were suggested to indicate an under-consolidated and therefore weak material. The ratio then increases

to values over 0.25 at depths shallower than 20 m, which was interpreted as over-consolidated and strong sediments (Riedel et al., 2006c).

## 2.4 Slide age

An important step to decrease the number of potential slide triggers is the assessment of the timing of slide initiation. Most trigger mechanisms are confined to certain time periods within climate and geological cycles such as peaks or hiatuses in sedimentation or the occurrence of megathrust earthquakes. In 2008, radiocarbon-age dating was performed on five piston cores taken across the Slipstream slide (Expedition Scientists, 2008). Cores 11 and 25 were collected along the headwall scar; cores 7, 9, and 10 came from the ridge toe and the abyssal plain in front of the Slipstream Ridge (see inset of Fig. 2.15). Although all cores downslope showed a linear increase in age, the ones collected at the headwall scar revealed a reversal in sediment age at depths between 220 and 230 cmbsf corresponding to the depth of the failure plane.

The estimated age range for all slumps of between 9,000 and 14,000 years is in good agreement with the age of the turbidite sequences used to date past megathrust earthquakes on the Cascadia subduction margin (Goldfinger et al., 2003). Goldfinger et al. (2003) overcame the lack of historic earthquake data by conducting a turbidite paleoseismic analysis. From the count of post-Mazama turbidites they derived an average interval between megathrust earthquakes of 587 years. The method uses the synchronicity of turbidite events triggered by large earthquakes thus extending the record on historic major seismic events.

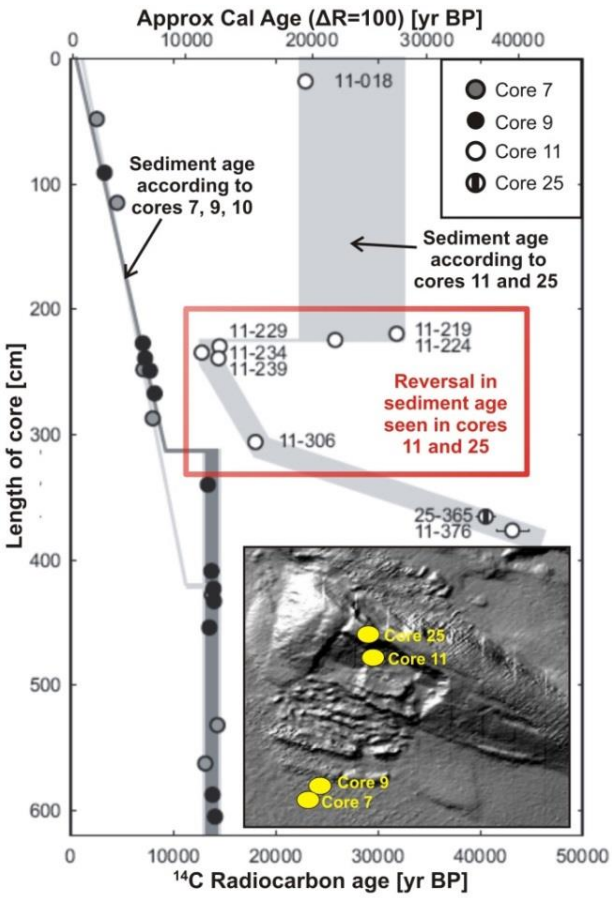


**Figure 2.15**: Uncorrected radiocarbon ages for the last 50 ka for cores 7, 9, 11 and 25 showing reversal in sediment age seen in piston cores taken at Slipstream Ridge; inset: location of cores on Slipstream Slide (adapted from Hamilton T.S., personal communication)

Goldfinger et al. (2003) were able to extend the Holocene record for earthquake-generated turbidites to ~9850 BP, encompassing 18 events. That the turbidites were triggered by great earthquakes is substantiated by the record of great earthquake coastal marsh subsidence (Leonard et al., 2010). Together with the 17 turbidites found in the Slipstream cores in 2008, a minimum age of about 9900 BP was suggested (Expedition Scientists, 2008). Pohlman et al. (2009) modeled the time that the sediment at Site U1326 had been exposed to oxic and sulfate-reducing conditions and came to a similar result for the age of the Orca Slide.

# Chapter 3: PRESENT-DAY PORE PRESSURE REGIME AT THE NORTHERN CASCADIA MARGIN

Sediments at subduction zones have a large potential to experience excess pore pressures. Sediments on the incoming oceanic plate often consist of 50% to 80% of pore fluid and are in stark contrast to the small amount of fluids that are found in already dewatered accretionary complexes (e.g. Vrolijk, 1987). Fluids play an important role in subduction zones. They are involved in the shaping of accretionary wedges, in thrust faulting and fold vergence, and in heat transport, diagenesis and metamorphism (e.g. Hubbert and Rubey, 1959; Vrolijk, 1987). On a smaller scale, structures at the deformation front too are partly shaped by the ambient pore pressure regime. When sediment permeability is low pore pressures can induce fracturing and contribute to regional fluid transport (e.g. Saffer and Bekins, 2002; Saffer, 2003). Pore pressure is also known to influence earthquake cycles (Hu and Wang, 2008) and post-failure evolution (e.g. Dugan and Flemings, 2002; Stigall and Dugan, 2010; Dugan, 2012). It also drives fluid flow and transports hydrocarbons to shallower depths, which has important implications for subsequent gas hydrate formation (e.g. Dugan and Flemings, 2000; Flemings et al., 2002). In regions with prominent topography, such as in submarine canyons or at the deformation front, the highest pore pressures do not necessarily occur at the highest elevation. Where sedimentation rates change over distance, asymmetrical loading can also lead to a lateral flow along more permeable layers, leading to low effective stresses in the toe area of a slope (Flemings et al., 2002).

Lastly, pore pressure and pore pressure-induced fluid transport also strongly influence slope stability (e.g. Prior and Coleman, 1982b; Dugan and Flemings, 2002; Dugan, 2003). Slope

failure related to high fluid pressures is mostly due to low effective stresses and accompanying low sediment shear resistance. The reduction of effective stress $\sigma'$ through an increase in pore pressure and its link to shear stress $\tau$ is expressed by the well-known Mohr – Coulomb failure criterion:

$$\tau = c + \sigma' * tan\Phi_f \quad (3.1)$$

where *c* represents sediment cohesion and and $\Phi_f$ the internal friction angle.

Carson and Screaton (1998) describe overpressure-related slumps and mudflows as a ubiquitous feature of deformation fronts. Anticlines such as Hydrate Ridge, Orca Ridge and Slipstream Ridge are formed as sediment layers are pushed upwards along thrust faults. Overpressure and fluid expulsion can be caused as older, compacted sediments move along the frontal thrust fault onto younger, less consolidated ones (e.g. Carson and Screaton, 1998). The combination of locally high pore pressure and the existence of faults then could lead to the lateral transport of fluids, also reaching the ridges at the deformation front.

In general, overpressure is most often the result of a combination of a high sedimentation rate (> 1 mm/yr) and low sediment permeability, preventing dissipation. At convergent margins, additional vertical thickening, horizontal shortening, and subsequent fluid expulsion all promote the generation of overpressure (Hyndman et al., 1993; Saffer and Bekins, 2002). Other sources of excess pore pressure are free gas occurrence or transient pressure pulses that tend to be generated during earthquake shaking. Free gas occurrence can be the result of gas seepage along high-permeability pathways or due to gas hydrate dissociation. Depending on the sediment permeability and the volume of dissociated hydrate, the amount of generated excess pore pressure can be substantial (e.g. Nixon and Grozic, 2007).

In all cases, sediment permeability probably plays the most important role in the control of pore pressure levels. Low permeability sediments do not drain quickly enough to accommodate the increase in pore pressure when overburden loads increase rapidly (e.g. Gibson, 1958; Flemings et al., 2002; Flemings et al., 2008; Stigall and Dugan, 2010). With permeability values of the order of $10^{-16}$ $m^2$, time scales for pressure dissipation can be up to several hundred years depending on the spatial scale (Flemings et al., 2002). There is still fairly little known about the relationships between porosity / void ratio, compressibility, permeability, and pore size-distribution in mudstones although they play an important role in the fundamental processes of convergent margin tectonics. Furthermore, the magnitude of generated overpressure is also linked to local sedimentation history, since the pore pressure also depends on the stress history that a sediment unit has experienced (e.g. Flemings et al., 2002; Zoback, 2007).

## 3.1 Overview of pore pressure estimation

In regions where normal sediment compaction can be expected, the estimation of pore pressure is possible when the trend of porosity with depth is known. Especially at passive margins or sedimentary basins, porosity is expected to decrease with depth according to Athy's Law which allows pore pressure to directly be inferred from sediment porosity and sediment compressibility (Zoback, 2007). However, this is not possible at active tectonic settings where horizontal compression has to be taken into account which makes the horizontal component of the effective stress hard to determine.

The amount of fluid that escapes across a subduction margin has been estimated by recognizing that porosity decreases with depth and that the amount of porosity loss can be equated to the amount of fluid that escapes (e.g. Yuan et al., 1994; Saffer and Bekins, 2002). Pore pressure is also estimated by using basin modeling techniques or derived from seismic data

and well logs. The latter makes use of the observed correlation between seismic velocities and porosity, as well as between porosity and effective stress (e.g. Mukerji et al., 2002).

One way to infer pore pressure empirically, is based on a relationship between porosity (or void ratio) and vertical effective stress. While overburden stress can be derived from density logs, effective stress has to be calculated from site-specific empirical relationships (Flemings et al., 2002; Dugan, 2003; Schneider et al., 2009). Porosity is thought to depend on effective stress via Athy's relation (e.g. Athy, 1930; Hart et al., 1995):

$$\Phi = \Phi_0 * exp(-\beta \sigma_v') \tag{3.2}$$

Here, $\Phi_0$ is the reference porosity and $\beta$ the sediment compressibility, and $\sigma_v'$ the vertical effective stress. It should be noted that Athy's original work is valid for clay-dominated sediments at depths larger than 400 m. In this work the exponential dependence of porosity with depth is transferred to shallower depths in order to simplify the derivations of pore pressure.

In the following, present-day pore pressure is calculated at several sites along the Cascadia margin using an estimation of the consolidation behaviour of the sediment. The method has previously been applied successfully to the passive ocean basin of the Gulf of Mexico (Schneider et al., 2009), the passive continental margin offshore New Jersey (Dugan, 2003), and at several different accretionary wedge locations such as offshore northern Barbados, Costa Rica, and Nankai (e.g. Screaton et al., 2002; Saffer, 2003; Screaton and Saffer, 2005). The necessary parameter values have been inferred via linear regression on bulk density data from a reference site in the abyssal plain that can be assumed to be under hydrostatic pressure conditions.

### 3.1.1 Methodology

The origin of the methodology is based on the work of Terzaghi (1943) and Gibson (1958) which investigated 1D sediment consolidation. The associated laboratory tests have their roots in Terzaghi's (1925) principle of effective stress. For example, constant-rate-of-strain consolidation (CRSC) tests examine the stress-strain curves of a sample by increasing the load acting on it at the same time preventing the dissipation of pore fluid. The slopes of the elastic and plastic portions of the resulting curve then provide the information on the compressibility of the sediment. The compressibility is reflected by a decrease in porosity or void ratio with increasing vertical effective stress, a process that models the effects of sediment dewatering with 'burial' (i.e. pore pressure is dissipated). Pore pressure can then be predicted when the relationship between porosity/void ratio and vertical effective stress of the sediment is known (e.g. Terzaghi and Peck, 1948; Lambe and Whitman, 1979; Hart et al., 1995; Screaton et al., 2002; Saffer, 2003; Dugan, 2003; Schneider et al., 2009). The virgin consolidation curve (which is usually different for different types of sediments) can be described by:

$$e = e_0 - Cc * log\left(\frac{\sigma_v'}{\sigma_0'}\right) \tag{3.3}$$

with *e* as the void ratio which can be written as

$$e = \frac{\Phi}{1-\Phi}. \tag{3.4}$$

*Cc* is the compression index which describes the deformation for the primary consolidation along the stress path and $e_0$ is the reference void ratio at a reference vertical effective stress $\sigma'_0$ (here $\sigma'_0$ equals 1 MPa). The logarithm of the vertical effective stress in equation 3.3 implies that the material can be considered as normally consolidated (e.g. Koppula and Morgenstern, 1982). In equation 3.3 only the void ratio *e* can be directly measured and $e_0$ and *Cc* have to be derived.

In cases where *in situ* pore pressure from a reference borehole is available the vertical effective stress can be calculated. $e_0$ and *Cc* can then be derived via a linear regression of the observed void ratio with the logarithm of the vertical effective stress whereby *Cc* equals the slope of the resulting curve (e.g. Dugan, 2003; Schneider et al., 2009).

In cases where both direct pore pressure measurements and consolidation experiments are lacking but where bulk density-data are available from an oceanic site seaward from the deformation front, field-based consolidation curves can derived (Screaton et al., 2002; Saffer, 2003). At such sites, hydrostatic conditions are assumed and porosity is expected to decrease exponentially with depth (Athy's Law, 1930).

With $e_0$ and *Cc* available, the pore pressure *u* and pore overpressure *u** can then be calculated via:

$$u = \sigma_v - \sigma_v'$$

$$\sigma_v' = \sigma_0' \left(10^{\left(\frac{-(e_0 - e)}{Cc}\right)}\right) \tag{3.5}$$

$$u^* = u - u_h \tag{3.6}$$

Here, $\sigma_V$ is the overburden stress in MPa calculated from bulk density logs and $u_h$ is the hydrostatic pressure. The magnitude of overpressure $u^*$ can also be represented in form of the overpressure ratio $\lambda$ :

$$\lambda = \frac{u^* - u_h}{\sigma_v - u_h} \tag{3.7}$$

such that a $\lambda$ of zero equals hydrostatic and a $\lambda$ of unity stands for the lithostatic pressure.

### 3.1.2 Derivation of $e_0$ and $Cc$

Values for $e_0$ and $Cc$ are derived via a linear regression on bulk-density data belonging to a site of homogeneous sediment type that is assumed to be under hydrostatic pressure. For the Cascadia margin Site 888 of the ODP Leg 146 was chosen as a reference borehole, situated in the abyssal plain 7 km seaward of the deformation front (Fig. 3.1).

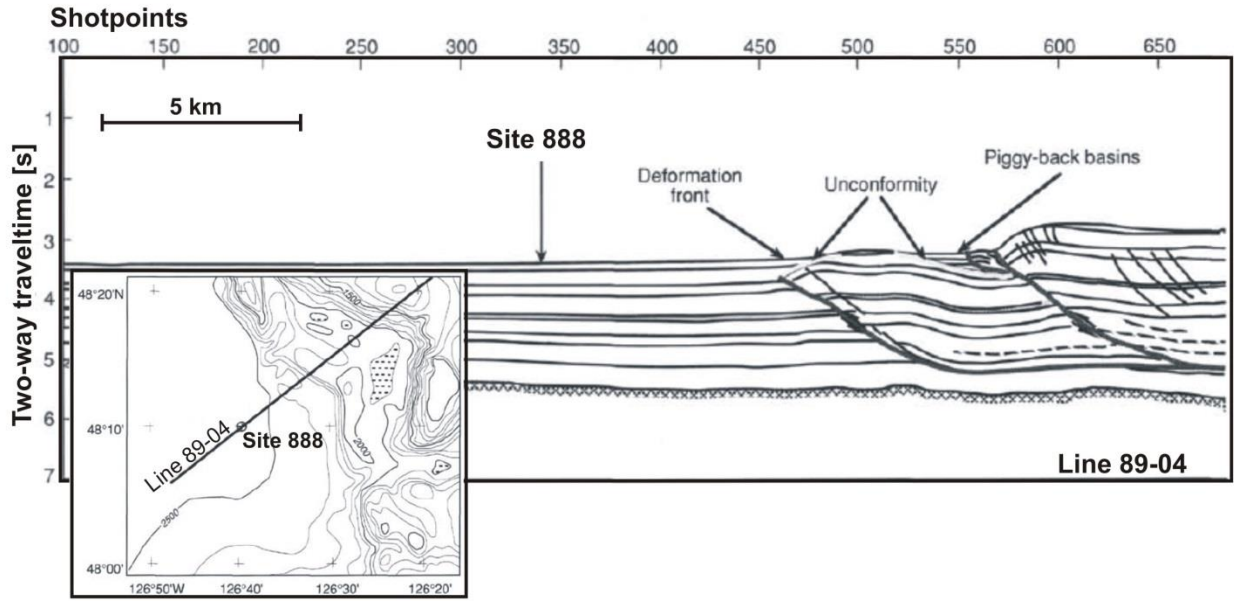


**Figure 3.1**: Location of Site 888 seawards of the deformation front and interpretative drawing of seismic reflection line 89-04 (adapted from Westbrook et al., 1994)

This site was drilled in 1992 as a reference to study types, age, and physical properties of sediment in the accretionary wedge. The expedition focused on the structural development and tectonic dewatering along the Cascadia margin and how these are linked to the occurrence of the regional BSR.

Due to the lack of log-data in the crucial uppermost 100 m below seafloor, MAD-derived bulk density was used to derive the void ratio as a function of vertical effective stress. Porosity and void ratio were calculated from bulk density assuming a grain density of 2.7 g/cm$^3$ and a water density of 1.04 g/cm$^3$ (Fig. 3.2).

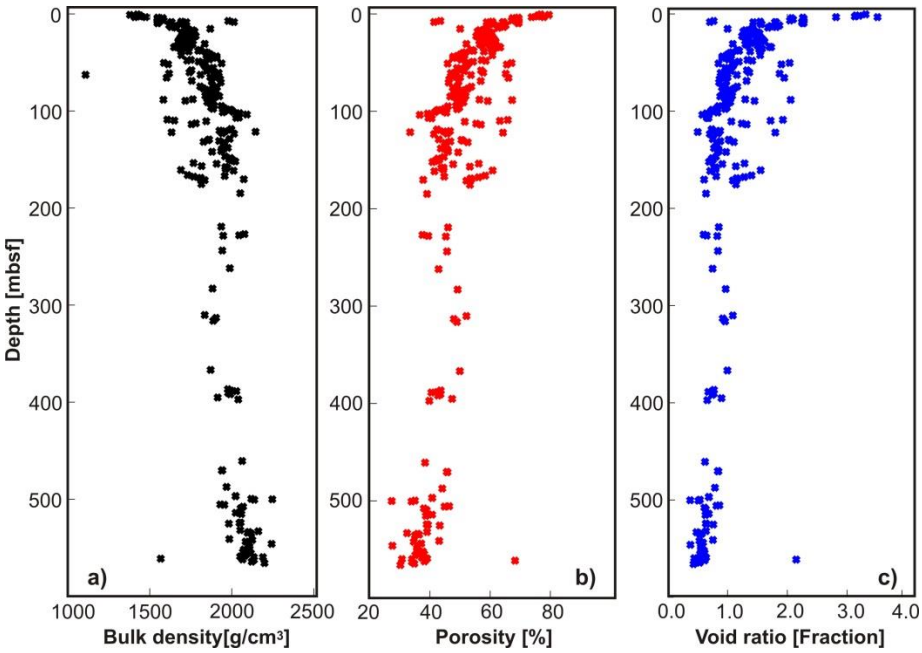


**Figure 3.2**: MAD physical properties: a) bulk density, b) bulk-density–derived porosity, c) bulk-density–derived void ratio at Site 888

An important unknown was the depth range to calculate the linear regression. Data points at larger depths have the potential to be affected by the onset of cementation and lithification, both significantly alter sediment behaviour under loading. Dugan (2003), for example, restricted the depth over which he applied the regression to the uppermost 85 mbsf to avoid the influence of cemented material on the derived geotechnical parameters. Since information of the onset of cementation at Site 888 is missing, results for $e_0$ and $Cc$ for different depth intervals were compared (Table 3.1) to study the significance of the choice in depth interval. A lower limit for the regression was kept at a depth of 170 mbsf due to the scarcity of data points below this depth. The table also includes the $R^2$-value of each linear regression to help assess the quality of the linear regression results. Additionally, cases e) to h) exclude the uppermost 17 mbsf to investigate the effect on the regression result of omitting the low-quality data just below the seafloor (Fig. 3.3).

| Case | Depth interval [mbsf] | $e_0$ | Cc | $R^2$ |
|---|---|---|---|---|
| **a)** | 0-85 | 0.71 | 0.43 | 0.751 |
| **b)** | 0-100 | 0.77 | 0.41 | 0.741 |
| **c)** | 0-150 | 0.84 | 0.38 | 0.735 |
| **d)** | 0-170 | 0.88 | 0.37 | 0.717 |
| **e)** | 17-85 | 0.83 | 0.36 | 0.453 |
| **f)** | 17-100 | 0.86 | 0.34 | 0.452 |
| **g)** | 17-150 | 0.89 | 0.34 | 0.482 |
| **h)** | 17-170 | 0.92 | 0.31 | 0.450 |

**Table 3.1**: Overview of regression results; dark red box indicates parameters with which further calculations were conducted

For different depth intervals, the reference void ratio ranges between 0.71 and 0.92 and the compression index varies between 0.31 and 0.43. This indicates that both parameters are only moderately sensitive to variations in the depth interval over which the linear regression is applied. The omission of the uppermost 17 m slightly decreases the *Cc*-value (i.e. compressibility) which was expected due the strong variability in void ratio close to the seafloor. There is also a slight increase in the average $e_0$ (for cases *a* to *d*, which have an average $e_0$ of 0.80; for cases *e* to *h* the average $e_0$ is 0.88). The $R^2$-values are satisfactory as data points are scarce and the actual behaviour of void ratio with depth is not linear. The omission of the uppermost 17 mbsf leads to a strong decrease of the $R^2$-value indicating that the uppermost parts of the data contain important information on the behaviour of the sediment with depth.

Case *a* was chosen for all subsequent pore pressure calculations as it is associated with the highest $R^2$-value. As the main focus lies on the relative differences in pore pressure rather than on absolute values, $e_0$ and *Cc* of case *b* could also have been appropriate for pore pressure calculations. The linear regression for case *a* is depicted in Fig. 3.3.

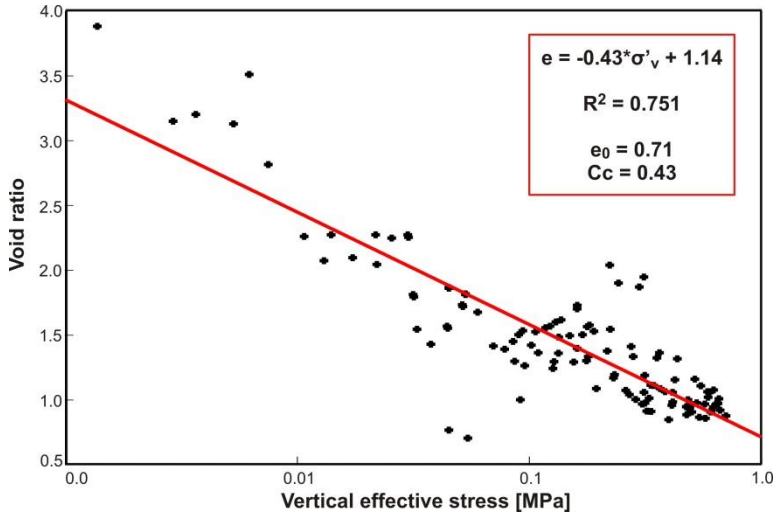


**Figure 3.3**: Linear regression of void ratio data of Site 888 for case a): regression interval from 0 to 85 mbsf; black dots: void ratio data from MAD-derived bulk density, red line: resulting regression; assumption: vertical effective pressure is calculated under the assumption of no existing overpressure at this site; the red box shows the resulting linear equation, its $R^2$-value and the resulting geotechnical parameters

### 3.1.3 Application to previously studied sites

To ensure consistency of the application of equations 3.4 and 3.5, I first reconstructed the results at two locations where the technique of pore pressure estimation has already been proven to be successful. Among them are two sites of IODP Expedition 308 in the Gulf of Mexico (Schneider et al., 2009) as well as one site that was part of ODP Expedition 174A offshore New Jersey (Dugan, 2003). At both sites it was possible to reproduce the former results within ± 5 to 10% (Figs. 3.4 and 3.5). The remaining difference might derive from small differences in the usage of the input data set or smoothing of the results for illustration.

***IODP 308***

As part of the IODP Leg 308 the Brazos-Trinity Basin IV was drilled in 2005. It is part of a system of several mini-basins within the Gulf of Mexico and is located about 250 km south-southeast of Houston along the northwestern part of the continental slope of the Gulf of Mexico at water depths between 1000 m and 1480 m. The basin is characterized by a lack of sediment outlets and thus it represents a depocenter for gravity flows (Schneider et al., 2009). The location of the Brazos-Trinity region as well as Sites U1319 and U1320 can be seen in Fig. A.1 in the Appendix.

I calculated pore pressure using porosity and void ratio from log-derived bulk density with a grain density of 2.69 g/cm$^3$ and a water density of 1.024 g/cm$^3$ as well as values for $e_0$ and $Cc$ of 0.47 and 0.54 which were previously determined by Schneider et al. (2009).

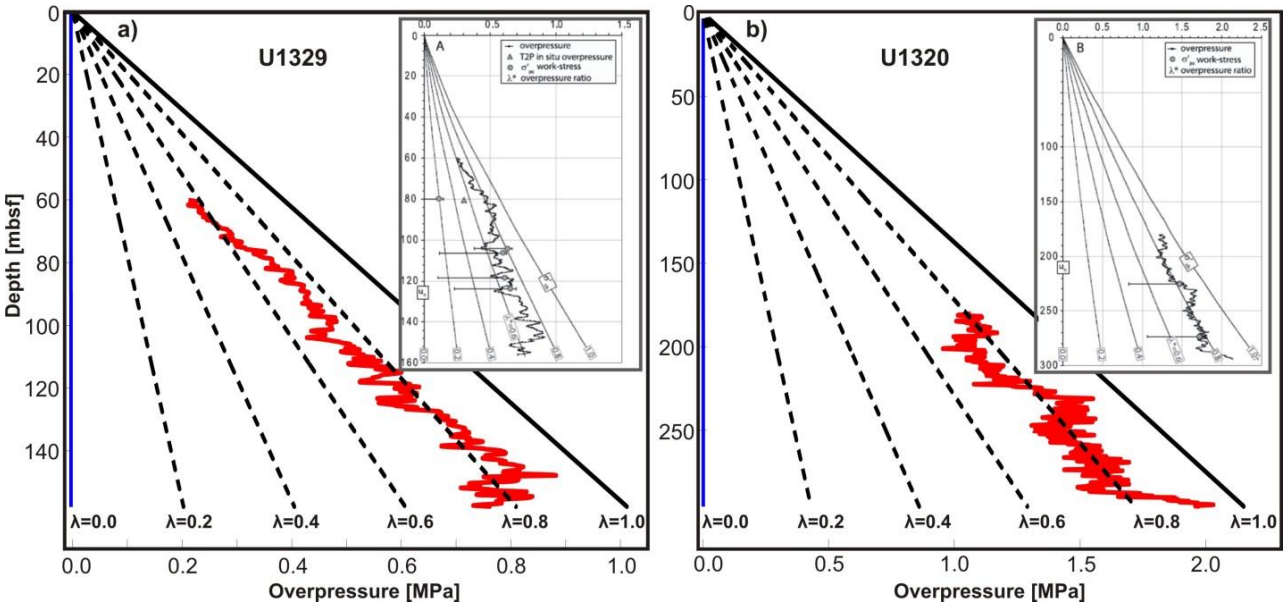


**Figure 3.4**: Pore pressure results for the sites a) U1319, and b) U1320; red line: overpressure, blue line: hydrostatic pressure, black line: vertical effective stress (i.e. maximum overpressure possible), dashed black lines: overpressure of 20% to 80% of vertical effective stress shown for reference; insets show original results of Schneider et al. (2009) for comparison

The results for the Gulf of Mexico as seen in Fig. 3.4a and b indicate that sediments are under considerable overpressure (i.e. up to about 80% of vertical effective stress). It has been suggested that this is the consequence of the high sedimentation rates that are prevalent in this region (Schneider et al., 2009).

***ODP 174A***

ODP Leg 174A was conducted in 1997 at the Hudson Apron along the upper continental slope offshore New Jersey (for location see Fig. A.2 in the Appendix).

Dugan (2003) constrained $e_0$ and $Cc$ via CRSC and triaxial strength tests that he performed solely on clay and silt sediments. The resulting values for $e_0$ and $Cc$ are 0.85 and 0.51, respectively. A water density of 1.022 g/cm$^3$ and a grain density of 2.69 g/cm$^3$ were used for the calculation of pore pressure (Fig. 3.5).

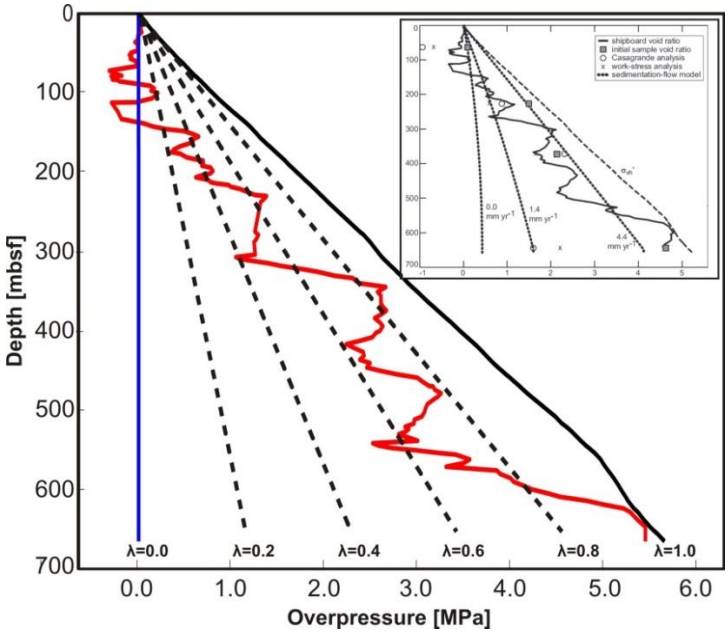


**Figure 3.5**: Pore pressure estimates at Site 1073: overpressure (red), maximum possible overpressure (black), no overpressure (blue); dashed black lines: overpressure of 20% to 80% of vertical effective stress shown for reference; inset: original result by Dugan (2003) for comparison

Here the rapid deposition of low-permeability Plio-Pleistocene silty clay sediments on top of high-permeability Miocene strata are believed to be responsible for the high pore pressure which reaches up to 95% of lithostatic pressure. High overpressure is in accordance with the existence of low-permeability sediment throughout the borehole (e.g. Dugan and Flemings, 2002; Dugan, 2003).

### 3.1.4 Limitations of the method

The method with which pore pressure is estimated makes assumptions and limitations that could potentially lead to a bias in the results. At subduction zones, Saffer (2003) states that the method provides the most robust results when the incoming sediment section is uniform in thickness and is completely subducted beneath the continental plate. In cases where the incoming material varies in its thickness or is partly accreted such as along the northern Cascadia margin, the results of the method are obscured by the influence of the combination of the effects of dewatering and the differences in initial stress states. In this study lithological differences are ignored; however it is acknowledged that excluding grain-characteristics (i.e. differences between clay and sand) yield oversimplified results. In the absence of detailed lithological logs this approach therefore provides a first order approximation of the actual pore pressure regime.

Another source of uncertainty is the derivation of $e_0$ and $Cc$ via a linear regression and the subsequent assumption of a 1D consolidation process neglecting the lateral component of the effective stress (e.g. Gibson et al., 1981). The behaviour of the lateral component is complex and Karig and Hou (1992) argued that the ratio between vertical and horizontal effective stress can be only considered constant in low vertical stress environments (i.e. < 1 MPa). Furthermore, the calculation of $e_0$ and $Cc$ relies on the assumption that Site 888 is hydrostatically pressured and that no data point has been affected by the onset of consolidation or lithification. Thus, the depth

range over which the linear regression has to be applied is not known. If pore pressure at Site 888 is greater than hydrostatic, pore pressure at all other Cascadia sites is systematically underestimated. Since sediment thickness at Site 888 is irregular, channel development is inferred, and syn-sedimentary deformation might have taken place all still within Site 888 (Shipboard Scientific Party, 1994). The assumption of a linear relationship between void ratio and the logarithm of effective stress is further put into question as the number of data points is low and the scatter in the data is fairly large.

Furthermore, the linear regression was done on MAD data which are derived directly from the cores. Physical properties can be biased due to potential free gas expansion during recovery of the cores which mainly leads to an overestimation of sediment porosity. Additionally, potential changes in sea-water density are not taken into account when data are processed, potentially leading to an underestimation of porosity and void ratio.

## 3.2 Application to the Cascadia margin

In the following pore pressure at each site of ODP Expedition 204 offshore Oregon and IODP Expedition X311 offshore Vancouver Island was estimated using equations 3.4 and 3.5. The inherent shortcomings of the linear regression and the uncertainties in application are taken into account by varying bulk and grain density by ± 10%, as well as $e_0$ and $Cc$ by ± 40%. The locations of the Cascadia margin ODP and IODP expeditions were shown in Fig. 1.9.

### 3.2.1 Estimation of pore pressure for ODP Leg 204

Nine sites were drilled in 2004 as part of ODP Leg 204 offshore Oregon (Fig. 1.9) in order to help understand the process of gas hydrate occurrence within the framework of accretionary complexes (Tréhu et al., 2006). They are spread out on a frontal ridge called

Hydrate Ridge (HR) situated about 17.5 km to the east of the deformation front, further landward compared to the Orca and Slipstream Ridges. Hydrate Ridge is ~700 m high, 10 km wide, and 15 km long. It is composed of highly deformed, folded and faulted material and has been subjected to slope failure in the past (e.g. Tréhu et al., 2006; Chevallier et al., 2006). All Leg 204 sites (Fig. 3.6) lie in the vicinity of the southern summit of HR, called Southern Hydrate Ridge (SHR), a zone that is covered by 3D-seismic data.

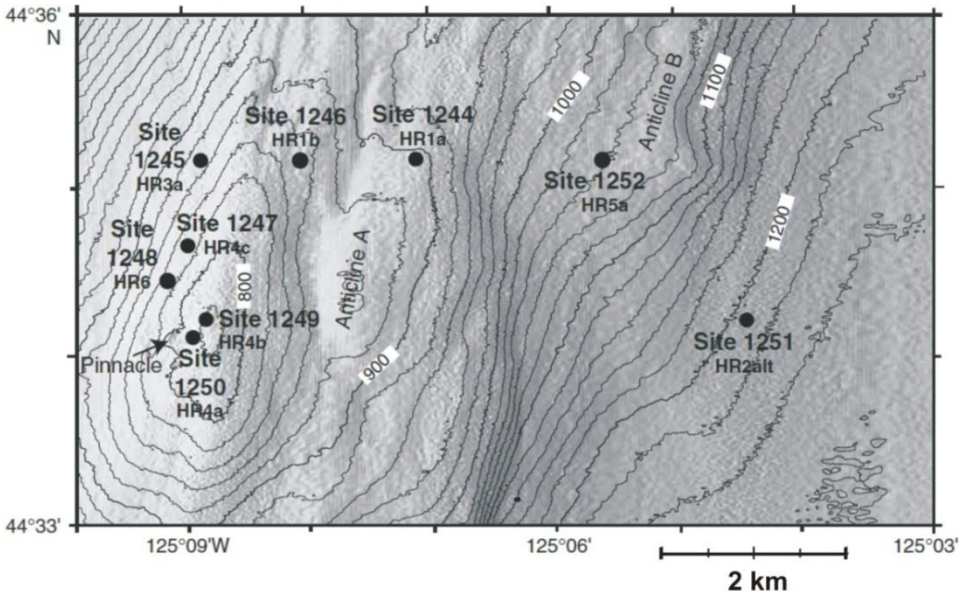


**Figure 3.6**: Location of the ODP Leg 204 sites (modified after Tréhu et al., 2003)

Detailed stratigraphic analysis (e.g. Chevallier et al., 2006) shows that HR has a very complex internal structure. The core of HR has previously been uplifted rapidly and shows signs of substantial internal deformation. The two smaller anticlines visible in Fig. 3.6 are localized uplifts and one of them - Anticline B - may potentially contain a significant amount of free gas. The uplift of the core of HR was followed by a period of slope failure (0.5-0.3 Ma) which repositioned the sedimentary units above the core. At present HR is under the sole influence of pelagic sedimentation (Chevallier et al., 2006).

The lithology at SHR consists of turbidite-derived mud- and siltstones and remainders of several debris flows interbedded with hemipelagic clay and silty clay. Sedimentation rates above the BSR are estimated to be between 60 and 160 cm/kyr (Tréhu et al., 2006).

The transport of turbidites and subsequent deposition of silts and sands, have provided the host material for gas hydrate formation. Gas hydrates occur at the northern and southern summits of HR. The former (NHR) is known for its abundant gas hydrate occurrence and existence of authigenic carbonates at the seafloor, while SHR reveals generally lower gas hydrate concentrations with only one gas venting site and one massive hydrate accumulation near the summit. Thus, the strong internal deformation and heterogeneity of the stratigraphic layers as well as the occurrence of focused fluid pathways support a generally heterogeneous distribution of gas hydrates at SHR.

SHR is currently landward-verging but has been seaward-verging in the past. The change from seaward to landward vergence occurred about 1.2 Ma ago, when abyssal plain sediments were thrust over older, more deformed and accreted units. In contrast, NHR still verges seaward. The transition of the style in vergence between NHR and SHR, coinciding with the occurrence of two west–northwest-striking left lateral strike-slip faults, is suggested to explain increased fluid flow and occurrence of authigenic carbonate at NHR. At SHR the only major fluid venting site is controlled by a volcanic ash-bearing turbidite layer and has been termed Horizon A (Chevallier et al., 2006; Johnson et al., 2006).

Pore pressure at the ODP Leg 204-sites is estimated using log-derived bulk density and values for $e_0$ and $Cc$ of case a) (Table 3.1). Results are expressed as percentage of the vertical effective stress as well as in form of the overpressure ratio $\lambda$.

***Site descriptions***

Table 3.2 gives an overview of all nine sites, including water depths, maximum depth for the log data, and the depth of the BSR below the seafloor. The table also includes the size of the variation in void ratio at each site.

| | **Water depth [mbsl]** | **Depth of log [m]** | **BSR depth [mbsf]** | **Range in void ratio** |
|---|---|---|---|---|
| **1244** | 906 | 352 | 125[a,b] | 0.59 – 3.99 |
| **1245** | 887 | 357 | 134[a] | 0.78 – 3.92 |
| **1246** | 862 | 155 | 114[a] | 0.69 – 3.99 |
| **1247** | 845 | 250 | 124[a] | 0.84 – 4.00 |
| **1248** | 843 | 170 | 115[a] | 0.99 – 3.29 |
| **1249** | 788 | 64 | 115 | 1.25 – 3.95 |
| **1250** | 807 | 184 | 114[a] | 0.89 – 3.74 |
| **1251** | 1228 | 365 | 200[a] | 0.77 – 3.93 |
| **1252** | 1051 | 74-250 | 170[a] | 0.61 – 3.64 |

**Table 3.2**: Site overview for all ODP Leg 204 sites; BSR depths derived from thermal data and pore water composition

[a]: Leg 204 summary (Tréhu et al., 2003)

[b]: BSR in seismic data depicted at ~145 m

Fig. 3.7 shows the measured bulk densities at all ODP Leg 204 sites. Bulk density at Site 1252 is derived from the Hostile Environment Lithodensity tool (HLDT).

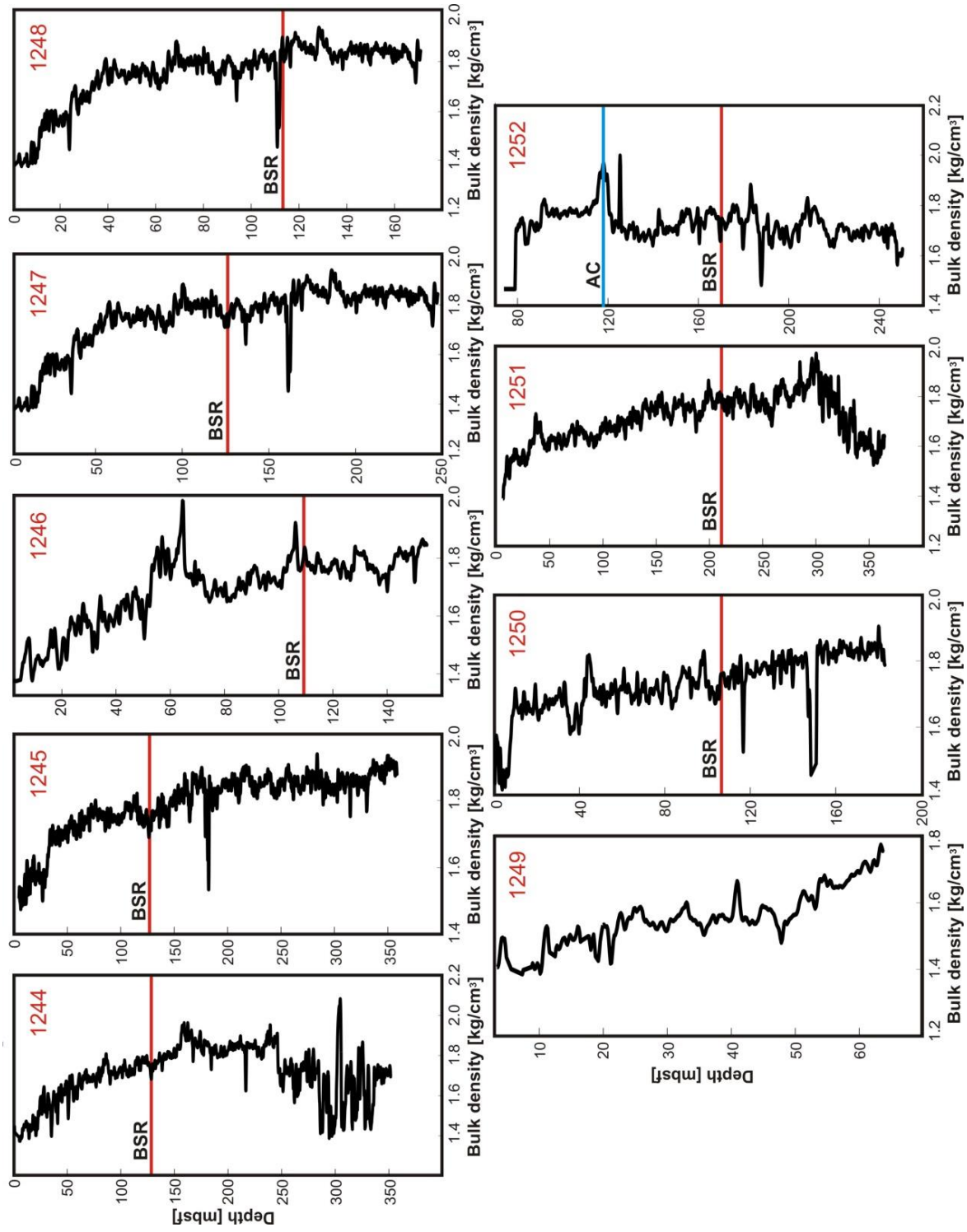


**Figure 3.7**: LWD-bulk density for all ODP Leg 204 sites; red lines indicate location of BSR as inferred from thermal data and pore water composition (Tréhu et al. 2003); blue line at Site 1252 indicates onset of accretionary prism (AC)

The bulk density is fairly similar at all ODP 204 Sites. The uppermost 20 to 40 m all start at very low bulk densities with a strong increase in values which has been attributed to degraded logging quality due to borehole breakouts. Site 1252 is the only site departing from this trend but this is due to the deep onset of the log (i.e. ~70 mbsf). This is followed by a section of steady increase in bulk density from ~1.6 to 1.8 or 1.9 g/cm$^3$. This section coincides with the sand and clay turbidite sequences that have been found in the cores. Where the borehole meets the accretionary prism (see blue line in Fig. 3.8), bulk densities are mostly constant at ~1.9 g/cm$^3$. The strong variability in the lowermost part of Sites 1244 and 1251 is due to borehole breakouts. Fig. 3.7 also shows the approximate location of the BSR, which mostly coincides with a small decrease in bulk density. For purely pore-filling gas hydrate occurrences bulk density does not show noticeable changes with gas hydrate content as has been reported for electrical resistivity. In the case of pore-filling gas hydrate pore water with the density of approximately 1.04 g/cm$^3$ is replaced by gas hydrate with a density of approximate 0.96 g/cm$^3$, without displacing any sediment. In contrast, if gas hydrates occur as grain-displacing veins and nodules, bulk density is significantly reduced.

In order to reveal possible structural influences on estimated overpressure, the results are compared to the lithostratigraphic units described by Chevallier et al. (2006). Table 3.3 gives an overview about each of these units.

Furthermore, changes in pore pressure magnitude were compared with seismic data images and color-coded to the different regions (see Fig. 3.8). The percentage values in Fig. 3.8 should be seen as a means to illustrate the relative change in pore pressure as no conclusion on absolute values can be made.

| Unit | Description |
|---|---|
| S.IA and S.IB | Slope basin sediments, less than 1.0 Ma years old<br>Contain turbidites interlayered with hemipelagic clay |
| S.II | Slope basin sediments, less than 1.0 Ma years old<br>Contains turbidites interlayered with hemipelagic clay<br>Deposited in the western part of HR<br>Deformed during the uplift of the core of HR |
| S.III | Slope basin sediments, less than 1.0 Ma years old<br>Contains turbidites interlayered with hemipelagic clay<br>Deposited in the western part of HR<br>Deformed during the uplift of the core of HR |
| S.IV | Slope basin sediments, less than 1.0 Ma years old<br>Contains turbidites interlayered with hemipelagic clay<br>Deposited in a basin east of HR but contemporary with S.II and S.III<br>Associated with another anticline (B)<br>Was deposited rapidly with ~160cm/k.y.<br>Shows higher frequency in turbidite deposition than S.II and S.III |
| S.V | Deep-sea fan sediments consisting of nannofossil-rich silty claystone<br>1.1-1.6 Ma years old<br>Deposited at ~70cm/k.y.<br>Top of this unit coincides with Horizon A |
| S.VI | Constitutes the core of HR<br>Has been deposited contemporarily with S.V but at slower rate<br>Material is lithified and fractured and has been deposited with a slow rate |
| S.VII | Constitutes the core of HR<br>Deep-sea fan sediments older than 1.6 Ma years<br>Has high degree of lithification and micro-fracturing |

**Table 3.3**: List of lithostratigraphic units as described by (Chevallier et al., 2006)

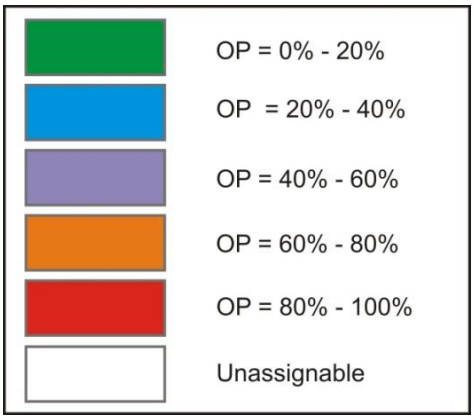


**Figure 3.8**: Color code used to highlight the changes in estimated overpressure (OP) at the Cascadia sites where an overpressure value 0% corresponds to hydrostatic pressure conditions (see Figs. 3.10, 3.14, 3.15, 3.16, A.4, and A.5)

***Results***

The results of the pore pressure estimation at each site together with error margins and a comparison with the lithostratigraphic units and seismic data can be seen in Fig. 3.9 and 3.10 as well as in Figs. A.3-A.5 in the Appendix. A running mean over a depth of 3 m was applied to smooth the small-scale variability in the results.

All sites in Fig. 3.9 show fairly high overpressure ratios (i.e. 0.7-0.8) suggesting that HR could be under significant overpressure even with the error margins taken into account. At Site 1244 overpressures ratios fall below 0.8 within a short depth interval from about 150 to 250 mbsf and then increase back to their initial value.

The lithostratigraphic units correlate only moderately well with pore pressure. The younger or uppermost units do not show as much variability in pore pressure with the exception of Site 1246 where estimated pore pressure decreases substantially between ~55 mbsf and ~65 mbsf (Fig. 3.9). Site 1245 also differs from the other three sites as pore pressures show a slow but steady decrease at depths coinciding with unit S.V.

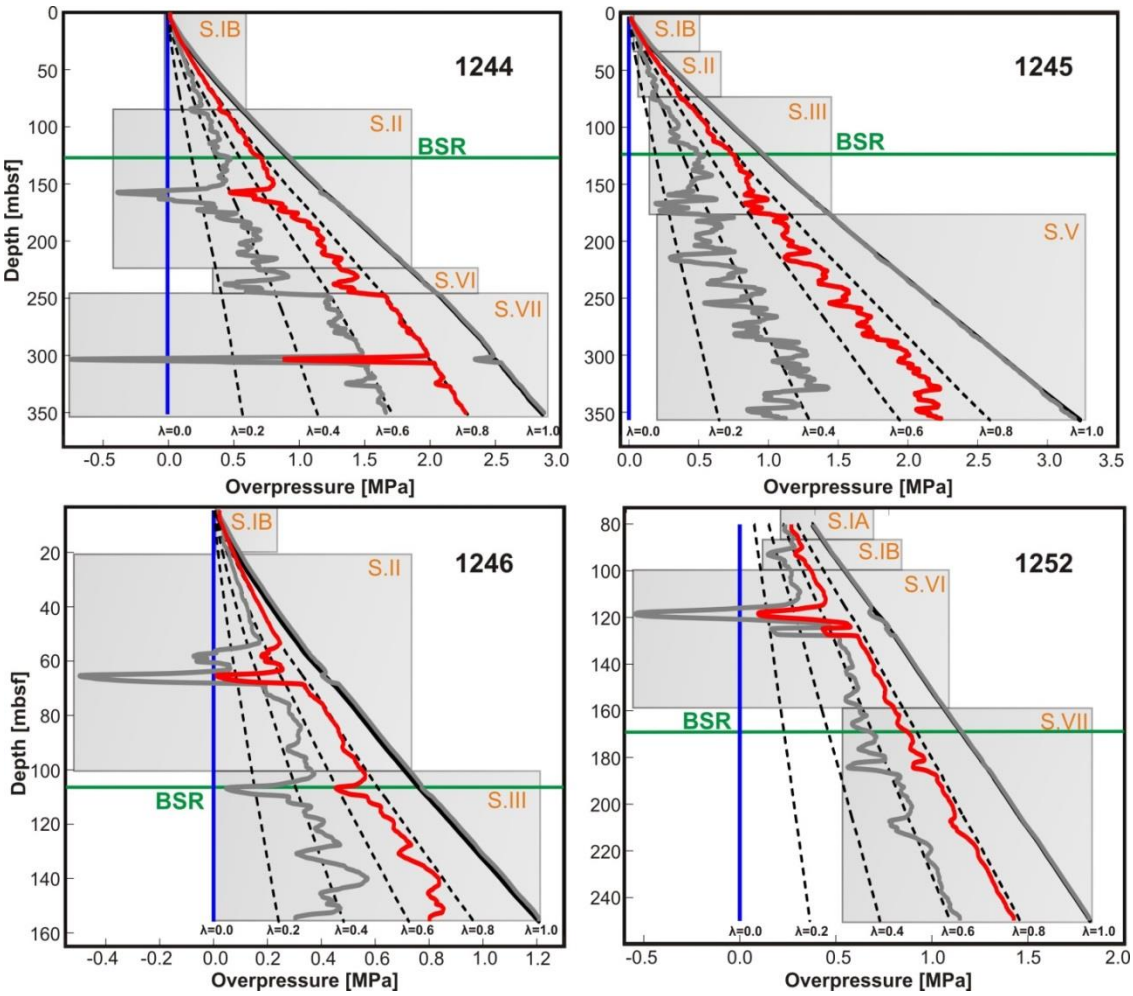


**Figure 3.9**: Pore pressure results for the sites 1244, 1245, 1246, and 1252: red line: overpressure, grey lines: error limits, blue line: hydrostatic pressure, black line: vertical effective stress (equals maximum possible overpressure); green line: BSR depth; grey boxes represent the locations of the lithostratigraphic units described by Chevallier et al. (2006)

Pore pressure at Site 1252 remains fairly steady at $\lambda$ = 0.7-0.8 with the exception of two strong negative pore pressure peaks situated between ~115 mbsf and ~130 mbsf. Generally, pore pressure ratios slightly decrease below the BSR and at Site 1246 the BSR even coincides with a strong negative peak in pore pressure.

The seismic image (Fig. 3.10) shows several strongly reflective horizons as well as acoustically blank regions in the vicinity of the four sites. Horizon A is the main conduit for fluid transport and might contain abundant free gas. It represents the top of unit S.V and consists of a

thick, coarse-grained turbidite rich in volcanic ash. Horizons B and B' are coarse-grained layers that seem to have been conduits in the past but have been segmented by normal faulting. Both horizons show signs of gas hydrates (Chevallier et al., 2006). Horizons Y and Y' are ash-bearing sand layers as well.

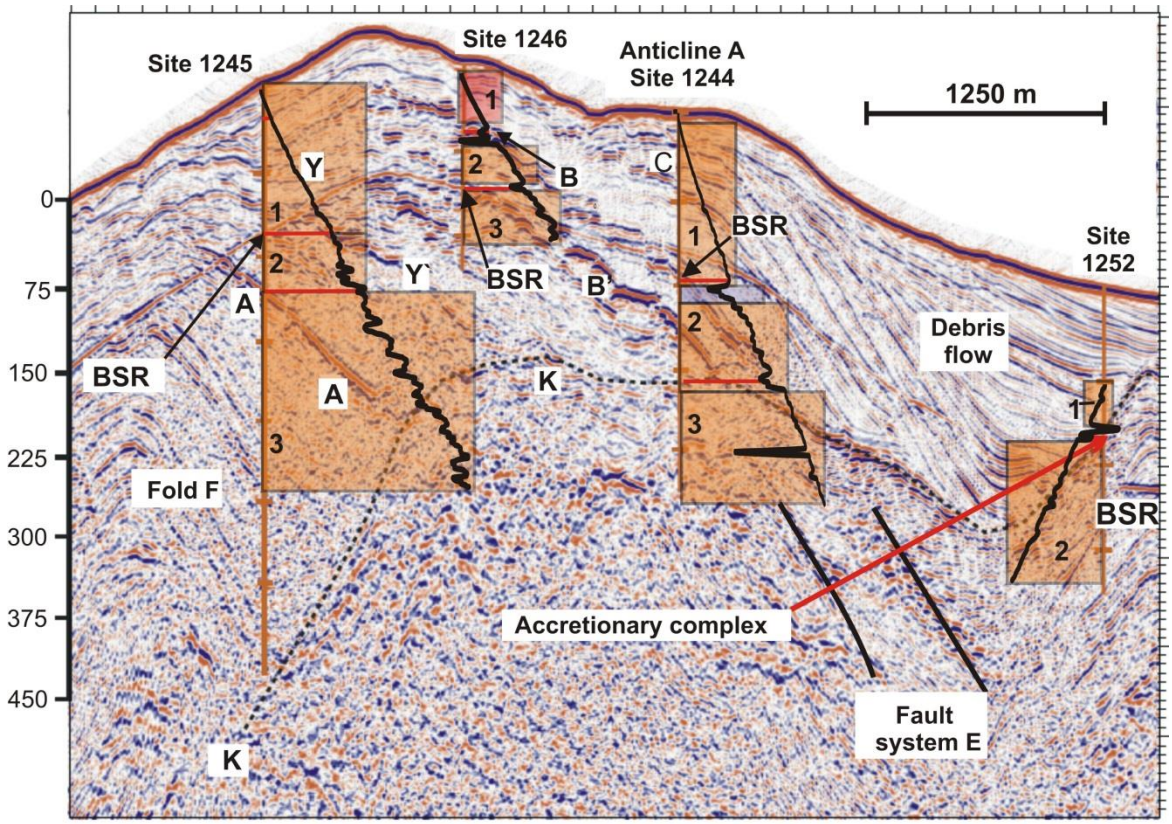


**Figure 3.10**: Overlay of estimated overpressure at Sites 1244, 1245, 1246, and 1252 with seismic image of these sites; blue = positive polarity; red = negative polarity; black line indicates overpressure; colored boxes indicating pore pressure in percentage of vertical effective stress (see color code Fig. 3.8); red lines indicate spatial coincidence of overpressure with horizons and the BSR; (modified after Tréhu and Banks, 2001)

There are also several other structures seen in the seismic data. Fold F seen in Fig. 3.10 represents the landward-vergent deformation front at an earlier stage of HR's development. Fold F has a controlling influence on the deformation of unit S.IV as well as on the geometry of units S.II and S.III. Horizon K (Fig. 3.10) has been interpreted as to be the top of what Chevallier et al.

(2006) describe as the core of HR. It shows considerable more topography than the present-day seafloor due to the strong deformational forces that have acted upon HR in the past.

Some of the seismic reflectors correlate with peaks or changes in calculated pore pressure while the blank areas mostly coincide with regions of steady pore pressure especially in the uppermost 150 mbsf. Examples for steady pore pressure within seismically attenuated areas can be seen above the BSR at Sites 1244, 1245, and 1246 (Box 1 at each of the sites).

Pore pressures then become increasingly more variable such as in the case of Site 1245 between the BSR and Horizon A (Box 2). The rapid increase in pore pressure with depth at Site 1245 at a depth corresponding to Horizon A is most likely due to fluid flow along the horizon. The remainder of Site 1245 has a moderately variable pore pressure that cannot be associated with any features in the seismic data (Box 3 of Site 1245).

Another example where features in the pore pressure can be linked to reflections in the seismic data is Site 1246. Here, Horizon B is associated with two turbidites coinciding with a strong double-peaked decrease in pore pressure probably due to low porosities. The seismically attenuated interval between Horizon B and B' is again associated with steady pore pressure ratios around 0.8. In contrast to the other sites, Site 1252 for the most part lies within the accretionary complex. The onset of the complex is mirrored in a strong negative peak in pore pressure (Fig. 3.10).

Similar observations can be made at the other 204 sites (see Figs. A.4 and A.5 in the Appendix) where average pore pressure ratios are ~0.8. Pressures decrease only slightly below the BSR together with an increase in variability. At Sites 1247, 1249, and 1251 pore pressure ratios partially lie above 0.8 at shallow depths (<100 mbsf). Site 1251 is the only site where

values return to >0.8 which is possibly related to a spatial coincidence with Anticline B (Box 4 in Fig. A.5b).

Some of the changes in pore pressure again correlate with seismic reflectors. At Site 1250 a positive pressure peak coincides with Horizon A and at Site 1249 pore pressure starts to fall immediately below Horizon Y (Fig. A.4). At Site 1247 a pressure peak at Horizon A is missing. This is consistent with the description of Tréhu et al. (2003) who state that at this site Horizon A consists of material from a soft-sediment debris flow. Furthermore, the absence of a change in pore pressure at Horizon A at Site 1248 might be due to the proximity to the BSR. Similarly, Site 1247 lies directly at the transition between lithostratigraphic units S.III to unit S.V which possibly disguises any effects of the BGHSZ on pore pressure. In contrast a few of the stronger peaks in the pore pressure can be tied to less pronounced seismic features. The decrease in pressure between 170 and 200 mbsf at Site 1247 and around 140 mbsf at Site 1248 coincide with comparatively weak reflectors below Horizon A (e.g Box 3 at Site 1247 in Fig. A.4).

### 3.2.2 Estimation of pore pressure for IODP Leg 311

The drill sites of IODP Expedition 311, conducted in 2005, lie along or close to a seismic transect running parallel to the direction of plate convergence. The transect extends from seaward of the deformation front, near Orca Ridge, to the easternmost limit of the gas hydrate occurrence zone on the upper section of the continental shelf (Fig. 3.11). The goal of the expedition was the characterization of the gas hydrate system offshore Vancouver Island.

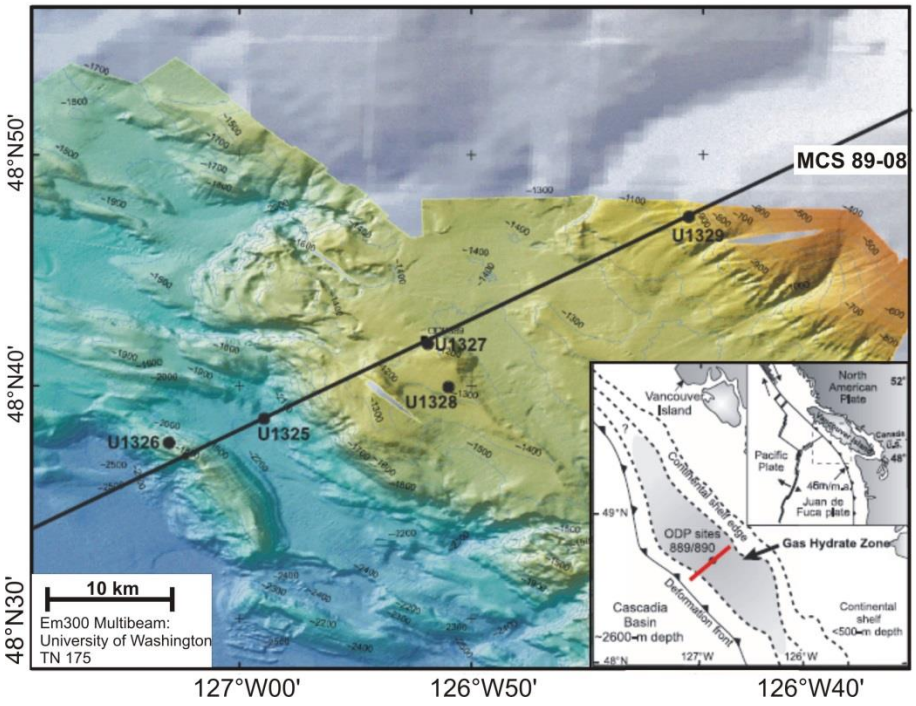


**Figure 3.11**: Locations of the IODP Expedition 311 drill sites (modified from Riedel et al., 2010)

At all sites LWD-bulk density (Fig. 3.12) was measured using the EcoScope tool. Bulk density at these sites shows markedly more variability than at Leg 204 sites but the general behaviour is similar. Sites U1325, U1326, and U1327 show a similar trend starting with an increase from 1.7 g/cm$^3$ to 2.0 g/cm$^3$ or 2.1 g/cm$^3$ within the first 120 mbsf and then depict fairly constant density (2.0 g/cm$^3$) for 130-150 mbsf. Site U1328 deviates from this by showing a decrease back to 1.75 g/cm$^3$. U1329 does not show the typical increase within the first ~150 mbsf but has a constant density of ~1.8 g/cm$^3$. At this site, density increases to 2.0 g/cm$^3$ between 130 and 185 mbsf. At greater depths Site U1329 has an even higher density of up to 2.5 g/cm$^3$, due to the consolidated sediment of the accretionary prism.

Bulk density logs were used to derive porosity and void ratio assuming a water density of 1.04 g/cm$^3$ and a grain density of 2.70 g/cm$^3$.

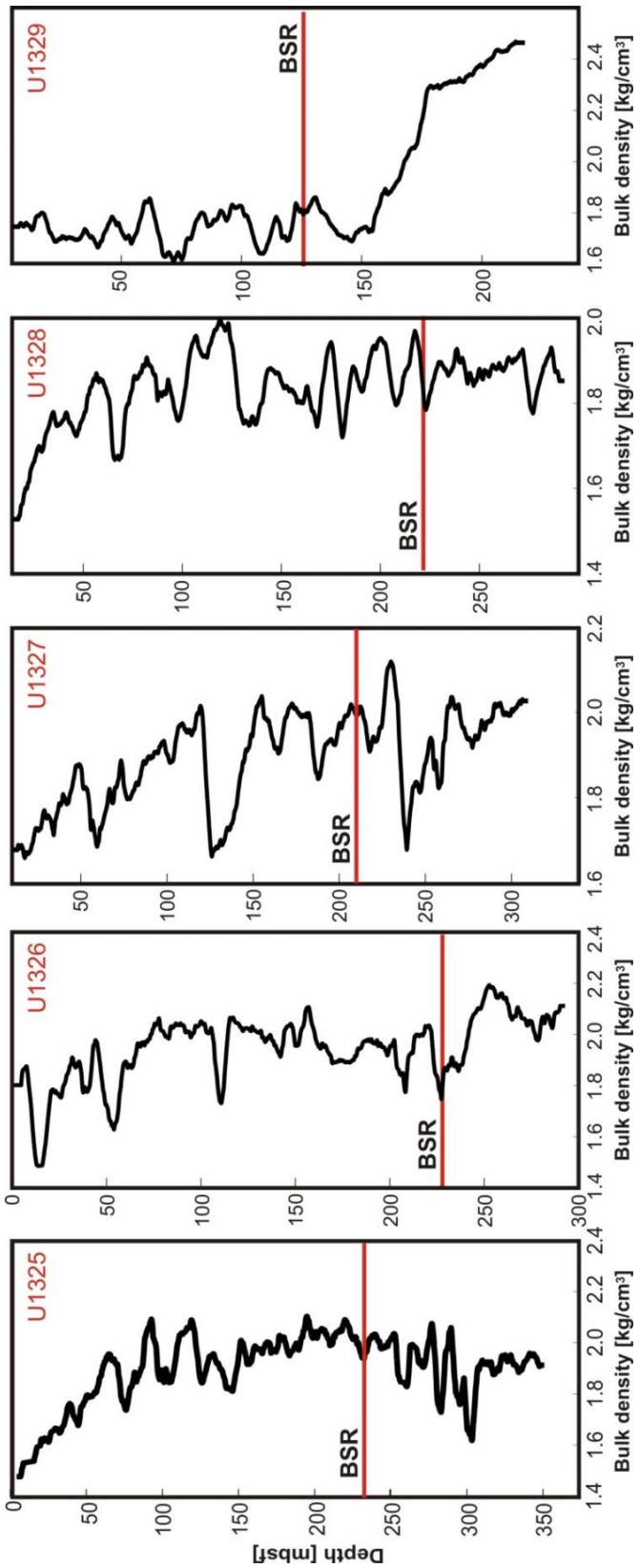


**Figure 3.12**: LWD-bulk densities for all X311 sites

No geotechnical tests have been conducted on the sediment samples in this region and case a) for $e_0$ and $Cc$ (Table 3.1) was assumed. Analogous to the sites at Hydrate Ridge, the pore pressure results were compared with the seismic images available for each site using the same color code as above (Fig. 3.8). In contrast to HR, no 3D seismic data were acquired during the X311 Expedition and only 2D seismic images from both MCS and SCS data were used.

***Site descriptions***

Table 3.4 gives a site overview, including depth below seafloor, maximum depth of the log, distance to the deformation front, seismically inferred BSR depth, and the size of the variations in log-derived void ratio.

| | **Water depth [mbsl]** | **Max depth of log [m]** | **Distance to deformation front [km]** | **BSR depth [mbsf]** | **Range in void ratios** |
|---|---|---|---|---|---|
| **U1325** | 2212 | 351 | 10 | 230[a] | 0.32 – 3.86 |
| **U1326** | 1838 | 293 | 4 | 234[a] | 0.31 – 3.99 |
| **U1327** | 1316 | 310 | 22 | 225[a] | 0.48 – 3.71 |
| **U1328** | 1278 | 14-293 | 22.5 | 219[a] | 0.59 – 4.00 |
| **U1329** | 956 | 4-218 | 47 | 126[a] | 0.12 – 3.71 |

**Table 3.4**: X311 Site overview; [a]: BSR depths taken from the IODP 311 Site descriptions

U1326 is situated on the crest of Orca Ridge, to the northeast of the failure area. At this site gas hydrate concentrations were estimated to be about 40% of the pore space with the highest concentration at about 70 to 100 mbsf. U1325 is located just landward of Orca Ridge within the first slope basin landward of the deformation front and has the greatest water depth of all sites. With an estimated 43 cm/kyr it also has the highest sedimentation rate. Similar to U1326, the sediment at this site mainly consists mainly of fine-grained clay and silt with occasional sand

layers derived from several turbidite events. U1327 is located on the mid-slope region of the continental shelf close to the ODP 146 Site 889 between two smaller, accreted ridges about 200 m in height, associated with thrust faults that have caused the uplift of the ridges and surrounding material. At this site, sediments of the accretionary complex are quite shallow beneath the seafloor and easy to discern from the overlying slope basin material. Sedimentation rates have been estimated to range from 12 to 22 cm/kyr. Gas hydrate occurrence was inferred from an increase in porosity between 123 and 141 mbsf with a gas hydrate concentration of 40-70% of the pore space. Site U1328 is located to the south of U1327 and lies within a field of active vents (Riedel et al., 2010). Gas hydrate occurs abundantly at this site with the highest concentrations at a depth of ~90 mbsf. Free gas has been inferred to exist underneath the BSR at U1328 (Riedel et al., 2002). Site U1329 is situated at the shallowest water depths and furthest landward along the transect, in a region with steep slope angles of ~6°. Sediments here consist almost exclusively of accretionary material. Lithostratigraphic units at all X311 sites predominantly consist of fine-grained detrital sediments but the abundance in sand layers and diatoms varies in between units. Unit I contains many coarse-grained turbidite layers and therefore was determined as to be of hemipelagic-turbiditic origin. At almost all Sites, Unit II shows a visible decrease in turbidite activity and an increase in biogenic material such as diatoms and foraminifers. Site U1325 in an exception as it shows an increase in coarse-grained interlayers.

***Results***

Due to the observed pronounced small-scale variability at all X311 sites, pore pressure results were imaged with a running mean over a depth of 12 m (Figs. 3.13-16) and compared to lithostratigraphic units and seismic data images available for each site.

Fig. 3.13 shows the pore pressure result together with the error bounds for Site U1326.

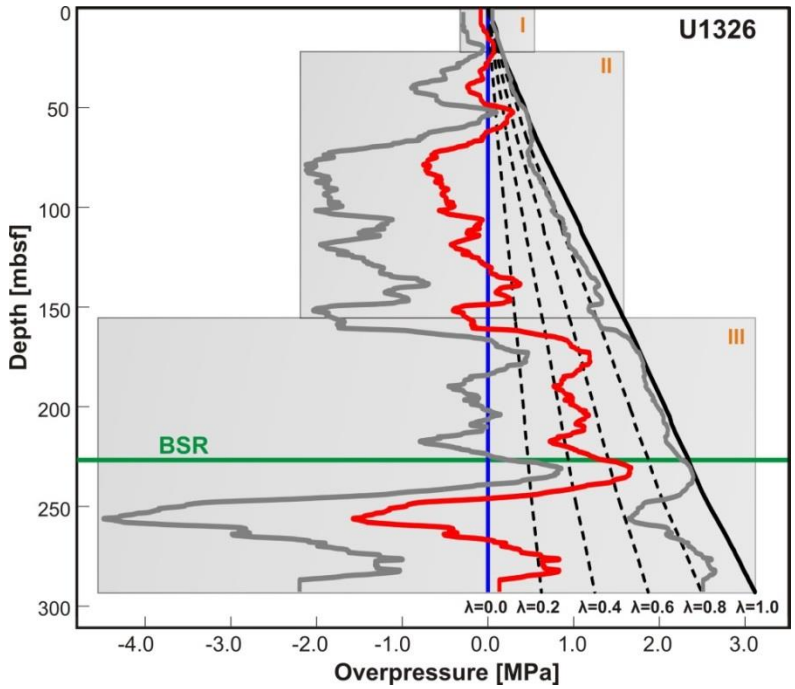


**Figure 3.13**: Pore pressure results for the Site U1326: red line: overpressure, grey lines: error limits (same assumed parameter variability as for the ODP Leg 204 sites), blue line: hydrostatic pressure, black line: vertical effective stress (equals maximum possible overpressure); green line shows depth of BSR; grey boxes indicate lithostratigraphic units at each site

In contrast to the ODP Leg 204 sites (Figs. 3.9 and A.3) - even with a larger window for the running mean - the estimated pore pressure behaves fairly erratically with $\lambda$-values from about -0.5 to about +0.7. The only interval with pressure above hydrostatic is situated between ~170 mbsf and 230 mbsf. Apart from an increase in pore pressure between unit II and unit III there is no apparent correlation with lithostratigraphic units. Below the BSR pore pressure increases visibly at first and then falls rapidly to values far below hydrostatic.

To search for any structural correlations pore pressure depth profiles were overlain on seismic images of the U1326. Fig. 3.14 shows an SCS line that crossed the site parallel to the ridge strike and an MSC line perpendicular to the ridge.

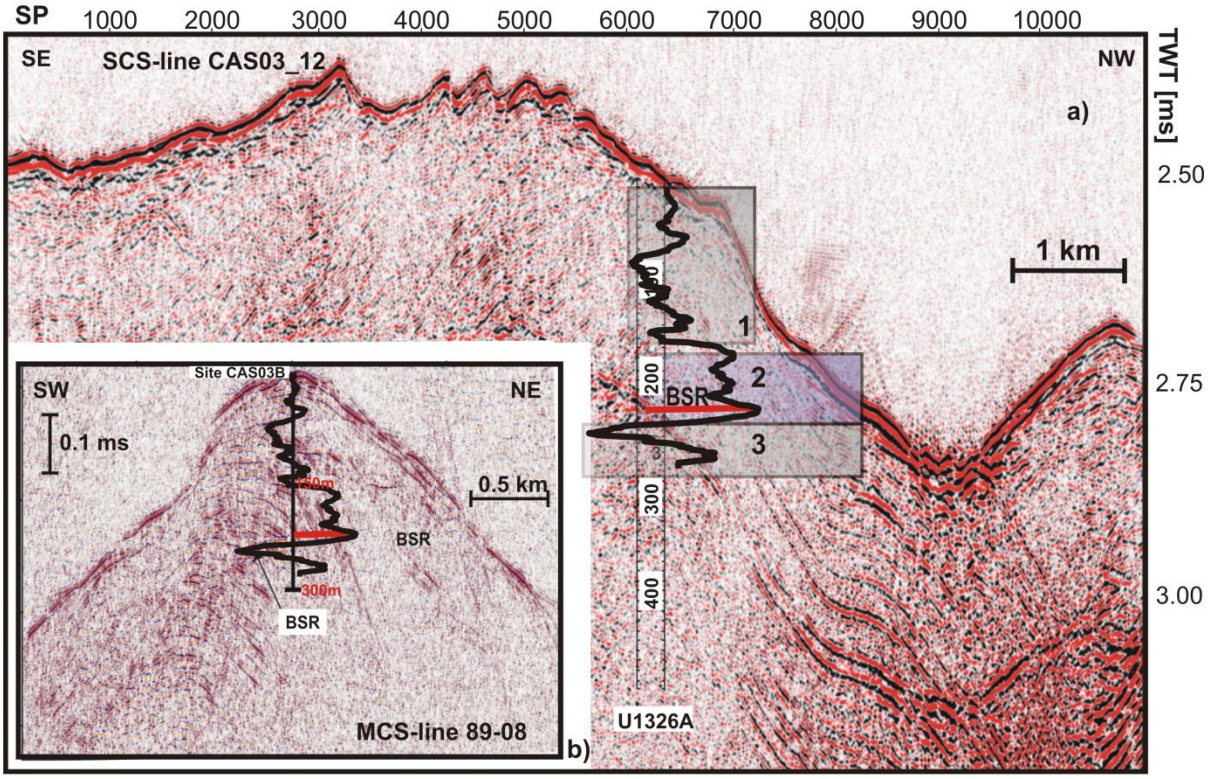


**Figure 3.14**: Estimated pore pressure at Site U1326; in both images the black line indicates pore fluid pressure (same as in Fig. 3.13); black = positive polarity; red = negative polarity; red lines indicate spatial coincidence of overpressure with BSR: a) Overlay of estimated pore fluid pressure on SCS seismic image along a profile parallel to the deformation front; colored boxes indicate pore pressure regimes (see color code in Fig. 3.8); b) Overlay of estimated pore fluid pressure on MCS section along a profile perpendicular to the deformation front

At U1326, the SCS line which strikes parallel to the ridge (Fig. 3.14a) does not depict many features other than the seafloor reflection and a strong BSR at ~260 mbsf. Perpendicular to the ridge (Fig. 3.14b) the seismic image reveals regions with lower and higher reflectivity above the BSR. A stronger reflection at ~110 mbsf coincides with a positive peak in pore pressure followed by a decrease to negative $\lambda$-values. Despite its fairly random character there is a discernible increase in pore pressure between ~60 mbsf and the BSR. This depth interval coincides with an interval of increased, steeply dipping seismic reflections while the sudden decrease matches an area characterized by seismic attenuation (Fig. 3.14b). The sub-divided pore pressure regions 1,

2, and 3 in Fig. 3.14a cannot be attributed to either the lithostratigraphic units in Fig. 3.13 or any features visible in the seismic image. It is not possible to assign a value to the pore pressure ratio $\lambda$ in Boxes 1 and 3 except within Box 2 where it remains within a range of 0.4 to 0.6.

Figs. 3.15a-d show estimated pore pressures and pore pressures with seismic data for Sites U1325 and U1327.

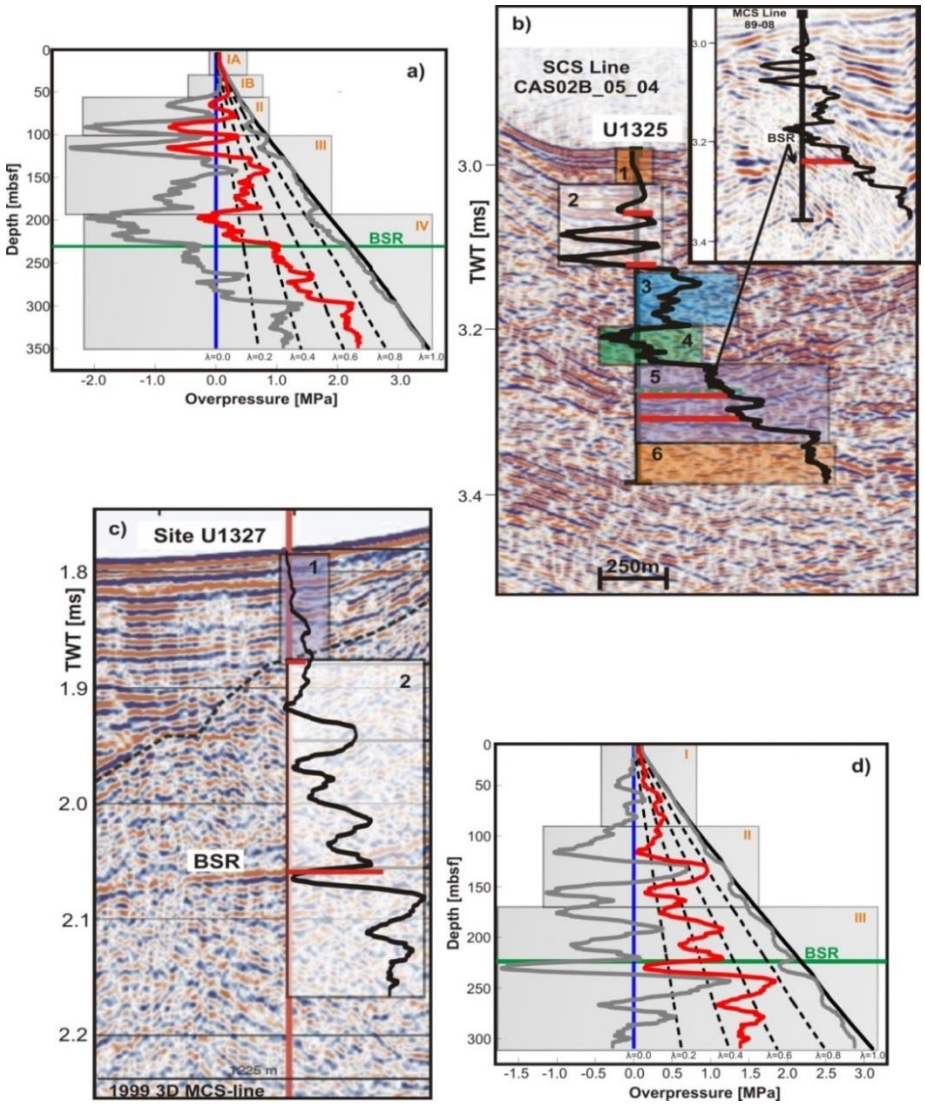


**Figure 3.15**: Pore pressure estimation for a) U1325 and d) U1327: red line: overpressure, grey lines: error limits, blue line: hydrostatic pressure, black line: vertical effective stress (equals maximum possible overpressure); grey boxes indicate lithostratigraphic unit at each site; green line shows depth of BSR; Overlay of estimated pore fluid pressure with seismic images for b) U1325 and c) U1327; in c) blue = positive polarity; red = negative polarity; black line indicates pore fluid pressure; colored boxes indicate pore pressure regimes (see color code in Fig. 3.8); red lines indicate spatial coincidence of overpressure with BSR; black horizontal lines indicate borders of different lithostratigraphic units

Similar to U1326, pore pressure variation is fairly strong (Fig. 3.15a and d) at both sites but in contrast to U1326 the values rarely fall below hydrostatic. The only exceptions are two depth intervals at U1325 at 70 mbsf to 125 mbsf as well as at ~190 mbsf to 210 mbsf where $\lambda$ reaches values below zero. At U1325 pore pressure first varies randomly until lithostratigraphic unit II transitions into unit III after which it increases gradually from less than hydrostatic to pore pressure ratios of 0.7. Pore pressures then increase strongly right underneath the BSR.

At Site U1327 $\lambda$ varies between 0.0 and 0.8 throughout the entire borehole. The strongest change in pore pressure occurs right below the BSR where it falls to almost zero and then increases again to a value close to 0.8 (Fig. 3.15d). Comparing this to Sites U1325 and U1326, pore pressure can be seen as to have no consistent behaviour with respect to the base of the GHSZ.

Figs. 3.15b and c compare these results with seismic images available at both sites. U1325 depicts widest range of overpressure at IODP Expedition 311, starting at values as high as 60% to 80% of lithostatic in the uppermost part (Box 1). This is underlain by an interval to which a $\lambda$-value is un-assignable (Box 2), and by an interval of $\lambda$ = 0.2-04 (Box 3), shortly decreasing further to approximately hydrostatic values (Box 4), to rise again (Box 5) and finally reach values of 0.6 to 0.8 in the lowest part of the borehole (Box 6). In contrast, pore pressures at Site U1327 can only be assigned stable values in the uppermost part (i.e. 0.4-0.6 in Box 1). Below the onset of the accretionary complex pore pressure starts to vary strongly.

At Site U1825 SCS seismic data (Fig. 3.15b) show several strong, almost horizontal reflectors. Some of them correlate fairly well with the occurrence of strong changes in pore pressure (e.g. Box 2 and 5), and coincide with landward dipping reflections to the west of the site (Fig. 3.15b inset). At Site U1327 (Fig. 3.15c), the image of the MCS data shows a clear

stratigraphic contrast between uniformly layered basin sediments and more chaotic abyssal plain sediments below. The boundary between these sections is not immediately evident from the pore pressure behaviour. However, variability increases markedly within the accreted sediments, although changes are not associated with specific features in the seismic image.

Calculated pore pressures at Sites U1328 and U1329 can be seen in Figs. 3.16a-d.

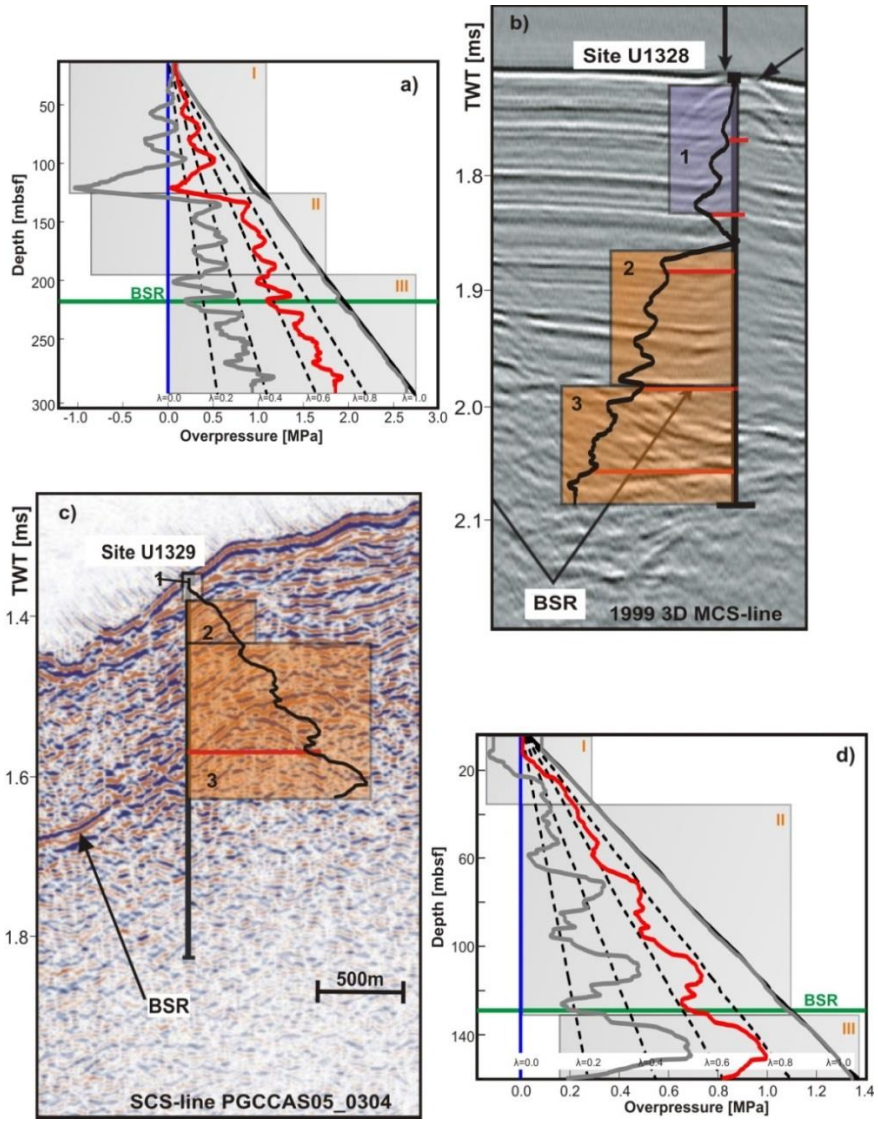


**Figure 3.16**: Pore pressure estimation for a) U1328 and d) U1329: red line: overpressure, grey lines: error limits, blue line: hydrostatic pressure, black line: vertical effective stress (equals maximum possible overpressure); grey boxes indicate lithostratigraphic unit at each site; green line shows depth of BSR; Overlay of estimated pore fluid pressure with seismic images for b) U1328 and c) U1329; black line indicates pore fluid pressure; colored boxes indicate pore pressure regimes (see color code in Fig. 3.8); red lines indicate spatial coincidence of overpressure with BSR; black horizontal lines indicate borders of different lithostratigraphic units;
Fig. 3.16c blue = positive polarity; red = negative polarity;

In Fig. 3.16, a reduced pore pressure variability is seen compared to Sites U1325 (Fig. 3.15a), U1327 (Fig. 3.15d) and U1326 (Fig. 3.13). At Site U1328 (Fig. 3.16a), $\lambda$-values largely remain between 0.4 and 0.6 within the uppermost 100 mbsf. Between 100 and ~125 mbsf pressure decreases to almost zero, after which it stays between 0.6 and 0.8 for the rest of the borehole. At U1329 (Fig. 3.16d), $\lambda$ remains between 0.6 and 0.8 throughout almost the entire borehole. Only the uppermost ~20 mbsf are at a lower pressure. Again, there is no consistent behaviour of the pore pressure relative to the BSR as pressure falls just below the BGHSZ in case of Site U1328 but increases strongly in case of Site U1329.

The seismic image for U1328 (Fig. 3.16b) reveals several reflections which only partially coincide with changes in pore pressure. Pressure mostly decreases slightly when it reaches the depth of a reflector. The uppermost ~130 mbsf have been described as consisting of several sand layers matching the depth range over which variability is high. At U1329, most of the borehole coincides with a region of high reflectivity ending just above the BSR (Fig. 3.16c). Below the BSR seismic energy is markedly attenuated and pore pressures increase to almost 90% of the lithostatic pressure.

### 3.2.3 Sensitivity of pore pressure to $e_0$ and $Cc$ at Site U1326

Due to the apparently inconsistent behaviour of pore pressure at Site U1326 (Fig. 3.13) the applicability of Site 888 as a reference site for this is especially uncertain. Therefore the values of $e_0$ and $Cc$ were varied to find a range of scenarios that lead to physically more realistic pore pressures. A selection of the results can be seen in Fig. 3.17.

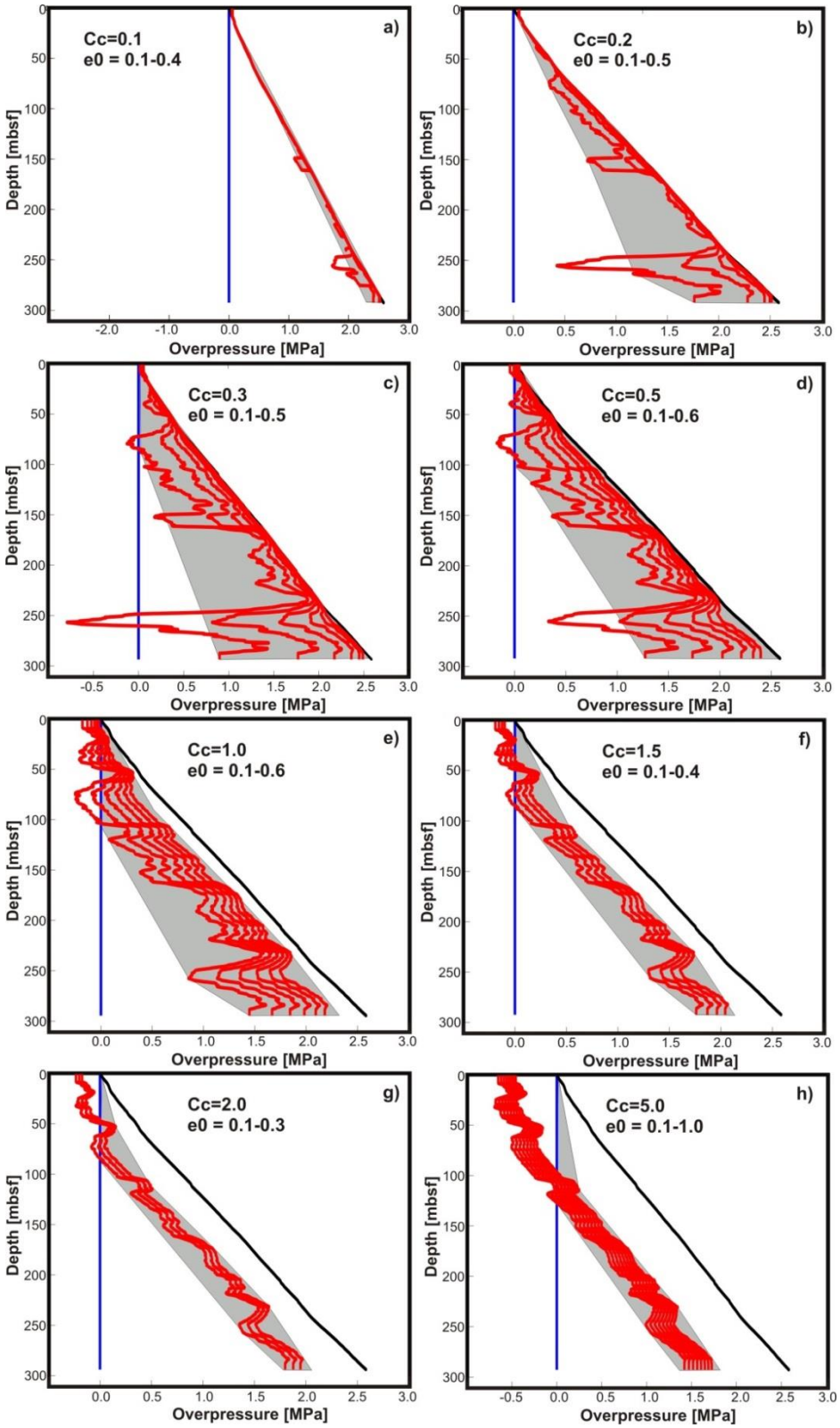


**Figure 3.17**: Comparison of pore pressure results at Site U1326 for different values of *e0* and *Cc*; red lines: pore pressure; black lines: lithostatic pressure; blue lines: hydrostatic pressure; in grey: range of pore pressure values for a given set of parameters

As expected, an increase in compression index and in reference void ratio leads to a decrease in estimated pore pressure. Highlighted in grey in Fig. 3.17 is the range of pore pressure values which also decrease with an increasing *Cc* as progressively stiffer material is implied. For pore pressure at Site U1326 to lie above hydrostatic an $e_0$ of 0.6 or lower would be required. The only exception exists with an extremely high compression index which would allow for higher $e_0$ values (Fig. 3.17h). However, for high compression indices of ≥ 1.0 a large part of the shallowest sediments at Site U1326 remains below hydrostatic suggesting that realistic *Cc* values for Site U1326 are lower.

### 3.2.4 Differences in pore pressure between ODP Leg 204 and IODP Leg 311

Fig. 3.18 summarizes the pore pressure results for the 204 and X311 sites.

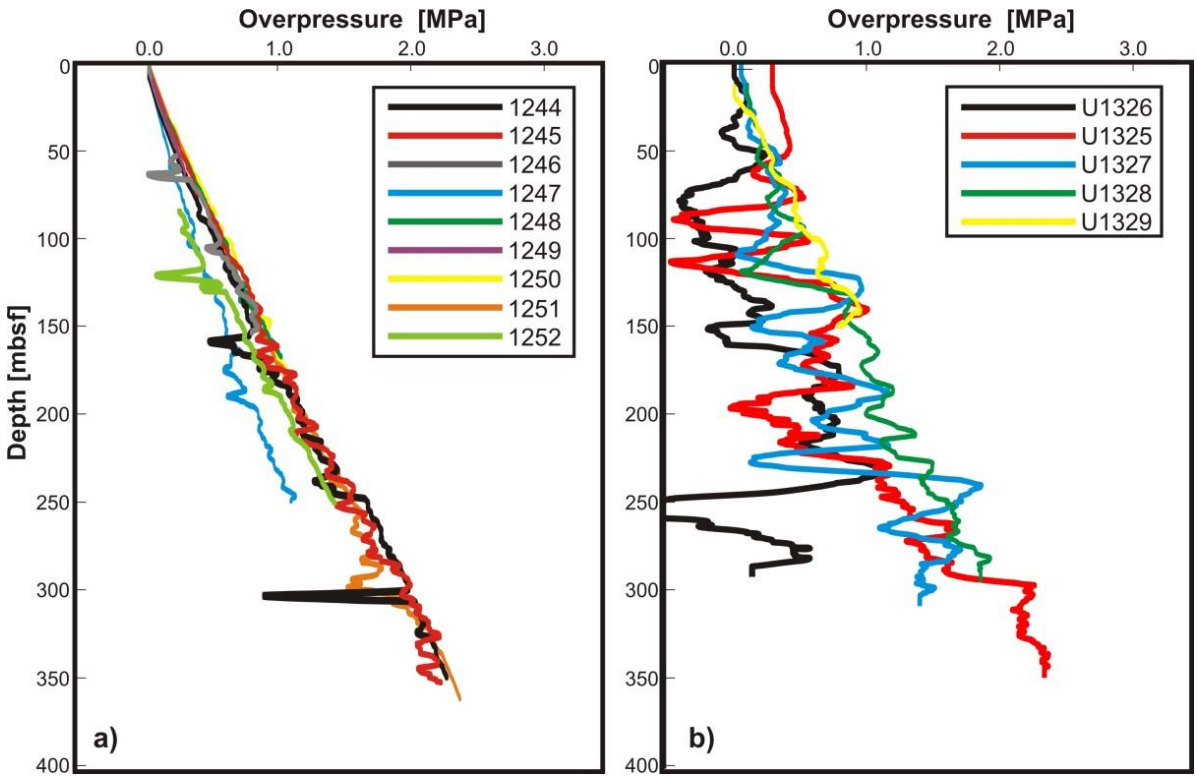


**Figure 3.18**: Comparison of pore pressure results for each site at a) Hydrate Ridge b) northern Cascadia margin

At the ODP Leg 204 sites, pore pressure gradients are mostly similar with the exception of Sites 1247 and 1252 which partly depict lower pressures than on average (Fig. 3.18a). In contrast, the results for the IODP Expedition 311 sites show an almost erratic behaviour that makes it difficult to identify general trends in the pore pressure estimates (Fig. 3.18b). Despite the strong variability, U1326 seems to be under a slightly lower pore pressure regime than the remaining Expedition 311 sites. In general, estimated fluid pressures vary much more strongly compared to the 204 sites (Fig. 3.18). This could be traced back to a larger difference between the reference void ratio $e_0$ and the calculated void ratio. The difference is additionally magnified by the exponential term in Equation 3.5. Table 3.5 summarizes the standard deviations of the difference ($e_0$-$e$) for all ODP Leh 204 and IODP Expedition 311 sites.

| **204 Site** | **Standard deviation** | **311 Site** | **Standard deviation** |
|---|---|---|---|
| 1244 | 0.594 | U1325 | 0.822 |
| 1245 | 0.361 | U1326 | 0.667 |
| 1246 | 0.548 | U1327 | 0.318 |
| 1247 | 0.541 | U1328 | 0.586 |
| 1248 | 0.239 | U1329 | 0.777 |
| 1249 | 0.404 | | |
| 1250 | 0.435 | | |
| 1251 | 0.353 | | |
| 1252 | 0.196 | | |
| **Average** | **0.408** | **Average** | **0.634** |

**Table 3.5**: Overview of the standard deviation in the difference between $e$ and $e_0$ ($e_0$-$e$) for all ODP Leg 204 and IODP Expedition 311 Sites

As mentioned above, at active continental margins additional tectonic forces play a role. For example, the high porosity values at SHR and also seen in part at the northern Cascadia

margin are either due to the occurrence of overpressure or caused by tectonically induced vertical thickening and subsequent shifts of high porosity values to greater depths. Hyndman et al. (1993) and Yuan et al. (1994) observed that the sediment porosity-depth profile at 10 to 15 km landward of the deformation front does not re-equilibrate. Similarly, the pore pressure results could also be an artifact of the changes in sedimentology as the stratigraphy at both regions varies strongly between turbidite-derived sands and hemipelagic clay.

The differences in the outcome for ODP Leg 204 and IODP Expedition 311 as summarized in Fig. 3.18 and Table 3.5 can be due to regional differences. For example, the continental slope offshore Oregon lacks landslide features (McAdoo et al. 2000) while there are many slope failures offshore Vancouver Island. Furthermore, pore pressure at both sites is expected to differ because of the significant difference in the scales of the area considered. The 204 sites are all located within a small area around Hydrate Ridge, while the 311 sites are spread over a large distance likely encountering very different geologic conditions.

Bekins and Dreiss (1992) and Vrolijk (1987) stated that the amount of fluid expulsion is a function of the velocity of the incoming sediment section, sediment thickness, prism taper angle, the initial porosity distribution, and the depth and distance relative to the deformation front. They suggest that a prism with a high taper angle loses most of its pore water within the first 20 km after the deformation front while in cases where the taper is narrow fluid expulsion occurs over a wider range. Additionally, thin sediment sections lose pore fluid earlier than thicker sections and additionally have higher initial porosity distributions. The Cascadia margin at the 204 and at the 311 sites differ in all of the aspects mentioned above as well as in the estimated sedimentation rate which is another major factor in overpressure generation. Davis and Hyndman (1989) reported that the northern Cascadia margin has a thinner incoming sediment section and a lower

taper angle than the southern Cascadia margin (e.g. Davis and Hyndman, 1989; Hu, 2011). Furthermore, there are substantial differences in the margin geometry between the northern and middle part of the Cascadia subduction zone. Apart from differing taper angles there is also an increase in the dip of the oceanic plate between northern and southern Cascadia (Davis and Hyndman, 1989). MacKay et al. (1992) also made the observation that the Cascadia margin offshore Oregon is greater in width than offshore Vancouver Island. Both parts of the Cascadia margin also differ in style in subduction. Offshore Vancouver Island all of the incoming sediment is scraped off and accreted to the continental slope (e.g. Davis and Hyndman, 1989). In contrast, there is some variation in the style of subduction along the coast of Oregon. Offshore Oregon, plate convergence has an oblique component adding to the structural complexity (MacKay et al., 1992).

Another important contrast in the tectonic setting between Oregon and Vancouver Island lies is the vergence of the ridges. Several studies, such as MacKay et al. (1992) or Johnson et al. (2006) have noticed that offshore Oregon frontal ridges are seaward-verging to the south of 44°42’ N, and whereas north of 44°52’ N they change to landward-verging. According to MacKay et al. (1992) landward vergence can be attributed to low shear strength of the basal décollement. Additionally, excess pore fluid pressures due to subduction of overpressured sediment are seen as a likely cause for the existence of a seaward dipping backstop. Johnson et al. (2006) mention that the incoming section is accreted to the continental margin coinciding with the landward verging section offshore the Oregon coast. Instead 1/3 of the incoming section is subducted and/or underplated in the seaward verging section.

Finally, there are also differences in the mechanism and magnitude of fluid transport. Hydrate Ridge possesses vertical faults that are acting as active fluid conduits (Tréhu et al.,

2006) while no such observation has been made at Orca or Slipstream Ridge. Seismic data do not show features attributable to focused fluid flow. However, it has been suggested that methane transport to shallow depths occurs via a fault or a steeply dipping sand layer in the case of Orca Ridge (Fig. 3.14b). Additionally, Lopez et al. (2010) have thoroughly discussed the occurrence of normal faults especially located around the failure area and partly reaching the depth of the BSR. The seafloor roughness as seen in Fig. 3.14a is a clear surface expression of the faults mentioned in Lopez et al. (2010).

### 3.3 Discussion

Results of the pore pressure estimation at the sites of ODP Leg 204 show significant overpressure (Figs. 3.9-3.12) even when a large margin of error is taken into account. At all ODP Leg 204 sites on Hydrate Ridge, overpressure generally remains at about 80% of the lithostatic pressure. Site 1249 is an exception having slightly higher values only reaching down to ~70 mbsf. In contrast no clear pore pressure prediction can be made for the X311 sites (Fig. 3.13-3.16). Here, pressure variations with depth are mostly very erratic. A stable estimate of overpressure ratio $\lambda$ can only be made for Sites U1328 and U1329 where it lies at 0.4-0.6. These values are higher than the average results at the other three X311 sites which is consistent with Yuan et al. (1994) who reported higher porosities in the lower midslope region of the accretionary wedge.

Estimated pore pressure was also compared to the seismic images of each site. Generally, there is a stronger correlation of changes in the pore pressure with stratigraphy compared to the BSR. Pore pressure behaviour at the 204 sites rarely correlates with the lithostratigraphic units described by Chevallier et al. (2006). In contrast, there is a stronger coincidence of pore pressure changes with seismic reflectors and blanking zones. The slight increase in estimated pore

pressure at Horizon A could be linked to fluid migration. Tréhu et al. (2006) previously mentioned pore pressures close to lithostatic at Site 1245 where high gas pressures occur due to fracture-controlled highly focused methane transport. Correlations of pore pressure with seismic data are less obvious at IODP Leg 311. No consistent behaviour with respect to the BSR could be found and there is only partially a coincidence with seismic reflectivity.

The results of the pore pressure estimation at the Cascadia margin are likely biased due to the inherent ambiguity of the linear regression, as well as the shortcomings inherent in the assumptions of the method itself. Therefore, only relative changes in pore pressure should be considered, and absolute pore pressure values along the Cascadia margin should be interpreted with caution.

Differences in the tectonic setting between both locations and results of previous studies support the conclusions that there are higher pore pressures offshore Oregon (Fig. 3.18a and b). However it remains uncertain whether Site 888 is a valid reference site for X311. The response of the calculated pore pressure at Site U1326 to changes in $e_0$ and $Cc$ (Fig. 3.17) suggest that a lower reference void ratio and maybe a slightly higher compression index might be more applicable for the IODP Leg 311 sites. Generally, the method has the potential to be a good indicator of relative pore pressure regimes in between sites and if better constrained parameters are available, its quantitative potential could be greatly enhanced.

The calculation of overpressure as done in this chapter is solely based on porosity trends. No lithologic variation (e.g. occurrence of sand) or effects of permeability are considered. Sediment layers such as Horizon A at Hydrate Ridge that consist of completely different sediments (i.e. volcanic ash) act as permeable conduits and could lead to pore pressure dissipation.

# Chapter 4: EARTHQUAKE GROUND RESPONSE AT THE NORTHERN CASCADIA MARGIN

The study of local earthquake occurrence in combination with the estimation of ground response to earthquake shaking represents a fundamental aspect of each slope failure hazard assessment. The Cascadia margin has experienced damaging earthquakes in the past (Rogers, 1998) and is known for its potential to be struck by a large, devastating 'megathrust' earthquake (e.g. Hyndman and Wang, 1995b; Goldfinger et al., 2003). To prevent future structural collapse onshore as well as offshore and to assess regional tsunami and landslide hazard, geo-engineers attempt to estimate average expected ground motion. This is done by using empirical relationships that link ground and structural response to the magnitude and distance of an earthquake (e.g. Atkinson, 2005).

In the following, earthquake ground response is estimated by using several different ground motion attenuation relationships (GMARs) for a range of earthquake scenarios. Then, the power spectral density (PSD) of OBS-measured ground motion is calculated to compare the spectral acceleration at different sites along the northern Cascadia margin and to estimate the region's prevalent ground motion characteristics.

## 4.1 GMARs – Theory, previous research, and limitations

GMARs are empirical descriptions of various intensity measures of local ground motion including the respective median and standard deviation (Erdik and Durukal, 2004). In a GMAR, ground shaking is calculated either in the time domain (e.g. peak ground displacement (PGD), peak ground velocity (PGV), peak ground acceleration (PGA)) or in the frequency domain (i.e.

peak spectral acceleration (PSA), Fourier amplitude and phase spectra, power spectra, etc.) and mostly represented in terms of the fraction of the gravitational acceleration *g*.

Earthquake ground shaking is a complex phenomenon and a function of the source characteristics such as fault plane rupture and irregularities in the rupture process as well as directivity and path effects and the local site conditions such as stratigraphy and topography. The latter can lead to amplification and de-amplification of ground response depending on the frequency content of the earthquake. In GMARs these phenomena are described in a simplified manner as a convolution of the source spectrum *E*, path effects *P*, site effects *G*, and type of motion *I*, as a function of seismic moment $M_0$, source-site distance *R*, and frequency $f$ (e.g. Boore, 2003; Atkinson, 2005):

$$Y(M_0, R, f) = E(M_0, f)P(R, f)G(f)I(f) \tag{4.1}$$

where *Y* represents the resulting site response subject to earthquake shaking.

Earthquake Fourier amplitude spectra are therefore of great importance in seismic hazard analyses as they are the graphical record of the terms illustrated by equation 4.1. If a significant number of recorded data is available, region-specific attenuation and source radiation characteristics can be derived by performing a regression analysis on the spectra.

GMARs have to account for the significant differences between earthquakes that arise due to the various source parameters, pathways, and site conditions. Youngs et al. (1997) stated that ground shaking varied markedly between earthquakes generated within the slab, crust or at the interface. The authors noted that peak ground motions from subduction earthquakes attenuated more slowly compared to shallow crustal events. Low-frequency earthquakes can generate strong ground shaking more effectively even at large distances compared to high-frequency events as the wave amplitudes attenuate more slowly (Atkinson and Macias, 2009).

It has been observed that the effect of magnitude on ground shaking is not strictly linear but varies as a function of frequency such that medium-sized events are capable of producing locally higher shaking amplitudes compared to bigger events. In-slab events seem to produce higher peak ground motions than megathrust earthquakes for the same magnitude and distance (Youngs et al., 1997). Similarly, tsunami-generation is not necessarily linked to very large earthquakes. The 1992 earthquake in Nicaragua produced wave heights of more than 10 m although it had a relatively small magnitude of 7.2. In 1946, a M7.1 earthquake caused a 42 m run-up on Unimak Island which is one of the Aleutian Islands. The event generated tsunami waves that traveled as far as the Marquesas Island and the Antarctic Peninsula where the tsunami still reached wave heights of up to 4 m due to wave focusing effects (e.g. Fryer et al., 2004; McAdoo et al., 2004).

Amongst the terms in equation 4.1 the site condition *G* (e.g. sub-bottom soil and rock properties, local stratigraphy including sedimentology, and topography) is described as the most elusive term (e.g. Gregor et al., 2002; Boore, 2003). Idriss (1991), for example, found that in comparison to rock sites soft sediments amplify ground motion at accelerations up until 0.4 g. Above this threshold value, ground shaking is de-amplified due to the reduction in effective stress. Sediments are expected to have an inelastic response behaviour that leads to a reduction in ground motion. However, amplifying effects of soil on the ground response have been experienced in cities such as Los Angeles, San Francisco, Lima, Tokyo, Osaka and Kobe, Katmandu, Lisbon, Thessaloniki, and Mexico City. During the 1989 Loma Prieta earthquake spectral accelerations at sediment sites were amplified by factors of 2 to 4 compared to adjacent bedrock (Housner, 1989). Amplification is mostly due to resonance, interference, and wave-conversion phenomena in the sub-bottom environment, or to the trapping of seismic waves in

layers consisting of soft sediment. In the presence of 2D or even 3D structures additional back and forth reverberations can be expected (Bard and Riepl-Thomas, 2000). This results in counter-intuitive ground motion behaviour such as higher peak accelerations as expected either at a location further away from the source or at smaller magnitudes (e.g. Campbell and Bozorgnia, 2003). Within basins, lateral heterogeneities or basin-edge effects have been reported to play a significant role in producing complex ground motions. Basin-edge effects are due to the constructive interference of incoming vertically directed and diffracted horizontal waves and can lead to substantial local amplification as was observed during the 1995 Kobe earthquake (e.g. Bard and Riepl-Thomas, 2000; Somerville and Graves, 2003).

Still scarcely studied phenomena are the focusing and defocusing, resonance, and interference effects due to strong gradients in topography (e.g. Geli et al., 1988; Ashford et al., 1997; Bouckovalas and Papadimitriou, 2005; Faccioli et al., 2005). As an example a site in the Southern Alps revealed that ground motion amplification differed by an order of a magnitude within a narrow frequency band around 5 Hz (Nechtschein et al., 1995). The 1994 earthquake in Northridge, California amplified ground motions by a factor of 5 at frequencies around 3 Hz (Celebi, 1995). Convexly formed structures such as ridges or canyons can lead to locally intensified shaking and strong contrasts in ground motion between the top and bottom of the structure. Structure geometry and seismic wavelength are the main controlling factors and can change the peak values of velocity and acceleration as well as the motion duration and its frequency content. The amount of amplification is thereby determined by the slope gradient as well as by the frequency at which the shear-wavelength equals the width of the base of the structure (e.g. Bard and Riepl-Thomas, 2000; Erdik and Dukural, 2004; Bouckovalas and Papadimitriou, 2005). Bouckovalas and Papadimitriou (2005) also mention that horizontally

incoming shear waves can to lead to considerable vertical motions of a ridge structure almost equal in strength to the horizontal motion, independent of any vertical excitation.

Due to the above mentioned complexity in ground response the limitations of GMARs have to be kept in mind. GMARs are essentially an oversimplification of the actual ground motion and therefore are not capable of fully capturing the natural strong variability of earthquake site response (e.g. Somerville and Graves, 2003). Furthermore, GMARs are essentially a one-dimensional representation of a three-dimensional problem. PGD, PGV, PGA, and PSA are calculated via a single equation representing the complex process inherent in earthquake shaking. Equation 4.1 is based on a regression on often broadly spread amplitude spectra leading to large error margins (e.g. Somerville and Graves, 2003; Atkinson and Goda, 2011).

Furthermore, the regression coefficients used to model the observations are non-unique. The combination of a different set of coefficients might produce similar results and lead to a misjudgement of important processes such as distance-dependant attenuation or the influence of in-elasticity (Atkinson, 2005). Additionally, every earthquake has a different source signature and each travel path can have a different effect on the waves that are passing through (e.g. Boore, 2003). Therefore, the assumptions made to capture source, path, and site effects pose a major part of the simplification inherent in GMARs.

Lastly, it has to be kept in mind that all existing GMARs have been developed for subaerial, predominantly urban areas and knowledge of the ground response in a submarine environment with fully saturated sediment is still insufficient.

## 4.2 Estimation of ground shaking at the northern Cascadia margin

Fig. 4.1a shows the distribution of a set of recent small to medium-sized earthquakes that occurred in the year between November 2010 and November 2011 and Fig. 4.1b illustrates a seismic cross-section of the northern Cascadia subduction zone together with the location of the locked, seismogenic and transition zone (Hyndman et al., 1994).

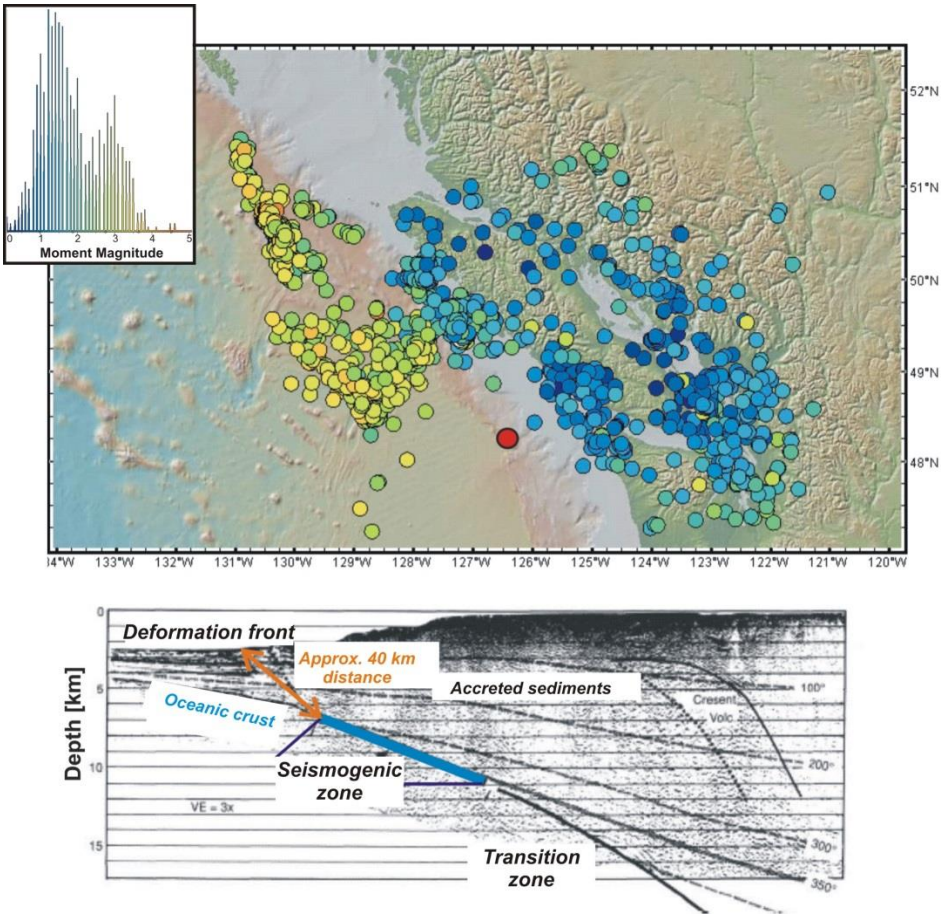


**Figure 4.1**: a) Distribution of recent earthquakes (period November 2010-November 2011); red spot representing study area; earthquake magnitudes are color-coded (color legend on upper left corner); b) cross-section through Cascadia subduction zone with location of interface between subducting slab and over-riding plate (modified after Hyndman et al., 1994)

Fig. 4.1a shows a strong spatial pattern of earthquake occurrence with the larger events clearly confined to the offshore region. Also, none of the earthquakes in this time period was located near any of the frontal ridges along the deformation front.

The earthquakes that have been recorded along the northern Cascadia margin have mostly been small- to medium sized. Despite this lack of quantitative instrumental strong-motion data, the development of empirical, semi-empirical, and stochastic attenuation relationships has been attempted (e.g. Frankel et al., 1996; Youngs et al., 1997; Gregor et al., 2002; Boore and Atkinson, 2008; Campbell (2003); Atkinson, 2005). The lack of large regional earthquake occurrence has also resulted in the development of hybrid-empirical relations that include information from earthquakes at other locations (e.g. Atkinson, 2005). This was done as the use of only small to mid-sized earthquake data would create a substantial bias, since the source properties and frequency characteristics of medium sized events are significantly different from those of megathrust earthquakes. GMARs for crustal earthquakes in Cascadia have been developed by using empirical ground-motion relations developed for California and accounting for differences in regional crustal amplification and attenuation rates. In contrast, ground motions for large subduction events are predicted via empirical relations based on global subduction databases (e.g. Atkinson, 2005; Frankel et al., 1996, 1999).

GMARs for the northern Cascadia margin also have to differentiate between earthquakes that originated in the continental crust, in the oceanic crust, within the subducting Juan de Fuca slab, or at the interface between the subducting Juan de Fuca plate and the overriding North American plate. Atkinson (2005) suggested that Cascadia earthquakes have complicated attenuation characteristics with notable differences in the wave amplitude behaviour between crustal, offshore, and in-slab events.

To calculate the expected ground response at the northern Cascadia margin and to estimate the influence of medium-to-large sized crustal, offshore, in-slab, and megathrust earthquakes, the GMARs of Atkinson (2005), Boore and Atkinson (2008), and Gregor et al.

(2002) were used. The description of the GMARS together with their respective regression coefficients can be found in Appendix B.

### 4.2.1 M5-M8 events

First, the PGA was calculated for crustal, offshore, and in-slab events with magnitudes from 5.0 to 8.0. Fig. 4.2 shows ground accelerations at rock sites for crustal and offshore earthquakes (Fig. 4.2a) using the hybrid-empirical approach of Atkinson (2005). The PGA for in-slab events in Fig. 4.2b was estimated with the GMAR developed by Boore and Atkinson (2008).

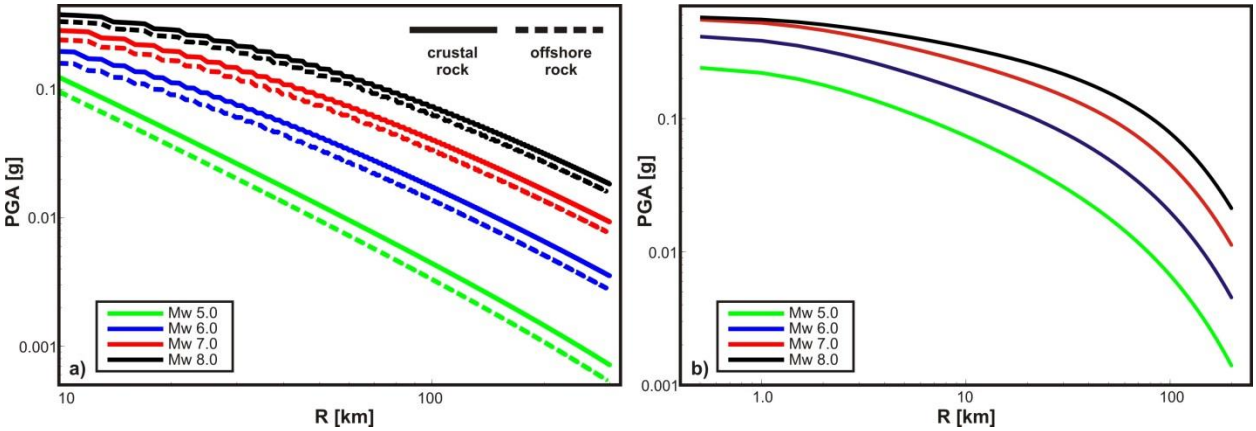


**Figure 4.2**: Expected PGA response of a) rock sites due to crustal (solid lines) and offshore (dashed lines) events calculated according to Atkinson (2005); b) in-slab events calculated after Boore and Atkinson (2008)

Offshore events of M5.0 to M8.0 at a distance of 10 km could cause considerable horizontal peak accelerations of between ~0.1 g and ~0.34 g (Fig. 4.2a). Crustal and offshore earthquakes of the same magnitude but located at a distance of 100 km would cause accelerations of ~0.0045 g to ~0.082 g and ~0.0032 g to ~0.063 g, respectively. In Fig. 4.2b expected ground accelerations due to earthquakes occurring in the down-going slab range between 0.072 g and 0.33 g at a distance of 10 km and between 0.0065 g and 0.076 g at a distance of 100 km. These results were obtained assuming an unspecified source mechanism.

With a normal faulting mechanism calculated accelerations decrease by as much as 10%-20% at small distances (Boore and Atkinson, 2008).

Differences in apparent curvature of the PGA in Figs. 4.2a and b due to the logarithmic scale indicate that in-slab events are slightly more attenuated compared to crustal and offshore earthquakes. Up until a distance of 30 km, the PGA values of in-slab events are lower than for their crustal and offshore counterparts. At larger distances in-slab events depict higher ground motions which confirms the observation of Atkinson (2005) that in-slab earthquakes propagate more efficiently in the crust than offshore events. Due to this difference in propagation efficiency, crustal and offshore events do not have the same PGA at similar magnitudes and differences (Fig. 4.2a). However, these differences diminish with increasing distance, not immediately visible in Fig. 4.2a due to the logarithmic scale.

### 4.2.2 Megathrust earthquakes

To estimate the ground response due to a megathrust earthquake the relation of Gregor et al. (2002) was used. The GMAR is based on the stochastic finite fault method by Silva et al. (1990) developed to overcome the scarcity of available earthquake records. To model earth movement along the Cascadia margin a fault dip of 9° was assumed and fault length varied between 150 km and 1100 km corresponding to the different earthquake magnitudes modeled. Furthermore, the authors used a regional crustal damping and velocity model for their simulations. The method allows the inclusion of critical parameters like finite fault effects such as rupture propagation, directivity, and source-to-site geometry together with the respective variability in parameters, source-to-site geometry, as well as their respective uncertainties.

Fig. 4.3 shows the resulting PGA for a M8.0, M8.5, and M9.0 earthquake for both rock and soil sites.

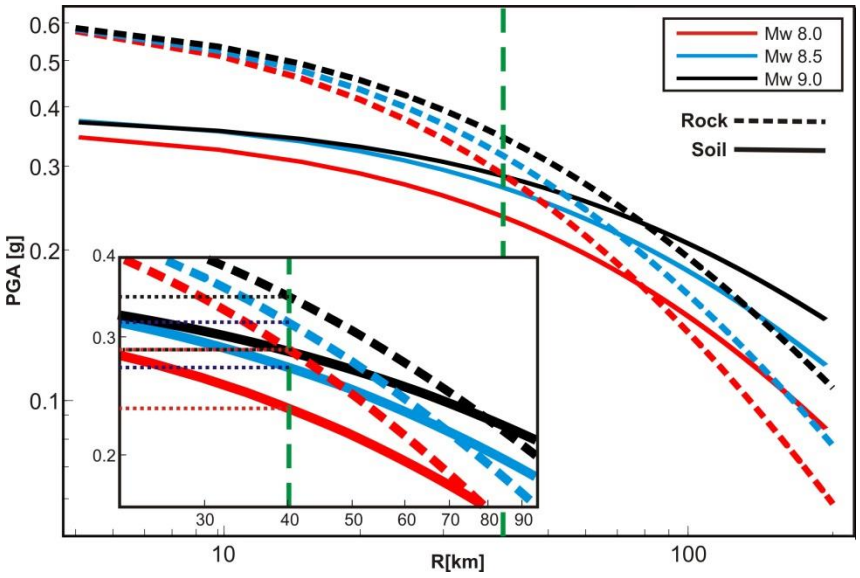


**Figure 4.3**: Expected PGA for megathrust earthquakes at rock and soil sites calculated according to Gregor et al. (2002); green line indicates distance to the up-dip limit of the seismogenic zone

At small distances soil sites have a weaker ground response to very large earthquakes compared to rock sites (Fig. 4.3). However, seismic amplitudes at soil sites do not diminish as much with increasing distance to the source and after about 80 km soil sites are predicted to have higher PGA values than rock sites. At a distance of 10 km the PGA due to a M8.0 and a M9.0 event varies between 0.32 g and 0.51 g and between 0.35 g and 0.53 g, for soil and rock sites respectively. In Fig. 4.3, the location of the up-dip limit of the seismogenic zone is indicated, the minimum distance of the rupture plane to the deformation front (see Fig. 4.1b). At this distance (40 km) the PGA for soil sites decreases to 0.24 g and 0.29 g and for rock sites to 0.28 g and 0.35 g, depending on the magnitude. Sites located at a distance of about 100 km from the source experience PGAs of 0.14 g and 0.15 g and 0.21 g and 0.19 g, showing the reversal in relative site response between soil and rock sites.

Table 4.1 summarizes the largest PGA values for each method and event magnitude. The results for the PGA at a distance of 10 km due a megathrust earthquake are printed in grey as they are most likely not applicable to the frontal ridges.

| GMAR | Case | 10km: Lower $M_w$ | 10km: Higher $M_w$ | 40km: Lower $M_w$ | 40km: Higher $M_w$ | 100km: Lower $M_w$ | 100km: Higher $M_w$ |
|---|---|---|---|---|---|---|---|
| Atk05 | Offshore | 0.1g | 0.34g | 0.013g | 0.16g | 0.003g | 0.07g |
| | Crust | 0.12g | 0.38g | 0.017g | 0.18g | 0.004g | 0.07g |
| BA08 | In-slab | 0.072g | 0.33g | 0.022g | 0.18g | 0.007g | 0.08g |
| G02 | Interface (rock site) | 0.51g | 0.53g | 0.29g | 0.35g | 0.14g | 0.19g |
| | Interface (soil site) | 0.32g | 0.35g | 0.24g | 0.28g | 0.15g | 0.21g |

**Table 4.1**: Overview of calculated PGA at different distances for lowest and highest magnitudes considered during the calculation of each GMAR; $M_w$ = Moment magnitude
Atk05 = Atkinson (2005), BA08 = Boore and Atkinson (2008), G02 = Gregor et al. (2002)

### 4.3 Site response estimation using SeaJade OBS data

The OBS-derived velocity data collected during the SeaJade expedition in 2010 allowed for the calculation of the power spectral density (PSD) of the ground acceleration along the northern Cascadia margin. This was done to look for differences in the local ground response due to contrasts in sediment characteristics or due to steep gradients in topography. Focus lay on the comparison of spectra recorded at Slipstream Ridge with spectra recorded from the abyssal plain and the continental slope. Fig. 4.4 and Table 4.2 summarize the OBS stations used in the comparison.

The Slipstream OBS (i.e. #30, #31, and #32) are all situated on the crest of the ridge (Fig. 4.4 inset) where the measured ground response can be expected to differ from the abyssal plain and continental slope sites.

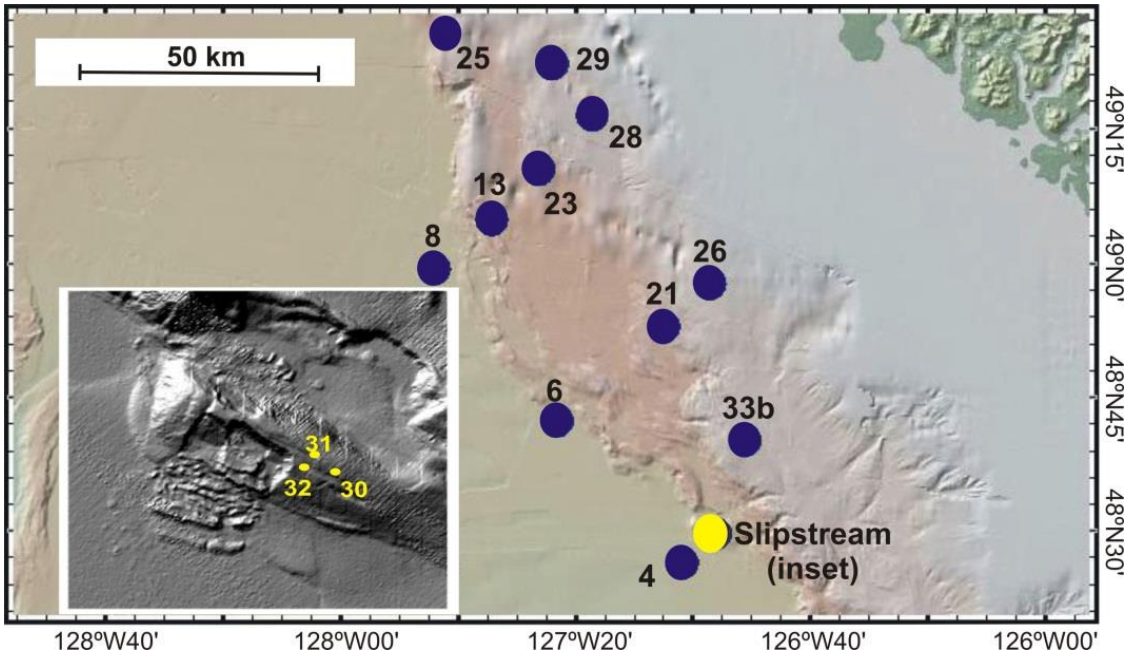


**Figure 4.4**: Location of the SeaJade OBS stations used for comparison of ground motion; inset shows locations of Slipstream OBS stations

| OBS Number | Latitude | Longitude | Location |
|---|---|---|---|
| 4 | 48.441407 | -127.029847 | Abyssal Plain |
| 6 | 48.707447 | -127.384658 | Abyssal Plain close to deformation front |
| 8 | 48.990487 | -127.733520 | Abyssal Plain |
| 13 | 49.081919 | -127.570952 | Deformation front |
| 21 | 48.883682 | -127.082763 | Continental slope |
| 23 | 49.175225 | -127.436982 | Continental slope |
| 25 | 48.446027 | -127.729828 | Abyssal Plain |
| 26 | 48.963168 | -126.951477 | Continental slope |
| 28 | 49.275482 | -127.286178 | Continental slope |
| 29 | 49.370288 | -127.398682 | Continental slope |
| 30 | 48.495598 | -126.935875 | Top of Slipstream |
| 31 | 48.498013 | -126.943023 | Top of Slipstream |
| 32 | 48.494667 | -126.946625 | Top of Slipstream |
| 33b | 48.671318 | -126.852248 | Continental Slope |

**Table 4.2**: SeaJade OBS stations used in the comparison of ground motions

The PSD was calculated for every OBS-component (i.e. E, N, Z) for each of the three major site categories. The results are depicted in decibel (dB) referenced to the highest value in the spectrum such that increasingly negative values indicate a relative decrease in signal power. Therefore, the PSD describes ground motion relative to the maximum measured acceleration at each OBS (i.e. 0 dB).

First, the PSD was derived from 4-hour long sections of the data that did not contain coherent signals such as ones caused by earthquakes or marine mammals. The resulting 'noise' spectra for the OBS #4, #6, #8 (abyssal plain), #26, #28, #29 (continental shelf), and #30, #31, #32 (Slipstream Ridge) can be seen in the Fig. 4.5.

Then, six 1-hour long time windows were picked matching the occurrence of six tele-seismic events with magnitudes > 6.0 (Table 4.3). OBS stations situated on the abyssal plain (e.g. #4, #6, and #8) are chosen to compare the Slipstream response to signals recorded on flat ground where no topographic influence should be expected. Sites near the top of the continental slope (e.g. #26, #28, and #29) are selected to include the effect of strongly irregular topography and steeper slopes.

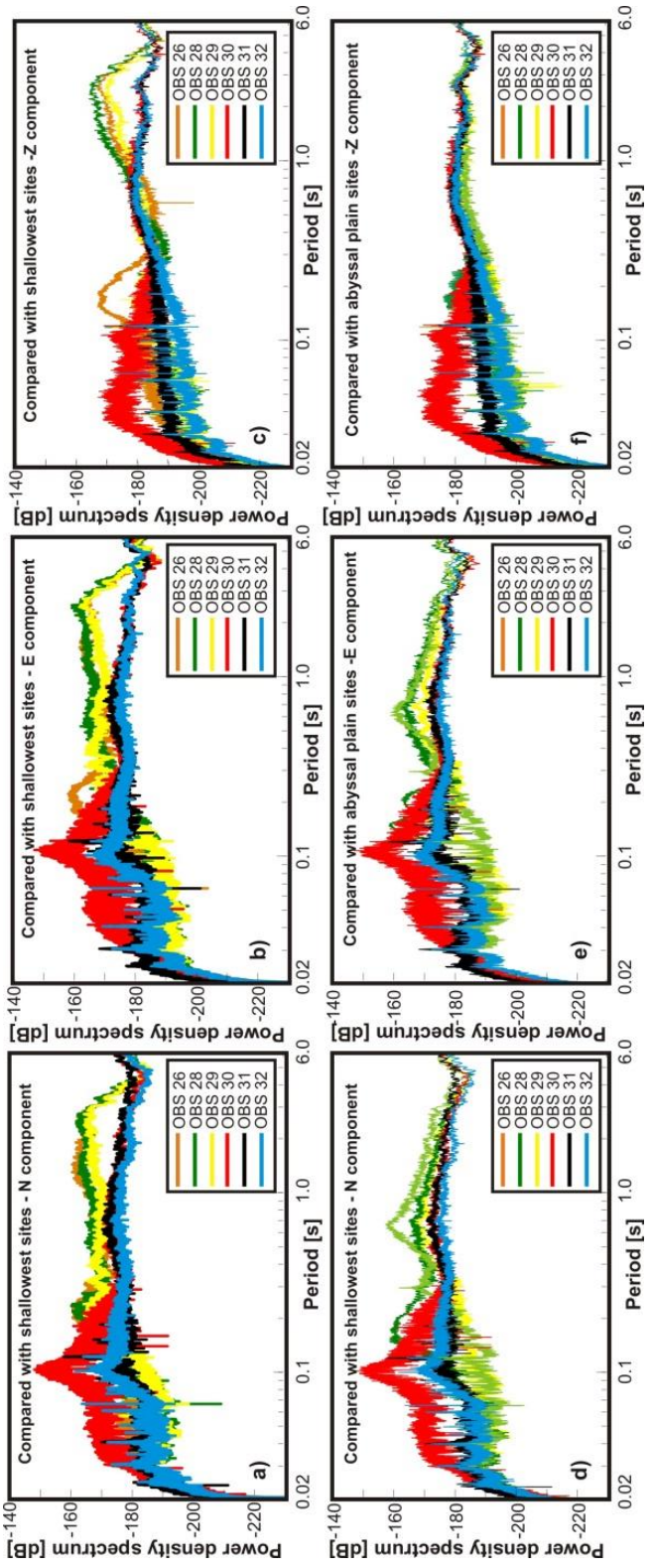


**Figure 4.5**: Ground acceleration response to 'noise' comparing Slipstream OBS to a) N-component of shallow sites, b) E-component of shallow sites, c) Z-component of shallow sites, d) N-compon-ent of abyssal plain sites, e) E-component of abyssal plain sites, f) Z-component of abyssal plain sites

| Location | Epicentral Distance from OBS #21[km] | Date | Moment Magnitude | Focal depth [km] |
|---|---|---|---|---|
| Fox Island, Aleutians, Alaska | 2987 | 18/7/2010 | 6.7 | 12 |
| Moro Gulf, Mindanao, Philippines | 10850 | 23/7/2010 | 7.3-7.6 | 576-600 |
| Vanuatu | 9967 | 10/8/2010 | 7.3 | 35 |
| Ecuador | 9068 | 13/8/2010 | 7.1 | 211 |
| Kuril Islands, Russia | 6844 | 13/8/2010 | 6.9 | 10 |
| Christchurch, New Zealand | 11860 | 3/9/2010 | 7.0 | 10 |

**Table 4.3**: Worldwide major earthquakes during the deployment of the SeaJade OBS

Signals from closer earthquakes were avoided to eliminate potential near-source effects. All six events took place along the borders of the Pacific Ocean and there were no significant arrivals from the east, southeast, or northeast of the northern Cascadia subduction zone. Fig. 4.6 shows a map of the event locations.

A selection of the resulting PSDs for each earthquake can be seen in Fig. 4.7. OBS #30, OBS #4, and OBS #26 represent the ground response of each site category (i.e. Slipstream Ridge, abyssal plain, and the continental shelf edge).

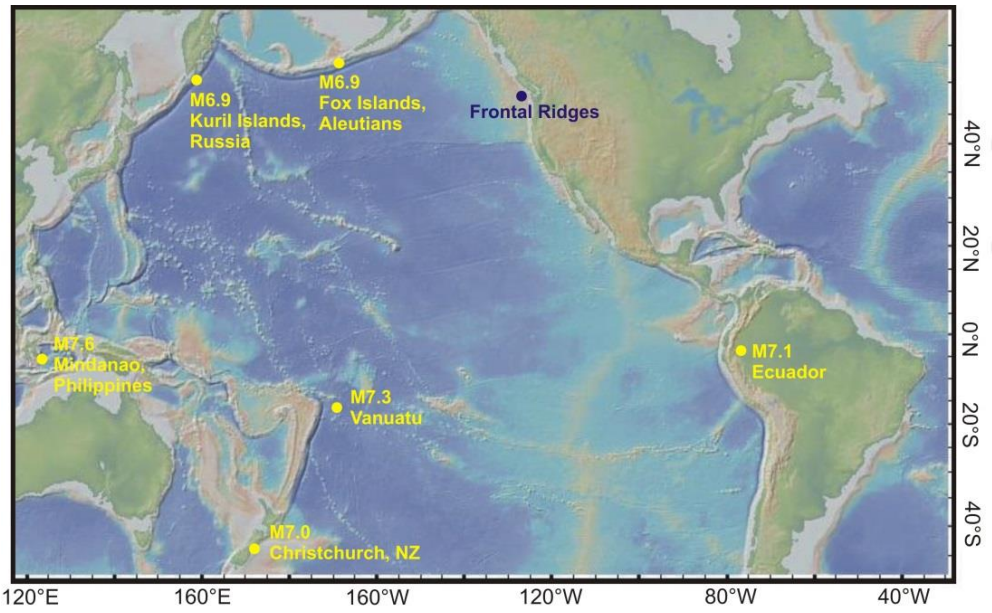


**Figure 4.6**: Location of tele-seismic events used in comparison of SeaJade OBS signals

In Figs. 4.5 and 4.7 the calculated signals are clearly frequency-dependent. The strongest variability and the most prominent signals occur at low periods corresponding to frequencies above ~2 Hz (≙ 0.5 s). At larger periods, the spectra of both the noise and the earthquake accelerations become almost flat and there are little differences between the site categories.

Surprisingly, the PSD of noise and earthquake data resemble each other strongly in their overall shape and there are only small differences in the strength of signal variability. While noise-derived PSDs vary strongly at periods below 0.3 s (≙ 3.3 Hz) (Fig. 4.6), the greatest signal variability due to earthquakes occurs at periods up until 0.6 s (≙ 1.6 Hz) (Fig. 4.7). At high frequencies (i.e. low periods) the noise spectra recorded on Slipstream Ridge show the lowest decrease in signal amplitudes relative to the reference value compared to all other sites.

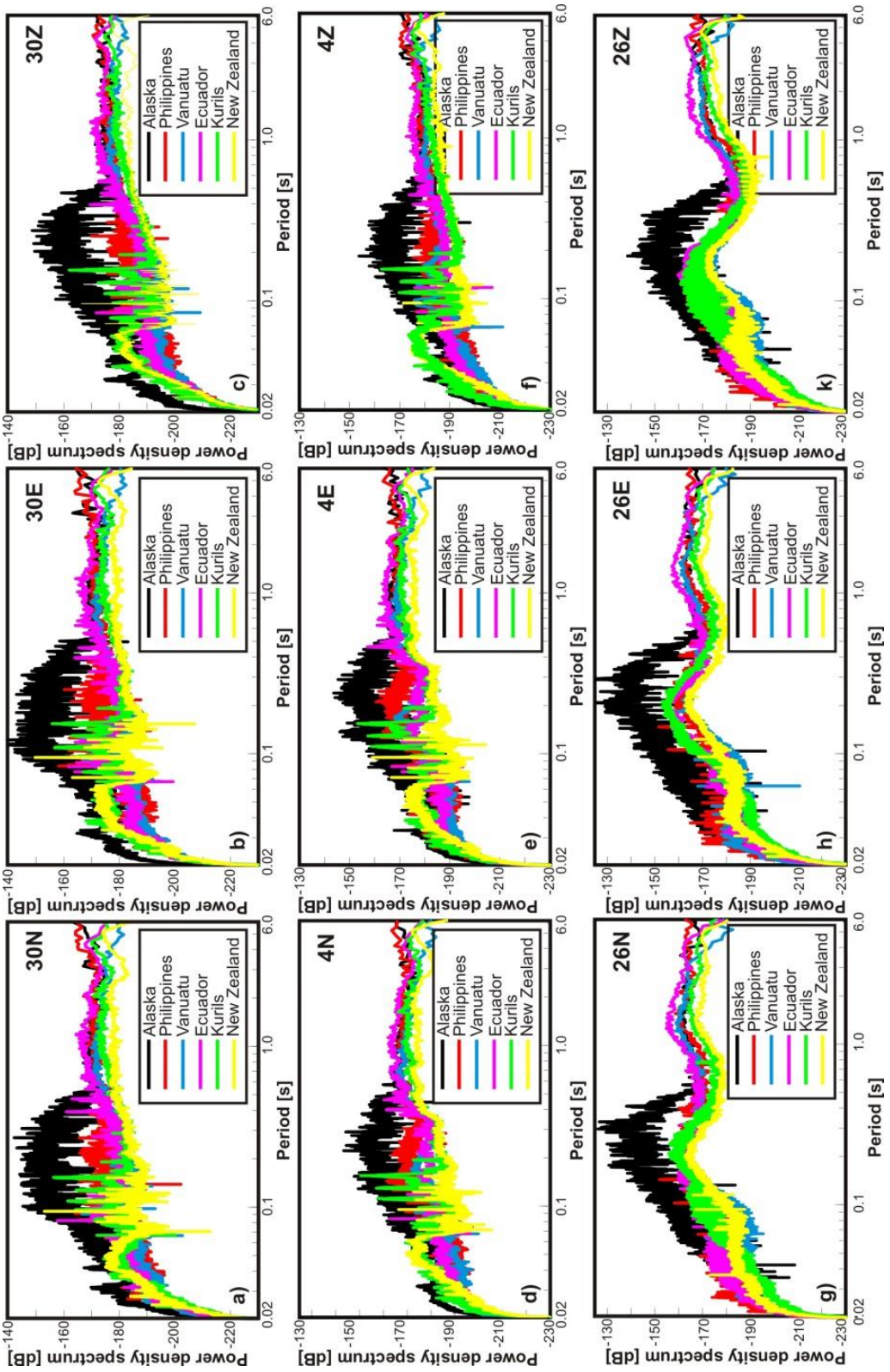


**Figure 4.7**: PSD response due to six large earthquakes at OBS 30 (non-failed ridge) a) E-component; b) N-component; c) Z-component; OBS 4 (abyssal plain) d) E-component; e) N-component; f) Z-component; OBS 26 (upper continental slope) g) E-component; h) N-component; k) Z-component

Fig. 4.7 therefore suggests that ground motions on the crest of the ridge experience the least attenuation at frequencies between ~1.67 Hz (≙ 0.6 s) and about 10.0 Hz (≙ 0.1 s). At lower frequencies, the sites on the continental slope (Fig. 4.6a-c) and abyssal plain (Fig. 4.6d-f) depict the lowest attenuation in signal strength relative to their respective maximum signal.

The earthquake-derived PSD at Slipstream Ridge shows the greatest frequency-dependent inter-event variability, especially at periods below 0.6 s (≙ 1.7 Hz) (Fig. 4.7a-c). In contrast, the continental slope sites have almost consistently the largest dB values (Fig. 4.7g-k) and at periods larger than 0.1 s (≙ 10 Hz) these sites also produce the strongest noise signals (Fig. 4.5). Continental slope sites depict the strongest variation over the whole range of periods as well as the most noticeable differences between each of their three components. In contrast, the abyssal plain sites have consistently weaker responses to noise and earthquakes at periods below <0.1 s (≙ 10 Hz) (Fig. 4.5d-f and Fig. 4.7d-f). However, their frequency-dependent shape resembles the ones of the Slipstream sites, especially on the vertical component (Fig. 4.5f) suggesting a very similar noise response behaviour (background response).

Attention was also paid to differences in the PSD between each earthquake. At all sites, the Fox Island event dominates at short periods, while at longer periods the Ecuador event has the strongest signal. Again, the strength of the PSD response only shows the relative value to the respective maximum signal, not an absolute value. The Fox Island event is the geographically closest event to the frontal ridges and it is therefore expected that the arrivals contain higher frequencies and less attenuation. The lowest PSD values belong to the Christchurch earthquake being the one furthest away from the frontal ridges (Fig. 4.7).

Some of the earthquakes depict a similarity in the shapes of the PSD. The response to the Fox and Kuril Island events resemble each other especially on OBS #26 on the shelf edge where

both have a peak response at 0.1-0.4 s (≙ 2.5-10 Hz) on the E- and N components (Fig. 4.7g and h) and between 0.07 s (≙ 14.29 Hz) and 0.6 s (≙ 1.7 Hz)on the Z-component (Fig. 4.7k). In contrast, the three M7 events of the Philippines, Vanuatu and Ecuador cause almost identical signals on each component of each site category. Although located on almost the opposite sides of the globe, the PSD of the Christchurch and Kuril Islands events are quite similar in shape. On each component of OBS #4 and #30 both earthquakes depict a strong signal variability peaking at around 0.03 s (≙ 3.33 Hz) to 0.05 s (≙ 2.0 Hz) as well as at ~1 s (Fig. 4.7a-f). On the shelf edge (Fig. 4.7g-k) the peak responses of those two events lie at slightly higher periods of 0.1-0.3 s (≙ 3.33-10 Hz) and at 1-2 s (≙ 0.5-1.0 Hz).

As there were no reference sites available to estimate absolute values for amplification and de-amplification at Slipstream Ridge, only the relative differences in ground response could be investigated. Fig. 4.8 shows the ground response when the PSD of the noise spectra are subtracted from the earthquake spectra.

The differences between each site category and each earthquake become almost insignificantly small at periods of 0.5 s (≙ 2.0 Hz) and higher. However, the abyssal and slope sites consistently have positive values, while Slipstream Ridge depicts negative differences at low periods. For periods of less than 1.0 s (≙ 1.0 Hz), Slipstream Ridge the amplitudes of the earthquake spectra do not seem to decrease as much relative to their peak response compared to the noise spectra. It has to be kept in mind that this observation rather points to differences in frequency response between sites than to differences in attenuation of seismic energy.

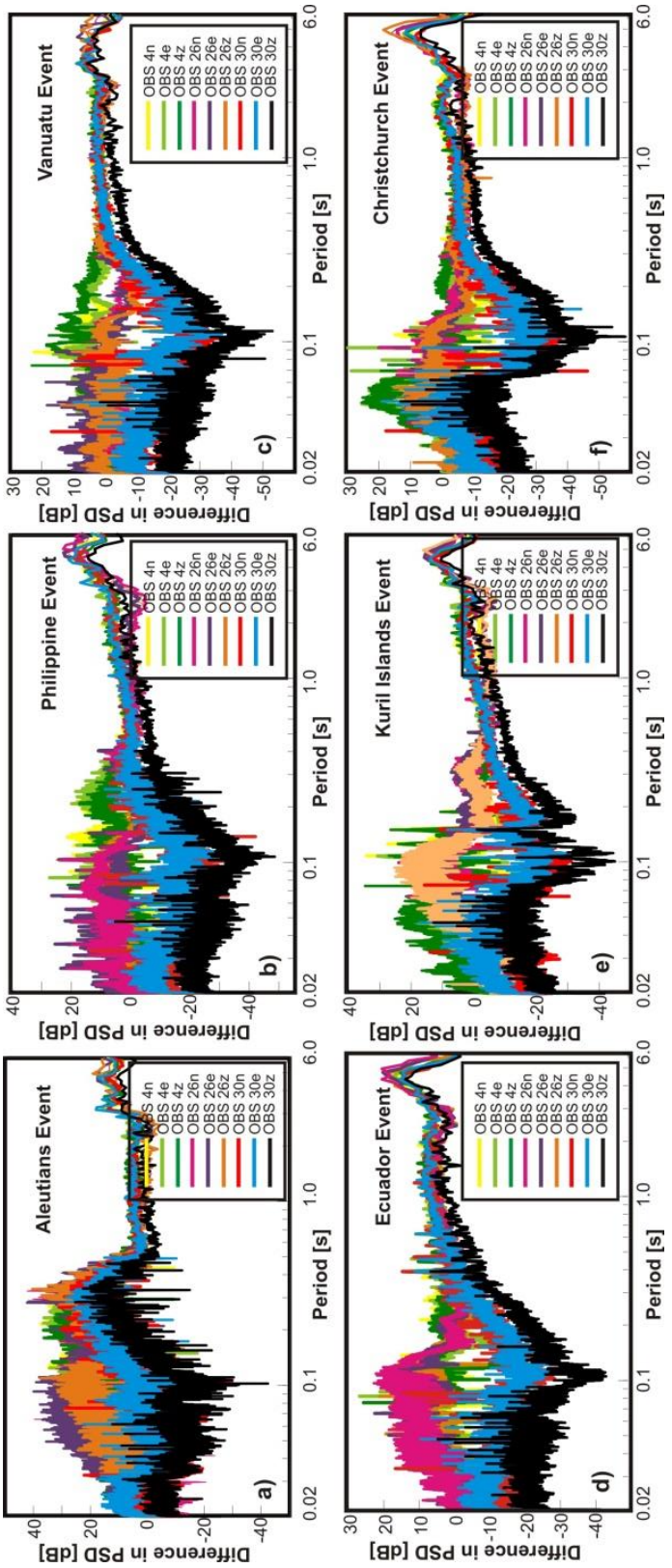


**Figure 4.8**: Difference in PSD response compared to noise spectrum for the a) Aleutian earthquake; b) Philippine earthquake; c) Vanuatu earthquake; d) Ecuador earthquake; e) Kuril Islands earthquake; f) Christchurch earthquake

## 4.4 Discussion

In this chapter earthquake-induced ground shaking was investigated using a variety of previously developed GMARs. Ground acceleration due to earthquakes of magnitudes between 5.0 and 9.0 were calculated, comparing the response of rock and soil sites as well as the effect of different source regions. Due to the distance limitation of subduction zone earthquakes the expected PGA values are lower than for M8.0 events originating in the oceanic crust or within the subducting slab. For a distance to the source of 10 km crustal and in-slab events cause maximal accelerations in the range of 0.33-0.38 g (Table 4.1) whereby the slightly higher accelerations of in-slab earthquakes can be explained by Atkinson's (2005) suggestion that seismic waves generated by offshore earthquakes propagate less effectively.

However, it has to be kept in mind that GMARs are oversimplifications of the actual earthquake process. To more accurately estimate ground motion seismological and geotechnical experiments have to be combined with non-linear modeling of ground response (Heuze et al. 2004). Complex soil behaviour such as a decreasing shear modulus and increases in strain amplitude due to hysteretic damping have to be taken into account (Seed et al., 1986). Topographic and soil effects are amongst the phenomena that would require extensive modeling backed up with information about local 3D-sub-seafloor geology, and physical and geotechnical property measurements.

Another possibility that was not considered in this study is the phenomenon of liquefaction. Dan et al. (2009) found that silt and sand layers at Algerian margin are susceptible to liquefaction and therefore are potential 'weak layers' during an earthquake.

It is not known how close the frontal ridges are to past and potential future large earthquake sources other than the approximate minimum distance to the megathrust rupture

plane. Fig. 4.1a showed the distribution of recent small- to medium-sized earthquakes. The surrounding area close to the frontal ridges suggests the existence of an aseismic gap, the minimum distance to an earthquake in Fig. 4.1a being 64 km. Judging from the results presented in Figs. 4.2 and 4.3, at this distance the acceleration of offshore or in-slab earthquakes is reduced considerably.

OBS-recorded velocity-data were used to estimate characteristic ground motion along the northern Cascadia margin. The PSD values of the ground acceleration at a set of different locations were compared to investigate relative differences between different geologic settings. The PSD of 'noise' and of tele-seismic events was compared at OBS stations situated on the crest of Slipstream Ridge, on the abyssal plain, and at the edge of the continental slope (Figs. 4.5 and 4.7). For low periods the signal strength at Slipstream Ridge was found to remain closer to the peak value compared to sites along the abyssal plain and continental slope (Fig. 4.7). Interpreting this observation as a weak attenuation suggests that the sediment at the ridge is stiffer than at other sites and thus capable of resisting stronger movement more efficiently. As the spectra are normalized to the peak values, a quantification of the attenuation cannot be carried out. However, there seems to be a frequency dependence of the ground response. Fig. 4.8 showed that at all sites, ground motion amplitudes at higher frequencies decrease less (relative to the maximum signal strength) than at lower frequencies.

There is only a small but detectable topographic effect at higher frequencies. The PSD at frequencies of 2 Hz (≙ 0.5 s) and higher varies more strongly on Slipstream than on the abyssal and continental slope sites. The latter have an additional slight increase in PSD at low frequencies between 0.5 Hz (≙ 2.0 s) and 1.0 Hz (≙ 1.0 s) (Fig. 4.7g-k). The differences between the PSDs along the abyssal plain and on the shallower part of the continental slope are probably

mainly due to the differences in water column pressure leading the more pronounced ground responses at OBS #26, #28, and #29.

No obvious directional pattern in the ground response was detected (Figs. 4.5, 4.7, and 4.8). Generally, the most variable response is found on the E-component of each OBS, especially at low periods (Fig. 4.5e and h) while the Z-component shows the flattest signals (Fig. 4.7f and k). The E-component also has the highest average response of all three components.

As the signals compared in Figs. 4.7 and 4.8 are derived from sources far away, it cannot be ruled out that stronger ground shaking due to local earthquakes could exhibit more pronounced topographic effects. A closer investigation of the ground response accounting for water-saturated sediment and strong gradients in topography would be necessary to develop ground motion predictions suitable for the underwater environment. A possibility to study site-amplification in the absence of a reference station and to estimate the fundamental frequencies of the sediment is the application of the H-V ratio technique of Nogoshi and Igarashi (1971). This method has mainly been used in Japan and uses the ratio between Fourier amplitude spectra of horizontal and vertical components of ambient noise to describe attenuation (e.g. Kudo, 1995; Bard and Riepl-Thomas, 2000; Bonnefoy-Claudet et al., 2006).

# Chapter 5: GAS HYDRATE STABILITY HISTORY

Sea-level, ocean-bottom temperatures, and sedimentation rates vary during climate cycles and change the sub-seafloor pressure and temperature conditions. Therefore the location of the P-T-stability boundaries as well as the concentration of gas hydrates are functions of climate cycles as well. A change in pressure, e.g. by sea-level fall, tectonic uplift, or by the sudden removal of overburden, can be assumed to have an almost immediate impact on the stability conditions at the BGHSZ. In contrast, it will take considerable more time for a temperature change to reach the BSR. Where the crust has previously been covered by glaciers, isostatic glacial rebound can be expected to have an additional influence.

Here, the evolution of the gas hydrate P-T-stability boundaries is compared to the timing of slope failure at the northern Cascadia margin.

## 5.1 Previous research

Studies of the role of gas hydrate dissociation in slope failure mainly focus on the influences of changes in the local pressure and temperature conditions over geological time scales (e.g. Dillon et al., 1998; Xu et al., 2001; Vogt and Jung, 2002). Others look for patterns in the spatial and temporal occurrence of submarine landslide events to find links to gas hydrate stability conditions especially during major changes in climate (e.g. Maslin et al., 2004).

In contrast to local sea-level less is known about the history of local sea-bottom temperatures. It has been proposed that since the Last Glacial Maximum (LGM) seafloor temperatures of the Pacific Ocean have increased by 2.0°C (e.g. Adkins et al., 2002; Vogt and Jung, 2002; Waelbrock et al., 2002; Siddal et al., 2010), comparable to the suggestion of Bangs et al. (2005) and Musgrave et al. (2006) that temperatures along the southern Cascadia margin

have increased by 1.75°C to 2.25°C. Another unknown is the timing of the sea-bottom temperature rise, especially relative to the event of slope failure. Vogt and Jung (2002), for example, placed the start of significant ocean-water warming between 15,000 BP and 11,000 years BP, while Siddal et al. (2010) stated that present-day ocean temperatures were not established before 9,000 years BP.

### 5.2 Timing of failure and previous stability conditions

Orca and Slipstream ridges experienced slope failure at the beginning of the Holocene during a time when both sea-level and ocean-water temperatures were rising. Fig. 5.1 shows the local sea-level curve for Orca Ridge and Slipstream Ridge (Dr. Thomas James, personal communication, 2010).

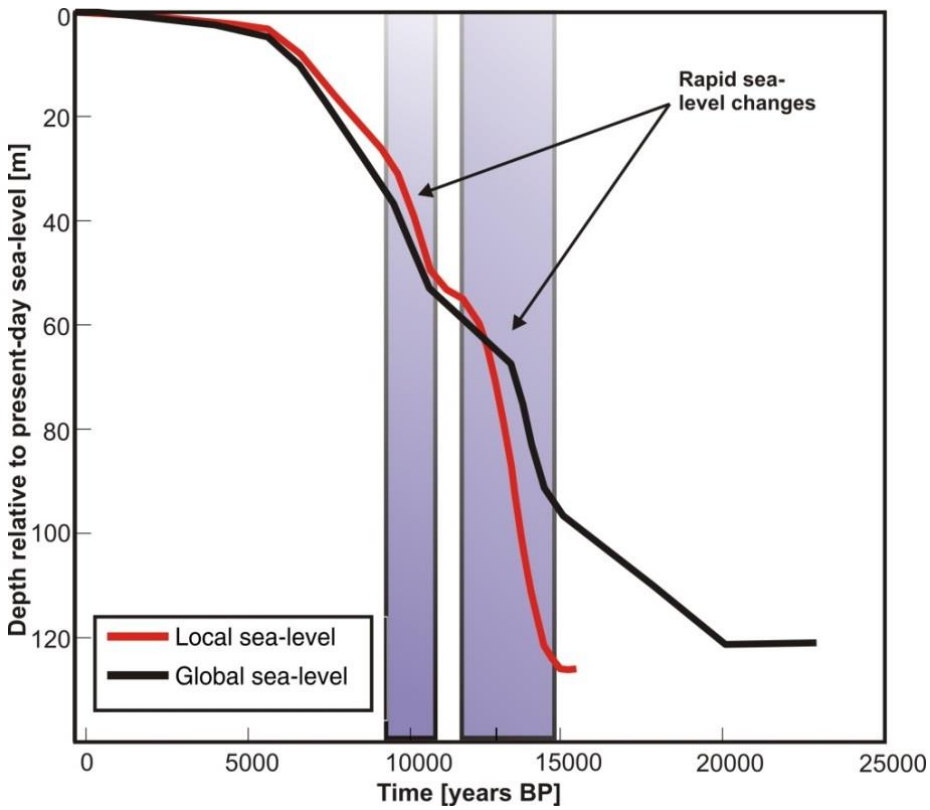


**Figure 5.1**: Local glaciostatic (red line) and eustatic sea-level curve (black line) according to Thomas James (personal communication, 2010); violet boxes indicate time intervals of especially rapid sea-level changes

Offshore Vancouver Island, sea-level changed especially rapidly during the time periods between 14,000 and 12,000 years BP as well as between 11,000 and 10,000 years BP (violet boxes in Fig. 5.1). This can be attributed to the glacial isostatic adjustment following the collapse of the Cordilleran ice sheet that had covered Vancouver Island, the Juan de Fuca Strait, and Puget Sound during the last glacial maximum (James et al., 2009). These time periods of rapid sea-level change coincide with periods of slope failure along the northern Cascadia continental margin. The influence of isostatic glacial rebound on slope stability has been emphasized by Maslin et al. (2004) who named it as the most dangerous factor for continental slope stability in a possible future greenhouse climate scenario. According to the authors, the vertical uplift would lead to a decrease in the hydrostatic pressure that acts on gas hydrates as well as to an increase in seismic activity due to the generation of vertical and horizontal strain (Mörner, 1991).

In the following, the depths of the BSR and the top of gas hydrate occurrence zone (TGHOZ) were calculated over a period of 15 ka to provide an estimate of the sensitivity of the stability limits to P- and T-changes. Present-day BSR and present-day TGHOZ are compared with Holocene conditions along several ridge-perpendicular profiles through the intact and failed parts of Orca Ridge and Slipstream Ridge (Fig. 5.2). Special focus lies on the time interval between 14 ka BP and 9 ka BP when sea-level rose by 82 m at Orca Ridge (from 108 m to 26 m below present-day sea-level) and by 83 m at Slipstream Ridge (from 109 m to 26 m below present-day sea-level). Uncertainties about absolute temperatures were included by assuming that ocean-bottom waters warmed by 1.0° C, 2.0° C, and 2.5° C in a time interval between 15 ka and 9 ka BP. Thermal gradient, salinity, methane solubility, and seawater density were held constant. Realistically, methane solubility is temperature-dependent and would enhance the shoaling-effect on the BSR during periods of warming (Xu et al., 2001).

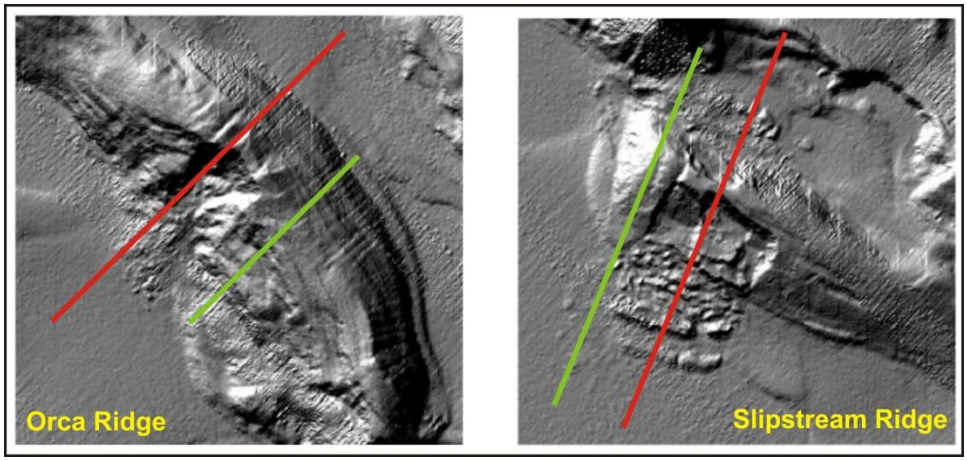


**Figure 5.2**: Profiles of Orca and Slipstream Ridge used for BSR and TGHOZ calculation; green line: intact ridge profile; red line: failed ridge profile

### 5.2.1 BSR

BSR depths can be calculated when water depth, thermal gradient, and seafloor temperature are known. Depths to the seafloor are derived from multi-beam swath bathymetry providing the information necessary to calculate hydrostatic pressure. Additionally, present-day sea-floor temperatures of 2.5° C and a constant temperature gradient of 0.06° C/m (Riedel et al., 2006c) were assumed. P-T stability conditions for structure I methane hydrate were calculated using CSMHyd (Sloan, 1998) with a salinity value of 3.4 wt%. The stability temperature-depth profile *T(z)* can be written as:

$$T(z) = 8.9854 * log(P(z)) - 9.1652 \quad (5.1)$$

Here, *P* is the hydrostatic pressure and *z* as the depth. The absolute error in the estimation of stability temperature is 0.65° Kelvin with this software (Koh et al., 2011).

The changes in hydrostatic pressure over time were inferred from local sea-level history (Fig. 5.1) and combined with equation 5.1 to calculate the evolution of the BSR at Orca and Slipstream Ridge along the profiles seen in Fig. 5.2.

***Results***

Fig. 5.3 shows the calculated BSR depths along the intact profiles of Orca and Slipstream Ridge and Table 5.1 provides a summary of the average depth differences relative to the present-day BSR.

| Ridge | Time [years BP] | Seafloor temperature [°C] | BSR depth [mbsf] | Depth difference relative to present [m] |
|---|---|---|---|---|
| **Orca** | 9,000 | 2.5 | 247 to 249 | -1 to -3 |
| | 9,000 | 1.5 | 266 to 267 | +16 to +17 |
| | 9,000 | 0.5 | 283 to 284 | +33 to +34 |
| | 9,000 | 0.0 | 293 to 294 | +43 to +44 |
| | 14,000 | 2.5 | 241 to 244 | -6 to -9 |
| | 14,000 | 0.5 | 277 to 279 | +27 to +29 |
| | 14,000 | 0.0 | 286 to 289 | +36 to +39 |
| **Slipstream** | 9,000 | 2.5 | 262 to 263 | -1 to -2 |
| | 9,000 | 1.5 | 278 to 279 | +16 to +17 |
| | 9,000 | 0.5 | 295 to 296 | +33 to +34 |
| | 9,000 | 0.0 | 304 to 305 | +42 to +43 |
| | 14,000 | 2.5 | 257 to 258 | -6 to -7 |
| | 14,000 | 0.5 | 290 to 292 | +28 to +30 |
| | 14,000 | 0.0 | 299 to 300 | +37 to +38 |

**Table 5.1**: BSR depths and depth differences of both ridges for different paleo-seafloor temperatures; the depth increase is indicated by positive values

It can be inferred that sea-level increase alone would have had a slight stabilizing effect on gas hydrate occurrence, increasing the BSR-depth by only a few meters since the beginning of the Holocene. However, when colder Holocene seafloor temperatures are assumed, BSR depths change more significantly. As an example, for a seafloor temperature of 0.5° C, the BSR depths

at Orca and Slipstream Ridge are up to 29 m and 30 m deeper compared to the present, respectively. In turn, sea-level increase reveals a more pronounced effect 9,000 years BP than at 14,000 years BP, probably attributable to the opposite effects of sea-level rise and temperature increase. Taking into account a deviation in stability temperature by 0.65° C, the absolute BSR-depths vary by up to ±11 m due to the strong temperature-dependence of the stability conditions.

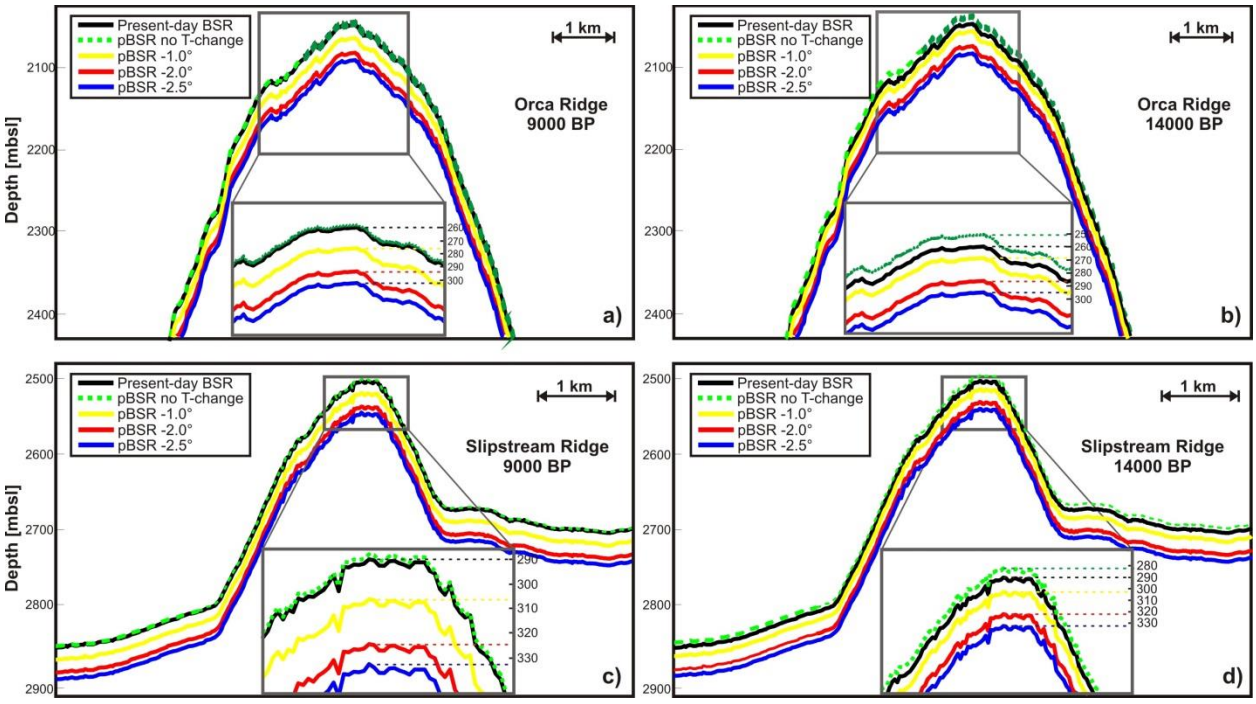


**Figure 5.3**: BSR depths along profiles of the intact part of Orca and Slipstream Ridge (Fig. 5.2) for different paleo-seafloor temperatures; the depth increase is indicated by positive values; a) Orca 9,000 years BP, b) Orca 14,000 years BP, c) Slipstream 9,000 years BP, d) Slipstream 14,000 years BP; insets show BSR depths below the crest of the ridges

The profiles crossing the failed part of the ridges only reflect the topography of the failed slopes and therefore the calculated BSR-depths in Fig. 5.3 mimic the shape of the gliding plane. To estimate the location of gliding plane relative to a more realistic paleo-BSR, the pre-failure slope was estimated by interpolating between the adjacent profiles cutting through intact parts of the ridges. Fig. 5.4 shows the results for the BSR-depths for both the interpolated paleo-seafloor

and the post-failure topography at both ridges. For plotting reasons the case of a simple change in sea-level therefore has been left out.

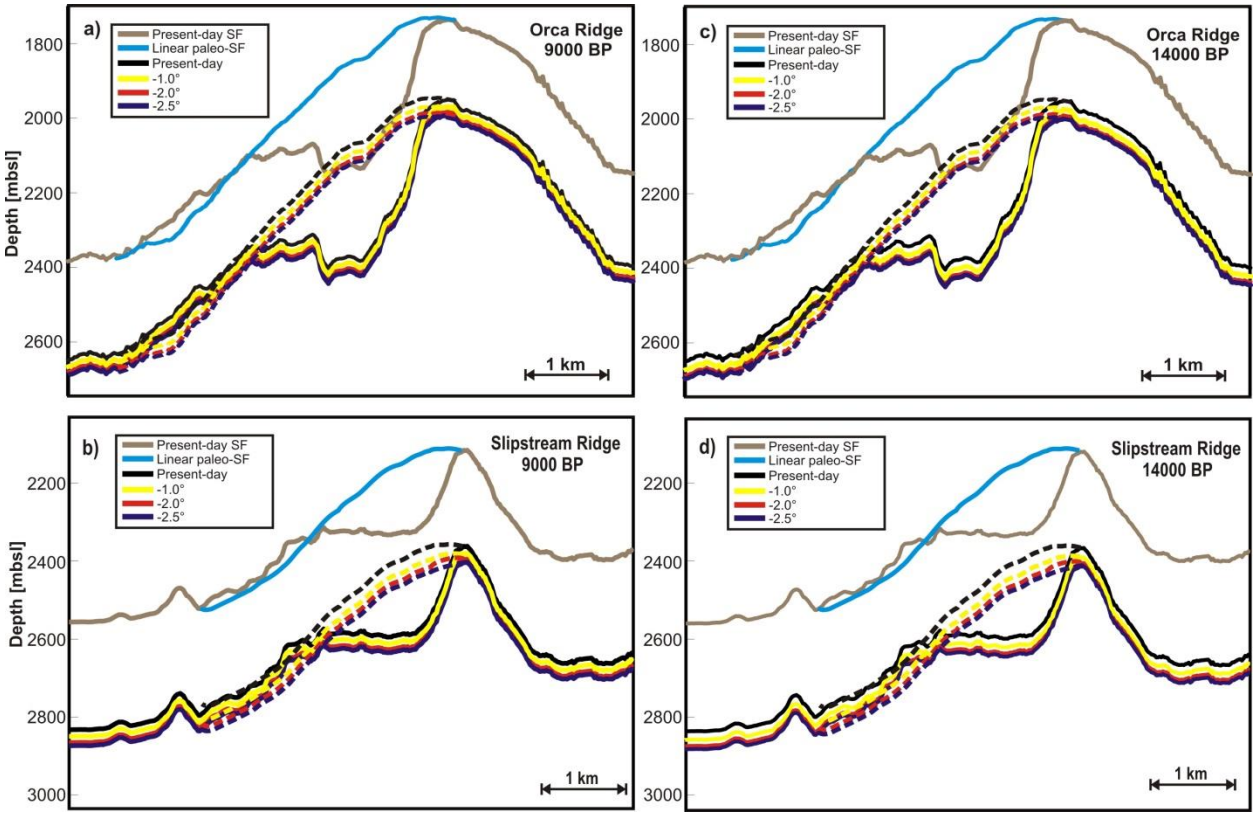


**Figure 5.4**: Present-day seafloor, interpolated paleo-seafloor and their respective BSR-depths for different Holocene temperature scenarios for a) Orca Ridge at 9,000 years BP, b) Slipstream Ridge at 9,000 years BP, c) Orca Ridge at 14,000 years BP, d) Slipstream Ridge at 14,000 years BP

For both Orca and Slipstream differences in BSR depth are similar to the results in Fig. 5.3 and Table 5.1. However, there are significant differences between the ridges with respect to the location of the estimated BSRs relative to the gliding plane. Fig. 5.4b and d show the BSR depths through the failed part of Slipstream Ridge. The blue line representing the pre-failure seafloor partially cuts through the present-day topography formed by a coherent sediment block that came to rest in the middle of the gliding plane. Compared to the BSR depths at Slipstream, a first order estimation of the shape of the pre-failure slope can be deemed sufficient as the gliding

plane remains far from the BSR-depths for all considered P-T-scenarios. Therefore, the BSR probably did not play a direct role in the triggering and evolution of Slipstream slide.

The case is different at Orca Ridge (Fig. 5.4a and c). Here, each considered scenario leads to a coincidence between the gliding plane and the corresponding BSRs and only a substantially different pre-failure seafloor topography would change this result. Thus, the BSR at Orca Ridge might have played a role in the sliding event (Lopez et al., 2010). Gas hydrate could have dissociated just above the BSR, thereby initiating a retrogressive slope failure. Or the shape of the failure surface could have been controlled by a stratigraphic contrast between gas hydrate-bearing sediment and free gas, or a combination of both.

### 5.2.2 Top of the gas hydrate occurrence zone (TGHOZ)

Likewise the influence of P-T-changes on the location of the TGHOZ was tested, using the mass balance modeling method developed by Malinverno (2008). The TGHOZ can be distinguished from the top of the gas hydrate stability zone (TGHSZ) as gas hydrate can only form if there is enough supply of methane to reach solubility, a point that is often reached significantly below the TGHSZ (e.g. Malinverno, 2008).

The method assumes purely biogenic methane source delivered by local sedimentation processes and compares the ensuing methane concentration *c* to the methane solubility *s*. It also assumes local thermodynamic equilibrium as well as a constant porosity with depth. The latter might lead to inaccurate results as porosity usually decreases with depth due to compaction. Additionally, gas hydrate is thought to be homogeneously distributed throughout sediment column and gas hydrates located in veins, nodules, and fractures of fine-grained sediment are not accounted for. Heat advection or heat conduction via cracks and faults are not considered in this method (Malinverno, 2008).

The methane solubility can be calculated via the following equation (Malinverno, 2008):

$$s(z) = s_{BGHSZ} * exp\left[-\frac{T_{grad}}{T^*} * (z - z_{BGHSZ})\right] \quad (5.2)$$

Here, solubility $s$ is in kg/m$^3$, $z$ is depth in meters, $s_{BGHSZ}$ is the solubility at the base of the GHSZ, $T_{grad}$ is the temperature gradient, $T$* is a characteristic temperature (set to 14.4°C according to Davie et al., 2004), and $z_{BGHSZ}$ is the depth to the base of the GHSZ. The solubility at the BGHSZ can be estimated by comparing the local P-T stability values to the solubility values of Davie et al. (2004) for the similar temperature and pressure conditions.

Methane concentration is expected to be low above the sulfate reduction zone (SRZ), a region in which methane is consumed by anerobic oxidation (e.g. Borowski et al., 1996). The base of the SRZ is thus a depth which can be used as an indicator for the magnitude of the local methane flux (e.g. a shallow SRZ corresponds to a strong methane flux). Only at depths greater than the SRZ does methane concentration start to increase with depth.

The production rate at which methane is generated from the deposited organic material can be formulated as:

$$\frac{\partial \alpha}{\partial t} = -\lambda \alpha - \omega \frac{\partial \alpha}{\partial z} \quad (5.3)$$

where $\lambda$ is reaction rate constant (1/s), $\omega$ is the sedimentation rate, and $\alpha$ is the dry weight fraction of metabolizable organic carbon. The reaction rate $\lambda$ itself scales with sedimentation rate and therefore can be written as:

$$\lambda = A * \omega^2$$

with $A$ being a scaling factor set to 2.30*10$^9$. The explicit expression for the microbial methane production then takes on the form:

$$q(z) = k_\alpha \lambda \alpha = k_\alpha \lambda \alpha_{BSRZ} \exp[-\frac{\lambda}{\omega}(z - z_{BSRZ})] \quad (5.4)$$

where $\alpha_{BSRZ}$ is the metabolizable organic carbon at the base of the SRZ here assumed to be 0.1 kg/m$^3$, and $z_{BSRZ}$ is the depth to the base of the SRZ. $k_\alpha$ is a conversion factor and is calculated via:

$$k_\alpha = \frac{16}{12} * \rho_g * \frac{1-\Phi}{\Phi}$$

The steady-state methane concentration is calculated via (for a more thorough derivation, see Malinverno, 2008):

$$c(z) = \frac{k_\alpha * \alpha_{BSRZ} * \omega^2}{D * \lambda + \omega^2} * \left\{1 - exp\left[-\frac{\lambda}{\omega} * (z - z_{BSRZ})\right]\right\} \quad (5.5)$$

Here, $c$ is the methane concentration in kg/m$^3$ (assuming no gas hydrate) and $D$ is the diffusion coefficient.

Some of the parameters in equation 5.5 are unknown. However, Riedel et al. (2010) reported that gas hydrates at Site U1326 were found at a minimum depth of 47 m. This can be used to back-calculate appropriate values for the other parameters. At the northern Cascadia margin, the depth of the SRZ ranges from 2.5 mbsf to 9.5 mbsf (Malinverno et al., 2008) and was held constant at 9 mbsf for all calculations. Using the knowledge of the present-day location of TGHOZ, SRZ, and BSR the remaining parameters were estimated and are summarized in Table 5.2.

In the following the parameters of Table 5.2 were assumed to remain constant over time. Although the sedimentation rate most likely varied considerably over glacial-interglacial periods it can be assumed to have remained fairly constant on the ridge crests as any sediment flow probably bypassed the topographical heights on their way down to the abyssal plain. The parameter values in Table 5.2 were assumed to also hold for Slipstream Ridge which is located relatively close to Orca Ridge and for which there are no measurements of the depth to the

TGHOZ. Since we are interested in the effects of changes in P-T-conditions on gas hydrate stability the absolute values of the TGHOZ depth are not the focus of this study.

| Parameter | Parameter Name | Value | Unit |
|---|---|---|---|
| $\Phi$ | Porosity | 42 | % |
| $\Omega$ | Sedimentation rate | 220 | m/Ma |
| $z_{SRZ}$ | Depth to SRZ | 9 | M |
| $\alpha_{BRSZ}$ | Fraction of organic carbon at BSRZ | 0.10 | % |
| $^{*}s_{BGHSZ}$ | Methane solubility at BGHSZ | 2.84 | $kg/m^3$ |
| D | Diffusion coefficient | $0.78*10^{-9}$ | $m^2/s$ |
| A | Scaling factor | $2.30*10^{9}$ | - |
| $\lambda=A*\omega^2$ | Reaction rate | $6.37*10^{-14}$ | 1/s |

**Table 5.2**: Parameter values for TGHOZ calculation
*: Taken from Davie et al. (2004)

***Results***

Fig. 5.5 shows both methane solubility and methane concentration profiles for the five different pressure-temperature scenarios at both ridges at the estimated beginning and end of the period of slope failure. The TGHOZ can be expected where the amount of methane reaches solubility. Realistically, methane concentration follows methane solubility once the cross-over point is surpassed but not pictured in Fig. 5.5.

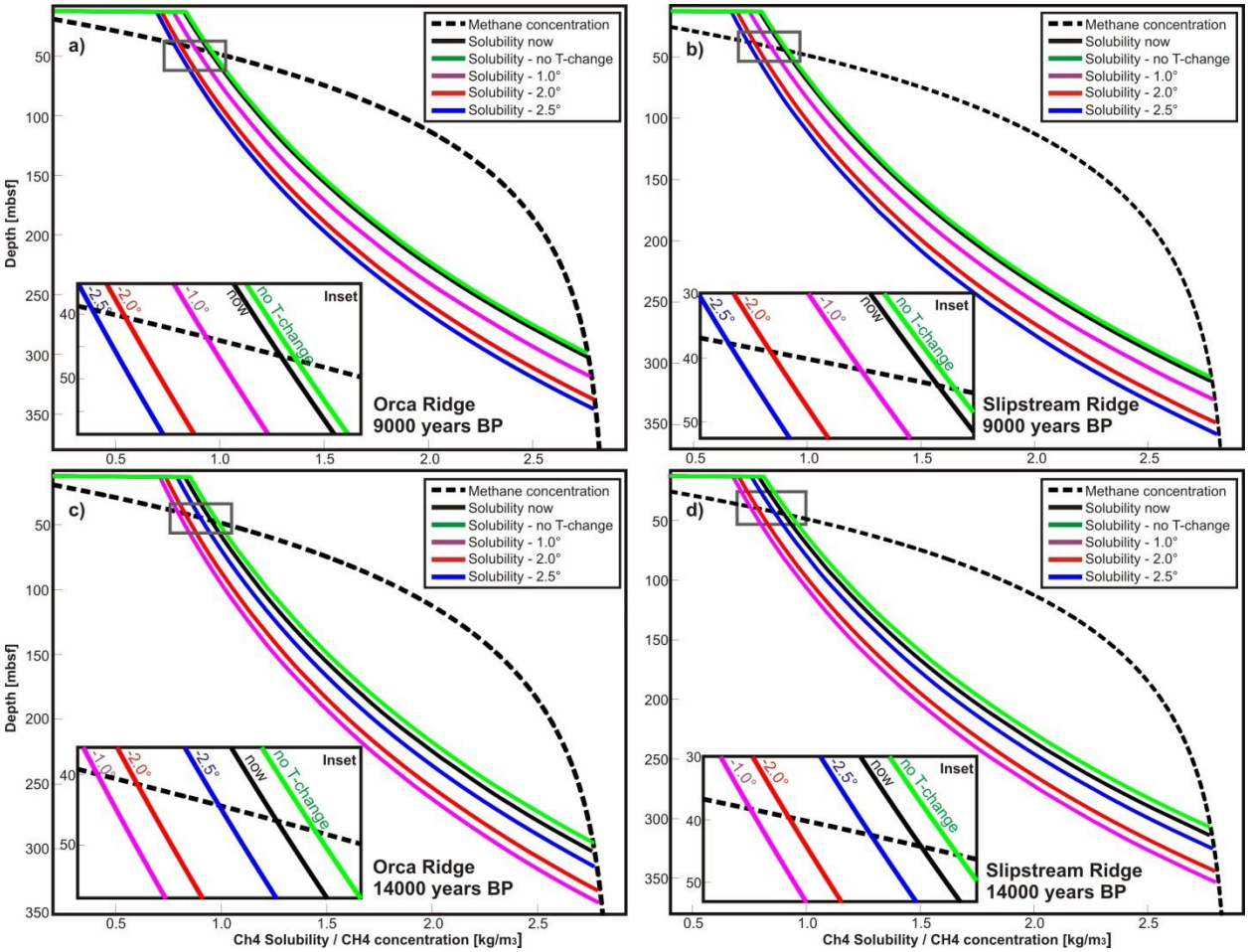


**Figure 5.5**: Methane solubility and methane concentration versus depth for a) Orca Ridge 9,000 years BP, b) Slipstream Ridge 9,000 years BP, c) Orca Ridge 14,000 years BP, d) Slipstream Ridge 14,000 years BP; not shown: methane concentration follows solubility curve once it reaches methane solubility; insets show close-up of the cross-over points

Results for the estimated depths of the TGHOZ at a random point along the intact profiles in Fig. 5.2 are summarized in Table 5.3.

| Ridge | Time [years BP] | Seafloor temperature [°C] | TGHOZ depth [mbsf] | Depth difference relative to present [m] |
|---|---|---|---|---|
| **Orca** | 9,000 | 2.5 | 48 | +1 |
| | 9,000 | 1.5 | 44 to 46 | -1 to -3m |
| | 9,000 | 0.5 | 40 to 42 | -5 to -7m |
| | 9,000 | 0.0 | 38 to 41 | -6 to -9m |
| | 14,000 | 2.5 | 48 to 50 | +1 to +3m |
| | 14,000 | 1.5 | 46 to 48 | +1 to -1m |
| | 14,000 | 0.5 | 40 to 42 | -5 to -7m |
| | 14,000 | 0.0 | 44 to 45 | -2 to -3m |
| **Slipstream** | 9,000 | 2.5 | 47 | 0 |
| | 9,000 | 1.5 | 44 to 45 | -2 to -3m |
| | 9,000 | 0.5 | 41 to 43 | -4 to -6m |
| | 9,000 | 0.0 | 40 to 43 | -5 to -7m |
| | 14,000 | 2.5 | 48 | +1 |
| | 14,000 | 1.5 | 46 to 48 | +1 to -1m |
| | 14,000 | 0.5 | 42 to 43 | -4 to -5m |
| | 14,000 | 0.0 | 45 to 46 | -1 to -2m |

**Table 5.3**: TGHOZ depths and depth differences along the intact profiles (Fig. 5.2) for several paleo-climate scenarios; a minus sign indicates a decrease in depth

The TGHOZ does not change significantly between different scenarios and reacts to P-T changes inversely to the BSR. Without any change in seafloor temperature the difference in depth compared to present-day conditions is at most 3 m. A colder ocean-bottom temperature generally leads to a shallower TGHOZ. As an example, if paleo-temperatures were at 0.5° C, depths are lower by a minimum of 4 m and a maximum of 9 m. Noteworthy is the ‘reversal’ of the resulting TGHOZ depths for the paleo-seafloor temperatures of 0.0° C, 0.5° C, and 1.5° C

between 9,000 years (Fig. 5.5a and c) and 14,000 years BP (Fig. 5.5b and d), indicating that the influence of pressure changes is more significant than at the BGHSZ.

Finally, Fig. 5.6 compares the present-day seafloor of the failed profiles (Fig. 5.2) with the depth-interval where the paleo-TGHOZ might have been located at the time of failure.

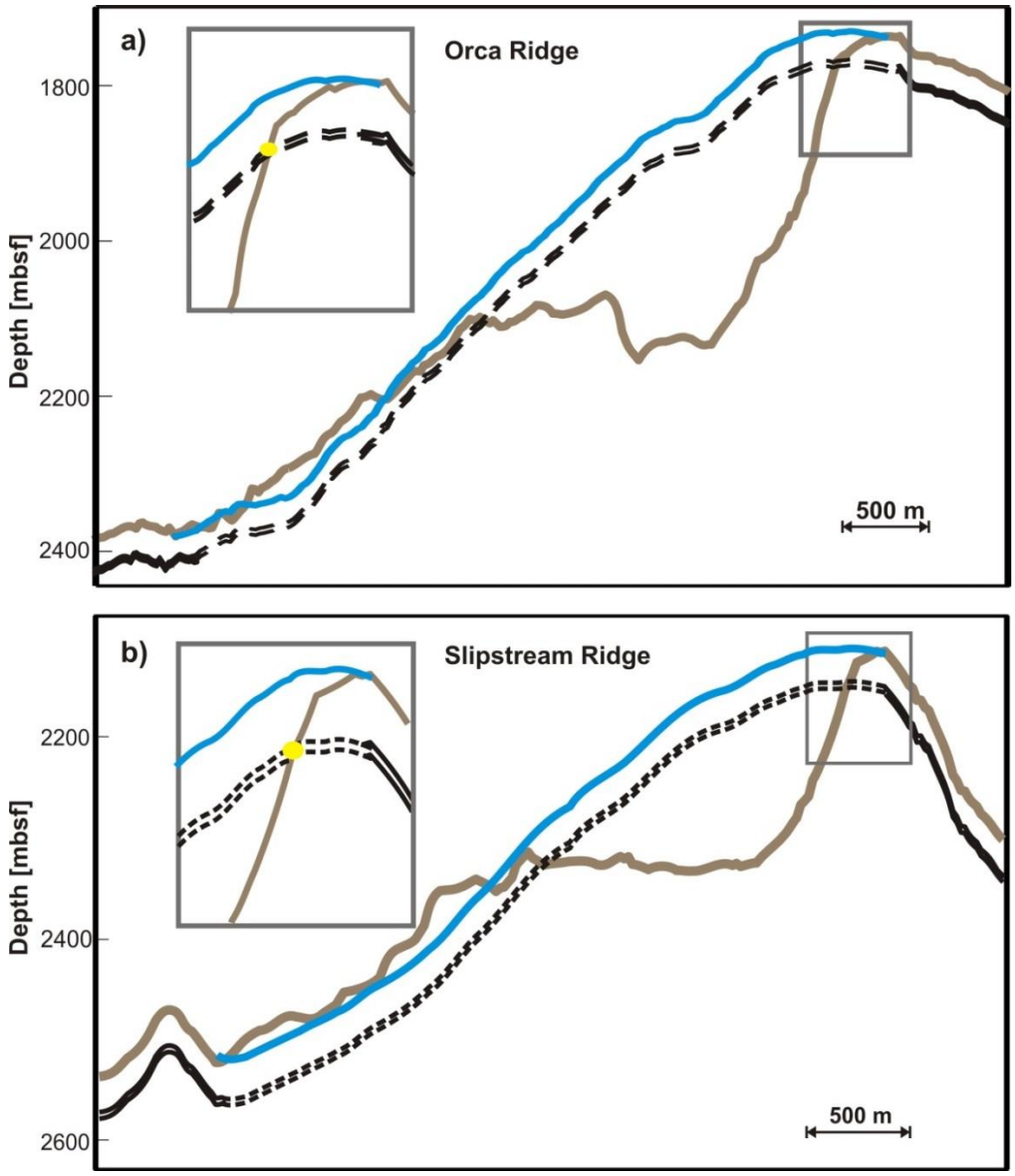


**Figure 5.6**: Present-day seafloor (brown), interpolated paleo-seafloor (blue) and the approximate depth interval of the paleo-TGHOZ (black lines and black dashed lines) at a) Orca Ridge and b) Slipstream Ridge; yellow dot indicates where gliding plane coincides with the estimated TGHOZ

In both cases there is a coincidence between the headwall and the estimated TGHOZ, situated between 28 m to 40 m beneath the crest of Orca Ridge and between 30 m to 39 m beneath the crest of Slipstream Ridge. Thus, if failure has progressed from the crest to the toe, the TGHOZ might have played a role in its initiation probably due to pressure- and temperature-induced gas hydrate dissolution. Any further matches with the gliding plane at locations cannot be determined with certainty as the present-day seafloor topography might partially be masked by failure deposits.

### 5.3 Temporal evolution of the GHOZ

Here, the time scales over which P-T-changes affect the gas hydrate stability boundaries are examined in order to compare the time of failure to the timing of the changes in the GHOZ. As mentioned above, changes in pressure act almost instantaneously everywhere throughout the sediment column, whereas temperature changes are delayed by significant time intervals due to the relatively slow process of heat conduction. As a first order estimation of the time $\tau$ needed for a temperature pulse to reach a certain depth the following approximation (Xu et al., 2001) can be used:

$$\tau \sim {L^2}/{a} \tag{5.6}$$

where $L$ is the depth below the seafloor and $a$ is the effective thermal diffusivity in $m^2/s$. It has to be kept in mind that time $\tau$ in equation 5.6 is strongly dependent on the value for the thermal diffusivity. In the following, any changes in methane solubility or methane flux caused by changes in the input of organic material are not taken into account and the dependence of solubility on temperature over the time period of interest is also neglected (e.g. Xu et al., 2001).

***The evolution of the GHOZ relative to the timing of slope failure***

As ocean-bottom water temperatures increased most likely sometime between 15,000 years and 9,000 years BP, four different times for the onset of ocean-bottom warming were assumed, namely at 15,000 years BP, 14,000 years BP, 11,000 years BP, and 9,000 years BP. A temperature increase of 2.0°C and a thermal diffusivity of $1.0*10^{-6}$ $m^2/s$ (Xu et al., 2001) were used to estimate the approximate travel-time of a temperature pulse using equation 5.6. The thermal diffusivity is higher than the value which Hyndman et al. (1979) measured at Hydrate Ridge (i.e. $0.32*10^{-6}$ $m^2/s$). No attention was paid to the effects of gas hydrate on the heat conduction. Gas hydrate dissociation would slow the process down due to its endothermic nature and subsequent release of latent heat (e.g. Golmshtok and Soloviev, 2006).

Fig. 5.7 shows the resulting evolution of the TGHOZ- and BSR-depths for the four different warming scenarios at a random point along the intact profile of Orca Ridge.

Due to sea-level and temperature increase the GHOZ becomes slightly thinner over time, supporting the possibility of the occurrence of hydrate dissolution and/or dissociation since the end of the LGM. However, Fig. 5.7 also shows that ocean-temperature warming would have had to start no later than 12,000-11,000 years BP if gas hydrate dissociation at the BGHSZ were to be the cause for slope failure at Orca Ridge (for time period of slope failure see grey box in Fig. 5.7). As a temperature pulse would in turn only need ~65 years to reach the TGHOZ, ocean-bottom water warming could have happened as late as 9,000 years BP and still have triggered the dissolution of gas hydrate close to the crest of Orca and Slipstream Ridge.

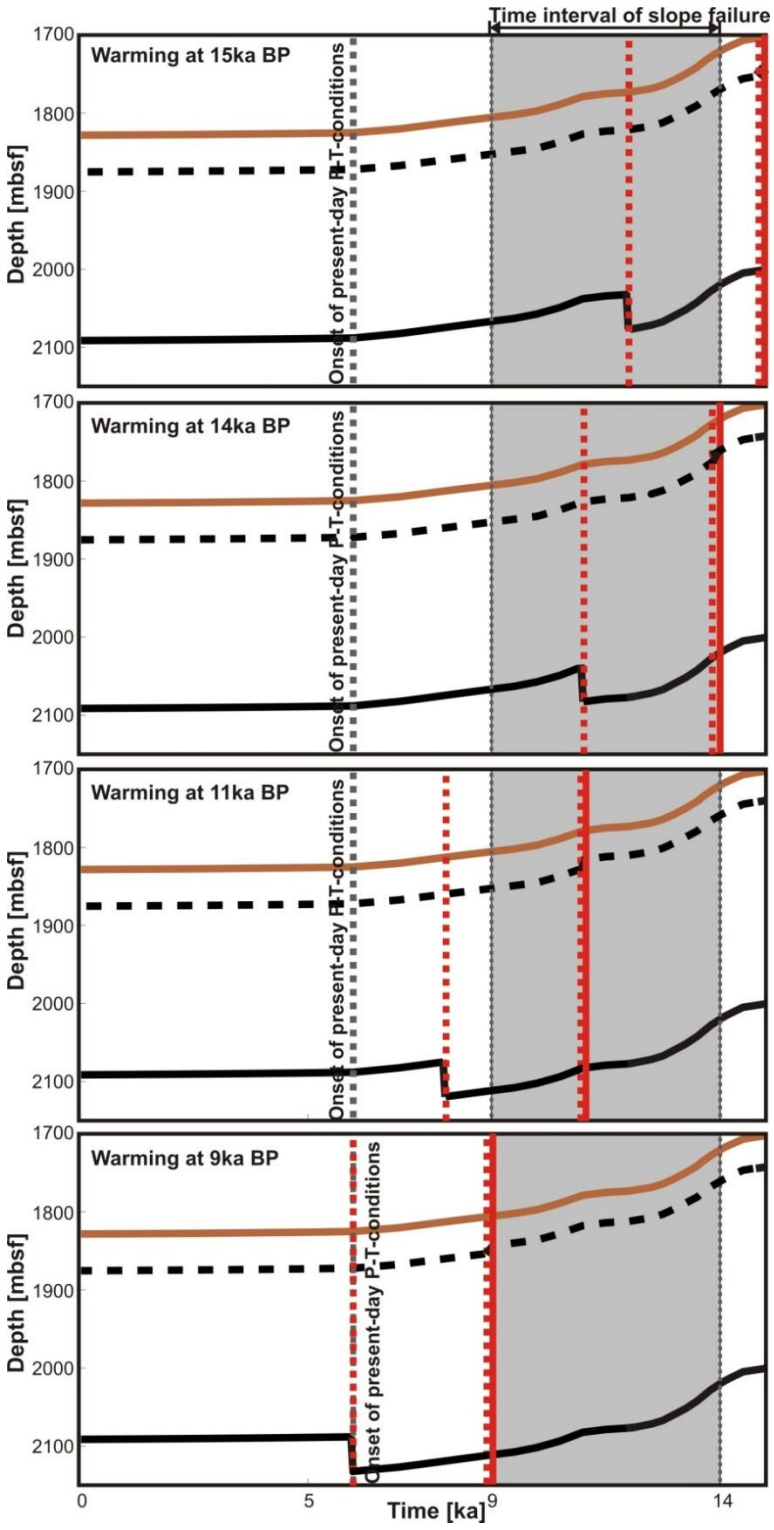


**Figure 5.7**: Temporal evolution of the TGHOZ and BSR for a random point along Orca Ridge assuming an ocean-temperature increase by 2.0°C at: a) 15,000 years BP, b) 14,000 years BP, c) 11,000 years BP, and d) 9,000 years BP; the brown line marks the seafloor depth with time, the black line is the depth of the BSR and the black dashed line is the depth of the TGHOZ over time; the red dashed line corresponds to the time when the warming pulse reached the limits of the GHOZ

***Re-equilibration of thermal gradients and the BSR after slope failure***

An alternative scenario includes slope failure that pre-dated any significant changes in gas hydrate stability and therefore was not caused by hydrate dissociation. Mass wasting, maybe triggered by an earthquake or overpressure, could have led to significant immediate as well as long-term changes in the pressure and temperature within the GHOZ underneath the frontal ridges. It would entail the almost instant removal of a large amount of overburden pressure and the relatively warm sediment at the failure plane would suddenly be exposed to cold water, leading to a disturbance of the thermal gradient. After a certain time period this negative temperature pulse would reach the BSR and lead to the re-equilibration of the BGHSZ. Fig. 5.8 shows several snapshots in time illustrating the transit of a temperature pulse down to the BSR. Again using equation 5.6 it would take an estimated 2670 and 3250 years to arrive at the BSR at Orca and Slipstream Ridge, respectively.

In the following, the process of re-equilibration is modeled as conduction-dominated heat transfer described by the following equation:

$$\frac{\partial T}{\partial t} = a * \frac{\partial^2 T}{\partial z^2} \tag{5.7}$$

where $T$ is the temperature, $t$ the time, $z$ is depth below seafloor and $a$ is the effective thermal diffusivity. Equation 5.7 is the well-known heat equation describing the spatial change in temperature over time. Including boundary conditions such as the temporal evolution of the seafloor temperature and the increase of temperature with depth, equation 5.7 takes on the following form:

$$T(z) = T_0 + q * \int_0^z \frac{dz\prime}{a(z')} \tag{5.8}$$

where $q$ is the steady-state heat-flux in W/m$^2$ and $T_0$ is the seafloor temperature.

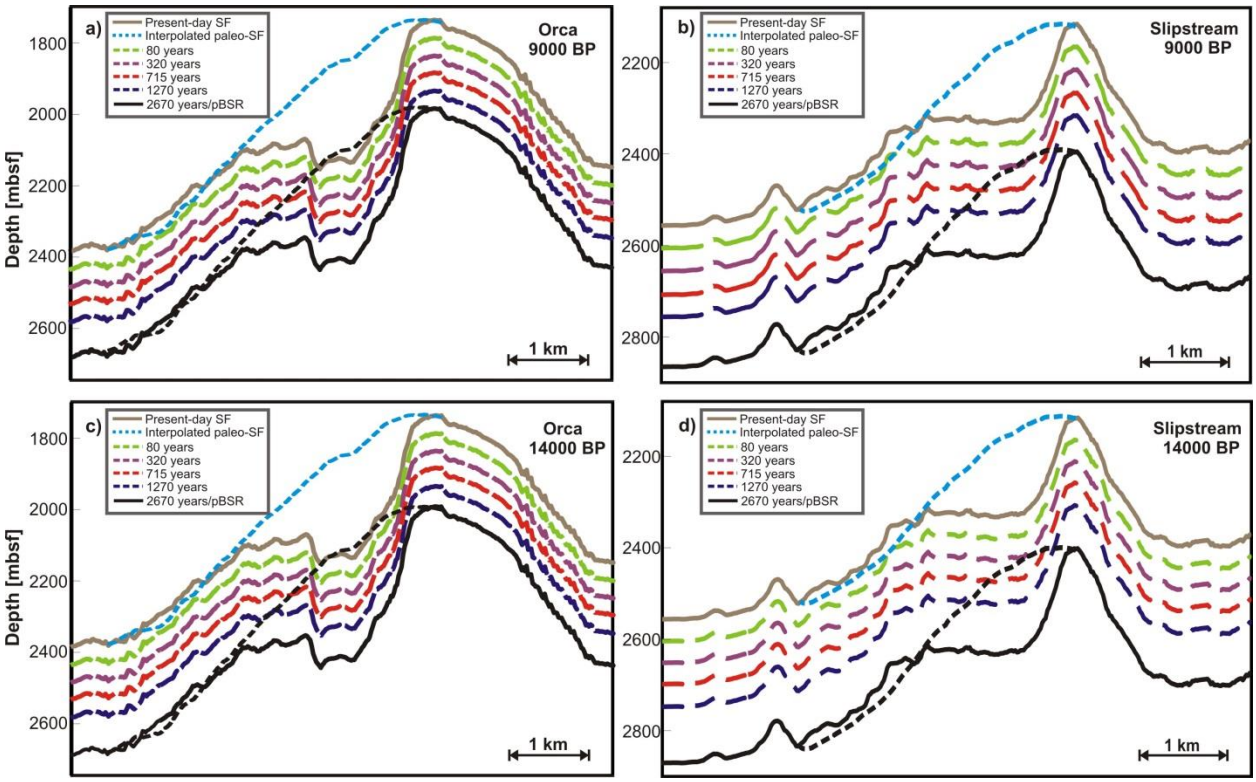


**Figure 5.8**: Travel-times for temperature pulse along the same profile as in Figs. 5.4 and 5.5: a) Orca 9,000 years BP, b) Orca 14,000 years BP, c) Slipstream 9,000 years BP, d) Slipstream 14,000 years BP; black dashed line indicates location of paleo-BSR

Although the initial temperature at the failure plane will vary with distance the problem was treated as one-dimensional and a temperature pulse was modeled propagating downward from the seafloor. The 2D-effect on the propagation of the temperature pulse and on the arrival-times at the BSR is caused by the shape of the failure scar. As an example, the deepest point of the failure scar at Orca Ridge reaches down to the BSR and re-equilibration can be expected to start relatively soon after the slide event. In turn, at this point the BSR will also have to cover the largest distance to adapt to the new seafloor topography. At Slipstream Ridge the failure reaches a depth of only ~100 m such that the temperature pulse needs approximately 320 years to reach the BSR.

Thermal conductivity was held constant and a constant value for the thickness of removed material was used, essentially modeling a point source of heat along the failure surface. According to Villinger et al. (2010) equation 5.8 can be solved by using the following initial and boundary conditions:

$$T(z,t)|_{t=0} = T_0 \;\; z > 0 \tag{5.9a}$$

$$T(z,t)|_{z=0} = T_s \;\; t \geq 0 \tag{5.9b}$$

where $T_s$ is the seafloor-temperature in form of a step-like function. The solution for the temperature pulse can then be written as (Villinger et al., 2010):

$$T(z,t) = T_0 + \sum_{i=1}^{n} \delta T_i erfc\left(\frac{z}{2\sqrt{at_i}}\right) \tag{5.10}$$

Equation 5.10 uses the difference between initial and final temperatures at each depth point to calculate the temporal evolution of the temperature distribution. A thermal diffusivity of $1.0*10^{-6}$ $m^2/s$ was again assumed.

Fig. 5.9 shows the evolution of the thermal gradient after slope failure. Here, at Orca Ridge the thickness of removed material was set to 255 m with a paleo-BSR estimated to lie between ~270 mbsf and ~290 mbsf (Fig. 5.9a). At Slipstream Ridge, the thickness of removed material is only 100 m and the depth of the paleo-BSR was calculated to lie between 310 mbsf and 320 mbsf (Fig. 5.9b).

The results in Fig. 5.9 suggest that the temperature gradient is not fully re-equilibrated even after 10,000 years. Moreover, due to the decreasing difference between current and final temperature the re-equilibration is decelerating over time. If the thermal diffusion is lower as suggested by Hyndman et al. (1979) the process might be even slower.

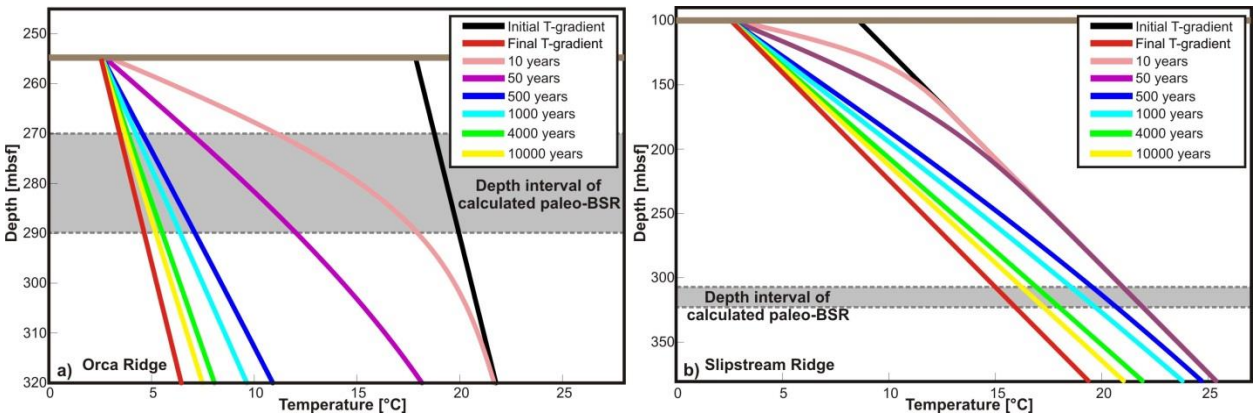


**Figure 5.9**: Temporal evolution of the thermal gradient after slope failure for several instances in time: a) Orca and Slipstream; approximate depth range of the paleo-BSR marked in grey; brown horizontal line indicates the depth of the gliding plane below the paleo-seafloor

One possible implication of Fig. 5.9 is that the BSR is still increasing in depth. If the temperature at the present-day BSR is still lower by about 0.5° C compared to fully equilibrated conditions, the BSR-depth underneath the ridges would still have to increase by another 7 m to 8 m. A slow re-equilibration process and subsequent transient BSRs have already been suggested by the works of Foucher et al. (2002), Golmshtok and Soloviev (2006), as well as Xu et al. (2001) who all modeled the time for the BSR to adapt to new thermal conditions.

### 5.4 A potential double-BSR beneath Slipstream Ridge

One possible explanation for the apparent doubling of the BSR underneath the crest of Slipstream Ridge (Fig. 2.11) is that it is a relic of past P-T stability conditions. So-called double-BSRs possibly stem from times when the P-T-stability conditions had been substantially different or represent the lower boundary of a transitional zone between gas hydrates and free gas (e.g. Foucher et al., 2002; Popescu et al., 2006) as was illustrated in Fig. 1.2b. Another suggested explanation is that gas hydrates composed of different host gases are stable over different depths (e.g. Foucher et al., 2002). However, gas hydrates at the northern Cascadia

margin almost exclusively consist of methane and therefore the second reflector could not be caused by a difference in gas composition.

The fact that the second BSR is preserved despite of the release of free gas from dissociation has previously been explained by upward migration due to 'methane recycling' which carries free gas back into the new GHSZ (e.g. Paull et al., 1994) or due to the up-dip movement of gas along stratified layers or fractures (e.g. Popescu et al., 2006). According to Foucher et al. (2002) the time of a layer of free gas that can remain at the location of the remnant BSR depends on the ratio between the total methane concentration and the concentration of dissolved methane. Foucher et al. (2002) cited the maximum characteristic diffusion time for methane gas to be 10,000 years.

Double-BSRs have already been detected and studied in other regions such as the Norwegian margin (e.g. Posewang and Mienert, 1999; Andreassen et al., 2000), the Nankai Trough (e.g. Matsumoto et al., 2000; Foucher et al., 2002), and the Black Sea (Popescu et al., 2006). The existence of a secondary BSR has also been suggested offshore Oregon lying 20 m to 40 m below the present-day BSR, spatially limited to the crest and western flank of Hydrate Ridge (e.g. Bangs et al., 2005; Musgrave et al., 2006) similar to the observation at Slipstream Ridge. If a seismic velocity of 1600 m/s is assumed, the distance between both reflectors beneath Slipstream Ridge amounts to about 32 m. This would fall between the expected BSR-depths for paleo-seafloor temperatures of 0.0° C and 0.5° C (see Table 5.1). Tectonic uplift could have played an additional role in increasing the distance between paleo- and present-day BSR.

## 5.5 Discussion

This chapter has focused on the possible implications of sea-level and temperature change on the stability conditions of gas hydrates offshore Vancouver Island. The effects of

isostatic glacial adjustment have been included in the calculations by using the local glaciostatic sea-level. Time intervals of rapid sea-level change approximately match the estimated age of the Orca and Slipstream Ridge failures similar to 70% of the submarine landslides studied by Maslin et al. (2004) who named the dissociation of gas hydrate as a likely common trigger. Additionally, Maslin et al. (2004) observed that the location of submarine slope failures migrated pole-ward during the Holocene. They inferred that lower latitudes responded more rapidly to the deglaciation process, possibly related to the increased deep- and intermediate-water temperatures. Higher-latitude failures, such as the Storegga Slide, fall into the second period of frequent slope failure, a time that can be linked to the isostatic rebound caused by ice sheet retreat. Isostatic rebound therefore could be another important mechanism as it causes a reduction in hydrostatic pressure as well as an increase in seismicity (Maslin et al., 2004). However, if only pressure changes due to sea-level rise are considered, it can be assumed that gas hydrates would have been stabilized since the end of the LGM (Table 5.1).

Siddal et al. (2002) and others suggested that seafloor temperatures have been substantially colder than today following the LGM. As neither magnitude nor timing of ocean-bottom warming has been stated with confidence, stability conditions were calculated for different scenarios (0.0° C, 0.5° C, and 1.5° C warming at 15 ka, 14 ka, 11 ka, and 9 ka BP). The influence of colder temperature on the location of the BSR is found to have a much stronger effect than the increase in pressure. The BSR would have been deeper by as much as 30 to 40 m compared to the present, therefore providing a depth interval over which gas hydrate dissociation could have taken place. The comparison of all BSR-scenarios with estimated former seafloor geometry as well as present-day seafloor topography showed that at Slipstream Ridge the BSR

could not have played a direct role in slope failure. But it might have played a role in the failure of Orca Ridge as parts of the BSR and the gliding plane nearly coincide.

Since a warming pulse can take hundreds to thousands of years to reach gas hydrate-bearing sediments, the pressure effect seems to dominate but it has been argued that temperature increases actually have a stronger influence on gas hydrate stability, especially in shallower waters (e.g. Paull et al., 1991; Xu et al., 2001). Thus, which factor outweighs the other depends on the time scale, the magnitude of the change in pressure and temperature conditions, as well as on the depth of the GHSZ below the seafloor.

The same scenarios have been tested on the TGHOZ which has been calculated analytically using the mass balance model of Malinverno (2008). Results suggest that the TGHOZ was about 7 m to 9 m shallower compared to the present when temperatures and sea-levels were lower. Gas hydrates are expected to dissolute when methane concentrations fall below the methane solubility and a potential deepening of the TGHOZ with time would have exposed some of the shallowest lying gas hydrates to dissolution. Although not explicitly addressed here, methane solubility increases with increasing temperature. Thus, a potentially even larger amount of gas hydrate could be affected compared to the case of temperature-independent methane solubility. As discussed in Chapter 1 gas hydrate dissolution is also thought to reduce sediment strength although it might not have the same destabilizing potential as gas hydrate dissociation. Dissociation results also in the release of free methane in addition to the loss of sediment strength associated with the reduction in hydrate content. The generation of overpressure and an increase in bulk volume at greater depths can be expected to have a stronger influence on the shear strength of the sediment. Results of IODP Expedition 311 showed that Site U1326 has locally high gas hydrate concentrations at shallow depths (Riedel et al., 2006d).

Resistivity as well as pore-water chlorinity data indicated that gas hydrate saturation is comparatively high at a depth of about 70 mbsf. TGHOZ-scenarios were compared to present-day seafloor, showing that they might have coincided with the present-day headwall thus supporting gas hydrate dissolution as a potential trigger (e.g. Sultan, 2007).

One further outcome of the calculations of the BSR and TGHOZ is that the double reflector underneath the crest of Slipstream Ridge could in fact be a double-BSR, with the lower reflector representing a relic of previous stability-conditions (e.g. Bangs et al., 2005).

Whether pressure or temperature influenced the BSR at the time of failure depends on the seafloor-temperature history as well as the speed of temperature conduction. If the temperature increase and subsequent gas hydrate dissociation at the BSR influenced slope stability, the warming event should have happened between 17 ka BP and 11 ka BP since it takes a temperature pulse at least a couple of thousand years to reach the BSR depending on its depth and the thermal properties of the sediment. If gas hydrate dissolution at the TGHOZ has been the trigger, temperature increase should have happened earlier than 9 ka ago.

An alternative scenario involves the destabilization of gas hydrate through slope failure itself. A larger amount of overburden would have suddenly been removed, decreasing hydrostatic pressure substantially. The exposure of the sediment at the gliding plane to colder seawater would have led to a disturbance of the thermal gradient and the subsequent re-equilibration of the BSR which both are very slow processes. Calculations suggest that the re-equilibration of the thermal gradient has not finished even after 10,000 years such that the BSR underneath the failed area has still not reached its steady-state position.

# Chapter 6: ESTIMATION OF PORE PRESSURE GENERATION DUE TO GAS HYDRATE DISSOCIATION

Natural gas hydrate dissociation (i.e. not induced for gas production) is mainly caused by changes in the P-T stability conditions linked to climate-related fluctuations in sea-level, sedimentation rates, tectonic uplift and seafloor temperature. Short-term causes are sudden seafloor mass movements or human activities such as ocean drilling/production operations.

The process of gas hydrate melting follows a 'dissociation front' which separates a sediment volume into one part in which gas hydrate is still intact and one in which free gas and water are being released. This is expected to lead to an increase in pore pressure that, if not dissipated, could cause a loss in sediment strength and cementation, or changes in local fluid flow, leading to slope failure (e.g. Xu and Germanovich, 2006). How much pore pressure is generated depends on factors such as the depth of the dissociation front, rate of pore pressure change, the amount and distribution of hydrate, and the relationship between hydraulic permeability and melting rate. It is usually assumed that dissociation only stops when gas hydrate is fully melted, or when new stability conditions are reached. The release of fresh pore water and increase in pressure can serve as a negative feedback and stop the melting process due to the endothermic nature of gas hydrate dissociation (e.g. Xu et al., 2001).

Results in Chapter 5 suggested that the BSR was situated at greater depths due to different Holocene P-T conditions and warming of the ocean-bottom water that led to the shoaling of the BSR to its present-day location. This upward motion of the BSR would have provided a depth interval over which dissociation of hydrate could have occurred. In this chapter, the analytical method of Xu and Germanovich (2006) is used to study potential pore pressure

generation directly above the base of the GHSZ. Overpressure is estimated for present-day and Holocene P-T conditions while varying initial hydrate and gas saturation, dissociation rate and sediment permeability.

### 6.1 Previous research

The theoretical estimation of pore pressure generated by gas hydrate dissociation has been attempted with a variety of different techniques ranging widely in their level of complexity. Flemings et al. (2003) quantified the possible amount of excess pore pressure beneath a gas hydrate layer at Blake Ridge from measured porosity assuming that all existing overpressure is a consequence of gas hydrate dissociation. Nixon and Grozic (2007) addressed the process of dissociation more directly by developing a geo-mechanical model that calculated pore pressure as a function of the deviation in pressure and temperature from equilibrium conditions and sediment compressibility. Other studies focus on the energy conservation, looking merely at the effects of pressure and temperature effects on the thickness of the GHSZ (e.g. Chaouch and Briaud, 1997; Mienert et al., 2001) whereas Delisle et al. (1998) additionally take into account the effect of latent heat.

The most complex modeling techniques simultaneously solve the equations for the conservation of momentum, fluid mass, and energy in steady-state and transient regimes. For example, Sultan et al. (2004) developed a numerical model that calculates the formation and dissociation of gas hydrate as a function of temperature, initial pressure, pore water chemistry and solubility, as well as pore size distribution. Volume conservation is assumed to quantify excess pore pressure in a four-component-system consisting of a solid, liquid, gas, and hydrate fraction. Others also take the gas supply into account, calculating advection and diffusion coupled with the transfer of heat (Rempel and Buffett, 1998; Xu and Ruppel, 1999). Davie and

Buffett (2001) add to this the effect of chloride content and the effects of dissolved methane in the pore fluid assuming methane migrates via diffusion or advection. Kwon et al.'s (2008) model quantifies the pressure- and temperature dependent volume changes of water, free gas, and hydrate via the influences of sediment compressibility, capillarity effects, and the relative solubility of fluids. Additional to the no-flow assumption the model treats the effects of thermal and elastic deformation as additive such that the total volumetric expansion equals the expansion of the granular skeleton.

## 6.2 Estimation of pore pressure generation during dissociation using the method of Xu and Germanovich (2006)

The method of Xu and Germanovich (2006) is chosen to obtain a first estimate of the pore pressure generated by the dissociation of gas hydrate at the depth of the BSR. No attention is paid to the nature of the destabilization, the effect of hydrate dissociation on the melting process itself, or its consequences such as changes in local heat and fluid flow.

### 6.2.1 Methodology

Xu and Germanovich (2006) calculate the amount of generated pore pressure $P_{ex}$ within the three-phase stability zone (i.e. close to the BSR) by quantifying the volume expansion $dV$ that is caused by hydrate dissociation. Volume change is thought to be due two different mechanisms. The first is related to the density contrast between hydrate, water, and free gas, the second is due to the compressibility of the pore volume constituents limiting further pore pressure generation. The total volume change due to a decrease in the volume fraction of gas hydrate $dS_h$ is then written as:

$$\frac{dV}{V_p} = -R_v dS_h - \kappa dP_{ex} \tag{6.1}$$

with $V_p$ as the total pore volume, and $R_v$ as the factor of volume expansion:

$$R_v = \frac{(1-r_g)\rho_h}{\rho_w} + \frac{r_g \rho_h}{\rho_g} - 1 \tag{6.2}$$

where $r_g$ is the mass fraction of methane in hydrate form (here assumed to be 0.1292 corresponding to 100% filling of the hydrate cages), and $\rho_w$, $\rho_h$ and $\rho_g$ are the densities of water, hydrate and free gas, respectively. With changing volume fractions of hydrate, water, and free gas there is also a change in effective compressibility $\kappa$ that can be calculated via:

$$\kappa = -\frac{1}{V}\left(\frac{\partial V}{\partial P} + \frac{\partial V}{\partial T}\frac{dT_e}{dP}\right)$$

$$= \frac{S_g}{\rho_g}\left(\frac{\partial \rho_g}{\partial P} + \frac{\partial \rho_g}{\partial T}\frac{dT_e}{dP}\right) + \frac{S_w}{\rho_w}\left(\frac{\partial \rho_w}{\partial P} + \frac{\partial \rho_w}{\partial T}\frac{dT_e}{dP}\right) + \frac{S_h}{\rho_h}\left(\frac{\partial \rho_g}{\partial P} + \frac{\partial \rho_g}{\partial T}\frac{dT_e}{dP}\right) \tag{6.3}$$

where $S_g$, $S_w$, and $S_h$ the pore space volume fractions of free gas, water, and gas hydrate, respectively and $T_e$ is the stability temperature of methane hydrate calculated via equation 5.1. If a confined pore space is assumed, no pore fluid escape can occur and equation 6.1 becomes:

$$R_v dS_h + \kappa dP_{ex} = 0 \tag{6.4}$$

The resulting excess pore pressure for the whole dissociation can be calculated via:

$$P_{ex} = \int_0^{-\Delta S_h} \frac{R_v}{\kappa} dS_h \tag{6.5}$$

However, if the pores are interconnected pressure is able to dissipate and fluid flow becomes possible. According to Darcy's law fluid flow $q_f$ in a 1D-system (ignoring the downward component) can be written as:

$$A\Delta q_f = \rho_f \frac{dV}{dt} = -\rho_f \Phi A \Delta D * \left(R_v \frac{dS_h}{dt} + \kappa \frac{dP_{ex}}{dt}\right) \approx \frac{Ak\rho_f P_{ex}}{\mu_f D} \tag{6.6}$$

where $A$ is the dissociation area, $\Delta D$ the interval of dissociation, $\Phi$ porosity, $k$ the sediment permeability, and $\mu_f$ is the fluid viscosity.

Simplifying equation 6.6 leads to:

$$\kappa \Phi \Delta D \frac{dP_{ex}}{dt} + \frac{k}{D\mu_f} P_{ex} = -R_v \Phi \Delta D \frac{dS_h}{dt} \quad (6.7)$$

which is rewritten as:

$$\frac{dP_{ex}}{dt} + aP_{ex} - b = 0 \quad (6.8)$$

$$a = \frac{k}{\kappa \mu_f D \Phi \Delta D} \quad (6.8a)$$

$$b = -\frac{R_v}{\kappa} \frac{dS_h}{dt} \quad (6.8b)$$

Using a constant dissociation rate $\frac{dS_h}{dt}$ the solution of equation 6.8 is:

$$P_{ex} = \frac{b}{a}(1 - e^{-at}) \quad (6.9a)$$

with a pressure maximum at:

$$P_{exmax} = \frac{b}{a} = -\frac{\mu_f R_v D \Phi \Delta D}{k} \frac{dS_h}{dt} \quad (6.9b)$$

The method calculates a slight pressure increase due to the dissociation of a certain fraction $dS_h/dt$ of the initial hydrate saturation that leads to a subsequent increase in stability temperature $T_e$. Therefore, the method remains close to the stability curve during the whole dissociation process.

Xu and Germanovichs' (2006) method was slightly modified as it was not possible to fully replicate their results for pore pressure generation in a fully impermeable environment. In contrast to Xu and Germanovich (2006), the compressibility of water and gas hydrate cannot be ignored at low to zero initial concentrations of free gas. If neglected, the effective compressibility (equation 6.3) reaches values close to zero, leading to an extremely rapid pore pressure increase (equations 6.5 and 6.9b). Therefore, the compressibility of seawater was calculated via the method of Fine and Millero (1973) whereas hydrate compressibility was

assumed to remain constant at $1.79*10^{-10}$ $Pa^{-1}$ due to the lack of information on its pressure and temperature behavior.

### 6.2.2 Assumptions and limitations

The method outlined above makes several simplifying assumptions. The potentially negative feedback of changes in temperature, pressure, and salinity is neglected and the production of latent heat, *in situ* methane production and sedimentation are not accounted for. Hydrate dissociation is assumed to closely follow the stability curve. Therefore at each time step the generated pressure increase is accompanied by a corresponding increase in stability temperature. The effects of *in situ* methane production and sedimentation are neglected. Hydrate dissolution is not taken into account as it can be assumed that at depths of the BSR there will not be a significant decrease in methane solubility. The method does not consider sedimentology and therefore does not account for differences between dissociation in clay, silt or sands.

Results are obtained regardless of the causes for dissociation, their magnitude or the time frame over which stability conditions are changed. As well, dissociation kinetics, multi-phase flow and sediment mechanics are not accounted for. For example, equation 6.3 only accounts for the compressibility of the pore space constituents. The flow of gases and liquids via advection, dissipation, diffusion, or sediment fracturing and changes in the sediment's hydraulic properties due to decreasing hydrate saturation and deformation of the solid matrix are neglected. Another possibility is that the free gas moves upwards and re-enters the GHSZ where it forms new gas hydrate deposits (Expedition Scientists, 2008).

The dissociation rate is held constant and only appears as a fraction of the initial amount of hydrate that is dissociated during each time step. In reality, the decomposition rate is a function of the specific surface area of gas hydrate, the rate of heat transfer, and the fugacity

difference between methane equilibrium pressure and decomposition pressure and therefore is dependent on the nature, magnitude and time frame of hydrate destabilization (e.g. Kim et al., 1987; Kwon et al., 2008).

The method only uses an ‘effective’ permeability and does not differentiate between the intrinsic permeability of a porous medium or the relative permeability of the aqueous and the gas phase. The gas-water capillary pressure which is inherently linked to permeability is neglected as well (e.g. Holtzman and Juanes, 2011). The effect of the presence of gas hydrate on both the permeability of the pore space and permeability of the whole formation is ignored. Also not taken into account is a potential heterogeneity in permeability. For example, layers alternating between coarse-grained sand and fine-grained mud can reveal differences in permeability of several orders of magnitude. This stratigraphy would consist of regions where pore pressure dissipation is prevented and regions which provide pathways for fluid flow (Bethke, 1989; Flemings et al., 2002). Hydrate could give rise to such a permeability-heterogeneity and a gas hydrate layer with a saturation that is sufficiently high could provide the right environment for pressure built-up from below (e.g. Crutchley et al., 2010; Daigle and Dugan, 2010).

The heating effect of dissociation temperature equilibration and the effects of heat capacity and thermal conductivity are neglected. The influence of latent heat or thermal expansion of the water and gas phase after dissociation is ignored as well.

Finally, as the focus lies only on the pore pressure equivalent of the dissociation of a certain amount of hydrate, no attention is paid to the time frame over which a thermal pulse acts upon gas hydrates at the BSR or the distance between generated pore pressure and the failure plane.

## 6.3 Application and results

With equations 6.3, 6.9a and 6.9b as well as the modifications mentioned above, pore pressure generation from hydrate dissociation was estimated.

Table 6.1 summarizes the fixed parameter values used in the calculations.

| Parameter | Name | Value | Unit |
|---|---|---|---|
| $\Phi$ | Porosity | 50 | % |
| $\rho_h$ | Hydrate density at STP | 0.94 | $g/cm^3$ |
| $r_g$ | Mass fraction | 0.1292 | - |
| $\kappa_h$ | Hydrate compressibility | $1.79*10^{-10}$ | $Pa^{-1}$ |
| dS/dt | Dissociation rate | $4*10^{-10}$ | $s^{-1}$ |

**Table 6.1**: Parameters used for calculation of generated pore pressure

The pore pressure result is independent of the value of $\Delta D$ as the method only considers the ratio of pore space filled with hydrate to the total pore space that is available, independent of the length of the depth interval. The dissociation rate in Table 6.1 is represented as a fraction of the initial amount of hydrate that is dissociated per second and taken from Xu and Germanovich (2006). At this rate, not taking into account the effects of ambient pressure and temperature, pore volume compressibility, the buffering effect of gas production, the heating rate, or the quantity of hydrate on the speed of dissociation, it would take more than 600 years until half of the gas hydrates have been dissociated.

In the following, pore pressure generation is calculated for both present-day and Holocene hydrate stability conditions to test if hydrate melting could have been or still is capable of producing significant amounts of pore pressure.

### 6.3.1 Present-day conditions

Generated pore pressure is calculated for sediment permeability values between $10^{-16}$ $m^2$ and $10^{-18}$ $m^2$ as well as for an initial gas hydrate saturation ranging from 5% to 50% (Fig. 6.1).

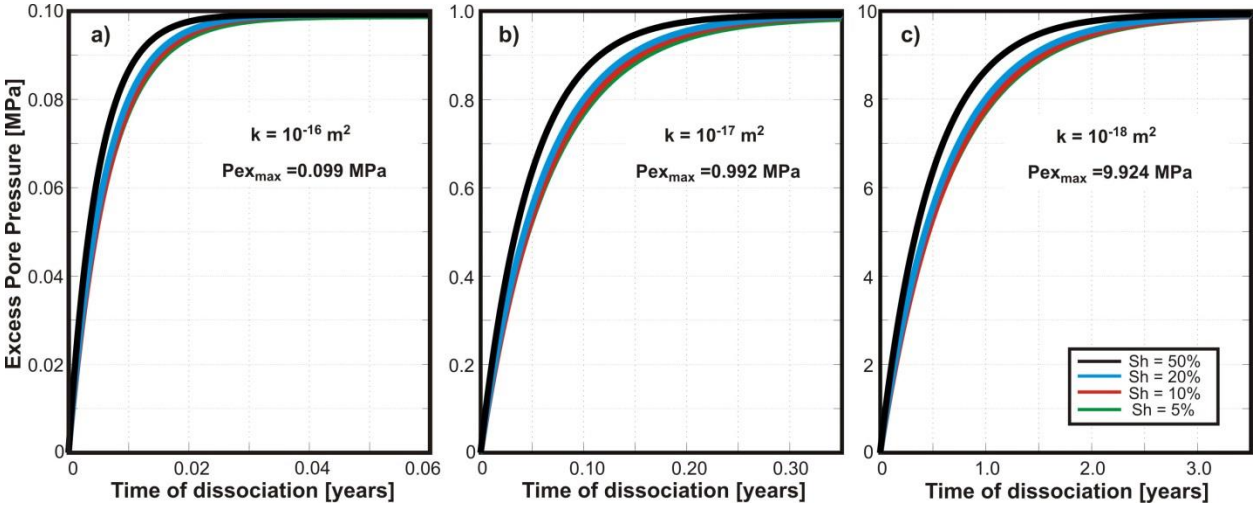


**Figure 6.1**: Generated pore pressure for several permeability values and several initial hydrate saturations; initial free gas saturation is 0%

Fig. 6.1 shows the strong influence of sediment permeability on pore pressure development. The amount of generated pore pressure and the duration of the process are proportional to the factor of volume increase $R_v$ (equation 6.2) and inversely proportional to the logarithm of the permeability. Maximum pore pressures of 0.10 MPa, 0.99 MPa, and 9.92 MPa are reached after about 9 to 10 days, three months, and 3 years, respectively. For a permeability of $10^{-16}$ $m^2$ and $10^{-17}$ $m^2$, these values correspond to overpressure ratios of 0.03 and 0.41, respectively. A permeability of $10^{-18}$ $m^2$ leads to pore pressures that exceed the lithostatic pressure by almost 8 MPa.

Pore pressure generation is rapid at the beginning and slows down as effective compressibility increases with the continuous release of free gas. Table 6.2 summarizes the characteristic time for the pore pressure generation depicted in Fig. 6.1.

| $S_{h0}$ | $k = 10^{-16}$ m$^2$ | $k = 10^{-17}$ m$^2$ | $k = 10^{-18}$ m$^2$ |
|---|---|---|---|
| 5% | 2.4 days | 24 days | 240 days |
| 10% | 2.3 days | 23 days | 234 days |
| 20% | 2.2 days | 22 days | 220 days |
| 50% | 1.8 days | 18 days | 180 days |

**Table 6.2**: Characteristic time of hydrate dissociation for several permeability values and initial hydrate saturations

The characteristic time of dissociation (i.e. the time needed for the pore pressure to reach a value 1/e$^{th}$ smaller than the total generated pore pressure) is found to increase by a factor of 10 between each permeability value (Table 6.2). Differences in initial hydrate saturation have an only small effect on how fast hydrate is melting or the maximum pore pressure value. This is at least in part due to the release of free gas which acts as a cushion for further pressure increase.

The compressibility of free gas plays a significant role. Generated pore pressure decreases with increasing depth of the dissociating layer as a lower overburden pressure leads to larger volume expansion of the released gas. The influence of gas compressibility can also be tested by increasing the initial amount of free gas as seen in Fig. 6.2a for a permeability of $10^{-18}$ m$^2$.

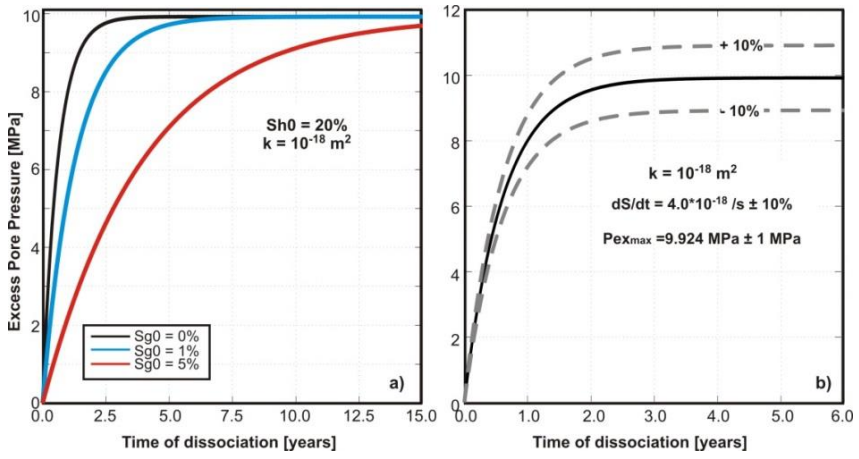


**Figure 6.2**: a) Generated pore pressure with different initial free gas saturations and b) changes in generated pore pressure with increasing dissociation rate *dS/dt*; for a permeability *k* of $10^{-18}$ m$^2$ and an initial gas hydrate saturation of 20%

In all cases the same maximum pressure is reached. However, the existence of only a small amount of free gas (i.e. 1% and 5% of the pore space) at the beginning of the dissociation significantly slows pore pressure generation. Whereas pore pressure reaches its peak value after about two and a half years for 0% initial free gas, it takes more than 15 years to reach the same value with 5% initial free gas saturation (Fig. 6.2a).

The effect of changes in dissociation rate was tested as well (Fig. 6.2b). Pore pressure is very sensitive to the dissociation rate and increases proportional to it. For example, a variation in *dS/dt* by ± 10% for a permeability of $10^{-18}$ $m^2$ results in a variation in generated pore pressure by ± 1 MPa, and for a permeability of $10^{-16}$ $m^2$ pore pressure differences are at about ± 0.01 MPa.

### 6.3.2 Holocene conditions

Next, pore pressure generation is estimated for four of the Holocene paleo-BSR scenarios discussed in Chapter 5. Table 6.3 summarizes the depths of the paleo-BSR at 9 ka (cases 1 and 2) and 14 ka BP (cases 3 and 4), the water depth, as well as the corresponding calculated overpressure ratios for $k$=$10^{-16}$ $m^2$ and $k$=$10^{-17}$ $m^2$. Results for a lower permeability are not shown as generated overpressures exceed lithostatic pressure in all cases by almost 10 MPa. Initial hydrate saturation is held at 20%.

| Case | Time [yrs BP] | Water depth [m] | Seafloor Temperature [°] | Paleo-BSR depth[m] | Overpressure ratio λ at $k=10^{-16}$ $m^2$ | Overpressure ratio λ at $k=10^{-17}$ $m^2$ |
|---|---|---|---|---|---|---|
| **1** | 9,000 | 1802 | 1.5 | 271 | 0.04 | 0.39 |
| **2** | 9,000 | 1802 | 0.0 | 298 | 0.04 | 0.36 |
| **3** | 14,000 | 1720 | 1.5 | 282 | 0.04 | 0.40 |
| **4** | 14,000 | 1720 | 0.0 | 294 | 0.04 | 0.38 |

**Table 6.3**: Overpressure ratios calculated from generated pore pressure at 9 ka and 14 ka BP

The results in Table 6.3 suggest that gas hydrate dissociation during the Holocene would not have given rise to a much different amount of overpressure compared to dissociation under present-day conditions.

## 6.4 Discussion

The pore pressure due to gas hydrate dissociation was estimated using the analytical method of Xu and Germanovich (2006). The focus solely lay on the pore pressure that a certain amount of hydrate can produce at a specific depth. The resulting pore pressures are largest possible estimates. Calculating the temporal evolution and the variety of feedbacks caused by gas hydrate dissociation following a thermal pulse is beyond the scope of this chapter and has been studied as an essential aspect of hydrate production (e.g. Wright et al., 2005; Moridis et al., 2009).

The interplay between permeability and dissociation rate was found to be the most important influencing factor in hydrate-related pore pressure build-up whereas initial gas hydrate saturation, or the size of the dissociation front, do not play a significant role. A permeability that is higher than $10^{-17}$ $m^2$ would allow free gas and water to dissipate before significant overpressure is developed. Sediment with a permeability that is equal or lower than $10^{-17}$ $m^2$ can develop high excess pore pressures that might lead to slope failure, especially when combined with another trigger mechanism. A permeability of this magnitude is realistic as sediment permeability within the uppermost 500 m has been estimated to be of the order of $10^{-17}$ $m^2$ along the northern Cascadia margin (Hyndman, 1995b).

Low-permeability sediments could also lead to the phenomenon of hydro-fracturing. It occurs when fluid pressures exceed the least confining stress and subsequently break the sediment, leading to a so-called ‘secondary permeability’ (e.g. Crutchley et al., 2010; Daigle and

Dugan, 2010). The results in Fig. 6.1c suggest that dissociation in sediment with a permeability of $10^{-18}$ $m^2$ would generate pore pressures of the order of 10 MPa. As this would greatly exceed lithostatic pressure resulting in hydrofracturing or even liquefaction to overcome the enormous pressure built-up (Xu and Germanovich, 2006).

Pore pressure results for present-day conditions do not show significant variations when compared to Holocene conditions. Therefore, pore pressure generation during the Holocene could also have only been significant in sediments that have a low permeability. However, even if pore pressure generation was fairly low, it could still have led to slope failure when combined with another external force such as earthquake shaking.

The results also show that significant pore pressure built-up is possible in sufficiently impermeable sediments. Hydrate-related slope failure could therefore have been possible during times of sea-level decrease such as at the beginning of ice ages.

# Chapter 7: SLOPE STABILITY ANALYSIS

The stability of a slope depends on the relationship between the forces driving failure and the strength of the slope material. A variety of methods are used to assess slope stability ranging from simple static analyses of the problem geometry to more rigorous Finite Element and Finite Difference calculations. These methods share the underlying principle of finding a threshold value at which a trigger initiates slope failure. The critical slope angle, for example, can be found using Dahlen's (1984) critical taper theory or calculated via the factor of safety (FS), a single parameter representing the ratio between the sum of the stresses resisting failure and the sum of the stresses promoting failure.

Here, a first-order regional margin stability analysis is performed using the critical taper theory, followed by a limit equilibrium FS analysis of Orca Ridge and Slipstream Ridge. The most likely factors causing regional slope failure are investigated, focusing on gravitational slide initiation due to simple oversteepening, as well as on earthquake shaking and overpressure. The threshold values are then compared to earlier estimates of regional pore pressure regime, expected ground accelerations, and possible hydrate-related excess pore pressures.

## 7.1 Application of the critical taper theory

The overall margin stability along northern Cascadia is calculated using the critical taper theory (Dahlen, 1984; Dahlen et al., 1984). The theory is based on the Mohr-Coulomb failure criterion (Equation 3.1) assuming an elasto-plastic rheology. The critical taper is the equilibrium angle at which an accretionary wedge is still stable and primarily depends on material properties, pore pressure, and strength of the décollement. Using critical taper theory, the critical slope angle $\alpha$ of a wedge can be calculated if values for the angle of subduction $\beta$ and the basal friction

coefficient $\mu_b$ are known (e.g. Lallemand et al., 1994; Kukowski et al., 2001). The critical taper is defined as the sum of angles $\alpha$ and $\beta$, written as:

$$\alpha + \beta = \frac{[(1-\lambda_b)*\mu_b+(1-\rho_w/\rho_r)*\beta\,]}{[(1-\rho_w/\rho_r)+(1-\lambda_b)*K]} \tag{7.1}$$

with angles $\alpha$ and $\beta$ in radians. $\rho_w$ is the density of water, $\rho_r$ is the density of the wedge material, $\lambda$ and $\lambda_b$ are the ratios of pore pressure to lithostatic pressure in the wedge, and at the base of the wedge, respectively, and $K$ is a geometrical parameter that is calculated via:

$$K = \frac{sin\phi}{1-sin\phi} + \frac{sin^2\phi_b+cos\phi(sin^2\phi-sin^2\phi_b)^{1/2}}{cos^2\phi_b-cos\phi(sin^2\phi-sin^2\phi_b)^{1/2}} \tag{7.2}$$

where $\varphi$ is the internal friction angle within the wedge and $\varphi_b$ the internal friction angle at the base of the wedge (Davis et al., 1983).

Along the Cascadia margin, values for $\mu_b$ lie between 0.55 and 0.85 and overpressure ratios at the base of the accretionary wedge are equal to the ratios within the wedge (i.e. $\lambda=\lambda_b$) (Dahlen, 1984; Saffer and Bekins, 2002). The respective internal friction angles within the wedge and at the base of the wedge can be calculated using the relations $\mu=tan(\varphi)$ and $\mu_b=tan(\varphi_b)$. Cohesion along the northern Cascadia margin is ignored. Although the subduction angle $\beta$ varies perpendicular to the strike of the subduction zone it is set to a constant value of 4.0° (Westbrook et al., 1994; Saffer and Bekins, 2002).

The critical slope angle $\alpha$ is calculated via equations 7.1 and 7.2. For a $\mu_b$ of 0.55 and pressure ratios of 0.5 to 0.6 (Hyndman et al., 1993) the $\alpha$ lies between 4.6° and 4.9° and with a $\mu_b$ of 0.85 between 9.8° and 10.4°.

Slope angles along the northern Cascadia margin, calculated using the GIS software package ArcGIS®, mostly lie between 0.0° and 2.8°. However, where accretion has led to a significant change in topography, angles increase to between 8.0° and 18.0°. The steepest slope angles are at the headwalls of the failure scars as well as along the walls of Barkley Canyon,

parts of the shelf edge and along seaward-facing structures. Slope angles along the northern Cascadia margin are then separated in critical- and sub-critical taper values with the critical slope angles additionally subdivided into 4.6° and 9.8°, representing the two different cases of the state of basal friction. The resulting slope angle distribution is seen in Fig. 7.1.

In Fig. 7.1 the more conservative estimate (i.e. 4.6°) is represented in orange, and red shows the critical regions with angles exceeding 9.8°. Most of the critically steep slopes occur where tectonic forces have compressed and deformed the slope material, here confined to two margin-parallel 'bands', one along the deformation front and the other 10-20 km landward of the deformation front. These slopes remain critical even when the larger critical taper is assumed. The walls of Barkley Canyon (Box 5) and a large part of the shelf edge covered by the multibeam swath-bathymetry (Box 1, Fig. 7.1 inset) reveal slopes that dip at critical angles as well. However, the 'background' slope angles of parts of the margin that have not been deformed or lifted up by compressional forces are all sub-critical.

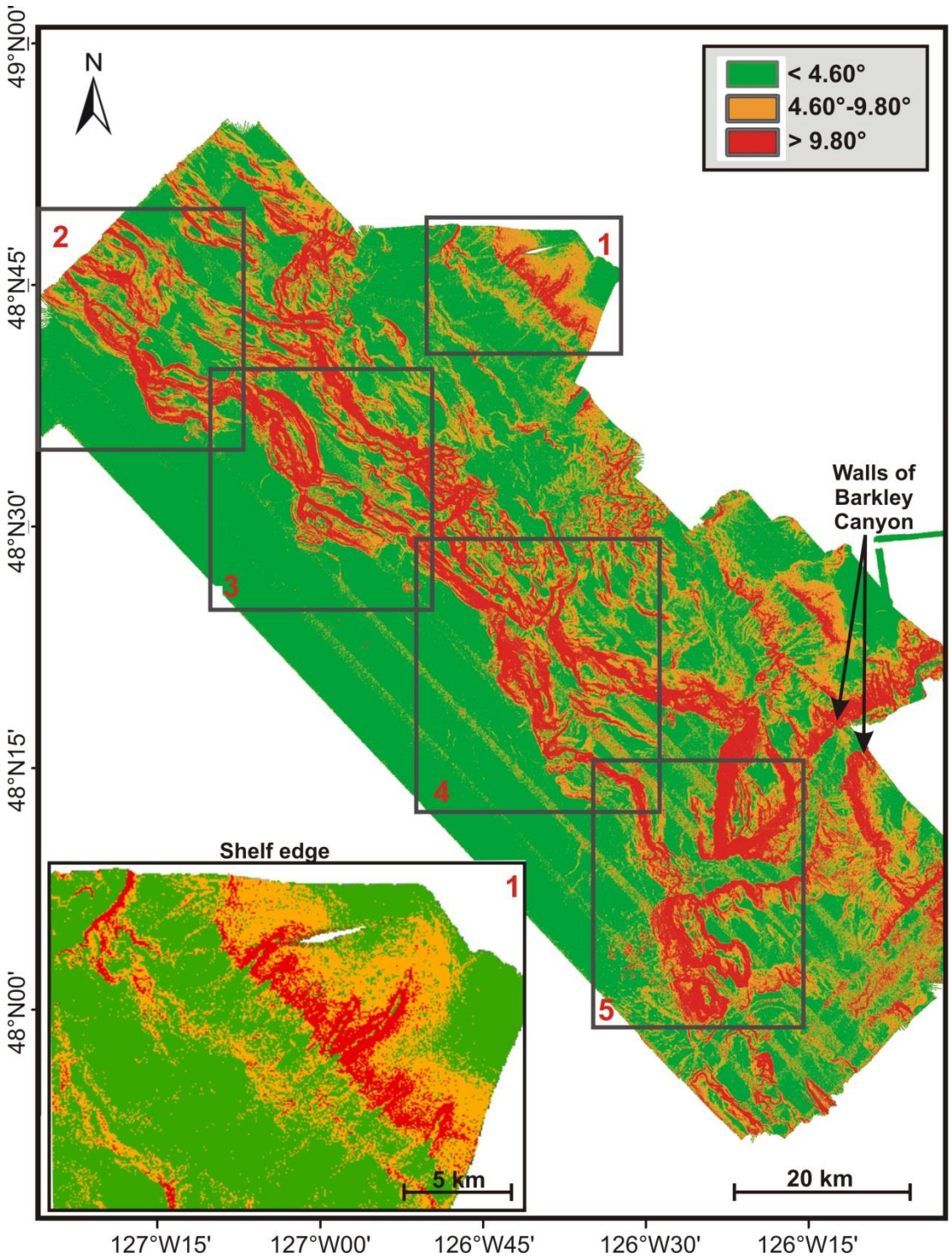


**Figure 7.1**: Slope angle distribution along the northern Cascadia margin divided into critical and sub-critical angles; critical taper angles are calculated for a $\mu_b$ of 0.55 (orange shaded regions) and a $\mu_b$ of 0.85 (red shaded regions); inset: zoom of Box 1, the shelf edge region; slope angles in Boxes 2-5 are seen in Fig. 7.2

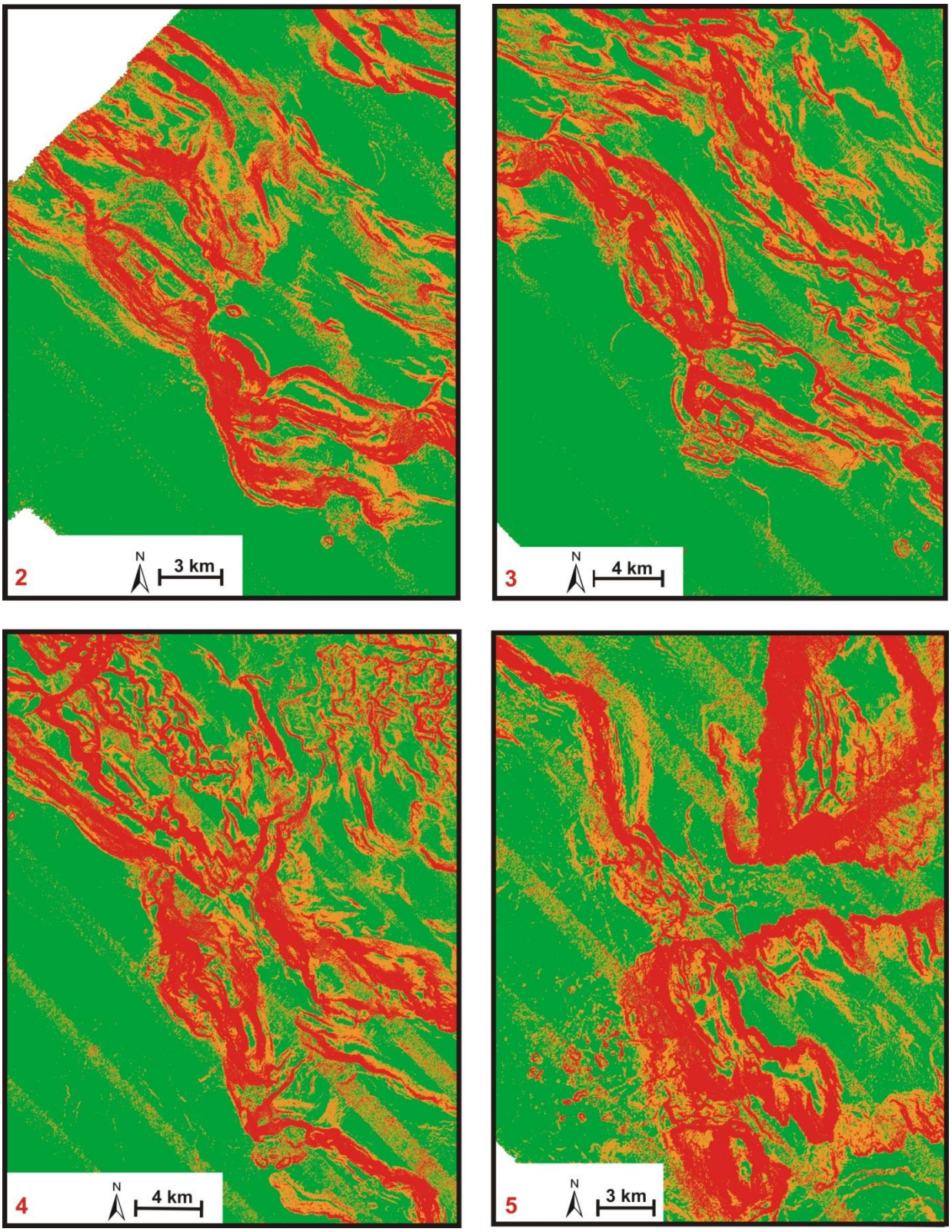


**Figure 7.2**: Zoom into the four grey boxes in Fig. 7.1 located along the deformation front

The detailed maps of slope angle along the deformation front (Fig. 7.2) show that all seaward-facing sides of the frontal ridges are critical. At Orca and Slipstream Ridge (Box 3) even the landward dipping slopes are critical as well, especially when a threshold angle of > 9.8° is assumed.

The results above are conservative as it is assumed that there is no sediment cohesion along the margin. A value larger than zero would lead to an increase in critical slope angle which might shift parts of the margin out of the critical range (Fig. 7.1). Sediment strength might locally be higher due to the existence of tectonically compressed and dewatered sediments. Furthermore, critical taper theory assumes that the horizontal scale is larger than the local thickness of a wedge and therefore might underestimate the stability of smaller-scale structures (Kukowski et al., 2010).

**7.2 Factor of safety analysis**

As critical taper theory most likely underestimates ridge stability, a limit equilibrium FS analysis is used to estimate the stability of Orca and Slipstream Ridge before failure and to calculate local threshold values for triggers such as overpressure and earthquake shaking. Limit equilibrium methods are among the computationally least expensive techniques to calculate the FS focusing only on a static representation of the forces that act on a slope.

The infinite slope analysis and the method of slices both belong to the family of limit equilibrium methods. While the former is based on an idealized slope of infinite length, the method of slices is more appropriate for finite slope failure geometries. It divides the sliding mass into vertical slices (or columns) and sums up the forces that are acting on each of them.

### 7.2.1 Previous FS studies and methodology

Limit equilibrium techniques were mainly developed in the 1950s and 1960s by Bishop (1955), Morgenstern and Price (1965), Spencer (1967), and Janbu (1968) based on the earlier work of Fellenius (1936). Individual techniques differ in their assumptions regarding the inter-column forces and in the way the equilibrium conditions are satisfied (Krahn, 2004). Limit equilibrium techniques have been applied in a range of different fields and over a range of different scales to assess the stability of embankments and excavations (Duncan, 1996), of rocky (Erismann and Abele, 2001), clayey or sandy slopes, or of unconsolidated sediments on the flanks of volcanoes (Carracedo, 1999; Donnadieu et al., 2001), of continental slopes (Dawson et al., 1988; Nisbet and Piper, 1998; Leynaud et al., 2004), or of earthquake triggered landslides (Keefer, 2002; Del Gaudio et al., 2003). According to Eberhardt (2008) it is essential for each FS analysis to be backed-up with detailed information on local sediment properties and detailed slope geometry, ideally including their variation in time and space.

Similar to the critical taper theory, FS analyses are also based on the Mohr-Coulomb failure criterion (Equation 3.1). Total stress conditions are assumed since the failure processes are mostly too fast for any fluid pressure dissipation to occur. The normal and shear forces acting on a sliding body can then be written as:

$$N = W * cos\alpha \tag{7.3a}$$

$$T = W * sin\alpha \tag{7.3b}$$

where $N$ is the normal and $T$ the shear force, $W$ is the weight of the body and $\alpha$ the slope angle.

### 7.2.2 Infinite slope method

Fig. 7.3 shows a sketch of the infinite slope geometry and the acting forces considered in the analysis.

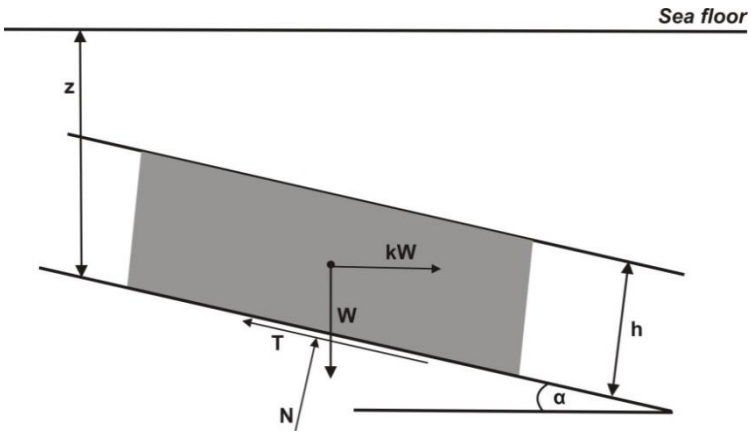


**Figure 7.3**: Sketch of infinite slope geometry and the forces acting on a sliding body

With the forces illustrated in Fig. 7.3 the FS in the case of an infinite slope can be written as:

$$FS = \frac{c + W*cos\alpha*tan\phi_f}{W*sin\alpha} \tag{7.4}$$

Including pore fluid pressure *u* the equation for the FS becomes:

$$FS = \frac{c + (W*cos\alpha - u)*tan\phi_f}{W*sin\alpha} \tag{7.5}$$

The analysis of the influence of earthquake acceleration is done using a pseudo-static analysis. The method dates back to Terzaghi (1950) and assumes that shaking creates vertical and horizontal inertial forces that act on the center of the body. As the vertical component only adds to the weight of the overburden only the forces that act in the horizontal direction are considered:

$$F_h = ma = \frac{Wa}{g} = \frac{Wa_{max}}{g} = k_h W \tag{7.6}$$

where $a$ is the horizontal ground acceleration and $a_{max}$ is its peak value, and $k_h$ is the dimensionless seismic coefficient represented as a fraction of the gravitational acceleration $g$. The FS for an infinite slope under the influence of earthquake shaking is then:

$$FS = \frac{c + W*cos\alpha*tan\phi_f}{W*sin\alpha + W*k_h*cos\alpha} \quad (7.7)$$

Both equations 7.5 and 7.7 can then be combined to calculate the FS under the influence of both excess pore pressure and earthquake acceleration:

$$FS = \frac{c + (W*cos\alpha - u)*tan\phi_f}{W*sin\alpha + W*k_h*cos\alpha} \quad (7.8)$$

### 7.2.3 Ordinary Method of Slices

For finite slope geometries the assumption of an infinite slope does not hold anymore and the Ordinary Method (also known as Swedish or Fellenius) of slices (Fellenius, 1936) becomes more useful. Generally, in a method of slices the failing material is divided into several vertical columns, each having a straight line as its base. Assumptions regarding the direction of the inter-slice forces are then made. The Ordinary Method in particular ignores inter-slice forces, resulting in the most conservative estimate of the FS. Fig. 7.4 illustrates the geometry assumed in the Ordinary Method of Slices in which the circular gliding plane is approximated by several columns with straight bases.

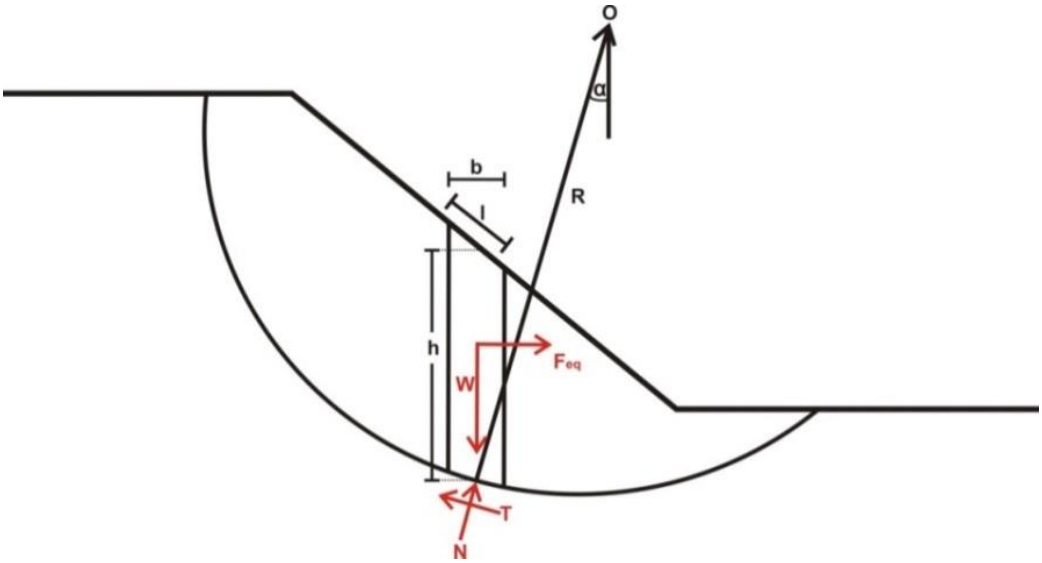


**Figure 7.4**: Sketch of geometry assumed in the ordinary method of slices as well as the forces acting on the sliding mass

Usually, the slopes under investigation have not yet failed and the limit equilibrium methods estimate the susceptibility to failure by searching for the critical slip surface that gives the lowest FS while the pre-failure surface is known by varying the location of Point *O* as well as radius *R* (Fig. 7.4).

With the body separated into slices the parameter *W* in equations 7.3a and b becomes the weight of each slice, written as $W=g*h*b*\rho_b$. The horizontal and vertical forces acting on the slice bases are then added up resulting in one FS for the whole slope:

$$FS = \frac{\sum Resisting\ Forces}{\sum Driving\ Forces} \tag{7.9}$$

which can be written as follows:

$$FS = \frac{\sum(c*l + W*cos\alpha*tan\phi_f)}{\sum W*sin\alpha} \tag{7.10}$$

Including the overpressure ratio $\lambda$, as defined in Equation 3.7, and earthquake shaking, Equation 7.10 becomes:

$$FS = \frac{\sum(c*l + (W*cos\alpha - \lambda*l)*tan\phi_f)}{\sum W*sin\alpha + \sum k_h*W*cos\alpha} \tag{7.11}$$

The term $\lambda*l$ in equation 7.11 represents a water-uplift force acting on the base of each slice.

### 7.2.4 Limitations

Limit equilibrium techniques have various limitations that have to be kept in mind when applied to a specific problem. In a FS analysis there are more unknowns than known parameters and several simplifying assumptions regarding the statics are made to render the problem determined. The primary unknown is the force acting in between each slice. The stress distribution along the slope that results from the assumptions made by each of the limit equilibrium methods can be unrealistic (e.g. Duncan, 1996; Krahn, 2004).

Although slope stability is a complex problem it is described by only one parameter. Localized points of weakness or differences in soil strength along the failure plane cannot be resolved with limit equilibrium techniques as any stress concentration or variations in the material properties or in slope angle are averaged over the whole slope. Furthermore, there is no possibility to account for strains and displacements such that limit equilibrium techniques violate the continuity of displacement (Krahn, 2004).

The Ordinary Method also only considers the moment equilibrium and the force equilibrium and the stabilizing influence of forces acting on the columns are not accounted for. Thus, the Ordinary Method of Slices provides the most conservative estimate for the FS (e.g. Duncan, 1996).

When analyzing the impact of earthquake accelerations, the method provides only a static analysis and the influence of cyclic loading or the temporally limited nature of earthquake shaking are not accounted for. Cyclic loading for example, can lead to a gradual decrease in shear stiffness. The difference in response of sand vs. clay to earthquake shaking can also not be addressed with FS analyses. Ideally, an estimation of the response of a slope to strong ground motions should include the nonlinear dynamic behaviour of soil properties with time (Duncan, 1996). All these phenomena cannot be addressed with a limit equilibrium analysis.

Furthermore, analyses are mostly performed in 2D. Ignoring the effect of the third dimension might underestimate the stability of a slope. The 3D-FS has been found to be higher by as much as 30% compared to the 2D case because the shear strength of the whole slide is increased by the side forces that are neglected in 2D. 3D methods however require several further assumptions to render the problem static and are hindered by end effects such as the shear resistance along the sides of the slide mass that parallel the direction of failure (Stark and Eid,

1998). 3D-analysis also needs detailed knowledge of local soil parameters and their respective spatial variations, information that is mostly not available. Therefore 2D-analyses are often deemed sufficient (e.g. Duncan et al., 1996; Albateineh, 2006).

Despite all its limitations the limit equilibrium technique is still a valid technique to assess slope stability when there is solid knowledge about its background, theory, and limitations to evaluate the results adequately (Albateineh, 2006).

### 7.3 Application to Orca and Slipstream Ridge

The FS was calculated along two profiles derived from the detailed swath bathymetry data set described in Chapter 3. The profiles are both ridge-normal through the failed part of Orca and Slipstream Ridge (Fig 7.5).

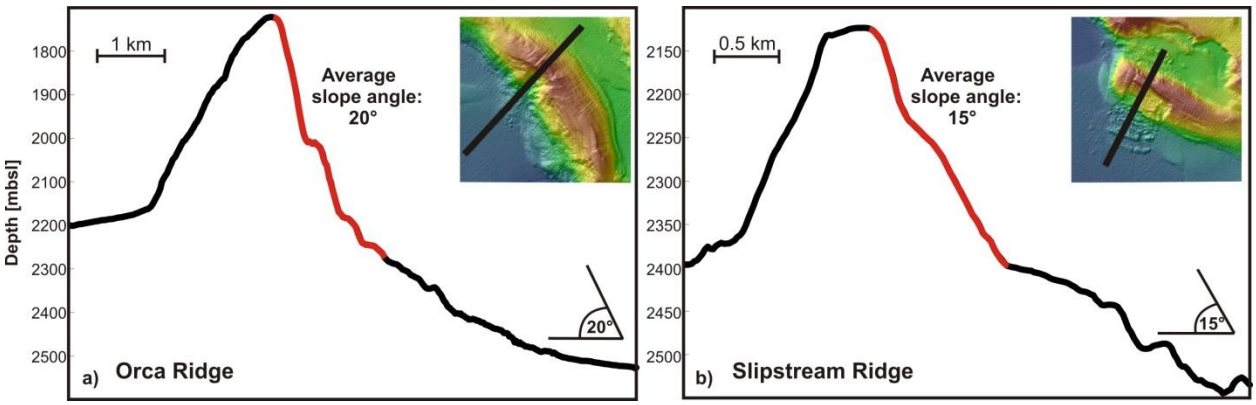


**Figure 7.5**: Profiles of a) Orca and b) Slipstream Ridge used in slope stability analysis; marked in red is the part over which the slope angle was averaged for infinite slope calculations; insets show location of profiles along the ridges

Cohesion and internal friction angle of sediments in this region are not known. Instead, internal friction angles that were previously derived at the southern Cascadia margin were used (Tan et al., 2005) and the relative influence of cohesion was estimated.

### 7.3.1 Infinite slope analysis

The average angle of the headwall part of the slide plane was chosen as an input (Fig. 7.5). The average headwall slope angle at Slipstream is about 20° which is slightly steeper than the headwall region at Orca Ridge which dips on average at ~15°. The internal friction angle was set to range between 27° and 37° based on the results of the constant rate of stress tests conducted by Tan et al. (2005).

The infinite slope analysis also assumes a single value for the slide thickness. Slide thicknesses were set to 250 m and 100 m for Orca and Slipstream Ridge, representing the thickest part of each of the slides with an assumed linear paleo-seafloor. However, slide thickness only has an influence on the FS if cohesion is non-zero.

The FS for an infinite slope in the absence of external triggers was then calculated using equation 7.5. The resulting FS for Orca Ridge are 1.36 and 2.02 for internal friction angles of 27° and 37°, respectively. At Slipstream the FS for these two angles are 1.91 and 2.82, respectively. Thus the FS at both ridges is low and just above the often cited critical value of 1.3 for engineered slopes (Duncan, 1996). As the cohesion was set to zero, the difference between the results for Orca and Slipstream Ridge is solely due to the difference in slope angle.

To estimate the influence of cohesion, internal friction angle, and slope angle, the FS was calculated with variations in these three parameters (Fig. 7.6). In Fig. 7.6a and b the internal friction angle was held at 27° and 37°, respectively while cohesion was varied from 0 MPa to 1 MPa. Fig. 7.6c and d depict the FS as a function of slope angle at internal friction angles between 5° and 50°. In Fig. 7.6c sediment is assumed to have no cohesion while cohesion was set to 1 MPa in Fig. 7.6d.

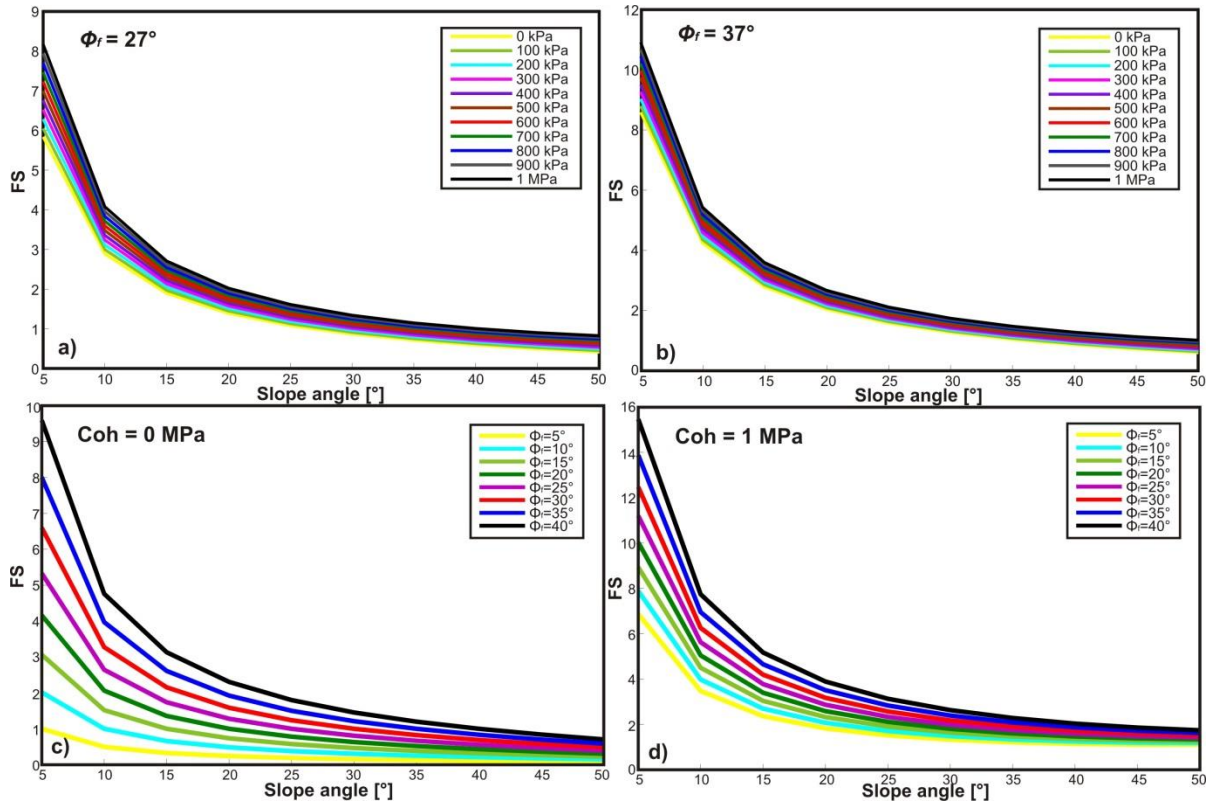


**Figure 7.6**: Infinite slope FS as a function of cohesion, internal friction angle, and slope angle: a) for different *c*-values, $\Phi_f$=27°; b) for different *c*-values, $\Phi_f$=37°; c) for different values of $\Phi_f$, *c*= 0 MPa; d) for different values of $\Phi_f$, *c*= 1 MPa

If slope angles are low the FS lies either between ~6 and ~8.5 or between ~8.4 and ~10.8 for internal friction angles of 27° and 37°. The FS decreases considerably with increasing slope angle and is as low as ~1.0 at slope angles of 27.5° (Fig. 7.6a) and 34° (Fig. 7.6b) and greater. At shallow slope angles, the FS increases by a factor of about 1.3-1.4 when cohesion is increased from 0 MPa to 1 MPa. At extremely high slope angles this factor increases to ~2.1 to ~2.6 depending on the assumed internal friction angle. In contrast to cohesion, an increase in internal friction angle from 5° to 40° increases the FS considerably. In the non-cohesive case, the FS increases from 1.0 to as high as 9.5 and from ~6.5 to as high as about 15.5 if *c*=1 MPa (Fig. 7.6c and d).

Thus, the friction angle $\Phi_f$ has a much stronger influence on slope stability than cohesion $c$ and in the following, sediment cohesion is ignored.

### 7.3.2 Ordinary Method of Slices

The assumption of infinite slide length, however, is unrealistic and further FS calculations were made using the Ordinary Method of Slices. Here, slide thickness does play a role and a pre-failure geometry has to be estimated. As it is not possible to accurately reconstruct the intact shape of the ridges the influence of pre-failure shape was tested by assuming both a linear and a slightly convex-upwards paleo-seafloor (Fig. 7.7). The sliding material was then divided into several slices. Initially, only a few slices are used for Orca and Slipstream Ridge and later on increased to test its influence on the resulting FS.

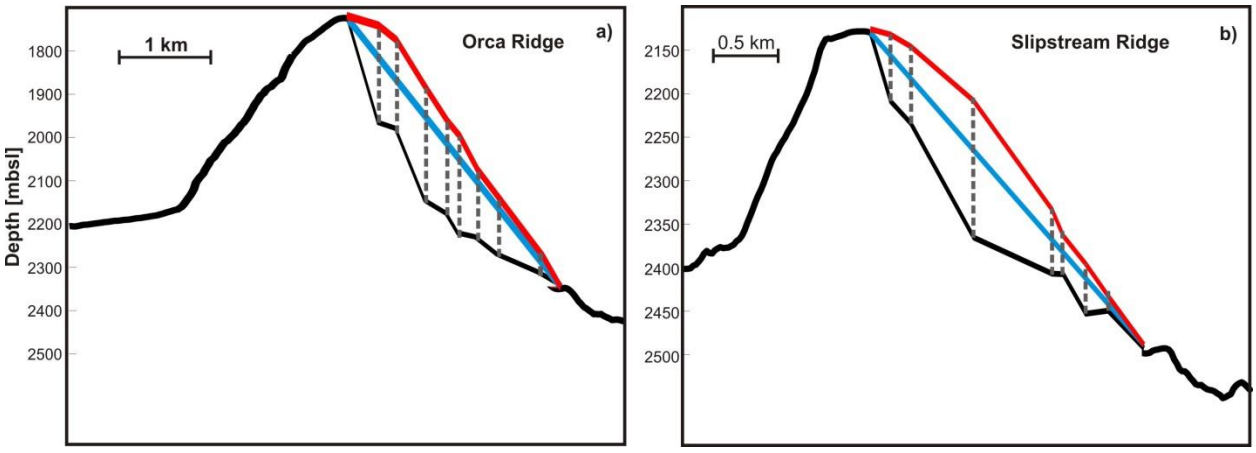


**Figure 7.7**: Profiles used in the Ordinary Method of Slices with the assumed pre-failure surfaces and columns for a) Orca and b) Slipstream; black line: seafloor topography, blue line: linear paleo-seafloor, red line: non-linear paleo-seafloor, grey dashed lines: border of slices

Cohesion was assumed to be zero, which is typical for over-consolidated, fine-grained marine sediments (e.g. Morgenstern, 1967; Skempton, 1970), and the internal friction angle was varied between 27° and 37°. Table 7.1 summarizes the results for Orca and Slipstream Ridge.

| | Orca Ridge $\Phi_f$ = 27° | Slipstream Ridge $\Phi_f$ = 27° | Orca Ridge $\Phi_f$ = 37° | Slipstream Ridge $\Phi_f$ = 37° |
|---|---|---|---|---|
| **Linear paleo-seafloor** | 1.27 | 2.02 | 1.89 | 2.99 |
| **Nonlinear paleo-seafloor** | 1.31 | 2.56 | 1.93 | 3.78 |

**Table 7.1**: FS-results calculated via the Ordinary Method of Slices for the assumption of a linear and nonlinear paleo-seafloor and no external forces

Compared to the previous results for the infinite slope case the FS at Orca slightly decreases and slightly increases at Slipstream Ridge. The assumption of a convex paleo-seafloor does not lead to a significant change in the results. Fig. 7.8 shows the distribution of slope angle, column weight, and column height along the slip surface used for these calculations.

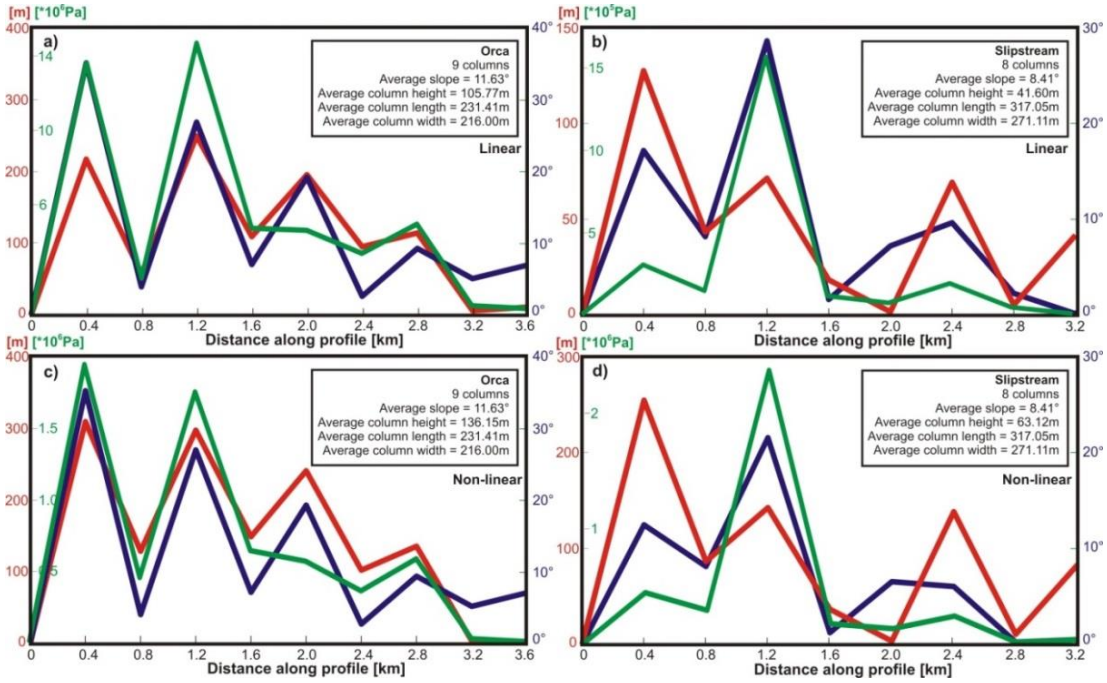


**Figure 7.8**: Distribution of column weights (green), column heights (red) and slope angles (blue) along slip surfaces of a) Orca, linear seafloor; b) Slipstream, linear seafloor; c) Orca, non-linear seafloor; d) Slipstream, non-linear seafloor; corresponding to the geometry in Fig. 7.7; boxes list average measurements for the geometry of each slice

At Orca Ridge (Fig. 7.8a and c) the assumption of a non-linear seafloor leads to an increase in column weight close to the crest of the ridge. Together with the steep slopes in the

headwall region this could be an explanation for the slight decrease in stability. Comparing Fig. 7.8b with 7.8d, the most noticeable difference between a linear and non-linear geometry is found in the middle of the slip surface of Slipstream Ridge where the ratio between overburden and slope angle increases visibly. This could be an explanation for the slight increase in stability. However, the effect of a non-linear seafloor surface on the FS is negligible and further calculations were conducted assuming a linear pre-failure geometry.

The influence of the number of slices was then tested to find a threshold after which the FS is independent of the slice number. It was found that the FS varies until the slice numbers reach 2400 and 2600 at Orca Ridge and Slipstream Ridge. This corresponds to an average slice width of ~1 m, representing the maximum width with which the slide should be divided. With the increase in slice number the FS increased to between 2.07 and 3.07 for Orca Ridge and between 3.19 and 4.71 at Slipstream. This is significantly higher than in the infinite slope case and can be explained by the difference in the geometry on which the calculations are based. Fig. 7.9 summarizes the column weights and heights as well as slope angles for Orca and Slipstream Ridge.

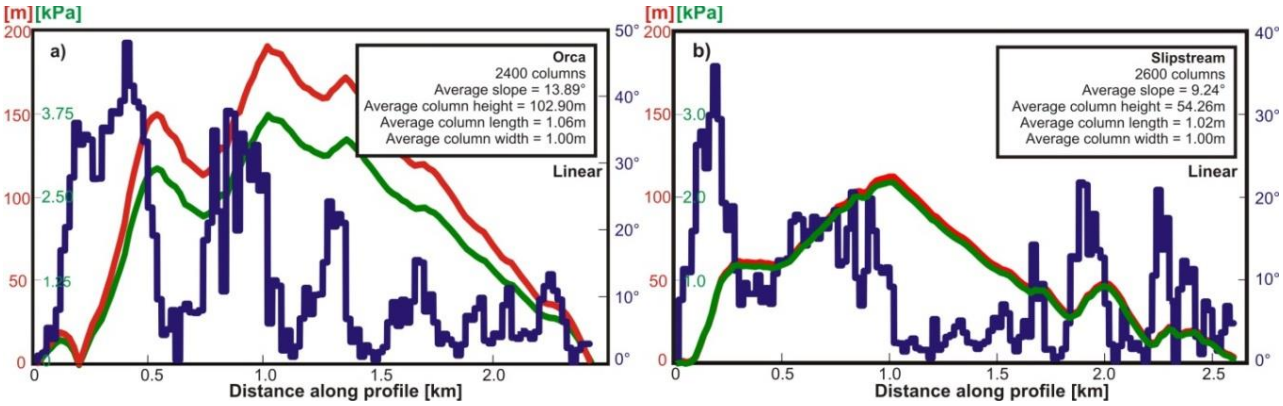


**Figure 7.9**: Distribution of column weights (green), column heights (red) and slope angles (blue) along slip surfaces of a) Orca and b) Slipstream corresponding to the geometry in Fig. 7.7; boxes list average values for the geometry of each slice

Comparing Fig. 7.9 to Fig. 7.8 it can be observed that with increasing number of slices the region with the highest slope angles ‘moves’ closer to the crest. At the same time, the bulk of the weight of all columns is concentrated in the middle part of the slope where it adds to the resisting force. This increase in resisting force in the middle of the slope is the cause for the stability increase compared to the results for lower slice numbers. In the following calculations, the number of slices was held fixed at 2400 and 2600 for Orca and Slipstream, respectively.

***Seismic coefficient and overpressure***

With the number of columns fixed for each ridge, Equation 7.11 is used to estimate the influence of earthquake shaking and overpressure on ridge stability. Fig. 7.10 shows the resulting relationship between FS, overpressure ratio, and seismic coefficient of shaking.

Critical overpressure ratios for Orca Ridge lie between 0.47 and 0.61, for Slipstream Ridge between 0.67 and 0.77 (Fig. 7.10a and b) and critical seismic coefficients in the absence of excess pore pressure lie between 0.27 and 0.51 as well as between 0.35 and 0.66 (Fig. 7.10c and d, Table 7.2). Fig. 7.10e and f illustrate the rapid decrease in critical values when seismic coefficient and overpressure ratio are combined. Stability is greatly reduced as excess pore pressures increases above 0, enhancing the slope’s sensitivity to ground shaking.

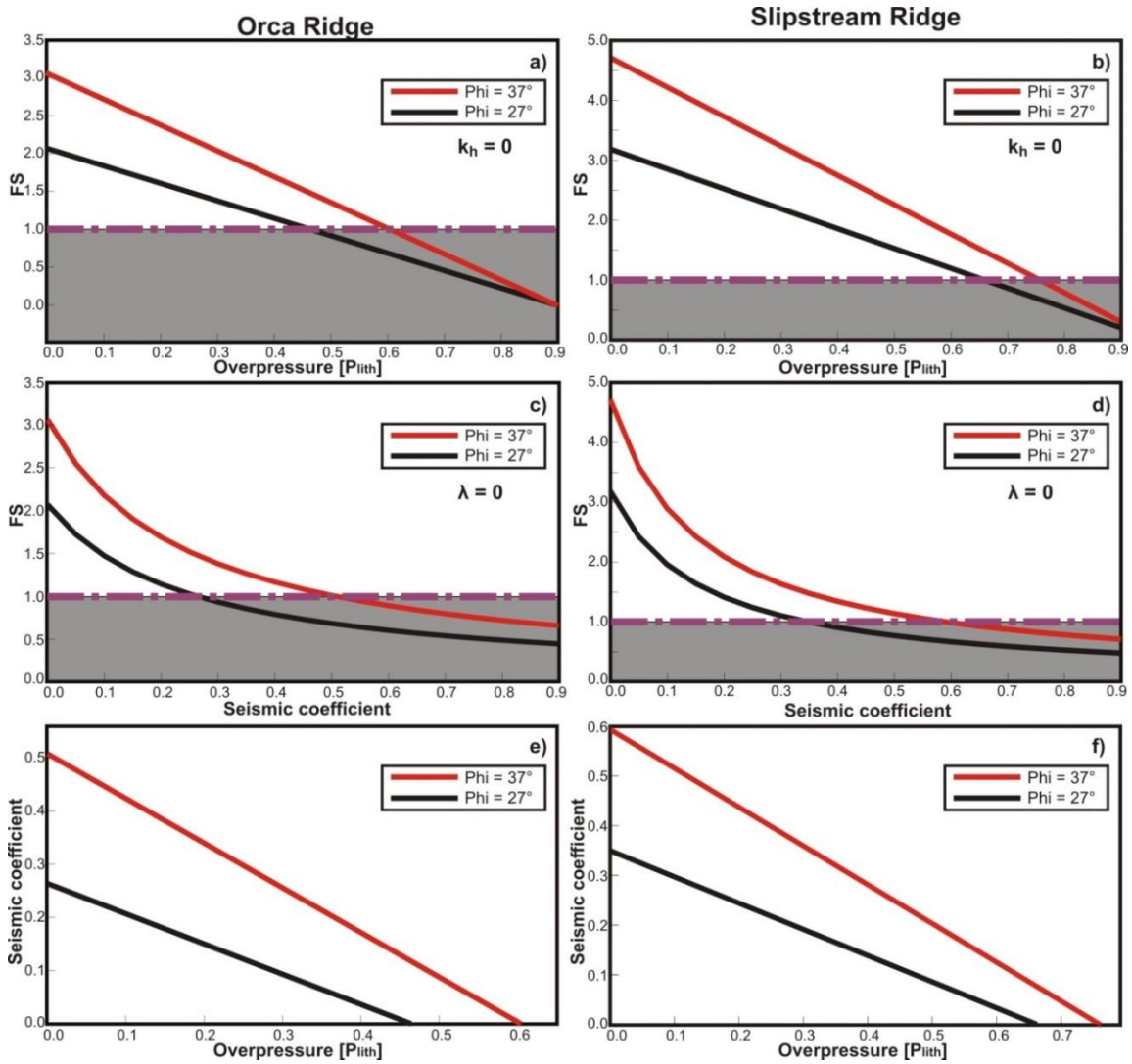


**Figure 7.10**: FS using the ordinary method: a) FS with overpressure ratio for Orca Ridge with 2400 columns; b) FS with overpressure ratio for Slipstream Ridge with 2600 columns; c) FS with seismic coefficient for Orca Ridge with 2400 columns; d) FS with seismic coefficient for Slipstream Ridge with 2600 columns; grey boxes showing interval where slopes become unstable, violet line marks FS=1; combinations of overpressure ratio and seismic coefficients corresponding to FS=1 for e) Orca Ridge and f) Slipstream Ridge

| | **Orca Ridge** $\Phi_f$ **= 27°** | **Slipstream Ridge** $\Phi_f$ **= 27°** | **Orca Ridge** $\Phi_f$ **= 37°** | **Slipstream Ridge** $\Phi_f$ **= 37°** |
|---|---|---|---|---|
| **Critical overpressure ratio** | 0.47 | 0.61 | 0.67 | 0.77 |
| **Critical seismic coefficient** | 0.27 | 0.51 | 0.35 | 0.66 |

**Table 7.2**: FS-results calculated via the Ordinary Method of Slices for critical overpressure ratios and seismic coefficients corresponding to FS=1

## 7.4 Comparison with estimated pore pressure and ground accelerations

### 7.4.1 Pore pressure

In Chapter 3 the pore pressure regime at the IODP Expedition 311 sites was estimated using log-density data. Results for Site U1326, located on the crest of Orca Ridge, showed very little if any excess pore pressure in the uppermost ~150 m of the borehole (Fig. 3.13). At greater depths the overpressure ratio $\lambda$ increases to values as high as 0.6 (where 0.0 equals hydrostatic conditions and 1.0 equals lithostatic pressure). Directly underneath the BSR, $\lambda$ increases to 0.7 and then decreases to negative values as depth increases. This is an interesting result as at Orca Ridge the failure plane approximately matches the depth of the BSR. With overpressure ratios between 0.6 and 0.7, the FS falls to very low values between 0.45 and 1.0 suggesting that failure conditions are met at Orca Ridge (Fig. 7.10a). If it is assumed that Slipstream Ridge is under similar pore pressure conditions, the FS falls below 1.0 only for the highest overpressure estimate and smaller angle of internal friction (i.e. $\varphi$=27 °) (Fig. 7.10b). This suggests that even if overpressure is close to lithostatic additional driving forces are required to meet failure conditions at Slipstream Ridge.

The expected pore pressure due to gas hydrate dissociation that was calculated in Chapter 6 corresponds to overpressure ratios of 0.04 to 0.4 for a permeability of $10^{-16}$ $m^2$ and $10^{-17}$ $m^2$, respectively. Lower permeability sediments were found to give rise to pore pressure regimes above lithostatic.

Fig. 7.11 shows the comparison between the critical pore pressures calculated in this chapter and pore pressure resulting from the dissociation of initially 20% hydrate during four different Holocene climate scenarios summarized in Table 6.2. The grey boxes represent the pressure intervals in which slope failure conditions are met.

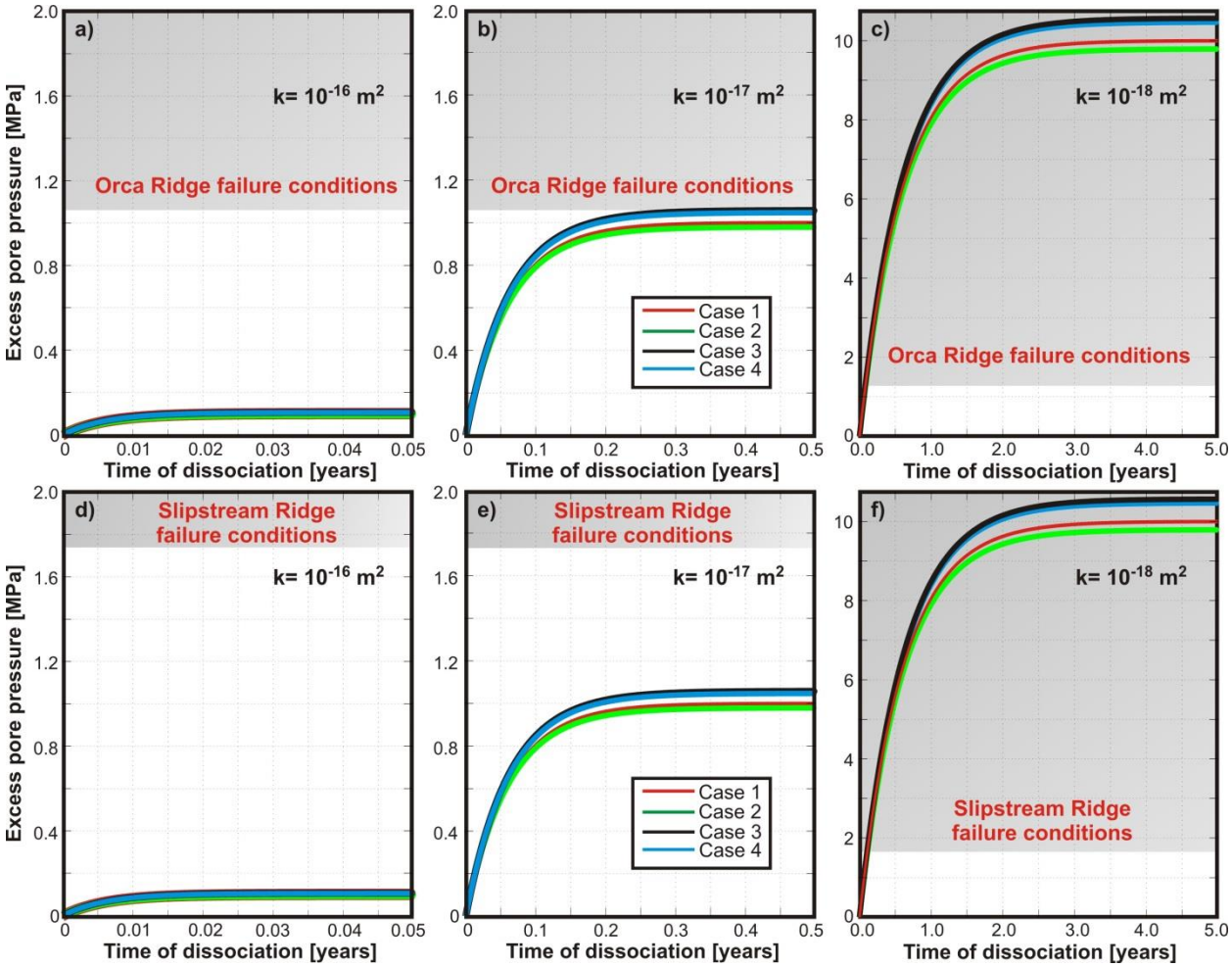


**Figure 7.11**: Estimated gas hydrate related pore pressure compared to critical overpressure (grey boxes) for the four different Holocene climate scenarios described in Chapter 6 (see Table 6.2) for several different permeability values at Orca Ridge (a-c) and Slipstream Ridge (d-f); assumptions: initial hydrate saturation of 20%, constant dissociation rate of $4 \cdot 10^{-10}$ parts of the initial hydrate amount per second

Comparing Fig. 7.11b with Fig. 7.11e reveals an important difference between Orca and Slipstream Ridge regarding the impact of gas hydrate dissociation. At a sediment permeability of $10^{-17}$ $m^2$ failure conditions are only met at Orca Ridge. Generated overpressure in Fig. 7.11a and d is either too low to cause slope failure at either ridge or greatly exceeds lithostatic stress as seen in Fig. 7.11c and f. Therefore, only for sediment permeability values of equal and less than $10^{-17}$ $m^2$ and/or dissociation rates equal or faster than $4 \cdot 10^{-10}$ $s^{-1}$ reduce the FS to below unity or lead to fracturing of the surrounding sediments.

Critical overpressure ratios can also be used to estimate a minimum rate of dissociation depending on permeability (Table 7.3).

| **Permeability [$m^2$]** | **Minimum dissociation rate [fraction per sec] at Orca** | **Minimum dissociation rate [$s^{-1}$] at Slipstream** |
|---|---|---|
| $10^{-16}$ | $4.75*10^{-9}$ -$6.40*10^{-9}$ | $6.40*10^{-9}$ -$7.80*10^{-9}$ |
| $10^{-17}$ | $4.75*10^{-10}$ -$6.40*10^{-10}$ | $6.40*10^{-10}$ -$7.80*10^{-10}$ |
| $10^{-18}$ | $4.75*10^{-11}$ -$6.40*10^{-11}$ | $6.40*10^{-11}$ -$7.80*10^{-11}$ |

**Table 7.3**: Minimum dissociation rates (as fraction of initial amount dissociated per second) to obtain critical overpressure values at different permeability values

Critical rates increase with the same magnitude as an increase in permeability (i.e. an order of magnitude increase in critical rate with an increase in permeability by an order of magnitude). Resulting maximum dissociation rates show that at a low permeability of $10^{-18}$ $m^2$, gas hydrate is only allowed to dissociate half as fast as assumed by Xu and Germanovich (2006) for the given initial hydrate saturation. It has to be kept in mind that the rates summarized in Table 7.3 are not absolute values but represent the fraction of the initial hydrate amount that is dissociated per second. Rather than suggesting specific dissociation rates, results in Table 7.3 indicate the important role of permeability in the control of pore pressure generation.

### 7.4.2 Ground acceleration

Chapter 4 dealt with the estimation of earthquake ground accelerations at the northern Cascadia margin. To compare expected shaking with critical values of shaking it has to be kept in mind that the seismic coefficient $k_h$ calculated in Section 7.3 does not equal the PGA of Chapter 4. $k_h$ is mostly smaller or equal to the PGA or PSA and the ratio between $k_h$ and PSA parameters is mentioned to be of the order of 0.15 or 0.17 (e.g. Hynes-Griffin and Franklin, 1984; Lee et al., 2000; ten Brink et al., 2009). To translate above results into the corresponding

critical PGA ($k_{PGA}$) or PSA ($k_{PSA}$) values, source, path, and site effects have to be taken into account (ten Brink et al., 2009).

Due to the lack of the necessary constraints to establish our own site-specific $k_h$/ $k_{PSA}$-ratio or to derive sediment amplification factors, previously established values were taken. In their study of submarine slope stability along the Cascadia margin, ten Brink et al. (2009) set $k_h$/ $k_{PSA}$ to be ≤ 0.15 and the amplification factor to 3.5, which is relative to bedrock. According to ten Brink et al. (2009) the relationship between $k_h$ and $k_{PSA}$ at a particular period $T$ (here, $T$=0.75 s) can then be expressed as:

$$0.15 \times 3.5 \times k_{PSA_{(T)}} \leq k_h \tag{7.12}$$

where $T$ is the fundamental period calculated via the quarter-wavelength approximation:

$$T = \frac{4H}{v_s}$$

where $H$ is the uppermost layer thickness and $v_s$ is the average shear wave velocity within this layer. Fig. 7.12 shows the FS and the overpressure ratio as a function of the resulting $k_{PSA}$.

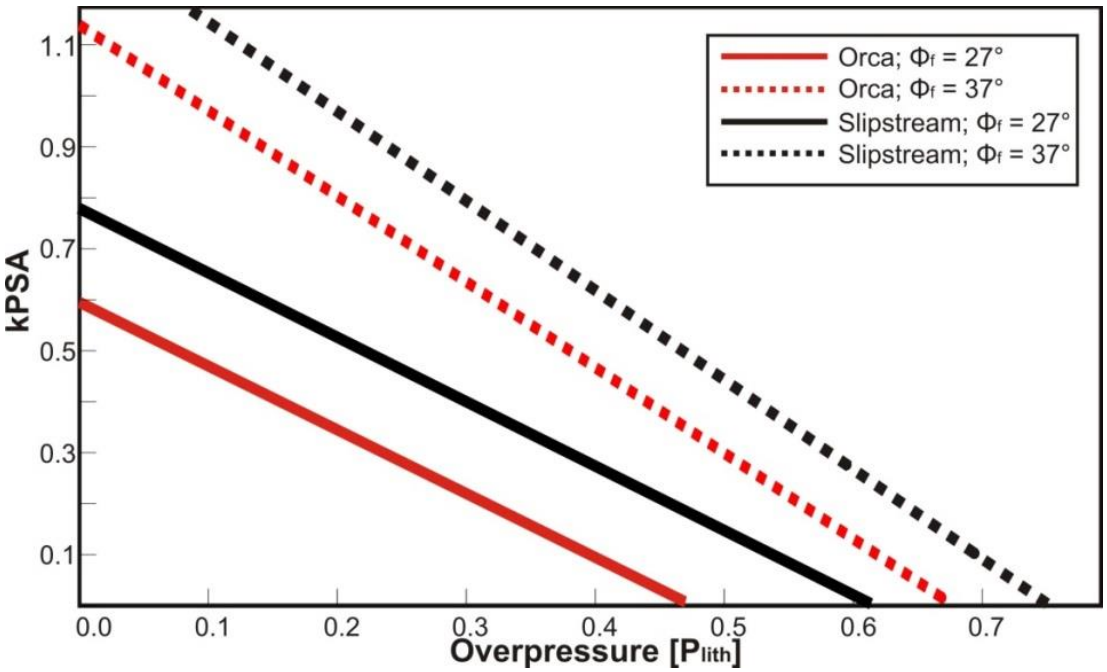


**Figure 7.12**: Overpressure with kPSA after using equation 7.12

Fig. 7.12 provides critical shaking in terms of PSA and it can be seen that ground accelerations have to be at least about 0.6 g to destabilize the slope of Orca Ridge and about 0.78 g to bring Orca Ridge to failure. According to results in Chapter 4, the highest estimated accelerations due to a crustal earthquake of magnitude M8 at a distance to the source of 10 km are at most 0.38 g (Fig. 4.2a). Boore and Atkinson's (2008) GMAR accelerations (Fig. 4.2b) resulted in accelerations of up to 0.6 g but only for an earthquake size of at least M8.0 at an unrealistically close distance to the source. Ground acceleration due to a megathrust earthquake was estimated to be lower than for crustal events due to the larger distance to the updip limit of the seismogenic zone.

Therefore, in the absence of any excess pore pressure both Orca and Slipstream Ridge could be resistant to earthquake-induced slope failure (Fig. 7.12). However, the influence of earthquake shaking on slope stability strongly increases if excess pore pressure is present at the frontal ridges (Fig. 7.12). With an estimated pore pressure ratio at Site U1326 of 0.6 to 0.7 both ridges become highly susceptible to even very low ground shaking accelerations. Table 7.4 summarizes of high $\lambda$-values of 0.6 and 0.7 on critical shaking and slope stability according to Fig. 7.12.

| **Overpressure Ratio** | **Slipstream Ridge $\Phi_f$ = 27°** | **Orca Ridge $\Phi_f$ = 27°** | **Slipstream Ridge $\Phi_f$ = 37°** | **Orca Ridge $\Phi_f$ = 37°** |
|---|---|---|---|---|
| **0.6** | Unstable | Unstable | 0.26 g | 0.13 g |
| **0.7** | Unstable | Unstable | 0.09 g | Unstable |

**Table 7.4**: Reduced values for the critical acceleration ($k_{PSA}$) in the presence of overpressure

Table 7.4 shows that only sediments with a higher internal friction angle can resist failure at excess pore pressures but would fail in case of a relatively small nearby earthquake with a magnitude of 5.0 (Table 4.1) occurred.

## 7.5 Discussion

A critical taper analysis was performed to look at overall margin stability. The results suggest that, on average, slopes along the margin are below critical. Where tectonic forces have significantly changed topography, such as along the frontal ridges and along the oversteepened toe of the continental shelf slopes, the slopes are at a critical state. This would suggest that these regions are prone to failure. The fact that they have remained intact could be a sign that sediments in this part of the continental slope consist of very strong, probably tectonically compacted material which keeps it from collapsing.

However, due to its inherent assumption that the horizontal scale is much greater than the vertical one it is more likely that critical taper theory underestimates the stability of the frontal ridges and of the slopes at the toe of the continental shelf. Therefore slope stability at Orca and Slipstream Ridge was estimated using a limit equilibrium FS analysis. The internal friction angle previously measured along the southern Cascadia margin was used. Due to its negligible influence compared to the internal friction angle, cohesion was set to zero.

Initial results show that the slope angle has a strong influence on the FS, especially when slope angles are lower than 10° (Fig. 7.6) and any excess pore pressure or ground acceleration is absent. The FS is also relatively insensitive to the exact shape of the pre-failure seafloor.

The difference in the resulting FS between the infinite slope analysis and Ordinary Method of Slices, however, is more significant. For an infinitely long slope, the FS calculated with the former method lies between 1.36 and 2.02 for Orca Ridge and between 1.91 and 2.82 for Slipstream Ridge. Applying the Ordinary Method of Slices and using a column width of about 1 m the FS increases to 2.07-3.07 for Orca Ridge and to 3.19 to 4.71 for Slipstream Ridge, indicating that both ridges are still above failure condition in absence of an external trigger. The

results of the infinite slope analysis are likely unrealistic as the weight of the sliding material as well as the corresponding inertial forces are neglected.

The FS analysis showed that overpressure and earthquake shaking lead to a rapid decrease in slope stability. At Orca and Slipstream Ridge slope failure conditions are met if the overpressure ratio is at least 0.47 or if the PGA is 0.58 g and higher (Fig. 7.12). The results in Fig. 7.12 can be compared to the pore pressures and ground accelerations calculated in Chapters 3, 4 and 6. Overpressure could have played a significant role in slope failure if pore pressure was of similar magnitude during the time of failure as has been estimated from log-density measured at Orca Ridge. For example, Fig. 3.13 indicated that pore pressure ratios at Site U1326 could be as high as 0.6-0.7 approaching and partly exceeding the critical pore pressure values at both ridges. Furthermore, high pore pressure values were found at depth interval of approximately 75 m above the BSR with pressures increasing even further directly below the GHSZ. Therefore the BSR potentially represents a plane of weakness and the 75 m thick intact interval above the BSR at Site U1326 adjacent to the failure scar of Orca Slide could still be prone to failure (Fig. 3.13).

Expected pore pressure generation from gas hydrate dissociation was calculated for different Holocene climate scenarios involving lower sea-levels and ocean bottom temperatures (Chapter 4 and 6). Results indicate that sediment permeability is the most important parameter in the generation of critical pore pressures. Critically high overpressures develop only at permeabilities of $10^{-17}$ $m^2$ and lower or if dissociation is rapid. Compared to the estimated ground accelerations in Chapter 4, critical PGA-values in absence of pore pressure are relatively high (Figure 7.12). Only an M8 crustal earthquake at a very close distance of about 10 km (Table 4.1) could trigger slope failure.

However, these results have to be treated with caution considering the various limitations and simplifying assumptions of both the limit equilibrium method and ground motion attenuation estimations. Results in Fig. 7.12 can only be regarded as a first-order estimate of ridge stability and the influence of pore pressure and earthquake-induced ground motion. The critical overpressure ratio calculated in this chapter is likely a fairly conservative estimate as illustrated by the fact that the present pore pressure calculated at Site U1326 is higher than the threshold overpressure at Orca Ridge. The calculated critical PGA is based on the seismic coefficient which represents a static value that does not include the effects of cyclic loading or temporal limitations and variations in earthquake shaking. The estimated PGA (Chapter 4), in turn, might not sufficiently reflect amplification and de-amplification effects of the local site conditions. Steep gradients in the topography could lead to non-linear ground response and thus to strong ground shaking even at low magnitudes and thereby increase the impact of a medium-sized earthquake on slope stability. This is especially important as megathrust earthquakes are rare along the northern Cascadia margin but medium-sized events can be expected to occur more regularly.

It also has to be kept in mind that any limit equilibrium method averages the slope angle along the whole gliding plane. Critical values can be expected to vary along the gliding plane and might even be drastically diminished within the headwall region where slope angles are very steep (Fig. 2.3). For instance, a contrast in stratigraphy and sediment layering has been described in a previous study (Expedition Scientists, 2008) but the FS method is not capable of accounting for localized areas of weakness or the tendency for slope failure to occur along stratigraphic boundaries. Such contrasts in stratigraphy would likely decrease the critical values for pore pressure or ground shaking.

Pore pressure generation due to gas hydrate dissociation could have triggered Holocene slope failure only if sediment permeability was very low (i.e. $\leq 10^{-17}$ $m^2$) or if the hydrate dissociated quickly. The resulting overpressure would otherwise have been too low to reach threshold values. In this case the combination of hydrate dissociation with earthquake shaking might have been able to initiate slope failure. In the absence of any excess pore pressure an M8 event at a distance of only a few kilometers would be required to destabilize the ridge slopes but with increasing overpressure threshold earthquake magnitudes decrease significantly (Fig. 7.12).

Similar conclusions can be drawn for the present slope stability. In the absence of any excess pore pressure earthquakes are not likely to trigger ridge failure. The pore pressure estimates of Chapter 3 in contrast suggest that ridge stability is low. However, the existence of significant overpressure is only possible if sediment permeability is very low, especially since the build-up of pore pressure is more likely to have happened several thousand years ago.

The critical taper theory indicates that the lower part of the continental slope, which has so far remained intact, is in a critical condition. If slope failure susceptibility does not differ significantly between the frontal ridges of the northern Cascadia subduction zone, results of the FS analysis suggest that at least parts of the sediments along the toe of the continental slope are very susceptible to the presence of overpressure. Further information on the local pore pressure regime and sediment permeability is necessary to better constrain the likelihood of future slope failure along the northern Cascadia margin.

# Chapter 8: MODELING THE SLOPE FAILURE PROCESS AND THE LINK TO TSUNAMI GENERATION

Probably the most important aspects of a submarine landslide include its dynamic behaviour, especially its velocity and run-out distance. These control its potential for destruction and they can also have significant consequences for tsunami generation and the dynamics and morphology of the continental slope and the deep-sea. Prediction of the post-failure motion, its tsunamigenic potential and the area affected by both the slide and a possible tsunami are therefore essential in a hazard assessment. Due to their remote and partly inaccessible location, submarine landslide deposits are hard to study experimentally and numerical methods are used to understand the run-out characteristics of a slide.

Here, the 2D-finite difference model BING is used to study the dynamics of submarine landslides offshore Vancouver Island. Initial slide geometry and final run-out are estimated based on present-day bathymetry, and observed travel distances are used to estimate the yield strength of the sediment. The run-out and strength characteristics are studied to further differentiate between debris flows and blocky slides and to explain the alternating slide morphologies observed along the northern Cascadia margin. To investigate the possibility that Orca and Slipstream Slide caused tsunami waves of significant height, a first-order tsunami wave estimation is carried out. This is done using a previously developed and applied analytical relationship that links slide dimensions and slide depth to the height of generated surface waves.

## 8.1 Previous work

The numerical modeling of landslides and landslide-generated tsunamis began in the 1980s and 1990s with the works of Iwasaki (1987, 1997), Harbitz (1992), Verriere and Lenoir

(1992), and Heinrich (1992), amongst others. A significant contribution came from the work of Jiang and LeBlond (1992, 1993, 1994) who developed a large part of the mathematical framework that is now used in the modeling of underwater landslides. Among the regions where submarine landslides have recently been simulated are offshore Norway (Gauer et al., 2005; Kvalstad et al., 2005), Alaska and Papua New Guinea (Watts et al., 2003), in the Barents Sea (Marr et al., 2002), in the Mediterranean Sea (e.g. Tinti et al., 2011) and along the coasts of Canada (Fine et al., 2005; Skvortsov and Bornhold, 2007).

Due to the different assumptions about the flow mechanics a variety of different approaches have been used. For example, the Storegga Slide has been modeled as a coherent mass of sediment blocks using finite element methods (FEM) (Kvalstad et al., 2005) as well as a fluid-type material applying computational fluid dynamics (CFD) methods (Gauer et al., 2005). Some researchers have developed models that can be used for both landslides and snow avalanches based on their inherent similarity (Dent and Lang, 1980; Dent, 1982; Jiang and LeBlond, 1993; McDougall and Hungr, 2004). Numerical models include important assumptions about the rheology of slides. Rheological properties depend on factors such as the solid concentration, cohesiveness, particle size distribution, shape of the particles, friction between grains, and pore pressure (Imran et al., 2001a). To simulate the rheological behaviour of a slide, viscous models (Johnson, 1970; Hunt, 1994), linear and nonlinear visco-plastic models (Johnson, 1970; Liu and Mei, 1989; Jiang and LeBlond, 1993; Huang and García, 1998), dilatant fluid models (Bagnold, 1954; Takahashi, 1978; Mainali and Rajaratnam, 1994) dispersive or turbulent stress models (Arai and Takahashi, 1986; Hunt, 1994), and frictional models (Iverson, 1997) have been used.

The visco-plastic or Bingham rheology is the most frequently used model for small-grain, clay-rich mud and debris flows. It is capable of incorporating the transition from solid to viscous material that often occurs during underwater mass movements. This transition can be formulated in the form of a yield strength which represents the threshold that a driving stress has to exceed for deformation to occur. The behaviour of a Bingham fluid is described by its shear stress $\tau$:

$$\tau = \tau_y + \eta\gamma \tag{8.1}$$

where $\tau_y$ is the yield stress, $\eta$ is the viscosity and $\gamma$ the shear rate.

Once the sliding process has started it is assumed that driving forces acting on the slide are proportional to the gravity acceleration and the pressure gradient which both act parallel to the seabed. Forces counteracting the movement are the internal resistance of the material, the seabed friction, and the drag force that is acted upon by the overlying water mass. Acceleration is ongoing until drag force and seabed friction reach a value opposing the force of gravity (De Blasio et al., 2004).

### 8.2 Landslide modeling using the 2D BING model

One model that makes use of the Bingham rheological model is BING, which was developed by Imran et al. (2001a, 2001b). It is based on the numerical scheme of Jiang and LeBlond (1993) and determines run-out distance, slide velocity, and deposit geometry of a submarine or subaerial landslide. The 2D-finite difference (FD) model has previously been applied to simulate mud-rich underwater landslides along the margin of the Svalbard-Barents Sea (Marr et al., 2002) as well as the Currituck Slide off the coast of Virginia (Locat et al., 2009), and Skvortsov (2005) used it to compare with the landslide model developed in his thesis.

### 8.2.1 Model description

BING uses the Herschel-Bulkley model (Herschel and Bulkley, 1926), a generalization of the Bingham rheology to simulate submarine landslides. The slide body is divided into a shear and a plug zone which move at different velocities (Fig. 8.1a). All internal deformation is confined to the lower lying shear layer (Imran et al., 2001a). BING is based on the solution of the equations of conservation of mass and momentum:

$$\frac{\partial u}{\partial x} + \frac{\partial v}{\partial y} = 0 \tag{8.2}$$

and:

$$\frac{\partial u}{\partial t} + u\frac{\partial u}{\partial x} + v\frac{\partial u}{\partial y} = -\left(1 - \frac{\rho_W}{\rho_m}\right) g \frac{\partial D}{\partial x} + \left(1 - \frac{\rho_W}{\rho_m}\right) g\alpha + \frac{1}{\rho_m} - \frac{\partial \tau}{\partial y} \tag{8.3}$$

where $u$ is the flow velocity in the $x$-direction, $v$ the flow velocity in the $y$-direction, $\rho_m$ is the density of the debris flow, $\rho_W$ the density of water, $\alpha$ is the slope angle, $g$ the gravitational acceleration, $\tau$ is short for the stress tensor $\tau_{xy}$, and $D$ the thickness of the debris flow.

Due to the application of a slender flow approximation only one component of the shear stress, i.e. the component $\tau_{xy}$, is accounted for. Here, $x$ denotes the downslope coordinate attached to the slide boundary and $y$ is the coordinate upward normal from the seafloor. Instead of assuming that the viscosity is a simple linear function of the strain rate as it is the case in the Bingham model, the Herschel-Bulkley rheology uses its non-linear equivalent, the 'effective viscosity' (e.g. Huang and García, 1999; Alexandrou et al., 2003).

The Herschel-Bulkley rheology is written as:

$$\frac{\gamma}{\gamma_r} = \begin{cases} 0 & for \quad \tau \le \tau_y \\ \left(\frac{\tau}{\tau_y} - 1\right)^{1/n} & for \quad \tau > \tau_y \end{cases} \tag{8.4}$$

where $\tau_y$ denotes the yield strength, $n$ is an exponent and

$$\gamma = \frac{\partial u}{\partial y} \tag{8.5}$$

stands for the *x*-*y* component of the local strain rate and $\gamma_r$ is a reference strain rate. If $\tau > \tau_y$, the rheology reduces to:

$$\tau = \tau_y + K\gamma^n \tag{8.6}$$

where

$$K = \frac{\tau_y}{\gamma_r^n} \tag{8.7}$$

For $n = 1$ equation 8.6 represents the Bingham rheology in which case $K$ becomes equal to the dynamic viscosity of the debris flow. If $n < 1$ the fluid is shear-thinning, if $n > 1$ it is shear-thickening – or dilatant (e.g. sand). Fig. 8.1b shows the principle of how exponent $n$ influences the layer velocity within the shear zone.

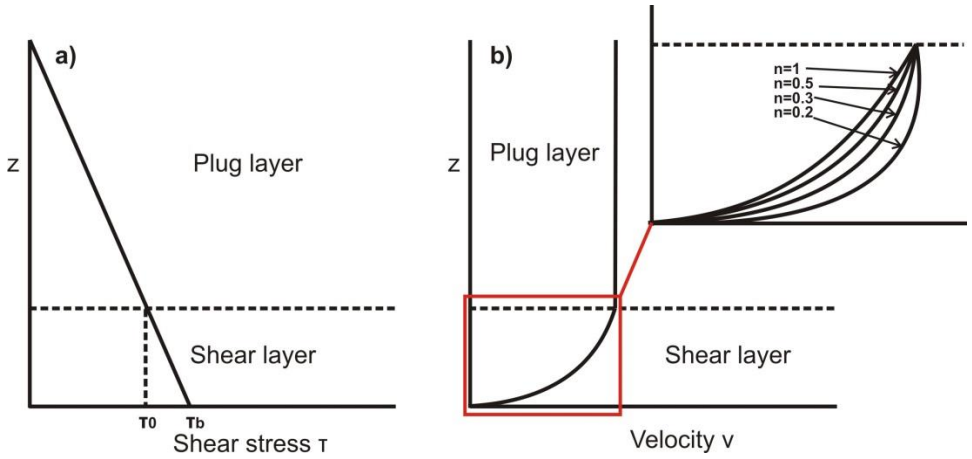


**Figure 8.1**: Sketch representing the (a) principle of yield stress as part of the Herschel-Bulkley rheology and (b) the influence of exponent *n* on the velocity distribution in the shear layer (after Huang and García, 1998)

As seen in Fig. 8.1b *n* controls the curvature of the velocity function in the shear layer. The smaller its numerical value the stronger the curvature within the shear layer and the lower the velocities near the gliding plane.

Equations 8.2 and 8.3 are solved by integrating over the shear and plug layer thickness using the combination of an explicit time-marching FD-scheme with the Kármán integral method

(Jiang and LeBlond, 1993; Imran et al., 2001b; Remaître et al., 2005). As BING solves one equation of mass conservation and two of momentum conservation for both the plug and the shear layer, equations 8.2 and 8.3 become:

$$\frac{\partial \mathrm{D}}{\partial \mathrm{t}} + \frac{\partial}{\partial \mathrm{x}}[\mathrm{U_t}(\mathrm{D_p} + \alpha_1 \mathrm{D_s})] = 0 \tag{8.8}$$

$$\frac{\partial}{\partial t}(U_t D_p) + U_t \frac{\partial D_s}{\partial t} + \frac{\partial}{\partial x}(U_t^2 D_p) + \alpha_1 U_t \frac{\partial}{\partial x}(U_t D_s) = -(1 - \frac{\rho_w}{\rho_s}) g D_p \frac{\partial D}{\partial x} + (1 - \frac{\rho_w}{\rho_s}) g D_p S - \frac{\tau_y}{\rho_s} \tag{8.9}$$

$$\alpha_1 \frac{\partial}{\partial t}(U_t D_s) - U_t \frac{\partial D_s}{\partial t} + \alpha_2 \frac{\partial}{\partial x}(U_t^2 D_s) - \alpha_1 U_t \frac{\partial}{\partial x}(U_t D_s) = -(1 - \frac{\rho_w}{\rho_s}) g D_s \frac{\partial D}{\partial x} + (1 - \frac{\rho_w}{\rho_s}) g D_s S - \beta \frac{\tau_y}{\rho_s} \frac{U_t}{\gamma_r D_s} \tag{8.10}$$

where $U_t$ denotes the stream-wise velocity of the plug layer, $D_p$ the thickness of the plug layer, $D_s$ the thickness of the shearing layer below, and $D$ is the sum of the plug and shear layer. The parameters $\alpha_1$, $\alpha_2$ and $\beta$ are functions of the exponent $n$ (Imran et al., 2001b).

Model input parameters are the depth-profile of the seafloor over which the mass movement is taking place, initial slide length and maximum height, as well as sediment properties such as bulk density, yield strength, and dynamic viscosity. As BING is a 2D model of a 3D process the program translates volume into volume per unit width $v$ (in $m^2$), essentially dividing the volume of the source area by the failure area width. BING uses a parabolic initial slide profile that is subsequently allowed to stretch and contract while it moves down-slope (Fig. 8.2). The slide itself is subdivided into $j$ columns with $i$ nodes ($i$=$j$-1).

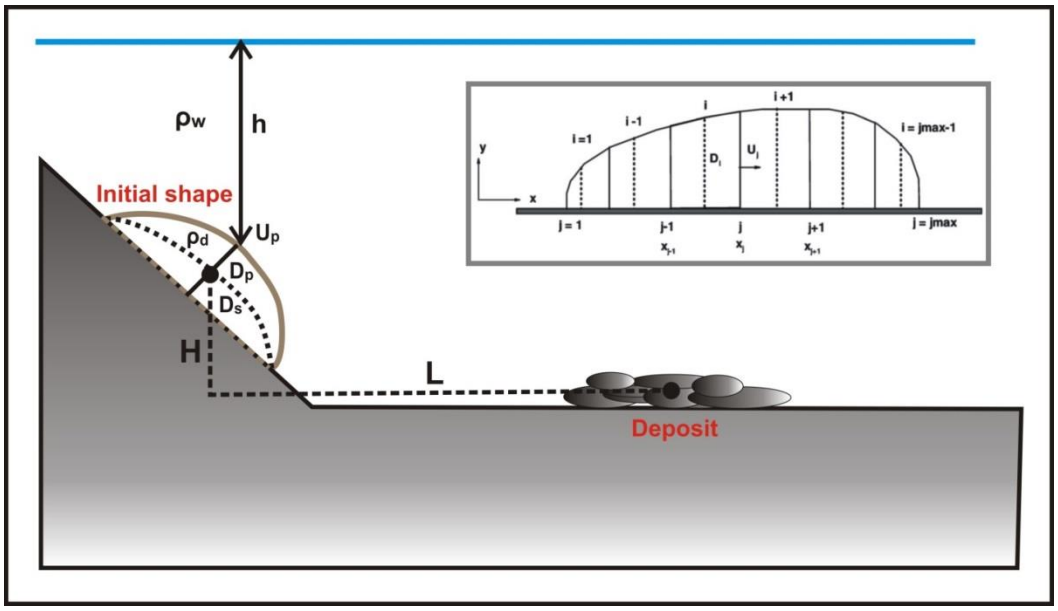


**Figure 8.2**: Sketch of the parabolic initial slide profile and the final deposit; H = height of center of gravity above seafloor, L= length of run-out; inset: model discretization used for calculation (taken from Imran et al., 2001b)

The model has a no-slip condition on the slide bottom and ignores erosion, deposition, and entrainment of water and sediment. Tangential stresses acting on the water-sediment interface are ignored as water viscosity is thought to be low compared to that of muddy material and as the basal shear of the debris flow is markedly higher than interfacial shear (Liu and Mei, 1989; Imran et al., 2001a,b; Marr et al., 2002; Syvitski and Hutton, 2003; Remaître et al., 2005).

### 8.2.2 Limitations

As BING has several important limitations and drawbacks it can only give a rough estimate of the differences between Orca and Slipstream Slide. For example, the software is not able to model seabed erosion, grain-to-grain interaction or the associated energy dissipation such that important phenomena such as the loss in sediment volume or particle and water entrainment cannot be accounted for (e.g. Iverson, 1997; Imran et al., 2001a,b). BING is also not capable of capturing pore pressure increase or decrease during sliding or the detachment of slide material.

The calculated slide velocity has been estimated to exceed observed velocities by a factor of up to 16 thought to be due to an overestimation of the potential energy and the underestimation of the viscosity during shearing. Furthermore, BING assumes the yield strength remains constant throughout the whole slide movement, although yield strength has shown to be a complex parameter that can both increase or decrease during sliding (Remaître et al., 2005). It has been observed that viscosity decreases with increasing shear rate and subsequently there is a weakening in resistance to deformation such that the Bingham model overestimates the true yield strength of a sliding material (O'Brien and Julien, 1988; Huang and Garcia, 1998).

The model does not distinguish between the physical properties and different behaviors of clay, silt, and sand during sliding such that the properties of the slide are a crude average. There is also no possibility to model the effects of grain size on slide behavior.

The Bingham model is also not suitable for cases in which hydroplaning has occurred as in the case of the Storegga Slide (Elverhøi et al., 2000; De Blasio et al., 2004). However, the Herschel-Bulkley rheology is used nonetheless as it is capable of capturing the shear-thinning behaviour of debris flows (e.g. Nguyen and Boger, 1992; Huang and Garcia, 1998).

It also has to be kept in mind that BING models a three-dimensional process in only two-dimensions. The slide is therefore treated as infinitely wide which likely leads to an underestimation of slide-resisting forces and an overestimation of run-out length.

### 8.3 Application to the northern Cascadia margin

As a first step, the appropriate numerical parameters are determined. The numerical viscosity used to support the model's stability is set to its advised maximum value of 0.01 (unit-less) as strong slope gradients of the slide mass as well as the locally very steep slope of the gliding plane led to considerable numerical instability. Following Remaître et al. (2005), $n$ is set

to 1/3. Theoretically, *n* can vary between 0 and 1 (Imran et al., 2001). An increase in *n* leads to a lower viscosity which slows the increase in shear strain with shear rate, leading to increased run-out, decreased deposit thickness, and increasing total slide time.

Another parameter that has to be specified is the reference strain rate $\gamma_r$ (equation 8.7). Previous reference strain rates of 1.0, 6.25 (Imran et al. (2001a)) and 10 (Imran et al., 2001b) have been used. An increase in the value of $\gamma_r$ leads to a decrease in the resistance to flow and an increase of the final run-out. Due to the observed short run-out distances discussed below, $\gamma_r$ is set to 1.0 for all further simulations.

Table 8.1 summarizes the values that were kept fixed throughout all calculations.

| Parameter | Value |
|---|---|
| $\rho_s$ (kg/m$^3$) | 2.00 |
| $\rho_w$ (kg/m$^3$) | 1.04 |
| n | 0.33 |
| $\gamma_r$ | 1.0 |
| Artificial viscosity | 0.01 |

**Table 8.1**: Fixed parameters used for BING modeling

The second step involves the assignment of the physical properties of each slide. While slide and water density as well as initial geometry are well constrained, yield strength values along the northern Cascadia margin are not known. Yield strength is an important parameter in slope stability but should not be confused with cohesion. While cohesion is defined as the part of the shear strength that is independent of friction (see equation 3.1), yield strength is the strength at which a material starts to deform plastically. It has a strong influence on slide initiation as well as on internal deformation, velocity and travel distance. Therefore, the only constraint on local

yield strength is the run-out distance which is observed in the side-scan sonar image in Fig. 8.3. Closer images of Orca and Slipstream Slide are seen in Fig. 8.4.

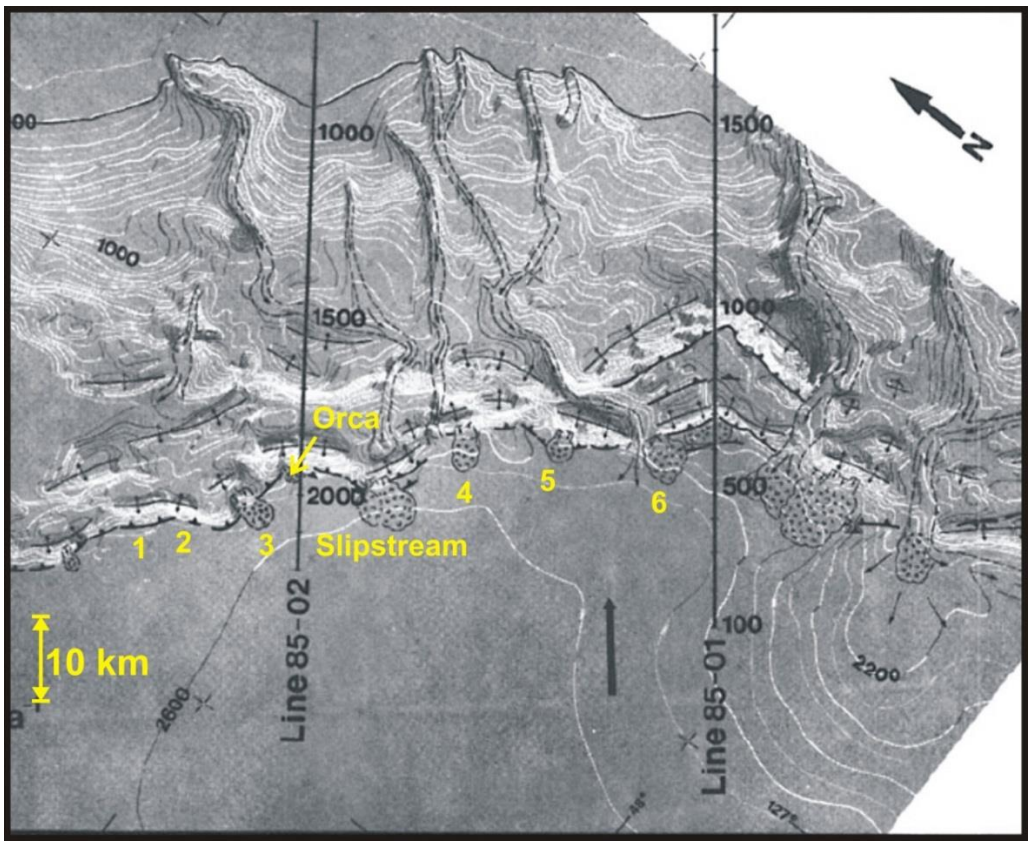


**Figure 8.3**: SeaMARC II image of the remaining slides (modified from Davis and Hyndman, 1989)

The side-scan sonar proved to be capable of better depicting the run-out of the finer slide material (Fig. 8.4b) at Slipstream Ridge compared to the multi-beam swath-bathymetry in Fig. 2.1. The deposition of finer, suspended material is usually the consequence of the transition of a denser slump into a turbidity current due to flow turbulence. Turbidity currents are capable of traveling farther than slides and slumps, which explains the approximate doubling of the run-out length at Slipstream Slide observed in the sidescan image (Fig. 8.4b) compared to the swath bathymetry image (e.g. Mulder and Cochonat, 1996; Iverson, 1997).

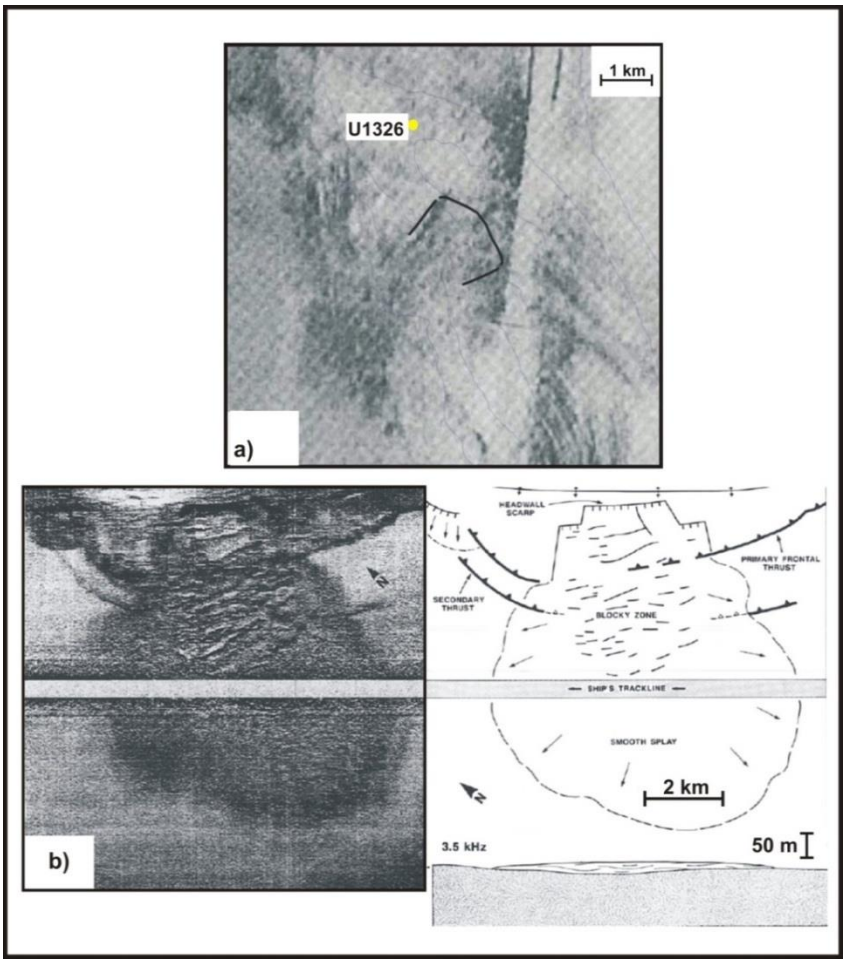


**Figure 8.4**: SeaMARC II side-scan sonar images and their interpretation: (a) Orca Slide (adapted from Lopez, 2007) and (b) Slipstream Slide (adapted from Davis and Hyndman, 1989)

Table 8.2 summarizes the input parameters for each slide along the northern Cascadia margin based on the observed run-out in Fig. 8.3. The values for initial length *l* as seen in Table 8.2 are based on the previous study by Naegeli (2010). Slide thickness *h* was derived by taking the difference in depths between profiles of the failure plane and the intact ridge adjacent to the failure plane. The run-out is estimated from observations in Figs. 8.3 and 8.4. Due to the low resolution of the side-scan sonar image (ca. 100 m x 100 m) and potential measuring errors, an uncertainty of ± 0.5 km is assigned to all estimated run-out distances.

| Slide | l(m) | h(m) | Estimated run-out (km) | #Nodes |
|---|---|---|---|---|
| Orca | 2500 | 250 | 5.0 ± 0.5 | 60 |
| Slipstream (1) | 2200 | 150 | 4.5 ± 0.5 | 120 |
| Slipstream (2) | 2200 | 150 | 9.0 ± 0.5 | 120 |
| 1 | 2300 | 50 | 4.5 ± 0.5 | 60 |
| 2 | 1600 | 200 | 3.8 ± 0.5 | 80 |
| 3 | 1500 | 150 | 5.7 ± 0.5 | 100 |
| 4 | 700 | 75 | 5.5 ± 0.5 | 60 |
| 5 | 2300 | 150 | 4.1 ± 0.5 | 130 |
| 6 | 1500 | 140 | 6.0 ± 0.5 | 100 |

**Table 8.2**: Input parameters used for each slide; parameter values are derived from Table 2.1 and Figs. 8.3 and 8.4; slide numbers refer to Fig. 8.3; the two cases are used for Slipstream Slide and refer to the run-out distances of the coherent (1) and the suspended material (2). Yellow highlighting indicates debris flow slides, while red highlighting indicates blocky slides

A first estimate of yield strength values for this region can be derived from slope angles in the depositional area and from the deposit thickness *H* (Marr et al., 2002):

$$\tau_y = (\rho_s - \rho_w) * g * H * sin\alpha_d \quad (8.11)$$

where $\tau_y$ is the yield strength and $\alpha_d$ is the slope angle where the slide came to rest.

Slope angles in the depositional area can be derived from Fig. 2.3 but the deposit thickness still has to be estimated. Although no specific values for deposit thickness can be determined, the 3D and acoustic images in Fig. 8.5 show the relation of the deposit to the total ridge height.

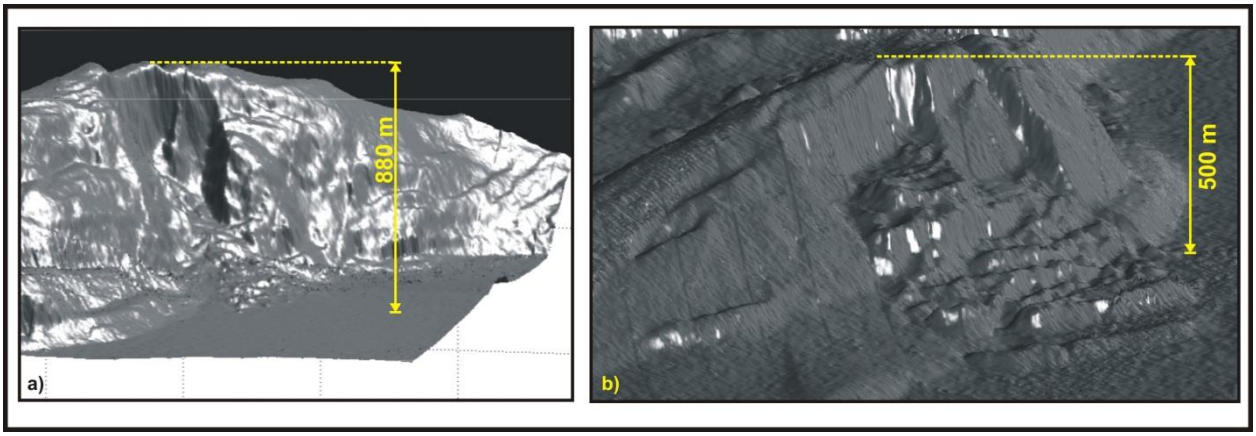


**Figure 8.5**: Bathymetry images indicating scale of deposit relative to total ridge height of a) Orca and b) Slipstream Slide

The remains of Orca Slide and the blocky deposits of Slipstream Slide can be estimated to be at least of the order of several tens of meters thick.

Using equation 8.11, the observed slope angles in Fig. 2.3 and a range of deposit thicknesses from 10 m to 100 m, the respective yield strength values are estimated (Fig. 8.6).

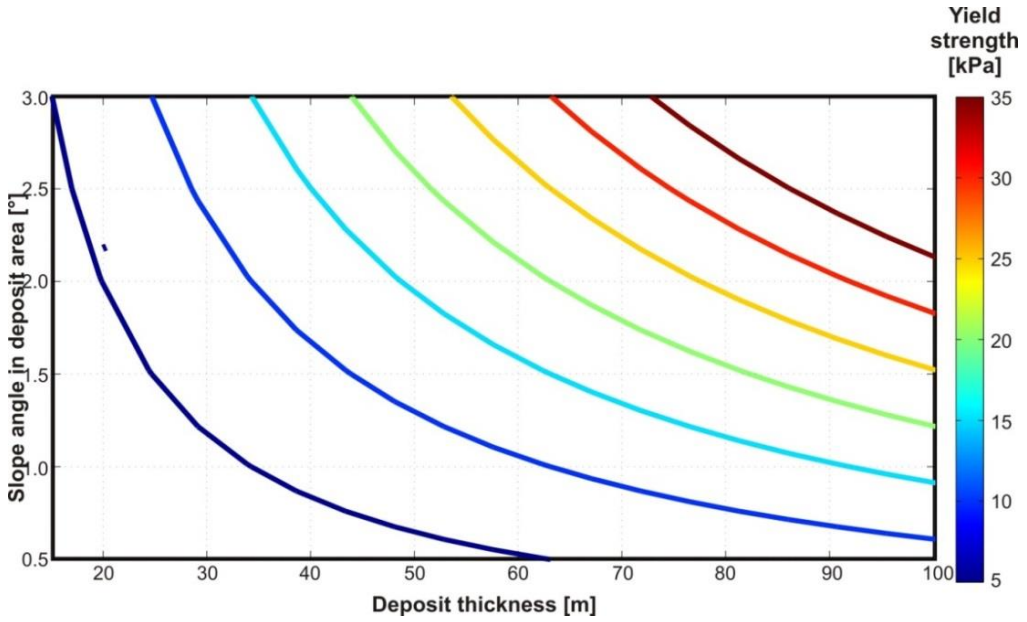


**Figure 8.6**: Estimated yield strength values as a function of slope angle and deposit thickness

Fig. 8.6 shows that, as deposits observed within the relatively short run-out interval as seen in Figs. 8.4 and 8.5 are fairly thick, yield strengths of up to several kPa might have to be assumed tor the model the run-out.

In the following, run-out length, deposit thickness, and slide velocity are calculated using the parameter values summarized in Tables 8.1 and 8.2 to find the yield strength value that leads to results closely matching the observed run-outs in Figs. 8.3 and 8.4.

### 8.3.1 Orca and Slipstream Slide

To model the run-out of Orca and Slipstream Slide the post-failure seafloor geometry as seen in Fig. 7.5 is used as input. For Slipstream Slide two cases are considered: 1) a run-out not including the fine material and 2) the run-out that includes the fines (Fig. 8.4b).

Table 8.3 summarizes the yield strength as well as the range in yield strengths that have to be assumed to replicate estimated run-out lengths within its error bounds. The table also contains the average and peak velocity as well as the average deposit thickness that result from the model.

| Slide | Yield Strength [kPa] | Uncertainty in yield strength [kPa] | Average frontal velocity [m/s] | Peak frontal velocity [m/s] | Average deposit thickness [m] |
|---|---|---|---|---|---|
| Slipstream (1) | 27.0 | -4.5 / +7.0 | 7.5 | 60. 9 | 33.3 |
| Slipstream (2) | 7.5 | ±0.8 | 29.0 | 77.1 | 16.9 |
| Orca | 52.0 | -8.0 / +12.0 | 8.3 | 41.6 | 78.1 |

**Table 8.3**: Yield strength values assumed during slide simulation to match observed run-out at Orca and Slipstream Slide; uncertainty in yield strength is based on uncertainty in estimated run-out

Although run-out for case 1 of Slipstream Slide is comparable to that of Orca Slide, a lower yield strength is needed to model the run-out of Slipstream Slide (Table 8.3 and Fig. 8.7a).

Sediment strength for Slipstream Slide ranges between 22.5 kPa and 34.0 kPa for the shorter run-out and between 6.7 kPa and 8.3 kPa for the longer run-out. In contrast, assigned yield strength values at Orca lie between 44 kPa and 64 kPa. The considerable differences in between assumed yield strength are likely due to the differences in the initial geometry between both slides.

Average deposit thicknesses of 72 m to 87 m are estimated for Orca Ridge. The results for Slipstream Ridge are markedly lower, ranging from about 30 m to 37 m in case (1) and from 16 m to 18 m in case (2) (Table 8.3).

Fig. 8.7 shows the resulting deposit geometry and slide velocity for each slide.

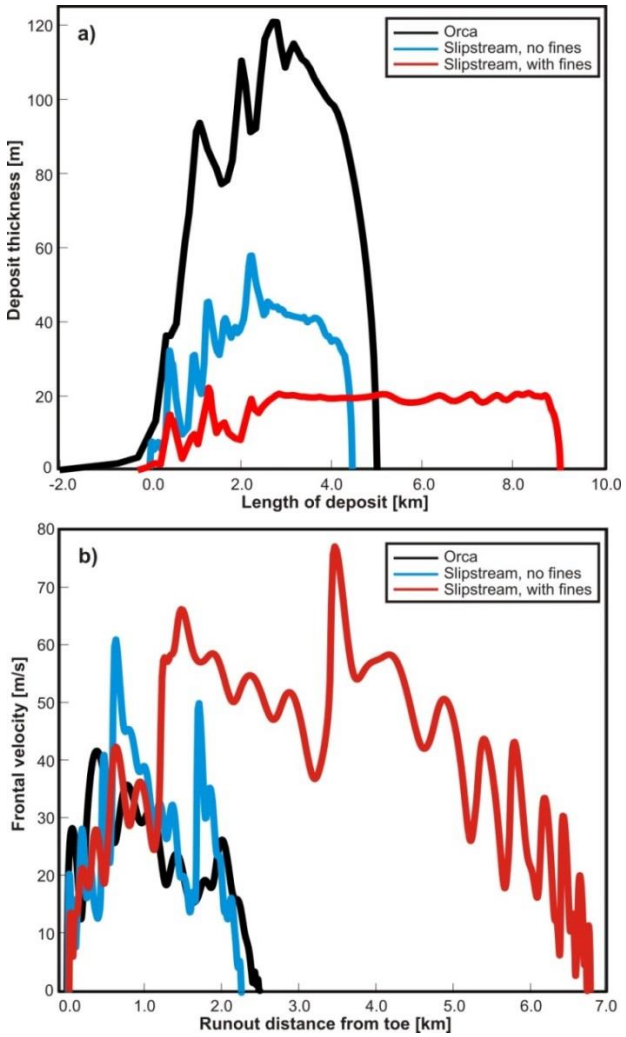


**Figure 8.7**: BING results for Orca and Slipstream: a) deposit thickness, b) frontal velocity with run-out; Slipstream results are for run-outs including (red) and excluding (blue) fines

The results calculated with BING suggest widely different slide velocities and configurations of the deposit. According to Fig. 8.7a, deposit geometry changes from parabolic to rectangular with decreasing yield strength. The deposit of Orca Slide is more than twice as thick as case (1) for Slipstream Slide.

Negative run-out distances at Orca and Slipstream Slide in Fig. 8.7a are likely due to the strong slope gradients in the parabolic shape of the initial slide geometry exceeding the ones of the sliding plane resulting in a net force directed upslope (Skvortsov, 2005).

Fig. 8.7b depicts the evolution of the frontal velocity throughout the slide process. The slides initially accelerate to their first peak values within the first 2 km of the movement. The repeated acceleration and deceleration of each slide-case visible in Fig. 8.7b suggests a surge-like movement of the slide.

The peak velocity at Orca Slide lies at about 42 m/s. Slipstream Slide seems to have higher velocities with the highest values lying between 61 m/s and 77 m/s in case (1) and (2), respectively. Greater sliding velocities are most likely due to the lower assumed yield strength but could also be in part due to steeper headwall slope angles observed at Slipstream Ridge (Fig. 7.5b). Unlike Orca Slide, Slipstream Slide shows two distinct velocity peaks during sliding. This is especially visible for a lower yield strength where the later velocity peak is higher than the first (blue line in Fig. 8.7b) which more likely is a numerical artifact rather than a second phase of slide acceleration.

### 8.3.2 Remaining slides

Chapter 2 described the variation of slide mechanism with ridge geometry and orientation (Fig. 2.2). To look for a correlation of yield strength with slide mechanism, the remaining slides along the northern Cascadia margin (Table 2.1) were also modeled using the input parameters in

Table 8.2. The resulting peak and average frontal velocities, average deposit thicknesses, and corresponding ranges in yield strengths for each slide are summarized in Table 8.4.

| Slide | Yield Strength [kPa] | Uncertainty in yield strength [kPa] | Average frontal velocity [m/s] | Peak frontal velocity [m/s] | Average deposit thickness [m] |
|---|---|---|---|---|---|
| **1** | 9.7 | -1.5 / +3.3 | 7.50 | 63.66 | 17.73 |
| **2** | 78.0 | -15.0 / +22.0 | 18.15 | 55.59 | 58.79 |
| **3** | 13.8 | -2.0 / +2.7 | 13.89 | 65.13 | 24.69 |
| **4** | 4.8 | -0.6 / +0.9 | 31.92 | 56.02 | 7.20 |
| **5** | 87 | -17.0 / +21.0 | 14.07 | 57.36 | 80.04 |
| **6** | 7.0 | -0.9 / +1.5 | 22.75 | 57.98 | 23.10 |

**Table 8.4**: Applied yield strengths and their uncertainty for the remaining slides in Fig. 8.3; results for blocky slides given in pink, results for debris flows given in yellow; uncertainty in yield strength is based on uncertainty in estimated run-out (Table 8.2)

Velocity and final slide thickness in Table 8.4 are of a similar order compared to Orca and Slipstream Slide. However, the values of the peak velocities of both debris flows and blocky slides show very little variation.

Fig. 8.8 shows the range in yield strengths for each slide along the northern Cascadia margin. Similar to Orca and Slipstream Slide and running counter to intuition, yield strength values are consistently lower for blocky slides (Fig. 8.8). For blocky slides values range between 4.2 kPa and 34 kPa which is relatively close to what is expected from Fig. 8.6. Debris flows, in contrast, need significantly higher yield strengths to explain observed run-out distances and the range of values is also much larger as well. The high yield strengths, which vary between 44 kPa and 108 kPa, suggest that the sediments involved in debris flows have a higher resistance to failure and/or less internal deformation, opposite to what would be expected.

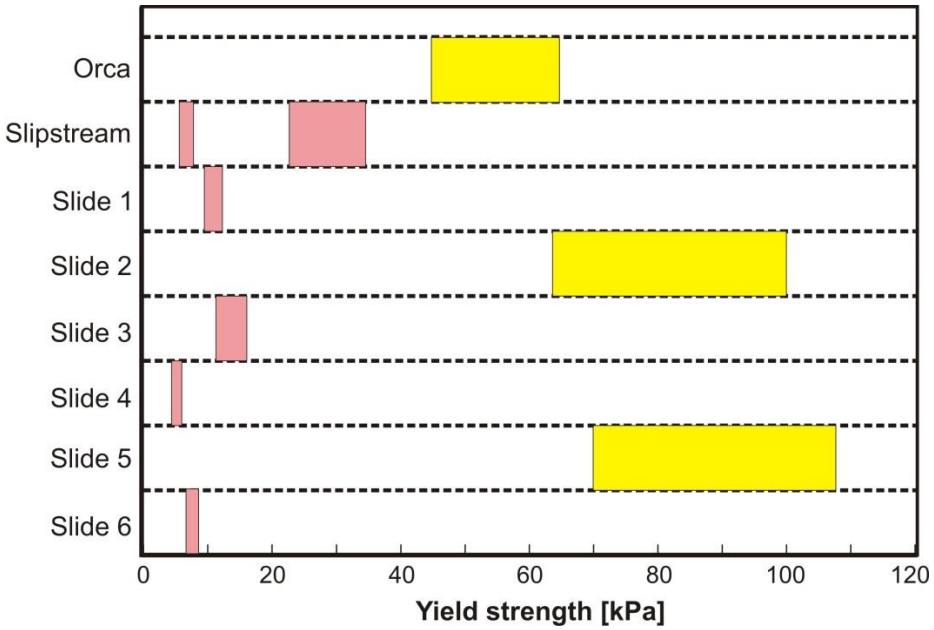


**Figure 8.8**: Range of yield strengths assumed in the modeling of all slides along northern Cascadia margin; yellow boxes: debris flows; pink boxes: blocky slides

## 8.4 Landslide-tsunamis and first-order wave height estimation from Orca and Slipstream Slide

The volume, vertical displacement and velocity of an underwater landslide represent three of the main controlling factors of tsunami generation. Large landslide masses moving at high velocities can lead to the conversion of a significant part of the potential energy into surface wave energy (Jiang and LeBlond, 1992). Tsunami amplitudes can range from close to zero to equal the vertical seafloor displacement of the slide (e.g. Murty, 1979). Both slides and slumps are able to generate tsunamis. For example, Prince William Sound in Alaska experienced local tsunamis in 1964 that were caused by underwater slides (Plafker et al., 1969), while the 1998 Papua New Guinea tsunami had an underwater slump as a source (Tappin et al., 2001).

Landslide-triggered tsunamis can be distinguished from earthquake-related tsunamis as they are more localized, have a more pronounced far-field directionality, and can produce significantly larger run-ups especially if the wave energy is trapped by coastal bathymetry such

as in bays, inlets or fjords (Jiang and LeBlond, 1992; Jiang and LeBlond, 1994; Tappin et al., 2001; Watts et al., 2001b; Fine et al., 2003; Fryer et al., 2004). Due to the substantial difference between the duration of an earthquake and the duration of a landslide, landslide-tsunamis also have much shorter periods (e.g. Watts et al., 2001a; Fryer et al., 2004).

Numerical models of landslide and tsunami propagation are commonly used to estimate the tsunamigenic potential of a submarine landslide (e.g. Liu and Mei 1989; Jiang and LeBlond, 1993; Skvortsov and Bornhold, 2007). The tsunami is generated due to a coupling between the slide material and the water column, an effect that has to be taken into account by the numerical models (Jiang and LeBlond 1992; 1994). According to Fine et al. (2003) the critical parameter in the generation of surface waves due to landslides is the ratio between the speed of the slide and the speed of the wave. If both velocities are the same a resonance effect can occur.

As BING produces results only in 2D, the output of the model cannot be used for tsunami modeling. Therefore, a first order estimation of landslide-generated tsunami wave heights is calculated with the help of a simple analytical theory based purely on slide geometry. Murty (1979) estimated wave heights resulting from a slide event in the Kitimat Inlet using a relationship that is based on work by Prins (1958), Wiegel (1964), and Striem and Miloh (1975). Instead of slide volume, Murty's calculation makes use of its center of mass. The main controlling factors are its dimensions, water depth, and density. A slide with a width $b$, a height $h$, and a length $l$ has a potential energy $E_p$ of:

$$E_P = g * l * b * h * (\rho_S - \rho_W) * (D_0 - D_S) \tag{8.12}$$

where $g$ is the gravitational acceleration, $\rho_s$ and $\rho_w$ are the densities of the slide and seawater, $D_0$ is the depth to the seafloor where the slide has come to rest and $D_s$ is the depth to the center of gravity of the slide. The energy per unit width of the crest of a solitary wave $E_W$ is then:

$$E_W = \frac{g\rho_W}{8(3)^{1/2}} * (H * D)^{3/2} \quad (8.13)$$

where *H* is the wave height, and *D* the depth to the sea-bottom. Equations 8.12 and 8.13 can then be used to calculate height *H* of the solitary wave:

$$H = \frac{1}{D}\left[8(3)^{1/2}\mu l h(\delta - 1)(D_0 - D_S)\right]^{2/3} \quad (8.14)$$

with $\delta = \rho_S/\rho_W$ and $\mu$ represents the fraction of the potential energy translated into wave energy, set to 0.01 according to Murty (1979).

If it is assumed that a slide causes more than one wave, equation 8.14 is written as:

$$H_m = H * m^{-2/3}; m = 2, 3, 4 \ldots. \quad (8.15)$$

Using equations 8.14 and 8.15 the wave height resulting from Orca Slide and Slipstream Slide were calculated using input values summarized in Table 8.5.

| Parameter | Orca Slide | Slipstream Slide |
|---|---|---|
| l(m) | 2500 | 2200 |
| h(m) | 250 | 100 |
| $D_0$(m) | 2600 | 2500 |
| $D_S$(m) | 2350 | 2100 |
| D(m) | 2500 | 2350 |
| $\rho_S$(kg/m$^3$) | 2.00 | 2.0 |
| $\rho_W$(kg/m$^3$) | 1.04 | 1.04 |
| m | 0.01 | 0.01 |

**Table 8.5**: Parameters for used in wave height estimation following Murty (1979)

Resulting wave heights for both slides are seen in Fig. 8.9. The tsunami wave resulting from Orca Slide is 50% higher than for Slipstream Slide which is mainly due to the difference in slide thickness.

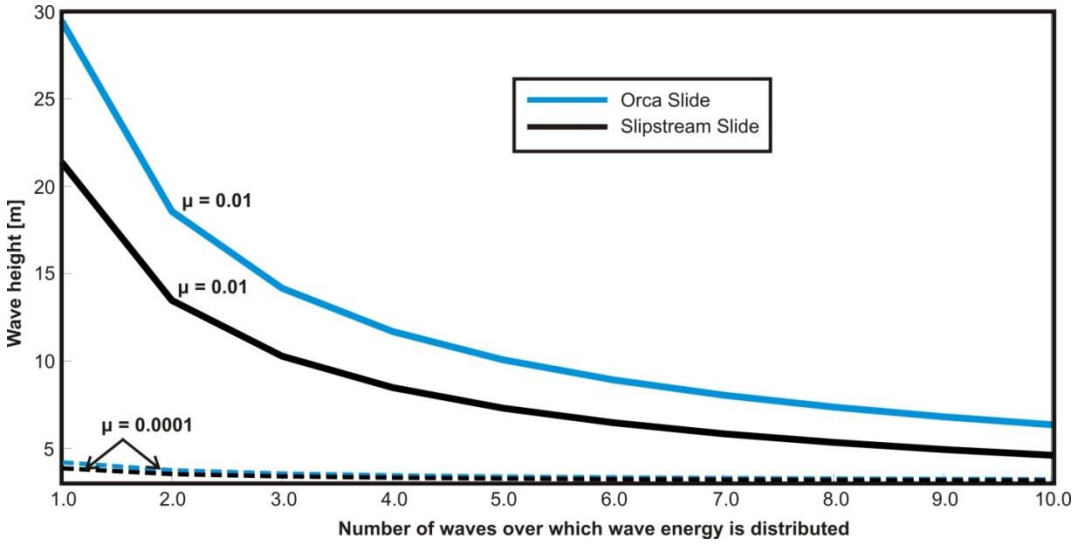


**Figure 8.9**: Murty Modeling results for tsunami wave height for Orca Slide (blue) and Slipstream Slide (black); for comparison results for a fraction of converted energy $\mu$ 100 times smaller than assumed by Murty (1979) shown as dashed lines

According to Fig. 8.9, solitary waves triggered by Orca and Slipstream Slide would reach heights of 29.5 m and 21.4 m, respectively. If the energy is distributed over ten waves the calculated wave heights for each slide are 6.3 m and 4.6 m which is still substantial (Fig. 8.9). For comparison, McAdoo et al. (2004) estimated potential wave heights for slides of similar size and at similar water depths offshore the Oregon coast to be of the order of 1.0 m or smaller. The results were derived from the morphology of the failure in combination with empirical equations for tsunami wavelength and maximum tsunami amplitude. The landslide-tsunami following the Papua New Guinea earthquake had comparable wave amplitudes to the ones depicted in Fig. 8.9. However, the volume of the landslide has been estimated to have been several tens of cubic kilometers with a headwall located at a water depth less than 1 km (e.g. Synolakis et al., 2002). Fig. 8.9 also shows the results for a fraction of converted energy $\mu$ 100 times smaller than suggested by Murty (1979). Assuming a significantly smaller amount of converted wave energy resulting wave heights are much more realistic ranging between 0.3 and 1.4 m for Orca Slide and between 0.2 and 1.0 m for Slipstream Ridge.

## 8.5 Discussion

In this chapter, the slide process has been modeled using the 2D finite-difference software BING. Focus lay on the reproduction of observed run-out distances and the estimation of the yield strength to derive an explanation for the contrasting slide mechanisms. Differences in run-out characteristics can either be due to differences in the initial volume, in the rheological properties, or in the flow mechanics. Naegeli's (2010) showed that the slide volumes of debris flows and blocky slides are similar, ruling initial volume out as a significant factor.

Differences in the assumed yield strength between both debris flows and blocky slides are more striking (Fig. 8.8.). Yield strength was constrained using observed slide run-out and estimated deposit thickness. For Orca and Slipstream Slide yield strengths ranging between 44 kPa and 64 kPa and between 7 kPa and 34 kPa best reproduce observated run-out lengths. Similar and even higher values have to be used for the remaining slides along the northern Cascadia margin. High yield strength values of this magnitude are generally not unrealistic. Debris flows at the Bear Island and Isfjorden fans offshore Svalbard were reported to contain sediments with yield strengths between 5 kPa and 25 kPa (Marr et al., 2002), Skvortsov (2005) mentioned values of up to 40 kPa for the Kitimat Slide, and laboratory tests on cores retrieved from the Lesser Antilles forearc accretionary prism resulted in estimates between 43 kPa and 384 kPa (Moran and Christian, 1990). Talling (2013) noted that high sediment strengths are found amongst debris flows rich in the occurrence of clasts such as in the Grand Banks Slide. Cores taken at Slipstream Ridge revealed the existence of a lithologic unit containing several clasts that could at least in part be an explanation for high sediment strengths in this region (Expedition Scientists, 2008). Talling (2013) further mentioned that high yield strengths could be the result of seismic sediment strengthening due to repeated earthquake shaking (Lee et al., 2004; Nelson et

al., 2011). This has previously been suggested for mass transport deposits in the Gulf of Alaska (Reece et al., 2010) and along the Western United States (Nelson et al., 2012).

The necessity to assume very high yield strengths for debris flows, however, is counter-intuitive. Lower yield strengths and more extensive internal deformation would be expected for debris flows which are by definition higher in fluid content (e.g. Mulder and Cochonat, 1996). The explanation for these observations lies most likely in the various shortcomings of BING. BING models the slides as two-dimensional objects. However, as seen in Table 2.1, blocky slide masses are broader than those of debris flows. Treating both only in 2D underestimates the actual amounted of material involved in blocky slides. No input of information about grain size variations, differences in density, or contrasts in sedimentology is possible, making BING too simplistic to model submarine landslides offshore Vancouver Island. As mentioned in Chapter 2, sediments at Orca and Slipstream Ridge consist of alternating layers of sand and clay, and are of a variety of grain sizes (Expedition Scientists, 2008). Therefore, more rigorous modeling techniques such as FEM and CFD are required to simulate the slide material in its complexity and to fully capture the evolution of the slides.

Alternatively, higher yield strengths for debris flows, as suggested by the BING results, could be a realistic phenomenon. Sediments at Orca Ridge and the ridges parallel to it might indeed have been more resistant to failure but could have undergone liquefaction due to strong earthquake shaking. Lower yield strengths in turn, could explain why liquefaction did not occur on ridges with blocky slides. More information on sediment composition and strength properties will have to be acquired in order to see if high yield strengths are unrealistic or if sediment intermixing and fluid entrainment might have played a significant role during the slide initiation and propagation.

Although there are no clear constraints on the scale of the deposits, deposit thicknesses of the order of several tens of meters can be deemed reasonable judged from 3D images of the ridges (Fig. 8.5). However, the significant difference in deposit thickness between Orca and Slipstream Slide is likely biased. As BING is a 2D-model, it is not possible to account for the fact that Slipstream Slide actually has a slightly larger volume (Table 2.1) compared to Orca Slide. Deposit thickness should therefore not be expected to differ as strongly as suggested by the BING results.

The calculated peak velocities (Tables 8.3 and 8.4) range between 41 m/s and 77 m/s and are likely too high. The overestimation of slide velocities by the BING model has already been observed elsewhere (Remaître et al., 2005). However, average velocities might be slightly more realistic. De Blasio et al. (2004), for example, reported velocities of 20 m/s to 50 m/s for landslides offshore Norway, similar to the velocities estimated for the Currituck slide (Locat et al., 2009). The Kitimat slide moved downslope with a maximum speed of ~25 m/s (Thomson et al., 2012), the speed of the Grand Banks Slide was estimated to be between 17 m/s and 28 m/s (Evans, 2001), and the Storegga Slide is thought to have had a maximum speed of 60 m/s (Haflidason et al., 2004; Bryn et al., 2005; Kvalstad et al., 2005).

Initial accelerations are high as peak velocities are reached shortly after the mass movement started. This is an important result as high initial accelerations are seen as a crucial factor in tsunami generation (Watts et al., 2005). The surge-like movement indicated in the calculated frontal velocity (Figs. 8.7b) matches previous observations of debris flow behaviour (e.g. Iverson, 1997) and might be the cause of the separation of the sediment blocks during Slipstream Slide (Fig. 8.5b). Although initial accelerations seem to be high, velocities for any of

the slides offshore Vancouver Island are likely far too low for tsunami generation which requires slide velocities at least close to those of a tsunami wave (e.g. Fine et al., 2003).

If yield strength (Fig. 8.8) is an additional parameter that varies with ridge orientation or not, the pattern in morphology observed along the northern Cascadia margin still suggests some sort of structural control on the dimensions and physics of the slides. A possible explanation is that blocky slides have a shallower gliding plane and thus might fail along only one stratigraphic boundary, whereas several stratigraphic layers might be involved in the failure of debris flows. Debris flows would therefore involve deeper, more consolidated and therefore stronger material which in turn would also explain the slightly steeper slope angles of the failure scar (Table 2.1). Steep slope angles in the failure scar have been found to be associated with shorter run-outs with deposits that are more broadly spread out (i.e. McAdoo et al., 2000).

Another possible reason for the differences in morphology could be that failure is fault-controlled. For example, faults detected at Orca Ridge (Lopez, 2007) are likely not parallel to each other but converge towards the toe of the ridge and could promote the intermixing of the slide material, leading to fluid entrainment. The ridges which failed as blocky slides have rectangular failure planes (Fig. 2.2) and therefore might have faults and fractures parallel to the ridge-strike. The failure along parallel faults and fractures could prevent the sediments from mixing or fluid entrainment, leading to more coherent deposits.

Apart from ridge sedimentology and stratigraphic control, ridge orientation relative to the predominant tectonic forces likely had a strong influence on the slide morphology. The nature of the zigzag formation of the frontal ridges has not been fully explained but might be a consequence of complex relative motions between the different tectonic plates in this area. However, observations of corresponding faults and offsets in between the ridges are lacking. The

only indication of a local tectonic influence comes from two extensional faults seaward of Slipstream Ridge and to the NW of Orca Ridge (Fig. 2.3). Both faults strike sub-parallel to the orientation of Slipstream Ridge. When compared to magnetic data from this region it is found that these faults are approximately parallel to the magnetic stripes on the seafloor which stem from the seafloor-spreading at the Juan de Fuca Ridge. Therefore the orientation of Slipstream Ridge and the ridges parallel to it might be controlled by the movement of the Juan de Fuca plate.

Finding an explanation for the rotated orientation of the remaining ridges is more difficult. A possible cause is the change in subduction direction from northwestwards to approximately westwards, producing a large bend in the subducting slab (Fig. 1.6). An outward bending of the subducting plate could induce tensile stresses in the overlying crust leading to a break up of sediments in between the ridges.

Several studies have reported the complexity of the plate system in this region which could at least in part be responsible for the clockwise rotation of some of the ridges. Margin-normal forces additional to the subduction-induced horizontal compression could explain why the ridges that face northwestward are bent into an arcuate shape and are higher compared to the ridges facing southwestwards. Observations of some studies might support the existence of margin-normal forces. For example, Currie et al. (2001) studied shear-wave splitting along the Cascadia margin and found signs for margin-normal compression (see Fig. 4a in Currie et al., 2001). Mazzotti et al. (2003) suggested that the Explorer Plate might subduct at a slower rate compared to the Juan de Fuca Plate. This might lead to the rotation and deformation of the frontal ridges due to the strains resulting from the relative movement between Explorer and Juan

de Fuca Plate. However, the Nootka Fault which separates the Explorer from the Juan de Fuca Plate might be too far away for the relative movement to still have a significant influence.

Audet et al. (2008) found that the zigzag shape of the frontal ridge alignment approximately coincides with negative velocity anomalies. The authors attribute the anomalies to lateral differences in slab buoyancy and the resulting changes in the depths of the subducting slab might in turn lead to tensile stresses in the overlying crust.

Furthermore, margin-parallel deformation could also be due to the previous subduction or the underplating of seafloor ridges or seamounts (e.g. Groome et al., 2003; Audet et al., 2008; Groome and Thorkelson, 2009). Among the possible effects are changes in rheological behavior, strain localization, and thermal weakening, all of which would support the deformation of the ridge alignment due to ridge subduction (Groome and Thorkelson, 2009).

No conclusions on the cause for the variability in ridge orientation can be made and more data are needed to test the different hypotheses. More extensive modeling is needed to better understand slide morphology and slide dynamics offshore Vancouver Island. Results above suggest that yield strength is an important factor in the slide mechanism. Yield strength is also an important input for a slope stability analysis as it represents a threshold for slide initiation. The higher the yield strength the less likely a trigger mechanism can lead to a landslide. In cases where a landslide is triggered, high yield strengths prevent the slide material from traveling large distances.

Tsunami wave heights resulting from Orca and Slipstream Slide are estimated using a simple analytical relationship but results are found to be unrealistic. Murty's model (1979) is likely too simplistic as important parameters such as the slide area, seafloor bathymetry, slide rheology and the complex interaction between waves are all not accounted for (Skvortsov and

Bornhold, 2007). The parameter $\mu$ which represents the fraction of the potential energy converted into wave energy has a significant influence on the outcome. Judging from the overestimated wave heights for Orca and Slipstream Ridge, $\mu$ should be much smaller than 0.01 while reducing $\mu$ to 0.0001 leads to much more realistic wave heights. Additionally, there is probably too little weight given to the influence of the approximately 2 km high water column overlying both ridges. Tsunami waves triggered by slides offshore Oregon that are comparable in size to Orca and Slipstream Slide have been estimated to be barely reach heights of 1.0 m (Marr et al., 2002). Tsunami waves with amplitudes of less than one meter would probably not have had a significant impact on the coast of Vancouver Island. However, to confirm this assumption more rigorous modeling techniques are required. Such methods should be capable of simulating slide propagation in 3D and include information of the surrounding bathymetry and the shape of the coast line.

# Chapter 9: THESIS SUMMARY AND CONCLUSIONS

In this dissertation the first slope failure analysis offshore the west coast of Vancouver Island has been conducted. Multi-beam swath bathymetry along the margin revealed that the occurrence of slope failure is largely confined to a system of frontal ridges situated close to the deformation front of the northern Cascadia subduction zone, directly above the local gas hydrate system. To investigate the nature of slope failure along the northern Cascadia margin, the impact of pore pressure and earthquake shaking on slide initiation and the influences on slide motion were studied as well as on the possible link between hydrates and slope failure. Orca and Slipstream Slide were studied in detail as they represent the two morphological end-members along the margin. Slide morphology was found to either resemble a debris flow or a blocky slide depending on the orientation in which the frontal ridges are facing suggesting some kind of structural or tectonic control of slope failure.

Critical taper theory predicted that the continental slope is in a stable condition. However, results also showed that large parts of the toe of the continental slope could be prone to failure. As most of these regions have so far remained intact critical taper theory likely underestimates slope stability on smaller scales. Therefore, a limit equilibrium factor of safety (FS) analysis was used to improve the stability estimate and to find the threshold values for excess pore pressure and earthquake acceleration in this region.

The ridge slopes were found to be especially sensitive to overpressure and peak ground accelerations of the order of 0.58 g and higher are needed to induce failure. Expected earthquake ground accelerations were estimated using previously developed ground motion attenuation relationships (GMARs). Results show that a nearby M8.0 crustal earthquake would produce the

highest horizontal ground accelerations of ~0.38 g which is still substantially lower than critical accelerations. However, if the lack in seismicity observed in Fig. 4.1a is the result of an aseismic gap, crustal earthquake sources might actually be located several tens of kilometers away and therefore have or have had a minor influence on ridge stability. Subduction zone earthquakes are expected to cause accelerations lower than 0.3 g at the Orca and Slipstream ridges due to their distance to the updip limit of the seismogenic zone situated about 40 km further landward.

Due to the inherent limitations of GMARs and the lack of knowledge on the behaviour of fluid-saturated sediments during earthquake shaking, the power spectral density (PSD) of OBS-measured ground motion was used to characterize ground-motion. Measured 'noise' spectra were compared to the spectra recorded during six tele-seismic events to partially overcome the lack of a reference site. Due to the lack of a reference spectrum only the differences in the amplitude of the PSD relative to a site's peak response could be evaluated. At most sites along the northern Cascadia margin the strongest ground response was found to mostly occur at frequencies around 2 Hz. The crest of Slipstream Ridge however, appeared to be more sensitive to a slightly higher frequency. Furthermore, the east-component of the OBS appeared to be more sensitive to the incoming seismic waves than the north- or the vertical component suggesting that ridge topography could increase susceptibility to earthquake-related slope failure.

Pore pressure estimates along the margin were derived from log-density data and found to be comparable to the critical overpressure derived from the FS analysis. The lowest overpressure ratios were calculated at Site U1326 which is located on the crest of Orca Ridge close to the head scar of Orca Slide. A clear contrast was observed between pore pressure within the 100 m thick interval above the BSR and pore pressure below, suggesting the BSR may have provided a zone of weakness during the failure of Orca Ridge.

Pore-pressure-related slope failure is further supported by the coincidence of increased rates in sea-level rise with the estimated timing of slide initiation. To address the role of hydrates in regional slope failure, the location of the GHSZ boundaries during the time of failure was calculated. An increase in ocean-bottom water temperatures by ~2° C could have overprinted the effects of a rise in sea-level on the stabilization of gas hydrates leading to dissociation over a depth interval of 30-40 m. At Orca Ridge, the paleo-BSR approximately coincided with the present gliding plane, and the subsequent release of free gas and water along the BGHSZ at could have led the initiation of slope failure.

The size of the depth interval between paleo- and present-day BSR is further supported by the observation of an apparent double BSR in the seismic data beneath Slipstream Ridge. The two parallel reflectors have a spatial separation of ~32 m, approximately matching the estimated differences between BSR depths in the Holocene and at present.

In contrast to the BSR, the TGHOZ seemed to be more susceptible to pressure changes. The paleo-TGHOZ was found to have been 4-9 m shallower during the Holocene increasing from an initial depth of 48 mbsf and 47 mbsf at Orca Ridge and Slipstream Ridge, respectively. Sea-level rise could therefore have led to gas hydrate dissolution closer to the seafloor. This is an important result as in the case of Slipstream Ridge, the TGHOZ coincides with the headwall region of the failure scar.

For the BSR, as well as gas hydrate dissociation, to have played a role in slope failure, ocean bottom water warming should have occurred not later than 11 ka BP as it would take several thousand years for a warming pulse to reach the BSR. In contrast, the warming pulse would have reached the paleo-TGHOZ after only about 65 years. Thus, hydrate dissolution could have happened anytime between the beginning and the end of the slope failure period.

An upperbound estimate of hydrate-generated pore pressure revealed the crucial role of sediment permeability in the control of the amount and rate of pore pressure increase. A permeability of less than $10^{-17}$ $m^2$ was found to allow for the generation of critical overpressure values further supporting the role of excess pore in the triggering of Orca and Slipstream Slide.

Results of a slope failure simulation using the 2D finite-difference code BING suggested that differences in sediment strength in part control the occurrence of debris flows and blocky slides. To recreate observed run-out distances, high yield strength material had to be assumed. The yield strength values were found to correlate with slide mechanism and thus followed the pattern in slide morphology observed along the margin. For example, at Orca Slide a yield strength between 44 kPa and 64 kPa had to be assumed while the run-out distance of Slipstream Slide required the assumption of lower values between 7 kPa and 34 kPa. Similar yield strengths had to be chosen for the remaining six slides along the margin. This, however, lead to the counter-intuitive conclusion that debris flows involve stronger material than blocky slides and is likely the result of the inherent short-comings of the BING model. Alternatively, earthquake-induced liquefaction during slope failure caused by strong ground motions and a rapid rise in pore pressure could have decreased sediment strength and turned the sliding mass into a debris flow.

Modeling results also indicated that initial slide acceleration was high, which is an important factor in tsunami generation. A first order estimation of the wave height of a possible landslide-tsunami was calculated according to Murty (1979). Results are likely a gross overestimation of the height of tsunami waves generated by Orca and Slipstream Slide, especially when compared to previously reported wave heights. Therefore, more rigorous

modeling techniques have to be applied in order to test if Orca and Slipstream Slide were capable of generating significant disturbances of the sea surface.

Thus, slope failure at the Orca and Slipstream ridges was likely the result of a combination of several factors. Comparing the age of the slides, megathrust earthquakes are a frequent phenomenon offshore Vancouver Island and seismically triggered sliding could have happened during any other period of time. The observed sensitivity to overpressure suggests that the rapid increase in sea-level and sediment deposition near the end of the Holocene could have played a significant role in slide triggering. A shift in the hydrate stability boundaries could have led to hydrate dissolution at the top and hydrate dissociation at the bottom of the GHSZ. Thus, Orca Slide might have been caused by a pore pressure increase at the BSR, while Slipstream Slide could have been initiated at the ridge crest closer to the TGHOZ. The evolution of the Slipstream Slide was controlled by a stratigraphic contrast between two sediment layers whereas Orca Slide failed along near-vertical normal faults at the crest of the ridge. Initial strength properties of the sediments linked to the structure and tectonic history of each ridge then led to the occurrence of either blocky slides or debris flows.

**Recommendations regarding future work**

Several recommendations for future studies can be made based on the work that has been conducted as part of this dissertation.

- More knowledge is required regarding the type of sediment and its physical properties involved in slope failure. The behaviour of fully saturated, free-gas- or hydrate-bearing sediments under external forces has to be studied further. Laboratory tests would be needed to investigate sediment deformation and estimate properties such as drained and

un-drained shear strength, compressibility, and stress history. A better assessment of the internal friction angle would substantially increase the estimate of regional slope stability.

- The local and regional pore pressure regimes have to be studied more closely to estimate present-day slope stability and assess the possibility of concentrated overpressure beneath topographic highs or pressure-driven fluid flow that could lead to localized sediment-weakening. Geotechnical tests on sediment samples such as consolidation and dissipation tests or *in situ* pore pressure measurements would be required. Long-term observations (e.g. by using borehole observatories) are preferable in order to capture fluctuations in pore pressure. Hydraulic permeability is another critical parameter that has to be thoroughly quantified due to its influence on pore pressure and fluid flow as well as on gas hydrate distribution.
- A more satisfying assessment of the effects of earthquake shaking on submarine sediments requires the understanding the interaction between sediments and fluids as well as the transmission of seismic energy. This could be done via a combination of cyclic strength tests on sediment samples or by numerically simulating the material response.
- The influence of topography and substrata on ground shaking could be studied by calculating the H-V ratio of earthquake waves or with the help of 2D and 3D tomography and numerical methods.
- High-resolution as well as 3D seismic data acquisition could substantially increase the ability to study the recurrence of slumps and slides and the structural control on slope failure. High-resolution seismic data could reveal faults and fractures that could act as fluid conduits or simply represent weak points for future slope failure. Mapping existing

faults and fractures could also help to assess regional gas hydrate formation and distribution.

- Seismic data could also help to investigate the cause for the zig-zag shape of the ridges and if strike-slip or normal faults play a part in the rotation of the ridges (Kimura, 1986; Goldfinger et al., 2000). Additionally, GPS measurements could provide information about possible relative movement between ridges.
- A better understanding of the gas hydrate distribution as well as hydrate and free gas concentrations is important. Localized gas hydrate accumulation can point to increased fluid flux. Further data acquisition such as S-wave surveys and seafloor compliance could provide a better understanding of in-place gas hydrate as well as a measure of sediment rigidity (Willoughby et al., 2005; Spence et al., 2010).
- Albateineh et al. (2006) suggested more advanced alternatives to the Ordinary Method of Slices including the coupling of FS methods such as the ones developed by Janbu (1957; 1973) and Morgenstern and Price (Morgenstern and Price, 1965) with a Monte Carlo search. This would provide a means to account for variability in each parameter value. Furthermore, finite element methods (FEM) are also used in slope stability analysis. They do not include as many simplifying assumptions, deal much better with the geometry of a slope, and can incorporate changes in shear strength or end effects of the adjoining material (e.g. Albateineh, 2006; Eberhardt, 2008).
- The numerical modeling of submarine landslide and tsunami propagation should be done in 3D. More rigorous techniques such as the Discrete Element Method (DEM) or Computational Fluid Dynamics (CFD) are better suited to study slide behaviour and its effects on the surrounding body of water.

# Bibliography

Adkins J.F., McIntyre K., Schrag D.P., 2002, *The salinity, temperature and $\delta^{18}O$ of the glacial deep ocean*, Science, **298**, 1769–1773

Albateineh N., 2006, *Slope stability analysis using 2D and 3D methods*, MSc thesis, University of Akron, OH

Alexandrou A.N., Le Menn P., Georgiou G., Entov V., 2003, *Flow instabilities of Herschel-Bulkley fluids*, Journal of Non-Newtonian Fluid Mechanics, **116**, 19-32

Andreassen K., Mienert J., Bryn P., Singh S.C., 2000, *A double gas-hydrate related bottom-simulating reflector at the Norwegian continental margin*, Annals of the New York Academy of Science, **912**, 126-135

Arai M., Takahashi I., 1986, *The Karman constant of the flow laden with high sediment*, Proceedings of the 3rd International Symposium on River Sedimentation, University of Mississippi, 824-833

Ashford S., Sitar N., Lysmer J., Deng N., 1997, *Topographic effects on the seismic response of steep slopes*, Bulletin of the Seismological Society of America, **87**(3), 701–709

Athy L.F., 1930, *Density, porosity, and compaction of sedimentary rocks*, AAPG Bulletin, **14**, 1-24

Atkinson G.M., 2005, *Ground motions for earthquakes in southwestern British Columbia and northwestern Washington: crustal, in-slab, and offshore events*, Bulletin of the Seismological Society of America, **95**(3), 1027-1044

Atkinson G.M., Macias M., 2009, *Predicted ground motions for great interface earthquakes in the Cascadia subduction zone*, Bulletin of the Seismological Society of America, **99**(3), 1552-1578

Atkinson G.M., Goda K., 2011, *Effects of Seismicity Models and New Ground-Motion Prediction Equations on Seismic Hazard Assessment for Four Canadian Cities*, Bulletin of the Seismological Society of America, **101**(1), 176-189

Atwater B. F., Nelson A.A., Clague .J.J, Carver G.A., Yamaguchi D.K., Bobrowsky, P.T. et al., 1995, *Summary of coastal geologic evidence for past great earthquakes at the Cascadia subduction zone*, Earthquake Spectra, **11**, 1 – 18

Audet P., Bostock M.G., Mercier J.-P., Cassidy J.F., 2008, *Morphology of the Explorer-Juan de Fuca slab edge in northern Cascadia: Imaging plate capture at a ridge-trench-transform triple junction*, Geology, **36**, 895-898

Bagnold R.A., 1954, *Experiments in a gravity-free dispersion of large solid spheres in a Newtonian fluid under shear*, Proceedings of Royal Society of London, **A-225**, 49-63

Bangs N.L., Musgrave R.J., Tréhu A.M., 2005, *Upward shifts in the southern hydrate ridge gas hydrate stability zone following postglacial warming, offshore Oregon*, Journal of Geophysical Research, **110**, B03102, doi:1029/2004BJ003293

Bard P.-Y., Riepl-Thomas J., 2000, *Wave propagation in complex geological structures and their effects on strong ground motion*, In: Wave Motion in Earthquake Engineering, Kausel E. and Manolis G. (Eds.), WIT Press Southampton, Boston, 37-95

Bekins B.A., Dreiss S.J., 1992, *A simplified analysis of parameters controlling dewatering in accretionary prisms*, Earth and Planetary Science Letters, **109**, 275-287

Bethke C.M., 1989, *Modeling subsurface flow in sedimentary basins*, Geologische Rundschau, **78**(1), 129-154

Bishop A.W., 1955, *The use of the slip circle in the stability analysis of slopes*, Geotechnique, **5,** 7–17

Blum P., 1997, *Physical properties handbook: a guide to the shipboard measurement of physical properties of deep-sea cores*, ODP Technical Note, **26**

Bonnefoy-Claudet S., Cornou C., Bard P.-Y., Cotton F., Moczo P., Kristek J., Fäh D., 2006, *H/V ratio: a tool for site effects evaluation. Results from 1-D noise simulations*, Geophysical Journal International, **167**, 827-837

Boore D.M., 2003, *Simulation of ground motion using the stochastic method*, Pure and Applied Geophysics, **160**, 635-676

Boore D.M., Atkinson G.M., 2008, *Ground-motion prediction equations for the average horizontal component of PGC, PGV, and 5%-damped PSA at spectral periods between 0.01s and 10.0s*, Earthquake Spectra, **24**(1), 99-138

Bornhold B., Prior D., 1989, *Sediment blocks on the seafloor in British Columbia fjords*, Geo-Marine Letters, **9**, 135-144

Borowski W.S., Paull C.K., Ussler III W., 1996, *Marine pore-water sulphate profiles indicate in situ methane flux from underlying gas hydrate*, Geology, **24**, 655-658

Bouckuvalas G.D., Papadimitriou A.G., 2005, *Numerical evaluation of slope topography effects on seismic ground motion*, Soil Dynamics and Earthquake Engineering, **25**, 547-558

Brewer P.G., Paull C., Peltzer E.T., Ussler W., Rehder G., Friederich G., 2002, *Measurements of the fate of gas hydrates during transit through the ocean water column*, Geophysical Research Letters, **29**, doi:10.1029/2002GL014727

Bryn P., Berg K., Forsberg C.F., Solheim A., Kvalstad T.J., 2005, *Explaining the Storegga Slide*, Journal of Marine Geology, **22**, 11-19

Buffett B., Archer D., 2004, *Global inventory of methane clathrate: sensitivity to changes in the deep ocean*, Earth and Planetary Science Letters, **227**(3-4), 185-199

Bugge T., Belderson R.H., Kenyon N.H., 1988, *The Storegga Slide*, Philosophical Transactions of the Royal Society of London A., **325**, 357-388

Bull S., Cartwright J., Huuse M., 2008, *A review of kinematic indicators from mass-transport complexes using 3D seismic data*, Marine and Petroleum Geology, **26**, 1132-1151

Camerlenghi A., Urgeles R., Ercilla G., Brückmann W., 2007, *Scientific ocean drilling behind the assessment of geo-hazards from submarine landslides*, Scientific Drilling, **4**, 45-47

Campbell K.W., 2003, *Prediction of strong ground motion using the hybrid empirical method and its use in development of ground-motion (attenuation) relations in Eastern North America*, Bulletin of the Seismological Society of America, **93**, 1012–1033

Campbell K.W., Bozorgnia Y., 2003, *Updated near-source ground-motion (attenuation) relations for the horizontal and vertical components of peak ground acceleration and acceleration response spectra*, Bulletin of the Seismological Society of America, **93**(1), 314-331

Carpenter G., 1981, *Coincident sediment slump/clathrate complexes on the US Atlantic continental slope*, Geo-Marine Letters, **1**, 29– 32

Carracedo J.C., 1999, *Growth, structure, instability, and collapse of Canarian volcanoes and comparison with Hawaiian volcanoes*, Journal of Volcanology and Geothermal Research, **94,** 1–19

Carson B., Screaton E.J., 1998, *Fluid flow in accretionary prisms: Evidence for focused, time-variable discharge*, Review of Geophysics, **36** (3), 329-351

Celebi M., 1995, *Northridge (California) earthquake: Unique ground motions and resulting spectral and site effects*, In: Proceedings of the Fifth International Conference on Seismic Zonation, October 17-19, Nice, France, Ouest Edition Nantes, **II**, 988-995

Chand, S., Minshull T.A., Gei D, Carcione J., 2004, *Elastic velocity models for gas-hydrate-bearing sediments – a comparison*, Geophysical Journal International, **159**, 573–590

Chaouch A., Briaud J.-L., 1997, *Post melting behavior of gas hydrates in soft ocean sediments*, OTC-8298, 29th Offshore Technology Conference Proceedings, Geology, Earth Sciences and Environmental Factors, **1**, Society of Petroleum Engineers, 217– 224

Chapman N. R., Gettrust J. F., Walia R., Hannay D, Spence G. D., Wood W. T., Hyndman R.D., 2002, *High-resolution, deep-towed, multichannel seismic survey of deep-sea gas hydrates off western Canada*, Geophysics, **67**, 1038-1047

Chen, M.-A., 2006, *Northern Cascadia marine gas hydrate: Constraints from resistivity, velocity, and AVO*, M.Sc. thesis, University of Victoria

Chen M.-A., Riedel M., Hyndman R.D., Dosso S.E., 2007, *AVO inversion of BSRs in marine gas hydrate studies*, Geophysics, **72(**2), 31-43

Chevallier J., Tréhu A.M., Bangs N.L., Johnson J.E., Meyer H.J. 2006, *Seismic Sequence Stratigraphy and Tectonic Evolution of Southern Hydrate Ridge*, In: Tréhu A.M., Bohrmann G., Torres M.E., Colwell F.S. (Eds.), Proceedings of the Ocean Drilling Program, Scientific Results, **204**

Clague J.J., Bobrowsky, P.T., 1994, *Evidence for a large earthquake and tsunami 100-400 years ago on western Vancouver Island, British Columbia*, Quaternary Research, **41**, 176-184

Clague J.J., 1997, *Evidence for large earthquakes at the Cascadia Subduction Zone*, Reviews of Geophysics, **35(**4), 439-460, doi:10.1029/97RG00222

Clennel M.N., Hovland M., Booth J.S., Henry P., Winters W.J., 1999, *Formation of natural gas hydrates in marine sediments: 1. Conceptual model of gas hydrate growth conditioned by host sediment properties*, Journal of Geophysical Research, **104**(B10), 22,985-23,003

Clowes R.M., Brandon M.T., Green A.G., Yorath C.J., Brown A.S., Kanaswich E.R., Spencer C., 1987, *LITHOPROBE-southern Vancouver Island: Cenozoic subduction complex imaged by deep seismic reflection*, Canadian Journal of Earth Sciences, **24**, 247-255

Collett T.S., 2004, *Alaska North Slope Gas Hydrate Energy Resources*, USGS Open File Report 2004-1454

Collett T.S., Riedel M., Cochran J., Boswell R., Presley J., Kumar P., Sathe A.V., Sethi A., Lall M., Sibal V., and the NGHP Expedition 01 Scientists, 2008, *Indian National Gas Hydrate Program (NGHP) Expedition 01, Initial Report*, Directorate General of Hydrocarbons, Ministry of Petroleum and Natural Gas, India

Crutchley G.J., Geiger S., Pecher I.A., Gorman A.R., Zhu H., Henrys S.A., 2010, *The potential influence of shallow gas and gas hydrates on sea floor erosion of Rock Garden, an uplifted ridge offshore of New Zealand*, Geo-Marine Letters, DOI 10.1007/s00367-010-0186-y

Currie C.A., Cassidy J.F., Hyndman R.D., 2001, *A regional study of shear wave splitting above the Cascadia subduction zone: Margin-parallel crustal stress*, Geophysical Research Letters, **28**(4), 659-662

Dahlen F.A., 1984, *Noncohesive critical Coulomb wedges: an exact solution*, Journal of Geophysical Research, **89**, 10,125-10,133

Dahlen F.A., Suppe J., Davis D.M., 1984, *Mechanics of fold- and-thrust belts and accretionary wedges: Cohesive Coulomb theory*, Journal of Geophysical Research, **89**, 10,087-10,101

Daigle H., Dugan B., 2010, *Origin and evolution of fracture-hosted methane hydrate deposits*, Journal of Geophysical Research, **115**(B11), doi:10.1029/2010JB007492

Dan G., Sultan N., Savoye B., Deverchere J., Yelles K., 2009, *Quantifying the role of sandy–silty sediments in generating slope failures during earthquakes: example from the Algerian margin*, International Journal of Earth Sciences, **98**(4), 769-789

Davie M. K., Buffett B. A., 2001, *A numerical model for the formation of gas hydrate below the seafloor*, Journal of Geophysical Research, **106**, 497– 514

Davie M.K., Zatsepina O.Y., Buffett B.A., 2004, *Methane solubility in marine hydrate environments*, Journal of Marine Geology, **203**, 177-184

Davis D., Suppe J., Dahlen F.A., 1983, *Mechanics of Fold-and-Thrust Belts and Accretionary Wedges*, Journal of Geophysical Research, **88**(B2), 1153-1178

Davis E.E., Hyndman R.D., 1989, *Accretion and recent deformation of sediments along the northern Cascadia subduction zone*, Geological Society of America Bulletin, **101**, 1465-1480

Davis E.E., Hyndman R.D., Villinger H., 1990, *Rates of fluid expulsion across the northern Cascadia accretionary prism: Constraints from new heat flow and multichannel seismic reflection data*, Journal of Geophysical Research, **99**(B6), 8869-8889

Dawson A.G., Long D., Smith D.E., 1988, *The Storegga slides: evidence from eastern Scotland for a possible tsunami*, Journal of Marine Geology, **82,** 271–276

De Blasio F.V., Engvik L., Harbitz C.B., Elverhøi A., 2004, *Hydroplaning and submarine debris flows*, Journal of Geophysical Research., **109**, C01002, doi: 10.1029/2002JC001714

De Blasio F.V., Elverhøi A., Issler D., Harbitz C.B., Bryn P., Lien R., 2005, *On the dynamics of subaqueous clay rich gravity mass flows – the giant Storegga Slide, Norway*, Journal of Marine and Petroleum Geology, **22**, 179-186

Del Gaudio V., Pierri P., Wasowsky J., 2003, *An approach to timeprobabilistic evaluation of seismically induced landslide hazard*, Bulletin of the Seismological Society of America, **93,** 557–569

Delisle G., Beiersdorf H., Neben S., Steinmann D., 1998, *The geothermal field of the North Sulawesi accretionary wedge and a model on BSR migration in unstable depositional environments*, In: Gas hydrates: Relevance to World Margin Stability and Climate Change, Henriet J.-P. and Mienert J. (eds.), Geological Society, London, Special Publications, **137**, 267-274

Dent J.D., 1982, *A biviscous modified Bingham model of snow avalanche motion*, Ph.D. thesis, Montana State University, Bozeman

Dent J.D., Lang T.E., 1980, *Modeling of snow flow*, Journal of Glaciology, **26**(94), 131-140

Dickens G.R., O'Neil J. R., Rea D. K., Owen R. M., 1995, *Dissociation of oceanic methane hydrate as a cause of the carbon isotope excursion at the end of the Paleocene*, Paleoceanography, **10**, 965-971

Dillon W.P., Danforth W.W., Hutchinson D.R. et al., 1998, *Evidence of faulting related to dissociation of gas hydrate and release of methane off the southeastern United States*, Geological Society, London, Special Publications, **137**, 293-302

Donnadieu F., Merle O., Besson J.C., 2001, *Volcanic edifice stability during cryptodome intrusion*, Bulletin of Volcanology, **63,** 61–72

Dragert H., Hyndman R.D., Rogers G.C., Wang K., 1994, *Current deformation and the width of the seismogenic zone of the northern Cascadia subduction thrust*, Journal of Geophysical Research, **99**, 653-668

Dugan B., and Flemings P.B., 2000, *Overpressure and fluid flow in the New Jersey continental slope: Implications for slope failure and cold seeps*, Science, **289**, 288–291

Dugan B., Flemings P.B., 2002, *Fluid flow and stability of the US continental slope offshore New Jersey from the Pleistocene to present*, Geofluids, **2**, 137-146

Dugan B., 2003, *Hydrodynamics of the US mid-Atlantic continental slope, offshore New Jersey*, PhD dissertation, Pennsylvania State University

Dugan B., 2012, *A review of overpressure, flow focusing, and slope failure*, In Submarine mass movements and their consequences, Advances in Natural and Technological Hazard Research **31**, eds: Y. Yamada et al.

Duncan J.M., 1996, *State of the art: Limit equilibrium and finite-element analysis of slopes*, Journal of Geotechnical Engineering, **122**, 577-595

Dvorkin J., Nur A., 1993, *Rock physics for characterization of gas hydrates*, in: The future of energy gases, U.S. Geological Survey Professional paper 1570

Dvorkin J., Helgerud M.B., Waite W.F., Kirby S.H., Nur A., 2000, *Introduction to physical properties and elasticity models*, In: M.D. Max (eds.), Natural Gas Hydrate in Oceanic and Permafrost Environments, p. 245-260, Kluwer Academic

Eberhardt E., 2008, *29$^{th}$ Canadian Geotechnical Colloquium: The role of advanced numerical methods and geotechnical field measurements in understanding complex deep-seated rock slope failure mechanisms*, Canadian Geotechnical Journal, **45**, 484-510

Edwards R.N., 1997, *On the resource evaluation of marine gas hydrate deposits using a seafloor transient electric dipole-dipole method*, Geophysics, **62**, 63-74

Elverhøi A., Harbitz C.B., Dimakis P., Marr J., Mohrig D., Parker D., 2000, *On the dynamics of subaqueous debris flows*, Oceanography, **13**, 109-117

Erdik M., Durukal E., 2004, *Strong Ground Motion*, In: Recent Advances in Earthquake Geotechnical Engineering and Microzonation, A. Ansal (ed.), 67-100

Erismann T.H., Abele G., 2001, *Dynamics of Rockslides and Rockfalls*, p. 316 Springer, Berlin

Expedition Scientists 308, 2006, *Site U1319*, In: Flemings, P.B., Behrmann, J.H., John, C.M., and the Expedition 308 Scientists, *Proc. IODP*, **308**: College Station TX (Integrated Ocean Drilling Program Management International, Inc.)

Evans S.G., 2001, *Landslides*, In: Brooks, G.R. (Ed.), A Synthesis of Geological Hazards in Canada, Geological Survey of Canada, Bulletin **548**, 43– 79

Faccioli E., Vanini M., Frassine L., 2005, *"Complex" site effects in earthquake ground motion, including topography*, 12th European Conference on Earthquake Engineering, **88**

Fellenius W., 1936, *Calculation of the Stability of Earth Dams*, Transactions, 2nd International Congress on Large Darns, International Commission on Large Dams, Washington, DC, 445-459

Fine R.A., Millero F.J., 1973, *Compressibility of water as a function of temperature and pressure*, Journal of Chemical Physics, **59**(10), 5529-5536

Fine I.V., Rabinovich A.B., Thomson R.E., Kulikov E.A., 2003, *Numerical modeling of tsunami generation by submarine and subaerial landslides*, In: Submarine Landslides and Tsunamis, Yalçiner A.C., Pelinovsky E., Okal E., Synolakis C.E. (eds.), Kluwer Academic Publishers, 69-88

Fine I.V., Rabinovich A.B., Bornhold B.D., Thomson R.E., Kulikov E.A., 2005, *The Grand Banks landslide-generated tsunami of November 18, 1929: preliminary analysis and numerical modeling*, Journal of Marine Geology, **215**, 45-57

Fink C. R., Spence G. D., 1999, *Methane hydrate distribution offshore Vancouver Island from detailed single channel seismic reflection data*, Journal of Geophysical Research, **104**, 2909-2922

Flemings P.B., Stump B.B., Finkbeiner T., Zoback M., 2002, *Flow focusing in overpressured sandstones: Theory, observations, and applications*, American Journal of Science, **302**, 827-855

Flemings P.B., Liu X., Winters W.J., 2003, *Critical pressure and multiphase flow in Blake Ridge gas hydrates*, Geology, **31**(12), 1057-1060

Flemings P.B., Long H., Dugan B., Germaine J., John C.M., Behrmann J.H., Sawyer D., IODP Expedition 308 Scientists, 2008, *Pore pressure penetrometers document high overpressure near the seafloor where multiple submarine landslides have occurred on the continental slope, offshore Louisiana, Gulf of Mexico*, Earth and Planetary Science Letters, **269**, 309-325

Foucher J.-P., Nouzé H., Henry P., 2002, *Observation and tentative interpretation of a double BSR on the Nankai slope*, Journal of Marine Geology., **187**, 161–175

Frankel A., Mueller C., Barnhard T., Perkins D., Leyendecker E., Dickman N., Hanson S., Hopper M., 1996, *National seismic hazard maps*, U.S. Geological Survey, Open-file Rept. 96-53

Frankel A., Mueller C., Barnhard T., Perkins D., Leyendecker E., Dickman N., Hanson S., Hopper M., 1999, *National seismic hazard mapping project*, //http://geohazards.cr.usgs.gov

Fryer G.J., Watts P., Pratson L.F., 2004, *Source of the great tsunami of 1 April 1946: a landslide in the upper Aleutian forearc*, Journal of Marine Geology, **203**, 201-218

Ganguly N., Spence G.D., Chapman N.R., Hyndman R.D., 2000, *Heat flow variations from bottom simulating reflectors on the Cascadia margin*, Journal of Marine Geology, **164**, 53-68

Gauer P., Kvalstad T.J., Forsberg C.F., Bryn P., Berg K., 2005, *The last phase of the Storegga slide: simulation of retrogressive slide dynamics and comparison with slide-scar morphology*, Journal of Marine and Petroleum Geology, **22**, 171-178

Geli L., Bard P.-Y., Jullien B., 1998, *The effect of topography on earthquake ground motion: a review and new results*, Bulletin of the Seismological Society of America, **78**, 42-63

Gettrust G., Wood W., Lindwall D., Chapman N.R., Walia R., Hannay D., Louden K., MacDonald R., Spence G.D., Hyndman R.D., 1999, *New seismic study of deep sea gas hydrates results in greatly improved resolution*, EOS, **80**, 439-440

Gibson R.E., 1958, *The progress of consolidation in a clay layer increasing in thickness with time*, Geotéchnique, **8**, 171– 182

Gibson R.E., Schiffman R.L., Cargill K.W., 1981, *The theory of one-dimensional consolidation of saturated clays, 11. Finite nonlinear consolidation of thick homogeneous layers*, Canadian Geotechnical Journal, **18**, 280-293

Ginsburg G.D., Soloviev V.A., 1998, *Submarine Gas Hydrates*, St.-Petersburg

Goldberg D., Wilkins R.H., Moos D., 1986, *Seismic modeling of diagenetic effects in Cenozoic marine sediments, Deep Sea Drilling Project*, Initial Reports, **95**, 589-599

Goldfinger C., Kulm L.D., McNeill L.C., Watts P., 2000, *Super-scale failure of the Southern Oregon Cascadia margin*, Pure and Applied Geophysics, **157**, 1189-1226

Goldfinger C., Nelson C.H., Johnson J.J., et al., 2003, *Deep-water turbidites as Holocene earthquake proxies: the Cascadia subduction zone and North San Andreas Fault system*, Annals of Geophysics, **46**(5), 1169-1191

Golmshtok A.Y., Soloviev V.A., 2006, *Some remarks on the thermal nature of the double BSR*, Journal of Marine Geology, **229**, 187-198

Gregor N.J., Silva N.J., Wong I.G., Youngs R.R., 2002, *Ground-Motion Attenuation Relationships for Cascadia Subduction Zone Megathrust Earthquakes Based on a Stochastic Finite-Fault Model*, Bulletin of the Seismological Society of America, **92**(5), 1923–1932

Groome W.G., Thorkelson D.J., Friedman R.M., Mortensen J.K., Massey N.W.D., Marshall D.D., Layer P.W., 2003, *Magmatism and tectonic history of the Leech River Complex, Vancouver Island: evidence for ridge–trench intersection and accretion of the Crescent Terrane*, In: Sisson, V.B., Roeske, S.M., Pavlis, T.L. (Eds.), Geology of a Transpressional Orogen Developed During Ridge–Trench Interaction Along the North Pacific Margin, GSA Special Paper, **371**, 327–353

Groome W. G., Thorkelson D.J., 2009, *The three-dimensional thermo-mechanical signature of ridge subduction and slab window migration*, Tectonophysics, **464**, 70-83

Haacke, R. R., Westbrook G. K., 2006, *A fast, robust method for detecting and characterising azimuthal anisotropy with marine PS converted waves, and its application to the west Svalbard continental slope*, Geophysical Journal International, **167**, 1402–1412

Haflidason H., Sejrup H.P.,Nygård A.,Mienert J., Bryn P., Lien R., Forsberg C.F., Berg K., Masson D., 2004, *The Storegga slide: architecture, geometry and slide development*, Journal of Marine Geology, **213**, 201-234

Hamilton E.L., 1976, *Variations of density and porosity with depth in deep-sea sediments*, Journal of Sedimentary Petrology, **46**, 280-300

Hance J.J., 2003, *Submarine Slope Stability*, MSc Thesis, University of Texas, Austin

Handa Y.P., 1990, *Effect of hydrostatic pressure and salinity of the stability of gas hydrates*, Journal of Physical Chemistry, **94**, 2652-2657

Harbitz C.B., 1992, *Model simulations of tsunamis generated by the Storegga Slides*, Journal of Marine Geology, **105**, 1-21

Hart B.S., Flemings P.B., Deshpande A., 1995, *Porosity and pressure: role of compaction disequilibrium in the development of geopressures in a Gulf Coast Pleistocene basin*, Geology, **23**, 45-48

Heinrich P., 1992, *Nonlinear water waves generated by submarine and aerial landslides*, Journal of Waterways, Port, Coastal and Ocean Engineering, **118**(3), 249–266

Helgerud M. B., Dvorkin J., Nur A, Sakai A., Collett T., 1999, *Elastic-wave velocity in marine sediments with gas hydrates: Effective medium modeling*, Geophysical Research Letters, **26**, 2021–2024

Herschel W.H., Bulkley R., 1926, *Konsistenzmessungen von Gummi-Benzollösungen*, Kolloid Zeitschrift **39**, 291–300

Heuze F., Archuleta R., Bonilla F., Day S., Doroudian M., Elgamal A., Gonzales S., Hoehler M., Lai T., Lavallee D., Lawrence B., Liu P.C., 2004, *Estimating site-specific strong earthquake motion*, Soil Dynamics and Earthquake Engineering, **24**, 199-223

Hobro J.W., 1999, *Three-dimensional tomographic inversion of combined reflection and refraction travel-time data*, Ph.D. thesis, University of Cambridge, U.K

Hobro J. W., Minshull T.A., Singh S.C., Chand S., 2005, *A three-dimensional seismic tomographic study of the gas hydrate stability zone, offshore Vancouver Island*, Journal of Geophysical Research, **110**, B09102, doi: 10.1029/2004JB003477, 1–14

Holtzman R., Juanes R., 2011, *Thermodynamic and hydrodynamic constraints on overpressure caused by hydrate dissociation: A pore-scale model*, Geophysical Research Letters, **38**, L14308

Hornbach M. J., Saffer D. A., Holbrook W.S., 2004, *Critically pressured free-gas reservoirs below gas-hydrate provinces*, Nature, **427**, 142– 144

Housner G.W., 1989, *Competing against time*, Report to Governor Deukmejian of California, Governor's Board of Inquiry on the (1989) Loma Prieta Earthquake, George W. Housner, Chairman

Hu, 2011, *Deformation processes in great subduction zone earthquake cycles*, PhD thesis, University of Victoria, British Columbia

Hu Y., Wang K., 2008, *Coseismic strengthening of the shallow portion of the subduction fault and the effects on the frontal prism taper*, Journal of Geophysical Research, **113**(B12), B12411, doi:10.1029/2008JB005724

Huang X., García M.H., 1998, *A Herschel-Bulkley model for mud flow down a slope*, Journal of Fluid Mechanics, **374**, 305-333

Huang X., García M.H., 1999, *Modelling of non-hydroplaning mudflows on continental slopes*, Journal of Marine Geology, **154**, 131- 142

Hubbert M.K., Rubey, W.W., 1959, *Role of fluid pressure in the mechanics of overthrust faulting. I: Mechanics of fluid-filled porous solids and its application to overthrust faulting*, Geological Society of America Bulletin, **70**, 115-166

Hunt B., 1994, *Newtonian fluid mechanics treatment of debris flows and avalanches*, Journal of Hydraulic Engineering, **120**(12), 1350-1363

Hyndman R.D., 1995a, *Giant earthquakes of the Pacific Northwest*, Scientific American, **273**(6), 68-75

Hyndman R.D., 1995b, *The Lithoprobe corridor across the Vancouver Island continental margin: the structural and tectonic consequences of subduction*, Canadian Journal of Earth Sciences, **32**, 1777-1802

Hyndman R.D., 2013, *Downdip landward limit of Cascadia great earthquake rupture*, Journal of Geophysical Research, **118**(10), 5530-5548

Hyndman R.D., Davis E.E., Wright J.A., 1979, *The measurement of marine geothermal heat flow by a multi-penetration probe with digital acoustic telemetry and insitu thermal conductivity*, Marine Geophysical Research, **4**(2), 181-205

Hyndman R.D., Yorath C.J., Clowes R.M., Davis E.E., 1990, *The northern Cascadia subduction zone at Vancouver Island: Seismic structure and tectonic history*, Canadian Journal of Earth Sciences, **27**, 313-329

Hyndman, R.D., Spence G.D., 1992a, *A seismic study of methane hydrate marine bottom simulating reflectors*, Journal of Geophysical Research, **97**, 6683-6698

Hyndman R.D., Spence G.D., 1992b, *A Mechanism for the Formation of Methane Hydrate and Seafloor Bottom-Simulating Reflectors by Vertical Fluid Expulsion*, Journal of Geophysical Research, **97**(B5), 7025-7041

Hyndman, R. D., Wang K., 1993, *Thermal constraints on the zone of major thrust earthquake failure: The Cascadia subduction zone*, Journal of Geophysical Research, **98**, 2039 – 2060

Hyndman R.D., Wang K., Yuan T., Spence G.D., 1993, *Tectonic sediment thickening, fluid expulsion, and the thermal regime of subduction zone accretionary prisms: the Cascadia margin off Vancouver Island*, Journal of Geophysical Research, **98**(B12), 21,865-21,876

Hyndman R.D., Spence G.D., Yuan T., Davis E.E., 1994, *Regional geophysics and structural framework of the Vancouver Island margin accretionary prism*, In: Proceedings of the Ocean Drilling Program Initial Report, **146** (1), Eds: Westbrook G.K., Carson B., Musgrave R.J.

Hyndman, R.D., Wang K., 1995a, *Constraints on the zone of potential great earthquakes on the Cascadia subduction thrust from current deformation and the thermal regime*, Journal of Geophysical Research, **100**(B8), 15,373-15,392

Hyndman R.D., Wang K., 1995b, *The rupture zone of Cascadia great earthquakes from current deformation and the thermal regime*, Journal of Geophysical Research, **100**(B11), 22,133-22,154

Hyndman R. D., Spence G. D., Chapman N. R., Riedel M., Edwards R. N., 2001, *Geophysical Studies of Marine Gas Hydrate in Northern Cascadia*, in*:* C. K. Paull and W. P. Dillon, eds., Natural gas hydrates: occurrence, distribution, detection, American Geophysical Union Monographs, **124**, 273-295

Hyndman R. D., Rogers G.C., 2010, *Great earthquakes on Canada's west coast: a review*, Canadian Journal of Earth Sciences, **47**, 801-829

Hynes-Griffin M.F., Franklin A.G., 1984, *Rationalizing the seismic coefficient method*, US Army Engineer Waterways Experiment Station Misc. pap., GL-84-13, 21 pp.

Idriss I.M., 1991, *Earthquake ground motion at soft soil sites*, In: Proceedings of the 2nd International Conference on Recent Advances in Geotechnical Earthquake Engineering and Soil Dynamics, March 11-15, 1991, St. Louis, MO, Ed., S. Prakesh, University of Missouri-Rolla

Imran J., Parker G., Locat J., Lee H., 2001a, *1D numerical model of muddy subaqueous and subaerial debris flows*, Journal of Hydraulic Engineering, **127**(11), 959-968

Imran J., Harff P., Parker G., 2001b, *A numerical model of submarine debris flow with Geographical User Interface*, Computers and Geoscience, **27**(6), 717-730

Iverson R.M., 1997, *The physics of debris flows*, Review of Geophysics, **35**, 245-296

Iwasaki S., 1987, *On the estimation of a tsunami generated by a submarine landslide*, Proceedings of the International Tsunami Symposium, Vancouver, Canada, 134–138

Iwasaki S., 1997, *The wave forms and directivity of a tsunami generated by an earthquake and a landslide*, Science of Tsunami Hazards, **15**, 23–40

James T., Gowan E.J., Hutchinson I., Clague J.J., Barrie J.V., Conway K.W., 2009, *Sea-level change and paleogeographic reconstructions,southern Vancouver Island, British Columbia, Canada*, Quaternary Science News, **28**, 1200-1216

Janbu N., 1957, *Earth pressure and bearing capacity calculations by generalized procedure of slices*, Proceedings of 4th International Conference on Soil Mechanics and Foundation Engineering, **2**, 207- 212

Janbu N., 1968, *Slope stability computations*, Soil Mechanics And Foundation Engineering Report, The Technical University of Norway, Trondheim, Norway

Janbu N., 1973, *Slope Stability Computations*, Embankment Dam Engineering - Casagrande Volume, John Wiley and Sons, N.Y.

Jiang L., LeBlond P.H., 1992, *The coupling of a submarine slide and the surface waves which it generates*, Journal of Geophysical Research, **97**(C8), 12,731-12,744

Jiang L., LeBlond P.H., 1993, *Numerical modeling of an underwater Bingham plastic mudslide and the waves which it generates*, Journal of Geophysical Research, **98**, 10,303-10,317

Jiang L., LeBlond P.H., 1994, *Three-dimensional modeling of tsunami generation due to a submarine landslide*, Journal of Physical Oceanography, **24**, 559-572

Johnson A., 1970, *A method for interpretation of natural phenomena – intrusions on igneous rocks, fractures and folds, flow of debris and ice*, Physical Processes in Geology, **570**

Johnson J.E., Goldfinger C., Tréhu, A.M., Bangs N.L.B., Torres M.E., Chevallier J., 2006, *North-south variability in the history of deformation and fluid venting across Hydrate Ridge, Cascadia margin*, *In*: Tréhu A.M., Bohrmann G., Torres M.F., Colwell F.S. (Eds.), Proceedings of the Ocean Drilling Program, Scientific Results Volume **204**, 1-16

Kanamori H., Kikuchi M., 1993, *The 1992 Nicaragua earthquake: a slow tsunami earthquake associated with subducted sediments*, Nature, **361**, 714-716

Karig D.E., Hou G., 1992, *High-stress consolidation experiments and their geologic implications*, Journal of Geophysical Research, **97**(B1), 289-300

Kelley D., Delaney J., 2005, Vancouver Margin Mapping cruise TN-175, November 7-14, 2005 University of Washington

Keefer D.K., 2002, *Investigating landslides caused by earthquakes – a historical review*, Surveys in Geophysics, **23**, 473-510

Kenyon N.H., 1987, *GLORIA study of the Indus Fan*, Institute of Oceanographic Sciences RRS Charles Darwin Cruise 20, Cruise Report **198**, 17 pp.

Kim H.C., Bishnoi P.R., Heideman R.A., Rizvi S.S.H., 1987, *Kinetics of methane hydrate decomposition*, Chemical Engineering Science, **42**(7), 1645-1653

Kimura G., 1986, *Oblique Subduction and Collision*: *Forearc Tectonics of the Kuril Arc*, Geology, **14**, 404–407

Koh C.A., Sloan D.E., Sum A.K., Wu D.T., 2011, *Fundamentals and applications of gas hydrates*, Annual Review of Chemical and Biomolecular Engineering, **2**, 237-257

Koppula S.D., Morgenstern N.R., 1982, *On the consolidation of sedimenting clays*, Canadian Geotechnical Journal, **19**, 260-268

Krahn J., 2004, *Stability Modeling with SLOPE/W – An Engineering Methodology*, GEO-SLOPE Software Manual

Kudo K., 1995, *Practical estimates of site response, State-of-the-Art report*, In: Proceedings of the Fifth International Conference on Seismic Zonation, October 17-19, Nice, France, Ouest Editions Nantes, **III**, 1878-1907

Kukowski N., Schillhorn T., Huhn K., von Rad U., Flueh E.R., Husen S., 2001, *The Makran accretionary wedge: morphotectonic analysis, erosive canyons, and implications for forearc mechanics*, Journal of Marine Geology, **173**, 1–19

Kukowski N., Greinert J., Henrys S., 2010, *Morphometric and critical taper analysis of the Rock Garden region, Hikurangi Margin, New Zealand: Implications for slope stability and potential tsunami generation*, Journal of Marine Geology, **272**, 141-153

Kumar D., Sen M. K., Bangs N. L., 2006, *Seismic characteristics of gas hydrates at Hydrate Ridge, offshore Oregon*, The Leading Edge, **25**, 610–615

Kvalstad T.J, Andresen L., Forsberg C.F., Berg K., Bryn P., Wangen M., 2005, *The Storegga slide: evaluation of triggering sources and slide mechanics*, Journal of Marine and Petroleum Geology, **22**, 245-256

Kvenvolden K.A., 1998, *A primer on the geological occurrence of gas hydrate*, In: J.P. Henriet and J. Mienert (eds.), Gas Hydrates: Relevance to World Margin Stability and Climate Change, **137**, p.9-30, Geological Society, London, Special Publications

Kwon T.-H., Cho G.-C., Santamarina J.C., 2008, *Gas hydrate dissociation in sediments: pressure-temperature evolution*, Geochemistry Geophysics Geosystems, **9**(3), doi:10.1029/2007GC001920

Lallemand S.E., Schnürle P., Malavieille J., 1994, *Coulomb theory applied to accretionary and nonaccretionary wedges: possible causes for tectonic erosion and/or frontal accretion*, Journal of Geophysical Research, **99**, 12033–12055

Lambe T.W., Whitman R.V., 1979, *Soil Mechanics:SI Version*, New York, Wiley, 553 p.

Lee, H.J., Locat, J., Dartnell, P., Minasian, D.,Wong, F., 2000, *A GIS-based regional analysis of the potential for shallow-seated submarine slope failure*, Proc. 8th International Symposium on Landslides, Cardiff, Wales, June 26–30, 917–922

Lee H. J., Orzech K., Locat J., Konrad J. M., Boulanger E., 2004, *Seismic strengthening, a conditioning factor influencing submarine landslide development*, 57th Canadian Geotechnical Conference, Proceedings, **8–14** [CD-ROM], 2004

Lee M.W., Hutchinson D.R., Dillon W.P., Miller J.J., Agena W.F., Swift B.A., 1993, *Method of estimating the amount of in-situ gas hydrates in deep marine sediments*, Journal of Marine and Petroleum Geology, **10**, 496 – 506

Leonard L.J., Rogers G.C., Hyndman R.D., 2010, *Annotated bibliography of references relevant to tsunami hazard in Canada*, Geological Survey of Canada, Open File 6559, 269 pages

Leonard L.J., Rogers G.C., Mazzotti S., 2013, *Tsunami hazard assessment of Canada*, Natural Hazards, doi 10.1007/s11069-013-0809-5

Leynaud D., Mienert J., Nadim F., 2004, *Slope stability assessment of the Helland Hansen area offshore the mid-Norwegian margin*, Journal of Marine Geology, **213,** 457–480

Liu K.F., Mei C.C., 1989, *Slow spreading of a sheet of Bingham fluid on an inclined plane*, Journal of Fluid Mechanics, **207**, 505-529

Liu X., Flemings P., 2009, *Dynamic response of oceanic hydrates to sea level drop*, Geophysical Research Letters, **36**, doi: 10.1029/2009GL039821

Locat J., Norem H., Schieldrup N., 1990, *Modélisation de la dynamique des glissements sous-marins*, In: Proceedings of the 6th Congress of the International Association of Engineering Geology, Amsterdam, 2849–2855

Locat J., Lee H.J., 2002, *Submarine landslides: advances and challenges*, Canadian Geotechnical Journal, **39**, 193-212

Locat J., Lee H.J., ten Brink U.S., Twitchell D., Geist E., Sansoucy M., 2009, *Geomorphology, stability, and mobility of the Currituck slide*, Journal of Marine Geology, **264**, 28-40

Lopez C., 2007, *Seismic velocity structure associated with gas hydrate at the frontal ridge of northern Cascadia margin*, MSc thesis, University of Victoria

Lopez C., Spence G.D., Hyndman R.D., Kelley D., 2010, *Frontal ridge slope failure at the northern Cascadia margin: Margin-normal fault and gas hydrate control*, Geology, **38**(11), 967-970

MacKay M.E., Moore G.F., Cochrane G.R., Moore J.C., Kulm L.D., 1992, *Landward vergence and oblique structural trends in the Oregon margin accretionary prism: Implications and effect on fluid flow*, Earth and Planetary Science Letters, **109**, 477-491

MacKay M.E., Jarrard R.D., Westbrook G.K., Hyndman R.D., and the Shipboard Scientific Party of ODP Leg 146, 1994, *Origin of bottom simulating reflectors: Geophysical evidence from the Cascadia accretionary prism*, Geology, **22**, 459-462

Mainali A., Rajaratnam N., 1994, *A Herschel-Bulkley model for mud flow down a slope*, Journal of Hydraulic Engineering, **120**(1), 104-123

Majorowicz J.A., Osadetz K.G., 2001, Gas hydrate distribution and volume in Canada, AAPG Bulletin, **85**(7), 1211-1230

Malinverno A., Kastner M., Torres M.E., Wortmann U.G., 2008, *Gas hydrate occurrence from pore water chlorinity and downhole logs in a transect across the northern Cascadia margin* (Integrated Ocean Drilling Program Expedition 311), Journal of Geophysical Research, 113(B8): B08103, doi:10.1029/2008JB005702

Malinverno A., 2010, *Marine gas hydrates in thin sand layers that soak up microbial methane*, Earth and Planetary Science Letters, **292** (3-4), 399-408. Doi:10.1016/j.epsl.2010.02.008

Marr J.G., Elverhøi A., Harbitz C., Imran J., Harff P., 2002, *Numerical simulation of mud-rich subaqueous debris flows on the glacially active margins of the Svalbard-Barents Sea*, Journal of Marine Geology, **188**, 351-364

Maslin M., Owen M., Day S., Long D., 2004, *Linking continental-slope failures and climate change: Testing the clathrate gun hypothesis*, Geology, **32**, 53-56

Masson D.G., Bett B.J., Birch K.G., 1997, *Atlantic margin environmental survey*, Sea Technology, **38**(10), 52-59

Matsumoto R., Masuda M., Foucher J., Tokuyama H., Ashi J., Tomaru H., 2000, *Double BSR in the Eastern Nankai Trough: fact or artifact*, AGU 2000 Western Pacific Geophys. Meeting (available at http://www.agu.org/meetings/waiswp00.html)

Mazzotti S., Dragert H., Henton J., Schmidt M., Hyndman R., James T., Lu Y., Craymer M., 2003, *Current tectonics of northern Cascadia from a decade of GPS measurements*, Journal of Geophysical Research, **108**(B12), doi:10.1029/2003JB002653

McAdoo, B. G., Pratson L. F., Orange D. L., 2000, *Submarine landslide geomorphology, US continental slope*, Journal of Marine Geology, **169**, 103 – 136

McAdoo B.G., Capone M.K., Minder J., 2004, *Tsunami hazard from submarine landslides on the Oregon continental slope*, Journal of Marine Geology, **203**, 235-245

McCaffrey R., King R.W., Payne S., Lancaster M., 2013, *Active tectonics of Northwestern US inferred GPS-derived surface velocity*, Journal of Geophysical Research, doi:10.1029/2012JB009473, *in press*

McDougall S., Hungr O., 2004, *A model for the analysis of rapid landslide motion across three-dimensional terrain*, Canadian Geotechnical Journal, **41**, 1084-1097

McIver R.D., 1977, *Hydrates of natural gas: important agent in geologic processes*, Abstracts with Programs – Geological Society of America, **9**(7), 1089-1090

McIver R.D., 1982, *Role of naturally occurring gas hydrates in sediment transport*, AAPG Bulletin, **66**, 789-792

Meyer M., Geersen J., Schwenk T., Krastel S., 2010, *Giant submarine landslides off NW-Africa*, EGU General Assembly, 2-7 May 2010 in Vienna, Austria, p.11099

Mienert J., Posewang J., Lukas D., 2001, *Changes in the hydrate stability zone on the Norwegian Margin and their consequence for methane and carbon releases into the Oceanosphere*, In: Schäfer P., Ritzrau W., Schlüter M., Thiede (Eds.), The Northern North Atlantic: A changing Environment, Springer Verlag, New York, 281–290

Mienert J., Vanneste M., Buenz S., Andreassen K., Haflidason H., Sejrup H. P., 2005, *Ocean warming and gas hydrate stability on the mid-Norwegian margin at the Storegga Slide*, Journal of Marine Petroleum Geology, **22**, 233–244

Milkov A.V., 2004, *Global estimates of hydrate-bound gas in marine sediments: how much is really out there?*, Earth-Science Reviews, **66**, 183-197

Mörner N.-A., 1991, *Intense earthquakes and seismotectonics as a function of glacial isostasy*, Tectonophysics, **188**(3-4), 407-410

Moran K., Christian H.A., 1990, *Strength and deformation behavior of sediment from the Lesser Antilles forearc accretionary prism*, Proceedings of the Ocean Drilling Program, Scientific Results, **110**

Morgenstern N.R., Price V.E., 1965, *The analysis of the stability of general slip surface*, Geotechnique, **15**(4), 289-290

Morgenstern N.R., 1967, *Submarine slumping and the initiation of turbidity currents*, Marine Geotechnique, 189 – 220

Moridis G.J., Reagan M.T., Boyle K.L., Zhang K., 2009, *Evaluation of the gas production potential of challenging hydrate deposits*, Proceedings TOUGH Symposium, Lawrence Berkeley National Laboratory, Berkeley, California, September 14-16

Mukerji T., Dutta N., Prasad M., Dvorkin J., 2002, *Seismic detection and estimation of overpressures – Part I: Rock physics basics*, CSEG Recorder

Mulder T., Tisot J.-P., Cochonat P., Bourillet J.-F., 1993, *Stabilité des pentes sous-marines dans la Baie des Anges, Nice, France: approche géotechnique*, Revue Française de Géotechnique, **64**, 21–30

Mulder T., Cochonat P., 1996, *Classification of offshore mass movements*, Journal of Sedimentary Research, **66**(1), 43-57

Murty T.S., 1979, *Submarine slide-generated water waves in Kitimat Inlet, British Columbia*, Journal of Geophysical Research, **84**, 7,777-7,779

Musgrave R.J., Bangs N.L., Larrasoaña J.C., Gràcia E., Hollamby J.A., Vega M.E., 2006, *Rise of the base of the gas hydrate zone since the last glacial recorded by rock magnetism*, Geology, **34**, 117-120

Naegeli K., 2010, Internship Report at the Geological Survey of Canada

Nechtschein S., Bard P.Y., Gariel J.C., Ménéroud J.P., Dervin P., Cushing M., Gaubert C., Vidal S., Duval A.M., 1995, *A topographic effect study in the Nice region*, Proceedings of the 5th International Conference on Seismic Zonation, Nice, **2**, 1067-1074

Nelson C.H., Escutia C., Goldfinger C., Twichell D. C., Damuth J. E., 2011, *Interplay of mass-transport and turbidite-system deposits in different active tectonic and passive continental margin settings: external and local controlling factors*, in: Mass Transport Deposits, Shipp, C., Weimer, P., and Posimentier, H. (eds.), SEPM Special Publication, **96**, 39–66

Nelson C.H., Gutiérrez Pastor J., Goldfinger C., Escutia C., 2012, *Great earthquakes along the Western United States continental margin: implications for hazards, stratigraphy and turbidite lithology*, Natural Hazards and Earth System Sciences, **12**(11), 3191-3208

Nguyen Q.D., Boger D. V., 1992, *Measuring the flow properties of yield stress fluids*, Annual Review of Fluid Mechanics, **24**, 47-88

Nisbet E.G., Piper D.J.W., 1998, *Giant submarine landslides*, Nature, **392**, 329-330

Nixon M.F., Grozic J.L.H., 2007, *Submarine slope failure due to gas hydrate dissociation: a preliminary quantification*, Canadian Geotechnical Journal, **44**, 314-325

Nogoshi M., Igarashi T., 1971, *On the amplitude characteristics of microtremor (part 2)*, Journal of seismological Society of Japan, **24**, 26-40

Novosel I., 2002, *Physical properties of gas hydrate related sediments offshore Vancouver Island*, M.Sc. Thesis, University of Victoria, Canada

Novosel I., Spence G.D., Hyndman R.D., 2005, *Reduced magnetization produced by increased methane flux at a gas hydrate vent*, Journal of Marine Geology, **216**, 265-274

O'Brien J.S., Julien P.Y., 1988, *Laboratory analysis of mudflow properties*, Journal of Hydraulic Engineering, ASCE, 114, 877-887

Paull C.K., Ussler W., Dillon W.P., 1991, *Is the extent of glaciation limited by marine gas hydrates?*, Geophysical Research Letters, **18**(3), 432-434

Paull C.K., Ussler W., Borowski W.S., 1994, Sources of biogenic methane to form marine gas hydrates, In: Sloan E.D., Happel J., Hnatow M.A. (Eds.), International Conference on Natural Gas Hydrates Ann. N.Y. Acad. Sci., **715**, 392–409

Paull C.K., Buelow W.J., Ussler W.III., Borowski W.S., 1996, *Increased continental-margin slumping frequency during sea-level lowstands above gas hydrate–bearing sediments*, Geology, **24**, 143-146

Paull C.K., Brewer P.G., Ussler III W., Peltzer E.T., Rehder G., Clague D., 2003, *An experiment demonstrating that marine slumping is a mechanism to transfer methane from seafloor gas-hydrate deposits into the upper ocean and atmosphere*, Geo-Marine Letters, **22**, 198-203

Paull C., Dallimore S.R., Enciso G., Green S., Koh C.A., et al., 2010, *Comm. Assess. Dept. Energy's Methane Hydrate Res. Dev. Prog.: Eval. Methane Hydrate Future Energy Resour.*, Realizing the energy potential of methane hydrate for the United States, Natl. Acad. NRC Rep., Washington DC: National Academic Press

Pecher I. A., Holbrook W., Sen M., Lizarralde D., Wood W., Hutchinson D., Dillon W., Hoskins H., Stephen R., 2003, *Seismic anisotropy in gas-hydrate and gas bearing sediments on the Blake Ridge, from a walkaway vertical seismic profile*, Geophysical Research Letters, **30**(14), SDE2-1–SDE2-4

Piper D.J.W., Cochonat P., Morrison M.L., 1999, *The sequence of events around the epicentre of the 1929 Grand Banks earthquake: initiation of debris flows and turbidity current inferred from sidescan sonar*, Sedimentology, **46**, 79-97

Plafker G., Kachadoorian R., Eckel E. B., Mayo L. R., 1969, *The Alaska earthquake March 27, 1964: Various communities*, U.S. Geological Survey Prof. Paper 542-G, U.S., Dept. of Interior, Washington, D.C.

Pohlman J.W., Canuel E.A., Chapman N.R., Spence G.D., Whiticar M.J., Coffin R.B., 2005, *The origin of thermogenic gas hydrates on the northern Cascadia Margin as inferred from isotopic ($^{13}C/^{12}C$ and D/H) and molecular composition of hydrate and vent gas*, Organic Chemistry, **36**(5), 703-716

Pohlman J.W., Kaneko M., Heuer V.B., Coffin R.B., Whitikar M., 2009, *Methane sources and production in the northern Cascadia margin gas hydrate system*, Earth and Planetary Science Letters, **287**, 504-512

Popescu I., De Batist, Lericolais G., Nouzé H., Poort J., Panin N., Versteeg W., Gillet H., 2006, *Multiple bottom-simulating reflectors in the Black Sea: Potential proxies of past climate conditions*, Journal of Marine Geology, **227**(3-4), 163-176

Posewang J., Mienert J., 1999, *The enigma of double BSRs: Indicators for changes in the hydrate stability field?*, Geo-Marine Letters, **19**, 157–163

Prins J. E., 1958, *Characteristics of waves generated by a local disturbance*, EOS Trans. AGU, **39**, 865

Prior D.B., Coleman J.M., 1982, *Active slides and flows in underconsolidated marine sediments on the slope of the Mississippi delta*, In: Saxov S., and Nieuwenhuis J.K. (eds.), Marine slides and other mass movements: New York, NY: Plenum Press, 21-49

Prior D.B., Bornhold B.D., Coleman J.M., Bryant W.R., 1982, *Morphology of a submarine slide, Kitimat Arm, British Columbia*, Geology, **10**, 588–592

Rabinovich B.R., Thomson R.E., Bornhold B.D., Fine I.V., Kulikov E.A., 2003, *Numerical modeling of tsunamis generated by hypothetical landslides in the Strait of Georgia, British Columbia*, Pure and Applied Geophysics, **160**, 1273-1313

Reece R., Gulick S.P., Christeson G.L., 2010, *Evidence for seismic strengthening and climate influence in creation of an anomalously large slope failure, Aleutian-Yakutat margin, Gulf of Alaska*, American Geophysical Union Fall Meeting

Remaître A., Malet J.-P., Maquaire O., Ancey C., Locat J., 2005, *Flow behavior and runout modeling of a complex debris flow in a clay-shale basin*, Earth and Surface Processes and Landforms, **30**, 479-488

Rempel A.W., Buffett B.A., 1998, *Mathematical models of gas hydrate accumulations*, In: Henriet J.-P., Mienert J. (Eds.), Gas Hydrates: Relevance to World Margin Stability and Climatic Change, Geological Society London Special Publication, **137**, 63– 74

Riedel M., Hyndman R.D., Spence G.D., Chapman N.R., 2002, *Seismic investigations of an apparent active vent field associated with gas hydrates, offshore Vancouver Island*, Journal of Geophysical Research, **107**, 5-1 to 5-16

Riedel M., Spence G. D., Chapman N. R., Hyndman R.D., 2006a, *Seismic investigations of a vent field associated with gas hydrates, offshore Vancouver Island*, Journal of Geophysical Research, **107**(B9)doi: 10.1029/2001JB000269

Riedel, M., Novosel I., Spence G. D., Hyndman R. D., Chapman N. R., Solem R. C., Lewis T., 2006b, *Geophysical and geochemical signatures associated with gas hydrate related venting at the North Cascadia margin*, Geological Society of America Bulletin, **118**, 23–38

Riedel M., Collett T.S., Malone M.J., and the Expedition 311 Scientists, 2006c, *Expedition 311 Summary*, Proceedings of the Intergrated Ocean Drilling Program, **311**

Riedel M., Collett T.S., Malone M.J., and the Expedition 311 Scientists, 2006d, *Site U1326*, Proceedings of the Integrated Ocean Drilling Program, **311**

Riedel M., Collett T.S., Malone M.J., and the Expedition 311 Scientists, 2006e, *Methods*, Proceedings of the Integrated Ocean Drilling Program, **311**

Riedel M., Collett T.S., Malone M.J., and the Expedition 311 Scientists, 2010, *Expedition 311 synthesis: scientific findings*, Proceedings of the Intergrated Ocean Drilling Program, **311**

Rogers G. C., 1998, *Earthquakes and earthquake hazard in the Vancouver area*, Geological Survey of Canada Bulletin, **525**, 17–25

Ronen S., Comeaux L., Miao X.G., 2005, *Imaging downgoing waves from ocean bottom stations*, 75th SEG Annual Meeting

Rothwell R.G., Thompson J., Kähler G., 1998, *Low-sea-level emplacement of a very large Late Pleistocene 'megaturbidite' in the western Mediterranean Sea*, Nature, **392**, 377-380

Ryu B.-J., Riedel M., Kim J.-H., Hyndman R.D., Lee Y.-J., Chung B.-H., Kim I.-S., 2009, *Gas hydrates in the western deep-water Ulleung Basin, East Sea of Korea*, Journal of Marine and Petroleum Geology, **26** (8), 1483-1498

Saffer D.M., Bekins B.A., 2002, *Hydrologic controls on the morphology and mechanics of accretionary wedges*, Geology, **30**, 271-274

Saffer D.M., 2003, *Pore pressure development and progressive dewatering in underthrust sediments at the Costa Rican subduction margin: Comparison with northern Barbados and Nankai*, Journal of Geophysical Research, **108**(B5), 2261

Satake K.,Shimazaki K., Tsuji Y., Ueda K., 1996, *Time and size of a giant earthquake in Cascadia inferred from Japanese tsunami records of January 1700*, Nature, **379**, 246-249

Scherwath M., Spence G.D., 2011, *Mirror-imaging processing if ocean bottom seismometer data*, Natural Resources Canada-Geological Survey of Canada – Pacific, Report No. 23445-112902/001/VIC

Schmuck E.A., Paull C.K., 1993, *Evidence for gas accumulation associated with diapirism and gas hydrates at the head of the Cape Fear Slide*, Geo-Marine Letters, **13**, 145-152

Schneider J., Flemings P.B., Dugan B., Long H., Germaine J.T., 2009, *Overpressure and consolidation neat the seafloor of Brazos-Trinity Basin IV, northwest deepwater Gulf of Mexico*, Journal of Geophysical Research, **115**(B05102), doi:10.1029/2008JB005922

Schultheiss P., Holland M., Rack F., 2010, *Borehole pressure coring techniques and core analysis at in situ pressure*, In: Geophysical characterization of gas hydrates, Riedel M., Willoughby E.C., Chopra S. (eds), SEG Geophysical Development Series No. 14

Schwalenberg K., Willoughby E., Mir E., Edwards R.N., 2005, *Marine gas hydrate electromagnetic signatures in Cascadia and their correlation with seismic blank zones*, First Break, **23**, 57-63

Screaton E., Saffer D., Henry P., Hunze S., 2002, *Porosity loss within the underthrust sediments of the Nankai accretion complex: Implications for overpressures*, Geology **30**(1), 19-22

Screaton E., Saffer D.M., 2005, *Fluid expulsion and overpressure development during initial subduction at the Costa Rica convergent margin*, Earth and Planetary Science Letters, 233(**3-4**), 361-374

Seed H.B., Wong R.T., Idriss I.M., Tokimatsu K., 1986, *Moduli and damping factors for dynamic analyses of cohesionless soils*, Journal of Geotechnical Engineering, **112**(11), 1016-1032

Shine K.P., Derwent R.G., Wuebblesand D.J., Morcrette J.J., 1990, *Radiative forcing of climate*, In: J.T. Houghton, G.J. Jenkins, J.J. Ephraums (eds.), Climate Change 1992, The Supplementary Report to the IPCC Scientific Assessment, p.41-68, Cambridge Univ. Press, New York

Shipboard Scientific Party, 1994, *Site 888*, In: Proceedings of the Ocean Drilling Program, Initial Reports, Vol. **164** (Part I)

Siddal M., Hönisch B., Waelbroeck C., Huybers P., 2010, *Changes in deep Pacific temperature during the mid-Pleistocene transition and Quaternary*, Quaternary Science Reviews, **29**, 170-181

Silva W., Darragh R., Stark C., Wong I., Stepp J., Schneider J., Chiou S., 1990, *A methodology to estimate design response spectra in the near-source region of large earthquakes using the Band-Limited-White-Noise ground motion model*, in: Proc. Fourth U.S. National Conference on Earthquake Engineering, **1**, 487-494

Skempton A.W., 1970, *The consolidation of clays by gravitational compaction*, Journal of Geological Society of London, **125**, 373 – 411

Skvortsov A., 2005, *Numerical Simulation of Landslide-Generated Tsunamis with Application to the 1975 Failure in Kitimat Arm, British Columbia, Canada*, MSc thesis, University of Victoria, British Columbia

Skvortsov A., Bornhold B., 2007, *Numerical simulation of the landslide-generated tsunami in Kitimat Arm, British Columbia, Canada, 27 April 1975*, Journal of Geophysical Research, **112**, F02028

Sloan E.D., 1998, *Physical/chemical properties of gas hydrates and application to world margin stability and climate change*, In: J.P. Henriet and J. Mienert (eds.), Gas Hydrates: Relevance to World Margin Stability and Climate Change, **137**, p.31-50, Geological Society, London, Special Publications

Sloan E.D. and Koh C., 2007, *Clathrate hydrates of natural gases*, CRC press.

Solem R.C., Spence G.D., Vukajlovich D., Hyndman R.D., Riedel M., Novosel I., Kastner M., 2002, *Methane advection and gas hydrate formation within an active vent field offshore Vancouver Island*, Proceedings of the Fourth International Conference on Gas Hydrates, Yokohama

Somerville P.G., Graves R.W., 2003, *Characterization of Earthquake Strong Ground Motion*, Pure and Applied Geophysics, **160**, 1811-1828

Spence G.D., Minshull T.A., Fink C., 1995, *Seismic structure of methane gas hydrate, offshore Vancouver Island*, Proc. Ocean Drill. Program, Sci. Results **146**, 163-174

Spence G.D., Haacke R.R., Hyndman R.D., 2010, *Seismic indicators of natural-gas hydrate and underlying free gas*, In: Geophysical characterization of gas hydrates, Editors: Michael Riedel, Eleanor C. Willoughby, Satinder Chopra, SEG Geophysical Developments Series No. 14

Spencer E., 1967, *A method of analysis of the stability of embankments assuming parallel interslice forces*, Geotechnique, **17**(1), 11-26

Stark T., Eid H., 1998, *Performance of Three-Dimensional Slope Stability Methods in Practice*, Journal of Geotechnical and Geoenvironmental Engineering, **124**(11), 1049-1060

Stigall J., Dugan B., 2010, *Overpressure and earthquake initiated slope failure in the Ursa region, northern Gulf of Mexico*, Journal of Geophysical Research, **115**(B04101)

Strasser M., Henry P., Kanamatsu T., Thu .K., Moore G.E., and the IODP Expedition 333 Scientists, 2010, *Scientific drilling of mass-transport deposits in the Nankai accretionary wedge: First results from IODP Expedition 333*, In: Submarine Mass Movements and Their Consequences, Advances in Natural and Technological Hazards Research, **28**, Mosher et al. (eds), Springer Science + Business Media B.C.

Striem H. L., Miloh T., 1975, *Tsunamis induced by submarine slumpings off the coast of Israel*, 23 pp., Israel Atomic Energy Commission

Sultan N., Cochonat P., Foucher J.-P., Mienert J., 2004, *Effect of gas hydrates melting on seafloor slope instability*, Journal of Marine Geology, **213**, 379-401

Sultan N., 2007, *Comment on ''Excess pore pressure resulting from methane hydrate dissociation in marine sediments: A theoretical approach'' by Wenyue Xu and Leonid N. Germanovich*, Journal of Geophysical Research, **112**, doi:10.1029/2006JB004527

Summerhayes C., Bornhold B., Embley R., 1979, *Surficial slides and slumps on the continental slope and rise of South West Africa: a reconnaissance study*, Journal of Marine Geology, **31**, 265-277

Synolakis C.E., Bardet J.-P., Borrero J.C., Davies H.L., Okal E.A., Silver E.A., Sweet S., Tappin D.R., 2002, *The slump origin of the 1998 Papua New Guinea Tsunami*, Proceedings of the Royal Society of London A., **458**, 763-789

Syvitski J.P.M., Hutton E.W.H., 2003, *Failure of marine deposits and their redistribution by sediment gravity flows*, Pure and Applied Geophysics, **160**, 2053-2069

Takahashi T., 1978, *Mechanical characteristics of debris flow*, Journal of Hydraulics Division, ASCE, **104**(8), 1153–1169

Talling P.J., 2013, *Hybrid submarine flows comprising turbidity current and cohesive debris flow: Deposits, theoretical and experimental analyses, and generalized models*, Geosphere, **9**(3), 460-488

Tan B., Germaine J.T., Flemings P.B., 2005, *Data Report: Consolidation and strength characteristics of sediments from ODP Site 1244, Hydrate Ridge, Cascadia Continental Margin*, In: Proceedings of the Ocean Drilling Program, Scientific Results, Volume **204**, Tréhu A.M., Bohrman G., Torres M.E., Colwell F.S. (Eds.)

Tappin D. R., Watts P., McMurtry G. M., Lafoy Y., Matsumoto T., 2001, *The Sissano, Papua New Guinea Tsunami of July 1998 -- Offshore Evidence on the Source Mechanism*, Journal of Marine Geology, **175**, 1-23

Ten Brink U.S., Lee H.J., Geist E.L., Twichell D., 2009, *Assessment of tsunami hazard to the U.S. East Coast using relationships between submarine landslides and earthquakes*, Journal of Marine Geology, **264**, 65-73

Terzaghi K., 1925, *Erdbaumechanik auf bodenphysikalischer Grundlage*, Leipzig, 399 p.

Terzaghi K., 1943, *Theoretical Soil Mechanics*, London, Chapman and Hall, 510 p.

Terzaghi K., Peck R.B., 1948, *Soil mechanics in engineering practice*, New York, Wiley

Terzaghi K., 1950, *Mechanisms of Landslides*, Engineering Geology Volume, Geological Society of America

Thomson R., Fine I., Krassovski M., Cherniawsky J., Conway L., Wills P., 2012, *Numerical simulation of tsunamis generated by submarine slope failures in Douglas Channel, British Columbia*, Canadian Science Advisory Secretariat, Research Document 2012/115, Pacific Region

Tinti S., Chiocci F.L., Zaniboni F., Pagnoni G., de Alteriis G., 2011, *Numerical simulation of the tsunami generated by a past catastrophic landslide on the volcanic island of Ischia, Italy*, Marine Geophysics Research, **32**, 287-297

Tréhu A.M., Bangs N., 2001, *3-D seismic imaging of an active margin hydrate system, Oregon continental margin*, report of cruise TTN112, Oregon State Univ. Data Report, **182**

Tréhu, A. M., Flueh E., 2001, *Estimating the thickness of the free gas zone beneath Hydrate Ridge, Oregon continental margin, from seismic velocities and attenuation*, Journal of Geophysical Research, **106,** 2035–2045

Tréhu A.M., Bohrmann G., Rack F.R., Torres M.E. et al., 2003, *Leg 204 Summary*, In: Proceedings of the Ocean Drilling Program, Initial Reports Volume **204**

Tréhu A.M., Torres M.E., Bohrmann G., Colwell F.S., 2006, *Leg 204 synthesis: gas hydrate distribution and dynamics in the central Cascadia accretionary complex*, *In* Tréhu A.M., Bohrmann G., Torres M.E., Colwell F.S. (Eds.), *Proceedings of the Ocean Drilling Program, Scientific Results*, **204**: College Station, TX (Ocean Drilling Program), 1–40

Verriere M., Lenoir M., 1992, *Computation of waves generated by submarine landslides*, International Journal of Numerical Methods in Fluids, **14**, 403–421

Viesca R.C., Rice J.R., 2010, *Modeling slope instability as shear rupture propagation in a saturated porous medium*, In: Submarine Mass Movements and Their Consequences, Advances in Natural and Technological Hazards Research, **28**, Mosher et al. (eds), Springer Science + Business Media B.C.

Villinger H.W., Tréhu A. M., Grevemeyer I., 2010, *Seafloor Marine Heat Flux Measurements and Estimation of Heat Flux from Seismic Observations of Bottom Simulating Reflectors*, In: Section 3: Borehole Studies from: Geophysical Characterization of Gas Hydrates, Editor(s): Michael Riedel, Eleanor C. Willoughby, Satinder Chopra

Vogt P.R., Jung W.-Y., 2002, *Holocene mass wasting on upper non-polar continental slopes – due to post-glacial ocean warming and hydrate dissociation?*, Geophysical Research Letters, **29**(9), 1341, 10.1029/2001GLo13488

Vrolijk P., 1987, *Tectonically driven fluid flow in the Kodiak accretionary complex, Alaska*, Geology, **15**, 466-469

Waelbroeck C., Labeyrie L., Michel E., Duplessy J.C., McManus J.F., Lambeck K., Balbon E., Labracherie M., 2002, *Sea-level and deep water temperature changes derived from benthic foraminifera isotopic records*, Quaternary Science Reviews, **21**, 295-305

Watts P., Gardner J.V., Yalçiner A.C., Imamura F., Synolakis C.E., 2001a, *Landslide tsunami scenario off Palos Verdes, California*, Natural Hazards

Watts P., Grilli S.T., Synolakis C. E., 2001b, *Tsunami generation by submarine mass failure I: Wavemaker models*, Journal of Waterways, Port, Coast, and Ocean Engineering

Watts P., Grilli S.T., Kirby J.T., Fryer G.J., Tappin D.R., 2003, *Landslide tsunami case studies using a Boussinesq model and a fully nonlinear tsunami generation model*, Natural Hazards and Earth System Sciences, **3**, 391-402

Watts P., Grilli S.T., Tappin D.R., Fryer G.J., 2005, *Tsunami Generation by Submarine Mass Failure. II: Predictive Equations and Case Studies*, Journal of Waterways, Ports, Coastal, and Ocean Engineering, **131**(6), 298-310

Westbrook G.K., Carson B., Musgrave R.J. et al., 1994, *Site 888*, Proceedings of the Ocean Drilling Program, Initial Reports, Vol. **146** (1)

Wiegel R. L., 1964, *Oceanographical Engineering*, 532 pp., Prentice-Hall, Englewood Cliffs, N.J.

Willoughby E., Schwalenberg K., Edwards R.N., Spence G.D., Hyndman R.D., 2005, *Assessment of marine gas hydrate deposits: a comparative study of seismic, electromagnetic and seafloor compliance methods*, 5th International Conference on Gas Hydrates, **3**, 802-811

Wright J.F., Dallimore S.R., Nixon F.M., Duchesne C., 2005, *In situ stability conditions of gas hydrate in sediments of the JAPEX/JNOC/GSC et al. Mallik 5L-38 gas hydrate production research well; in Scientific Results from the Mallik 2002 Gas Hydrate Production Research Well Program, Mackenzie Delta, Northwest Territories, Canada*, In: S.R. Dallimore, T.S. Collett, editor. Scientific Results from the Mallik 2002 Gas Hydrate Production Research Well Program, Mackenzie Delta, Northwest Territories, Canada, Geological Survey of Canada Bulletin **585**

Xu W., Ruppel C., 1999, *Predicting the occurrence, distribution, and evolution of methane gas hydrate in porous marine sediments*, Journal of Geophysical Research, **104**(B3), 5081-5095

Xu W., Lowell R.P., Peltzer E.T., 2001, *Effect of seafloor temperature and pressure variations on methane flux from a gas hydrate layer: Comparison between current and late Paleocene climate conditions*, Journal of Geophysical Research, **106**(B11), 26,413-26,423

Xu W., Germanovich L. N., 2006, *Excess pore pressure resulting from methane hydrate dissociation in marine sediments: A theoretical approach*, Journal of Geophysical Research, **111**, B01104, doi:10.1029/2004JB003600

Yorath C.J., Green A.G., Clowes R.., Sutherland Brown A., Brandon M.T., Kanasewich E.R., Hyndman R.D., Spencer C., 1985, *LITHOPROBE, southern Vancouver Island: Seismic reflection sees through Wrangellia to the Juan de Fuca plate*, Geology, **13**, 759-762

Youngs R. R., Chiou S. J., Silva W. J., Humphrey J. R., 1997, *Strong ground motion attenuation relationships for subduction zone earthquakes*, Seismological Research Letters, **68,** 58–73

Yuan T., Spence G.D., Hyndman R.D., 1994, *Seismic velocities and inferred porosities in the accretionary wedge*, Journal of Geophysical Research, **99**(B3), 4413-4427

Yuan, T., Hyndman R. D., Spence G. D., Desmons B., 1996, *Seismic velocity increase and deepsea gas hydrate concentration above a bottom simulating reflector on the northern Cascadia continental slope*, Journal of Geophysical Research, **101**, 13655–13671

Yuan, T., Spence G.D., Hyndman R. D., Minshull T. A., Singh S. C., 1999, *Seismic velocity studies of a gas hydrate bottom-simulating reflector on the northern Cascadia continental margin: Amplitude modeling and full waveform inversion*, Journal of Geophysical Research, **104**, 1179–1191

Zhang W., Durham W.B., Stern L.A., Kirby S.H., 1999, *Experimental deformation of methane hydrates: new results*, EOS, **80**(17), S337

Zoback M. D., 2007, *Reservoir Geomechanics*, Cambridge University Press

Zuehlsdorff L., Spiess V., 2004, *Three-dimensional seismic characterization of a venting site reveals compelling indications of natural hydraulic fracturing*, Geology, **32**(2), 101-104

# Appendix

## Appendix A: Pore pressure regime at the northern Cascadia margin

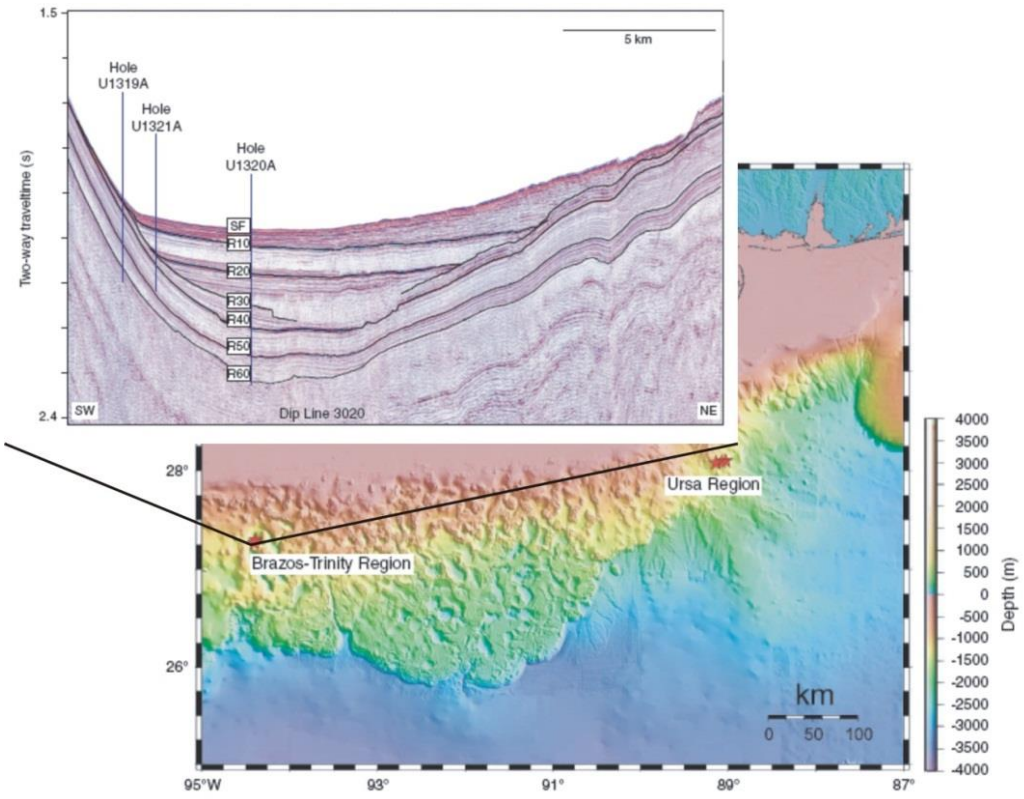


**Figure A.1**: Bathymetry map showing the location of the Brazos-Trinity region within the Gulf of Mexico; large inset: seismic image of the location of Sites U1319 and U1320 within Basin IV; annotations refer to seismic reflections horizons revealing the varied infill history of the basin; (modified after Expedition Scientists 308, 2006)

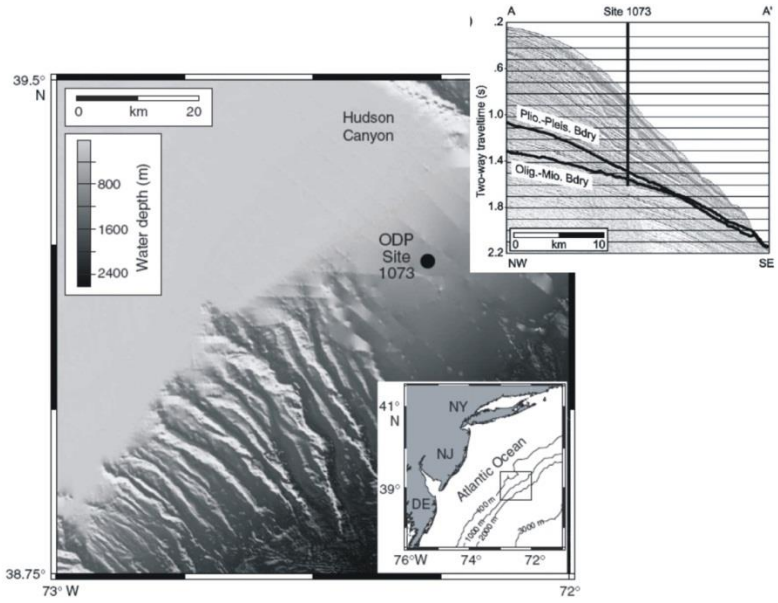


**Figure A.2**: Location of ODP Leg 174A Site 1073 along the continental slope offshore New Jersey; upper inset: seismic section perpendicular to the continental slope showing location of Site 1073; lower inset: location of study area offshore New Jersey (modified after Dugan (2003))

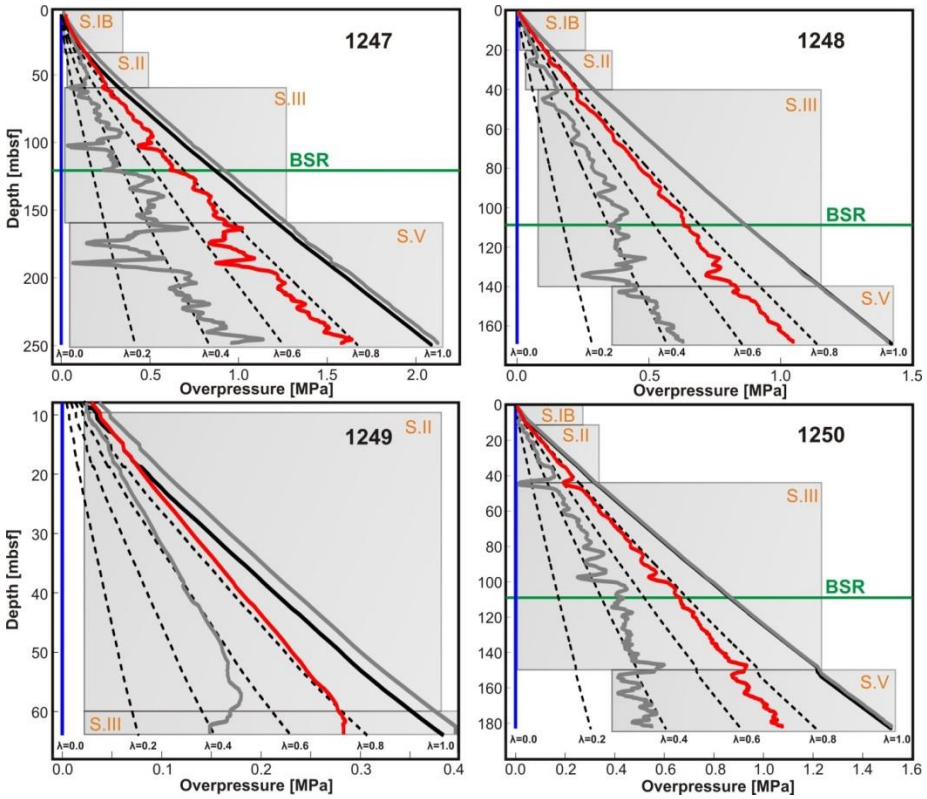


**Figure A.3**: Pore pressure results for the sites 1247, 1248, 1249, and 1250: red line: overpressure, grey lines: error limits, blue line: hydrostatic pressure, black line: vertical effective stress (equals maximum possible overpressure), grey boxes represent the locations of the lithostratigraphic units described by Chevallier et al. (2006)

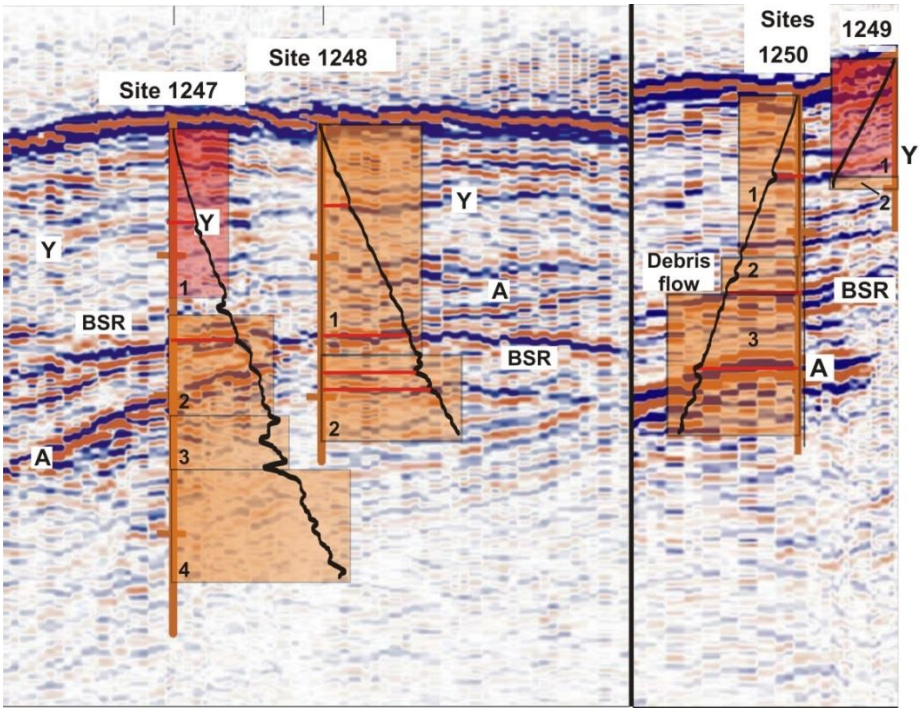


**Figure A.4**: Overlay of estimated overpressure at Sites 1247, 1248, 1249, and 1250 with seismic image of these sites; red = positive polarity; blue = negative polarity; black line indicates overpressure; colored boxes indicating pore pressure in percentage of vertical effective stress (see color code Fig. 3.9); red lines indicate spatial coincidence of overpressure with certain horizons (modified after Tréhu and Bangs, 2001)

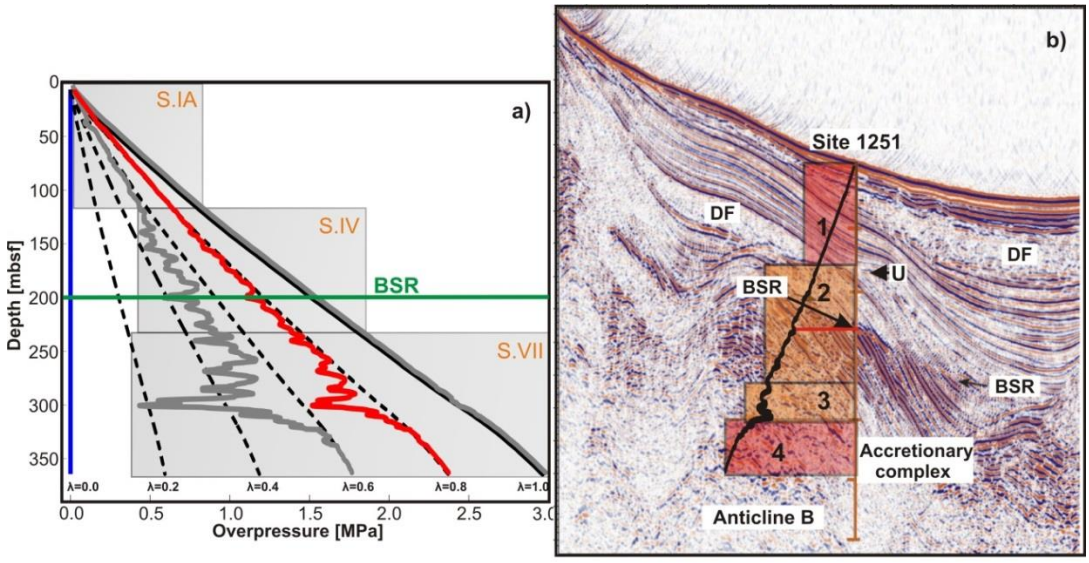


**Figure A.5**: a) Pore pressure results for the Sites 1251: red line: overpressure, grey lines: error limits, blue line: hydrostatic pressure, black line: vertical effective stress (equals maximum possible overpressure), grey boxes represent the locations of the lithostratigraphic units described by Chevallier et al. (2006); b) Overlay of estimated overpressure at Site 1251 with seismic image; blue = positive polarity; red = negative polarity; black line indicates overpressure; colored boxes indicate amount of overpressure (see color code Fig. 3.9); red lines indicate spatial coincidence of overpressure with certain horizons (modified after Tréhu and Bangs, 2001)

## Appendix B: Ground motion attenuation relationships

### B.1 Atkinson (2005)

Atkinson (2005) developed a GMAR for the horizontal acceleration due to crustal and offshore earthquakes along the Cascadia margin using a hybrid-empirical approach. Due to the apparent similarity to Cascadia events Atkinson (2005) multiplied Californian relations with frequency-dependent factors to account for regional differences in crustal amplification.

The resulting GMAR by Atkinson (2005) can be written as:

$$ln\,Y = a_1 + a_2(M - 6.0) + a_3(M - 6.0)^2 + a_4 logR + a_5 R \qquad \text{(B.1)}$$

where *Y* is the site response and *M* the moment magnitude.

Offshore events are calculated with the same equation and coefficients but the term (*M-6.0*) is replaced by (*M-6.5*). In equation A1.1 the distance parameter $R$ is calculated via $R = \sqrt{(D^2 + h^2)}$ where $D$ is the closest distance to the fault (i.e. hypocenter in the case of small earthquakes) and $h$ is calculated via $logh = -0.05 + 0.15M$. Table A.1 summarizes the coefficients resulting from Atkinson's (2005) regression.

| f(Hz) | $a_1$ | $a_2$ | $a_3$ | $a_4$ | $a_5$ |
|---|---|---|---|---|---|
| PGA | 2.3557 | 0.5796 | -0.0338 | -1.245 | 0 |
| 0.1 | 1.4172 | 0.9466 | -0.0587 | -1.0116 | 0 |
| 0.2 | 2.0247 | 0.8884 | -0.0809 | -1.0109 | 0 |
| 0.32 | 2.2116 | 0.8628 | -0.0886 | -1.0179 | 0 |
| 0.5 | 2.5913 | 0.7957 | -0.1069 | -1.0341 | 0 |
| 1.0 | 3.1283 | 0.6818 | -0.1158 | -1.0925 | -0.0002 |
| 2.0 | 3.552 | 0.5615 | -0.1031 | -1.0977 | -0.0013 |
| 3.2 | 3.816 | 0.4907 | -0.0844 | -1.1309 | -0.002 |
| 5.0 | 4.0439 | 0.4356 | -0.0626 | -1.1721 | -0.0028 |
| 10.0 | 4.3732 | 0.3972 | -0.0413 | -1.2977 | -0.0035 |
| 20.0 | 4.6827 | 0.4064 | -0.0378 | -1.4813 | -0.0018 |

**Table B.1**: Regression coefficients for equation (B.1) taken from Atkinson (2005)

## B.2 Boore and Atkinson (2008)

Boore and Atkinson (2008) developed an empirical GMAR for average horizontal ground accelerations for shaking periods between 0.01 s and 10 s. According to the authors the equations are valid for magnitudes between 5.0 and 8.0, for distances $R_{JB}$ < 200 km and $V_{S30}$ of 180-1300 m/s. $R_{JB}$ is the closest distance to the surface projection of the fault plane whereas $V_{S30}$ is the average S-wave velocity within the uppermost 30 m of the sediment column. In contrast to the other GMARs used in this study, the GMAR of Boore and Atkinson (2008) also includes the fault type.

The final form of the equation of Boore and Atkinson (2008) is:

$$ln\,Y = F_M\,(M) + F_D\,(R_{JB}, M) + F_S(V_{S30}, R_{JB}, M) \qquad \text{(B.2)}$$

where $F_M$, $F_D$, and $F_S$ stand for magnitude scaling, distance function, and site amplification, respectively. The distance function can be written as

$$F_D(R_{JB}, M) = [c_1 + c_2(M - M_{Ref})]ln(^{R}/_{R_{Ref}}) + c_3(R - R_{Ref}) \quad \text{(B.2a)}$$

with

$$R = \sqrt{(R_{JB}^2 + h^2)} \quad \text{(B.2b)}$$

with $M_{Ref}$ = 4.5 and $R_{Ref}$ = 1km.

The magnitude scaling term is calculated via:

a) $M \leq M_h$

$$F_M(M) = e_1 U + e_2 SS + e_3 NS + e_4 RS + e_5(M - M_h) + e_6(M - M_h)^2 \quad \text{(B.2c)}$$

b) $M > M_h$

$$F_M(M) = e_1 U + e_2 SS + e_3 NS + e_4 RS + e_7(M - M_h) \quad \text{(B.2d)}$$

where *U*, *SS*, *NS*, and *RS* stand for unspecified, strike-slip, normal-slip, and reverse-slip faults, having a value of One for the respective fault type. $M_h$ is the 'hinge magnitude' for the shape of the magnitude scaling.

The site amplification term is given by $F_S = F_{lin} + F_{NL}$ where $F_{lin}$ is the linear and $F_{NL}$ the non-linear part.

The linear term can be written as

$$F_{lin} = b_{lin} \ln(^{V_{S30}}/_{V_{Ref}}) \quad \text{(B.2e)}$$

$b_{lin}$ is a period dependent coefficient, and $V_{Ref}$ is a reference velocity here set to 760 m/s (Boore and Atkinson, 2008). The value for the non-linear term depends on the value for the PGA at $V = V_{Ref}$ as well as on a few threshold levels for linear and non-linear amplification.

a) $pga4nl \leq a_1$:

$$F_{NL} = b_{NL} \ln(pga_{low}/0.1) \quad \text{(B.2f)}$$

b) $a_1 < pga4nl \leq a_2$:

$$F_{NL} = b_{NL} \ln\left(\frac{pga_{low}}{0.1}\right) + c[\ln(\frac{pga4nl}{a_1})]^2 + d[\ln(\frac{pga4nl}{a_1})]^3 \quad \text{(B.2g)}$$

c) $a_2 < pga4nl$:

$$F_{NL} = b_{NL}\ln(pga4nl/0.1) \quad \text{(B.2h)}$$

with $a_1$ = 0.03g, $a_2$ = 0.09g, and *pga_low*= 0.06g. *pga4nl* is a reference PGA value for an average layer velocity of 760 m/s.

The coefficients *c* and *d* are calculated via:

$$c = (3\Delta y - b_{NL}\Delta x)/\Delta x^2 \quad \text{(B.2i)}$$

and

$$d = (-2\Delta y - b_{NL}\Delta x)/\Delta x^3 \quad \text{(B.2j)}$$

with $\Delta x = \ln\left(\frac{a_2}{a_1}\right)$ and $\Delta y = b_{nl}\ln(a_2/pga\_low)$ (B.2k)

$b_{NL}$, representing a non-linear slope, depends on both the shaking period and the average shear velocity of the uppermost 30 m below ground level:

*a)* $V_{S30} \leq V_1$

$$b_{NL} = b_1 \quad \text{(B.2l)}$$

*b)* $V_1 < V_{S30} \leq V_2$

$$b_{NL} = (b_1 - b_2)\ln\left(\frac{V_{S30}}{V_{Ref}}\right) / \ln\left(\frac{V_1}{V_2}\right) + b_2 \quad \text{(B.2m)}$$

*c)* $V_2 < V_{S30} \leq V_{ref}$

$$b_{NL} = b_2 \ln\left(\frac{V_{S30}}{V_{Ref}}\right) / \ln\left(\frac{V_2}{V_{Ref}}\right) \quad \text{(B.2n)}$$

*d)* $V_{Ref} \leq V_{S30}$

$$b_{NL} = 0.0 \qquad \text{(B.2o)}$$

with $V_1$ = 180 m/s and $V_2$ = 360 m/s.

Tables B.2 to B.4 summarize the coefficients resulting from the regression for the respective terms in equation B.2.

| f(Hz) | $c_1$ | $c_2$ | $c_3$ | h |
|---|---|---|---|---|
| PGA | -0.66050 | 0.11970 | -0.01151 | 1.35 |
| 0.1 | -0.09824 | -0.13800 | -0.00191 | 3.04 |
| 0.13 | -0.37240 | -0.06568 | -0.00191 | 3.00 |
| 0.2 | -0.50960 | -0.02391 | -0.00191 | 2.93 |
| 0.25 | -0.68540 | 0.03758 | -0.00191 | 2.89 |
| 0.33 | -0.78440 | 0.07282 | -0.00191 | 2.83 |
| 0.5 | -0.82850 | 0.09432 | -0.00217 | 2.73 |
| 0.67 | -0.83030 | 0.09793 | -0.00255 | 2.66 |
| 1.0 | -0.81830 | 0.10270 | -0.00334 | 2.54 |
| 1.33 | -0.74080 | 0.07518 | -0.00409 | 2.46 |
| 2.0 | -0.69140 | 0.06080 | -0.00540 | 2.32 |
| 2.5 | -0.64430 | 0.04394 | -0.00626 | 2.24 |
| 3.33 | -0.55430 | 0.01955 | -0.00750 | 2.14 |
| 4.0 | -0.57260 | 0.02977 | -0.00837 | 2.07 |
| 5.0 | -0.58300 | 0.04273 | -0.00952 | 1.98 |
| 6.67 | -0.69610 | 0.09884 | -0.01113 | 1.86 |
| 10 | -0.70810 | 0.11170 | -0.01151 | 1.68 |
| 13.33 | -0.72050 | 0.12370 | -0.01151 | 1.55 |
| 20 | -0.71700 | 0.13170 | -0.01151 | 1.35 |
| 33.3 | -0.69010 | 0.12830 | -0.01151 | 1.35 |
| 50 | -0.66600 | 0.12280 | -0.01151 | 1.35 |
| 100 | -0.66220 | 0.12000 | -0.01151 | 1.35 |

**Table B.2**: Regression coefficients for distance for equation (A.2) taken from Boore and Atkinson (2008)

| f (Hz) | $e_1$ | $e_2$ | $e_3$ | $e_4$ | $e_5$ | $e_6$ | $e_7$ | $M_h$ |
|---|---|---|---|---|---|---|---|---|
| PGA | -0.53804 | -0.50350 | -0.75472 | -0.50970 | 0.28805 | -0.10164 | 0.00000 | 6.75 |
| 0.1 | -2.15446 | -2.16137 | -2.53323 | -2.14635 | 0.40387 | -0.48492 | 0.00000 | 8.50 |
| 0.13 | -1.43145 | -1.31632 | -1.81022 | -1.59217 | 0.52407 | -0.37578 | 0.00000 | 8.50 |
| 0.2 | -1.28408 | -1.21270 | -1.50904 | -1.41093 | 0.14271 | -0.39006 | 0.00000 | 8.50 |
| 0.25 | -2.24656 | -2.15906 | -2.58228 | -2.38168 | 1.24961 | -0.35874 | 0.79508 | 6.75 |
| 0.33 | -1.82979 | -1.74690 | -2.22584 | -1.91814 | 0.77966 | -0.45384 | 0.67466 | 6.75 |
| 0.5 | -1.22652 | -1.15514 | -1.57697 | -1.27669 | 0.77989 | -0.29657 | 0.29888 | 6.75 |
| 0.67 | -0.86271 | -0.79593 | -1.20902 | -0.88085 | 0.70689 | -0.25950 | 0.19082 | 6.75 |
| 1.0 | -0.46896 | -0.43443 | -0.78465 | -0.39330 | 0.67880 | -0.18257 | 0.05393 | 6.75 |
| 1.33 | -0.21338 | -0.19496 | -0.49176 | -0.10813 | 0.75179 | -0.14053 | 0.10302 | 6.75 |
| 2.0 | 0.18957 | 0.19878 | 0.00967 | 0.26337 | 0.76837 | -0.09054 | 0.00000 | 6.75 |
| 2.5 | 0.39220 | 0.40602 | 0.21398 | 0.46080 | 0.78610 | -0.07843 | 0.02262 | 6.75 |
| 3.33 | 0.43825 | 0.44516 | 0.25356 | 0.51990 | 0.64472 | -0.15694 | 0.10601 | 6.75 |
| 4.0 | 0.51884 | 0.53496 | 0.33880 | 0.57747 | 0.60880 | -0.13843 | 0.08607 | 6.75 |
| 5.0 | 0.57180 | 0.59253 | 0.40860 | 0.61472 | 0.52729 | -0.12964 | 0.00102 | 6.75 |
| 6.67 | 0.46128 | 0.48661 | 0.30185 | 0.49328 | 0.17990 | -0.14539 | 0.00000 | 6.75 |
| 10 | 0.20109 | 0.23102 | 0.03058 | 0.22193 | 0.04697 | -0.15948 | 0.00000 | 6.75 |
| 13.33 | 0.00767 | 0.04912 | -0.20578 | 0.02706 | 0.01170 | -0.17051 | 0.00000 | 6.75 |
| 20 | -0.28476 | -0.25022 | -0.48462 | -0.26092 | 0.06369 | -0.15752 | 0.00000 | 6.75 |
| 33.3 | -0.45285 | -0.41831 | -0.66722 | -0.42229 | 0.17976 | -0.12858 | 0.00000 | 6.75 |
| 50 | -0.52192 | -0.48508 | -0.73906 | -0.48895 | 0.25144 | -0.11006 | 0.00000 | 6.75 |
| 100 | -0.52883 | -0.49429 | -0.74551 | -0.49966 | 0.28897 | -0.10019 | 0.00000 | 6.75 |

**Table B.3**: Regression coefficients for magnitude for equation (B.2) taken from Boore and Atkinson (2008)

| f (Hz) | $b_{lin}$ | $b_1$ | $b_2$ |
|---|---|---|---|
| PGA | -0.360 | -0.640 | -0.14 |
| 0.1 | -0.650 | -0.215 | 0.00 |
| 0.13 | -0.692 | -0.247 | 0.00 |
| 0.2 | -0.750 | -0.291 | 0.00 |
| 0.2 | -0.750 | -0.310 | 0.00 |
| 0.33 | -0.740 | -0.340 | 0.00 |
| 0.5 | -0.730 | -0.380 | 0.00 |
| 0.67 | -0.720 | -0.400 | 0.00 |
| 1.0 | -0.700 | -0.440 | 0.00 |
| 1.33 | -0.690 | -0.470 | 0.00 |
| 2.0 | -0.600 | -0.500 | -0.06 |
| 2.5 | -0.500 | -0.510 | -0.10 |
| 3.33 | -0.440 | -0.520 | -0.14 |
| 4.0 | -0.390 | -0.520 | -0.16 |
| 5.0 | -0.310 | -0.520 | -0.19 |
| 6.67 | -0.280 | -0.530 | -0.18 |
| 10 | -0.250 | -0.600 | -0.13 |
| 13.33 | -0.230 | -0.640 | -0.11 |
| 20 | -0.290 | -0.640 | -0.11 |
| 33.33 | -0.330 | -0.620 | -0.11 |
| 50 | -0.340 | -0.630 | -0.12 |
| 100 | -0.360 | -0.640 | -0.14 |

**Table B.4**: Regression coefficients for site effects for equation (B.2) taken from Boore and Atkinson (2008)

## B.3 Gregor et al. (2002)

Gregor et al. (2002) used a stochastic finite-fault calculation to develop a GMAR for megathrust earthquakes to avoid the uneven sampling of site and source geometries that come with empirical relationships. Empirical calculations also do not account for effects such as rupture propagation, directivity, and source-site geometry in a systematic way and uncertainties in source, path, and site parameters were included via parametric variations.

The resulting PGA and the 5% damped PSA for earthquake magnitudes of 8.0, 8.5, and 9.0 can be calculated using:

$$lnY = c_1 + c_2M + (c_3 + c_4M) * \log(R + \exp(c_5)) + c_6(M - 10)^3 \quad \text{(B.3)}$$

Here, *Y* is again the peak ground motion parameter, *R* is the closest distance to the rupture plane, *M* is the magnitude, and $c_1$-$c_6$ are coefficients fit to rock and soil conditions given in Tables B.5 and B.6. The model holds for earthquakes of $M_w$ =8.0 and higher and accounts for rock- and soil conditions and is based on extrapolating relationships up to Mw=9.0, the magnitude of the Cascadia megathrust earthquake in 1700.

| f(Hz) | $c_1$ | $c_2$ | $c_3$ | $c_4$ | $c_5$ | $c_6$ |
|---|---|---|---|---|---|---|
| PGA | 21.0686 | -1.7712 | -5.0631 | 0.4153 | 4.2 | 0.0017 |
| 0.01 | 20.9932 | -1.7658 | -5.0404 | 0.4132 | 4.2 | 0.0226 |
| 0.05 | 19.347 | -1.519 | -4.9731 | 0.3960 | 4.2 | -0.0155 |
| 0.1 | 30.005 | -2.349 | -6.3862 | 0.5009 | 4.7 | -0.0019 |
| 0.2 | 39.345 | -3.087 | -7.6002 | 0.5972 | 5.1 | 0.0060 |
| 0.33 | 34.787 | -2.899 | -6.7855 | 0.5616 | 4.9 | 0.0256 |
| 0.4 | 33.383 | -2.776 | -6.9595 | 0.5863 | 4.9 | -0.0039 |
| 0.5 | 29.159 | -2.424 | -6.2114 | 0.5216 | 4.7 | 0.0161 |
| 1.0 | 6.528 | -0.406 | -3.1991 | 0.2589 | 3.2 | -0.0225 |
| 2.0 | 8.657 | -0.851 | -2.7398 | 0.2339 | 2.8 | 0.0370 |
| 2.5 | 6.637 | -0.651 | -2.3124 | 0.1879 | 2.8 | 0.0364 |
| 5.0 | 8.013 | -0.943 | -2.4087 | 0.2154 | 2.3 | 0.0647 |

**Table B.5**: Regression coefficients for rock sites taken from Gregor et al. (2002)

| f(Hz) | $c_1$ | $c_2$ | $c_3$ | $c_4$ | $c_5$ | $c_6$ |
|---|---|---|---|---|---|---|
| PGA | 23.861 | 2.274 | -4.88 | 0.4399 | 4.7 | 0.036 |
| 0.01 | 25.451 | 2.420 | 5.1071 | 0.465 | 4.8 | 0.037 |
| 0.05 | 23.294 | 2.161 | 4.8855 | 0.433 | 4.8 | 0.026 |
| 0.1 | 29.969 | 2.725 | 5.8054 | 0.5098 | 5.2 | 0.022 |
| 0.2 | 75.821 | 6.839 | 12.068 | 1.0753 | 6.3 | 0.009 |
| 0.33 | 71.7967 | -6.499 | 11.6056 | 1.0415 | 6.2 | 0.0102 |
| 0.4 | 67.372 | 6.1755 | 11.1567 | 1.0167 | 6.1 | 0.0035 |
| 0.5 | 56.0088 | 5.1176 | -9.5083 | 0.8632 | 5.9 | 0.0164 |
| 0.77 | 26.3013 | 2.4482 | -5.3818 | 0.4957 | 4.8 | 0.0259 |
| 1 | 17.233 | 1.5506 | -4.3287 | 0.393 | 4.2 | 0.0133 |
| 2 | 17.9124 | 1.7505 | -3.815 | 0.3574 | 4.1 | 0.0583 |
| 5 | 7.4856 | -0.836 | -2.0627 | 0.1179 | -0.2 | 0.0821 |

**Table B.6**: Regression coefficients for soil sites taken from Gregor et al. (2002)

# Appendix C: Published Papers

## Introduction

Mass transport deposits (MTDs), the remains of past slope failure events, are a ubiquitous feature along continental margins (Canals et al., 2000; Piper, 2005) showing that submarine mass failures are an integral component in the transport of sediment from the continental shelf down to the abyssal plain. Sampling their physical properties and studying their geometry and morphology, MTDs can be used to investigate the nature of slope failure itself, including the trigger mechanism and the slide kinematics. Through their influence on the depositional environment, MTDs also change the sequence stratigraphy and local fluid flow and thus are important targets for reservoir characterization and resource exploitation (e.g. Yamada et al., 2012). Understanding the flow behavior of subaqueous slides including their ability to reach far distances and to move at a considerable speed, is of major importance for any slope stability hazard assessment.

The following two papers discuss two different aspects of a study conducted on an MTD, located in the Ulleung Basin, an active back-arc basin in the East Sea, South Korea. While one paper focusses on the role of MTDs as hosts for gas hydrate, the other contains the first elements of a slope failure hazard analysis in the Ulleung Basin. Both papers center on the depositional processes as well as the physical properties of the MTD. In the first paper, Scholz et al. (2012) highlight the efficacy of seismic attributes as a means to study MTD-flow behavior. The 3D seismic data helped to understand and define the three-dimensional geometry of the MTD and the slide kinematics involved. The study integrated seismic, core, and log data to show that the typical gas hydrate indicators such as seismic blanking, as well as log-derived increased P- wave velocity and electric resistivity can also be caused by the occurrence of MTDs.

The second paper discusses the physical properties within a MTD, infers its potential to host gas hydrates, and discerns between the intrinsic properties of the MTD and the occurrence of gas hydrate. Using seismic attributes as a descriptive tool, Riedel et al. (2012) show that MTD processes lead to oriented fractures that could constitute a host material for gas hydrate but at the same time complicate the quantification and lead to over-estimation of *in situ* gas hydrate due to anisotropic nature of fractured sediment. Thus, MTDs can significantly influence or alter the host sediment for gas hydrates either providing a better pre-condition or disguising the true amount of hydrate.

The understanding of the depositional history of a MTD is an important component in the basin-wide assessment of gas hydrate as potential resource for Korea and assists in the prediction of coarse-grained sandy sections that are known to represent preferred host sediments for gas hydrates (e.g. Clennell et al., 1999; Torres et al., 2008). The assessment of submarine landslide hazards then will become especially important if gas hydrates are found to be a viable energy resource for South Korea and gas hydrate production leads to a decades-long hydrocarbon-exploitation, mass flow dynamics will become a major issue for production safety.

***Bibliography***

Canals M., Urgeles R., Calafat A.M., 2000, *Deep sea-floor evidence of past ice streams off the Antarctic Peninsula*. Geology, **28**, 31–34

Clennel M.N., Hovland M., Booth J.S., Henry P., Winters W.J., 1999, *Formation of natural gas hydrates in marine sediments: 1. Conceptual model of gas hydrate growth conditioned by host sediment properties*, Journal of Geophysical Research, **104**(B10), 22,985-23,003

Piper D.J.W., 2005, *Late Cenozoic evolution of the continental margin of eastern Canada*, Norwegian Journal of Geology, **85**, 305–318

Riedel M., Bahk J.-J., Scholz N.A., Ryu B.-J., Yoo G.-D., Kim W., Kim G.Y., 2012, *Mass-transport deposits and gas hydrate occurrence in the Ulleung Basin, East Sea – Part 2: Gas hydrate content and fracture-induced anisotropy*, Journal of Marine and Petroleum Geology, **35**, 75-90

Ryu B.-J., Riedel M., Kim J.-H., Hyndman R.D., Lee Y.-J., Chung B.-H., Kim I.-S., 2009, *Gas hydrates in the western deep-water Ulleung Basin, East Sea of Korea*, Journal of Marine and Petroleum Geology, **26**, 1483-1498

Scholz N.A., Riedel M., Bahk J.-J., Yoo D.-G., Ryu B.-J., 2012, *Mass transport deposits and gas hydrate occurrences in the Ulleung Basin, East Sea - Part 1: Mapping sedimentation patterns using seismic coherency*, Journal of Marine and Petroleum Geology, **35**, 91-104

Torres M.E., Tréhu A.M., Cespedes N., Kastner M., Wortmann U.G., Kim J.-H., Long P., Malinverno A., Pohlman J.W., Riedel M., Collett T., 2008, *Methane hydrate formation in turbidite sediments of northern Cascadia, IODP Expedition 311*, Earth and Planetary Science Letters, **271**, 170-180

Yamada Y., Kawamura K., Ikehara K., Ogawa Y., Urgeles R., Mosher D., Chaytor J., Strasser M., 2012, *Submarine mass movements and their consequences*, In: Advances in Natural and Technological Hazard Research, **31**, Y. Yamada et al. (eds.), Springer Science+Business Media B.V, 2012

# Mass-transport deposits and gas hydrate occurrences in the Ulleung Basin, East Sea - Part 1: Mapping sedimentation patterns using seismic coherency


## Abstract

Seismic coherency measures, such as similarity and dip of maximum similarity, were used to characterize mass transport deposits (MTDs) in the Ulleung Basin, East Sea, offshore Korea. Using 2-D and 3-D seismic data several slope failure masses have been identified near drill site UBGH1-4. The MTDs have a distinct seismic character and exhibit physical properties similar to gas hydrate bearing sediment: elevated electrical resistivity and P-wave velocity. Sediments recovered from within the MTDs show a reworked nature with chaotic assemblage of mud-clasts. Additionally, the reflection at the base of MTDs is polarity reversed relative to the seafloor, similarly to the bottom-simulating reflector commonly used to infer the presence of gas hydrates. The MTDs further show regional seismic blanking (absence of internal reflectivity), which is yet another signature often attributed to gas hydrate bearing sediments. At the drill site UBGH1-4, no gas hydrate was recovered in sediment-cores from inside a prominent MTD unit. Instead, pore-filling gas hydrate was recovered only within thin turbidite sand layers near the base of the gas hydrate stability zone. With the analysis of seismic attributes, the seismic character of the prominent MTD (Unit 3) was investigated. The base of the MTD unit exhibits deep grooves interpreted as gliding tracks from either outrunner blocks or large clasts that were dragged along the paleo-seafloor. Similar seismic features were identified on the seafloor although the length of the gliding tracks on the seafloor is much shorter (a few hundred meters to

~1 km), compared to over 10 km long tracks at the base of the MTD. The seismic coherency attributes allowed to estimate the volume of the failed sediment as well as the direction of the flow of sediment. Tracking the MTD and extrapolating its spatial extent from the 3-D seismic volume to adjacent 2-D seismic profiles, a possible source region of this mass failure was defined ~50 km upslope of Site UBGH1-4.

## Introduction

As part of the South-Korean gas hydrate program regional 2-D and 3-D seismic data were acquired in the Ulleung Basin, East Sea, off Korea (Fig. 1), to characterize the sediment-depositional environments and map possible gas hydrate accumulations (Ryu et al., 2009; Park, 2008; Park et al., 2008; Lee et al., 2005).

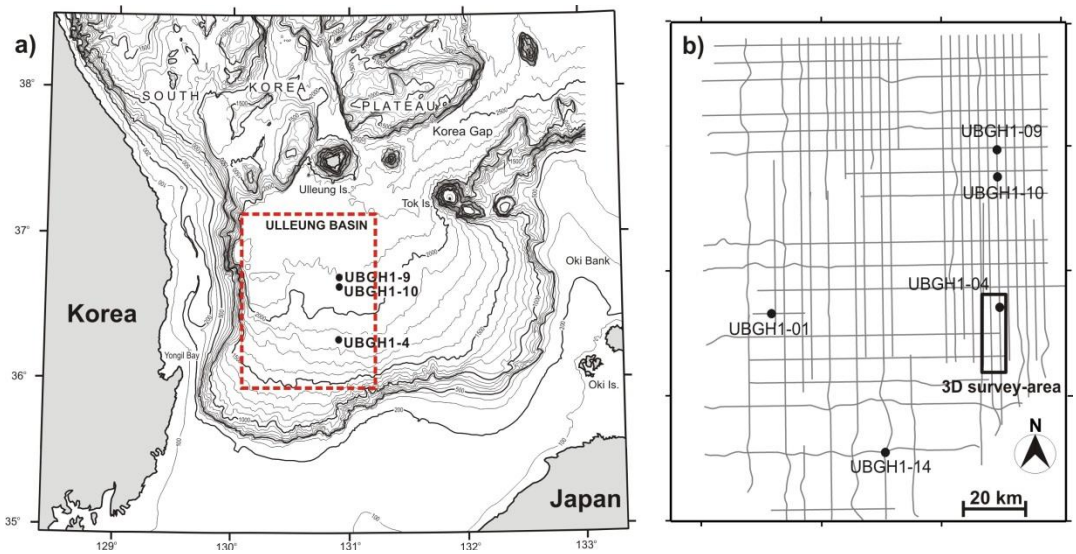


**Fig. 1**: Ulleung Basin, East Sea, South Korea; a) location of the Ulleung Basin in the East Sea; b) Area (see inset-box in a)) of the 2-D seismic lines and the 3-D survey, as well as the location of the drilling sites from UBGH1 expedition of 2007

The Ulleung Basin Gas Hydrate Drilling Expedition 1 (UBGH1) in 2007 (see Fig. 1 for location of drill sites) consisted of a logging-while-drilling (LWD) operation at five sites (UBGH1-1, UBGH1-4, UBGH1-9, UBGH1-10, and UBGH1-14), spot-coring operation at three

of those sites (UBGH1-4, UBGH1-9, and UBGH1-10), as well as wire-line logging and vertical seismic profiling at Site UBGH1-9. The core and logging data together with the pre-drilling seismic data were used to assess the gas hydrate potential and to estimate the possible amount of in place methane resource in the basin (Park et al., 2008; Chun et al., 2008).

Regional seismic blanking has initially been considered as an indicator for the presence of gas hydrates within the Ulleung Basin, following similar observations elsewhere (e.g. at the Blake Ridge (Lee and Dillon, 2001) and the Cascadia margin, (Riedel et al., 2002)). However, several authors suggested that sedimentation in the slope regions of the Ulleung Basin is dominated by MTDs, (e.g. Lee et al., 2001; Lee and Kim, 2002; Bahk et al., 2004). Compared to the seafloor the base of the MTDs is polarity reversed indicating a reduction in acoustic impedance. The widespread occurrence of MTDs across the Ulleung Basin together with their polarity-reversed characteristics and an accompanying lack in seismic internal reflectivity can complicate the definition of the base of the gas hydrate stability zone (GHSZ). Seismically the base of the GHSZ is seen as a bottom-simulating reflector (BSR), also having an opposite-to-seafloor reflection polarity. In this study we focus on the characteristics of MTDs in seismic, core, and log data and show that seismic blanking, as well as log-derived increased P- wave velocity and electric resistivity can also be caused by the occurrence of MTDs and not just by pore-filling gas hydrate. The goal is to understand and define the three-dimensional geometry of the MTD especially gliding tracks and outrunner blocks. The understanding of the depositional history of a MTD is an important component in the basin-wide assessment of gas hydrate as potential resource for Korea, and to predict coarse-grained sandy sections that are known to represent preferred host sediments for gas hydrates (e.g. Clennell et al., 1999; Torres et al., 2008). The role of MTDs and possible linkages with gas hydrate occurrences have previously

been studied especially at the Storegga Slide offshore Norway (e.g. Bouriak et al., 2000; Bünz et al., 2005; Mienert et al., 2005). Gas hydrate dissociation may have played a role in the slide-initiation at the Norwegian margin (e.g. Mienert et al., 1998; Vogt and Jung, 2002). Slide mechanics, possible trigger mechanisms, and sliding behaviour such as hydroplaning of the slide have been extensively studied at the Storegga Slide as well (e.g. de Blasio et al., 2005; Gauer et al., 2005; Kvalstad et al 2005).

Understanding the flow behaviour of subaqueous slides is of major importance to the protection of any existing or future offshore infrastructure. The Ulleung Basin has experienced a large number of slope failures in the past and results show that it most likely is still experiencing underwater sliding events.

This study presents the first elements of a risk analysis in the Ulleung Basin that will become especially necessary if gas hydrates are found to be a viable energy resource for South Korea. With the completion of UBGH1 and recently also UBGH2, an assessment of local gas hydrate occurrence has already been conducted (Kim et al., 2011; Bahk et al., 2011a) and gas hydrate production tests will soon be under way. Should those test results demonstrate the feasibility of a decades-long hydrocarbon-exploitation based on gas hydrates then mass flow dynamics will become a major issue for production safety.

With this in mind we want to highlight the efficacy of seismic attributes such as the measurement of coherency (or similarity) between neighboring traces as a means to thoroughly study MTD flow behaviour as well as to discern MTDs from gas hydrate hosting sediment and to characterize important sediment features. Our interpretation of seismic coherency is guided by comparisons with studies by Nissen et al. (1999) from the Nigerian continental slope, Prior et al. (1982) from the Kitimat-slide, off British Columbia, as well as by Posamentier and Walker

(2006). In the companion paper by Riedel et al., the LWD logging data are further used to estimate gas hydrate concentrations and linking fracture patterns seen on electrical resistivity data to the seismically defined flow-pattern in the MTD.

**Geologic setting of the Ulleung Basin**

The Ulleung Basin, a continental back-arc basin, lies on the eastern margin of the Eurasian Plate and is separated from the Pacific by the Japanese Islands. The East Sea, to the west of Japan, has its origin in the Oligocene when crustal thinning and seafloor spreading led to the development of the Ulleung, Japan, and Yamato basins (e.g. Barg, 1987; Lee et al., 2001; Ryu et al., 2009).

These basins in the East Sea are separated from each other by the Korea Gap and continental remnants such as the Oki Bank and the Korea Plateau (Park, 2007). The Ulleung Basin is bound by the steep slopes of the Korean Peninsula to the west and by the Korea Plateau to the north (Fig. 1a). To the east and southeast lie the more gentle slopes of Oki Bank and the Japanese Islands. The ocean floor of the Ulleung Basin is fairly smooth in the center, and deepens north-eastwards from 1000 m water depth on the basin margin to about 2300 m near the Korea Gap (Park, 2007). The crustal thickness decreases from 10 km in the south to 5 km in the central part, thus having a wedge-like shape (Lee and Suk, 1998). This was interpreted by Lee and Suk (1998) as an indication that the main sediment source and the location of maximum subsidence lies in the south. As the depositional energy of the mass transport processes dropped with increasing distance to the source, interbedded turbidites and hemipelagic sediments were deposited further to the northeast of the basin. The mass transport processes were reduced in scale but reached regions further to the north.

Lee et al. (2001) mention two distinct phases consisting of widespread distribution of MTDs in the late Neogene and extensive turbidite and hemipelagic sedimentation in the Pleistocene and Holocene. Uplift and deformation in the south and southeast, having started in the middle Miocene due to back-arc closure, are seen as causes for the enormous volumes of sediments found in the basin (Lee et al., 2001). The southern basin subsided due to sediment loading and lithospheric cooling. The Ulleung Basin margin experienced a subsidence rate of 700 m/m.y. until the middle Miocene, with an especially rapid initial phase, characteristic for the Ulleung Basin (Chough and Barg, 1987). This was followed by a phase of uplifting in the late Miocene and slight subsidence in the Pliocene-Pleistocene. As the number of mass transport flows decreased in the late Miocene, a prominent change in sedimentary facies in the central basin occurred, with a transition from coarse-grained, high energy deposits to more fine-grained -low-energy turbidites and hemipelagic sediments (Lee and Suk, 1998). With its large number of MTDs the sedimentation pattern in the Ulleung Basin is different from the sedimentation in the Japan and Yamato basins in the East Sea, which both are dominated by slowly deposited, hemipelagic sediments, and turbidites.

**Data and methods**

The data-set to investigate the area around drill site UBGH1-4 consists of 2-D and 3-D multichannel seismic lines (Fig. 1b). The data were acquired in 2005 and 2006, using the research vessel TAMHAE-II of the Korea Institute of Geoscience and Mineral Resources (KIGAM). The seismic profiles were acquired using an airgun source volume of 4.9 l (1035 $in^3$), and a streamer of 240 channels, with shot and group intervals of 12.5 m and 6.25 m, respectively. The 3-D data set as a bin-spacing of 25 m by 25 m,with a total of 320 inlines and 1000 cross-lines (Fig. 1b). The 3-D data set covers an area of 400 $km^2$ surrounding the drilling site UBGH1-

4. The frequency spectrum of the 2-D and 3-D seismic surveys ranges from 10 to 80 Hz, but dominantly at 50 Hz, which corresponds to an approximate vertical resolution of 8m (using average seismic velocities of 1600 m/s).

To map the MTD and to depict its features, geometric attributes such as seismic coherency (semblance) and dip of maximum similarity were used. Seismic coherency is a measure of similarity between adjacent traces with low values indicating the presence of fractures, faults, and other incoherent features. Seismic coherency is able to show these features more clearly than common seismic amplitude data (e.g. Bahorich and Farmer, 1995; Marfurt et al., 1998; Chopra, 2002; Chopra and Marfurt, 2006). The algorithm used in this paper is based on calculating the semblance, which is a form of seismic coherency. This is done by computing the cross-correlation between adjacent traces as a function of variable time lag (e.g. Marfurt et al., 1998). The method of calculating the semblance dates back to the work of Taner and Koehler (1969) who used it as a tool for conventional seismic velocity analysis. The advantage of this method next to obtaining clearer structural images is the absence of an interpretative bias as the stratigraphic analysis is done before picking faults. Additionally, the seismic attribute dip of maximum similarity, which gives the rate at which similarity changes, is very effective in depicting features such as channels and fractures where the similarity between traces decreases quickly.

The interpretation of the features found was guided by the results of Nissen et al. (1999), who used seismic coherency to interpret the depositional settings of a MTD offshore Nigeria, by Prior et al. (1982) on the Kitimat-slide offshore British Columbia, Canada, as well as by the research of Posamentier and Walker (2006).

In addition to the 2-D and 3-D seismic data, the interpretation was supported by LWD-derived resistivity, P-wave velocity, gamma ray, and porosity at drill site UBGH1-4, as well as split-core images, and physical properties (density, shear strength) of the recovered core to define the vertical extent of the MTD and related seismic signatures.

**Seismic attributes**

Several examples of seismic lines cutting through the 3-D seismic data volume are analyzed for the illustration of the observed reflection characteristics and sedimentary units (Fig. 2). The seismic lines in Fig. 2 (see Fig. 3 for the location of the arbitrary lines) are chosen arbitrarily through the seismic volume but are overall in the direction of and perpendicular to the assumed flow-path of the main MTD.

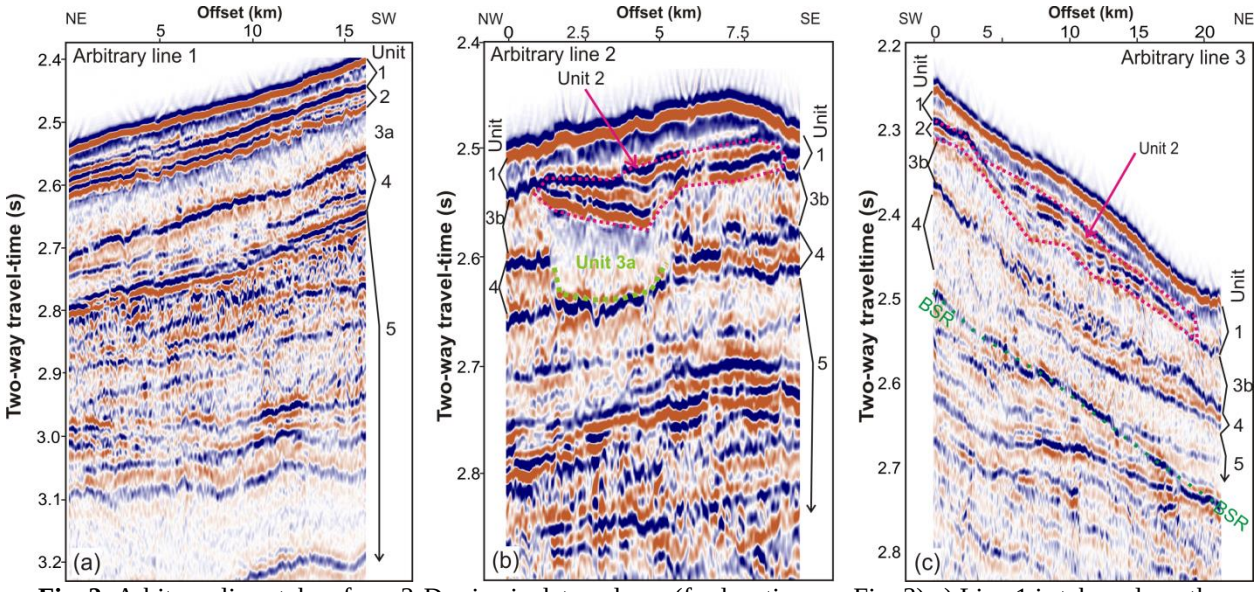


**Fig. 2**: Arbitrary lines taken from 3-D seismic data volume (for location see Fig. 3) a) Line 1 is taken along the major MTD (Unit 3a) and individual units are highlighted; b) Line 2 crossing the MTD Unit 3 parallel to Line 1 through the 3-D volume, but containing only Sub-Unit 3b, green dashed line indicating the bottom horizon of Units 3a and 3b; c) Line 3 cutting through Sub-Unit 3b with indication of location of the assumed BSR

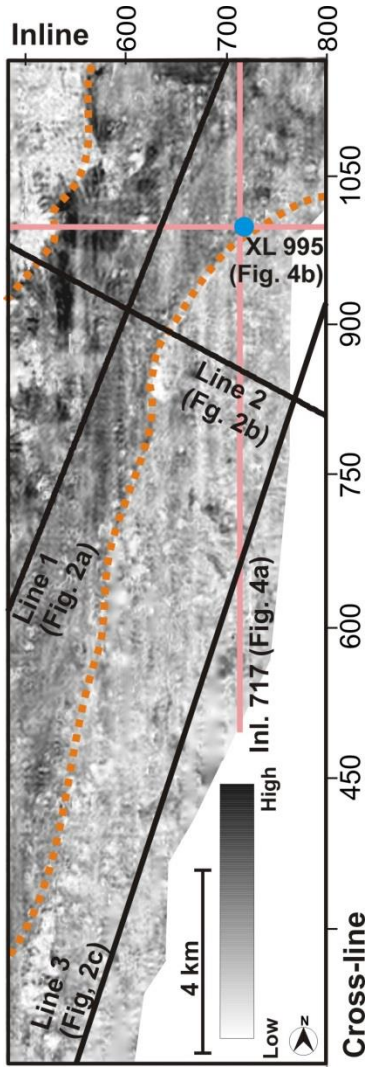


**Fig. 3**: Map of the amplitudes contained in part of the 3-D data set belonging to the top of Unit 3 (MTD) reflection event. This unit was subdivided into two units: 3a and 3b, using the distinct reflection amplitude characteristics. The extent of Sub-unit 3a is highlighted by the orange dashed line. Location of the three arbitrary lines in Figs. 2a, 2b, and 2c shown in yellow; locations of the in-line and cross-line containing Site UBGH1-4 shown in light pink

Based on the absence of distinct sediment layers as well as on the internal blanking and prominent top and bottom reflections in seismic amplitude data we identify five separate units, henceforth called Units 1 to 5:

Unit 1 is comprised of the most recent MTD, identified as an seismically almost transparent layer right beneath the seafloor reflection. Based on a P-wave velocity of 1500 m/s this unit has a thickness of 25 m at Site UBGH1-4. Underneath, Unit 2 is made up of about 30-40

m thick relatively uniform, seafloor-parallel reflections, comprises hemipelagic and pelagic sediments mixed with thin turbidites (Bahk et al., 2011b).

The main focus of our study, Unit 3, is underlying the stratified hemipelagic and pelagic section. Based mainly on differences in the internal reflection characteristics and in the amplitude of the top-reflection (Fig. 3), Unit 3 was divided into two Sub-units 3a and 3b. The arbitrary lines in Fig. 2 provide a good image of Sub-Unit 3a cutting through older deposits. Sub-Unit 3a shows almost no internal reflections (Fig. 2a), while Sub-Unit 3b reveals internal, chaotic reflections of only a few tens of meters (Fig. 2b, c).

Below Unit 3, lies an approximately 70 m thick stratigraphic sequence (labeled Unit 4), which is composed of a mix of hemipelagic sediments and a series of thinner MTDs. The base of Unit 4 is difficult to assess as it is near (or at) the depth of the BSR. In part, Unit 4 resembles a similar seismic character as Unit 2. The sediments below Unit 4 show intervals of chaotic reflections caused by the presence of free gas below the GHSZ. We have not defined deeper units as they are not essential for investigating the sedimentation history of the MTD (Unit 3a and b) and the presence of gas hydrates and/or free gas below the GHSZ.

Two prominent reflections framing the top and bottom of Unit 3 as well as the present-day seafloor were manually picked to delineate this MTD and aid in subsequent volume-calculations. The picks of the different horizons were then used to image different aspects of the data such as time (depth), amplitude, similarity (coherence), and dip of maximum similarity. They are useful tools to better describe the sedimentation characteristics and the behaviour of the flow. Fig. 4 shows the two-way travel-time for both the top and bottom reflection of the MTD (including the picks of the adjacent 2-D lines).

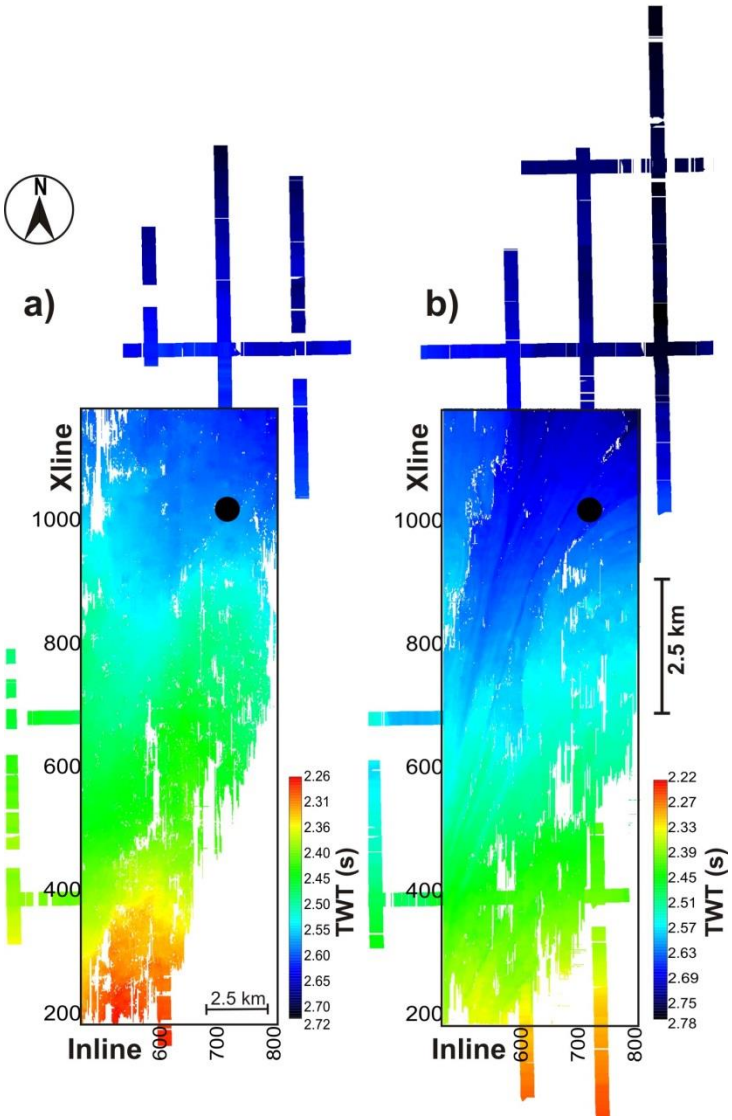


**Fig. 4**: Two-way travel-time for the (a) top and (b) bottom reflection of the MTD including picks of the 3-D data-volume as well as adjacent 2-D seismic lines

The travel-time of the upper reflection increases steadily from the southwest to the northeast with a markedly larger increase in TWT in the north-eastern corner of the mapped horizon. The bottom horizon of the MTD has a similar depth increase which trends in the same direction (especially when including the 2-D seismic lines). It additionally reveals a broadening distinct graben-like incision, forming a fan-like topography which is only weakly observable in the upper reflection. Equally noteworthy is the presence of long, straight, and deep grooves. Fig. 5 shows the reflection amplitude, similarity, and dip of maximum similarity attributes for the MTD-base.

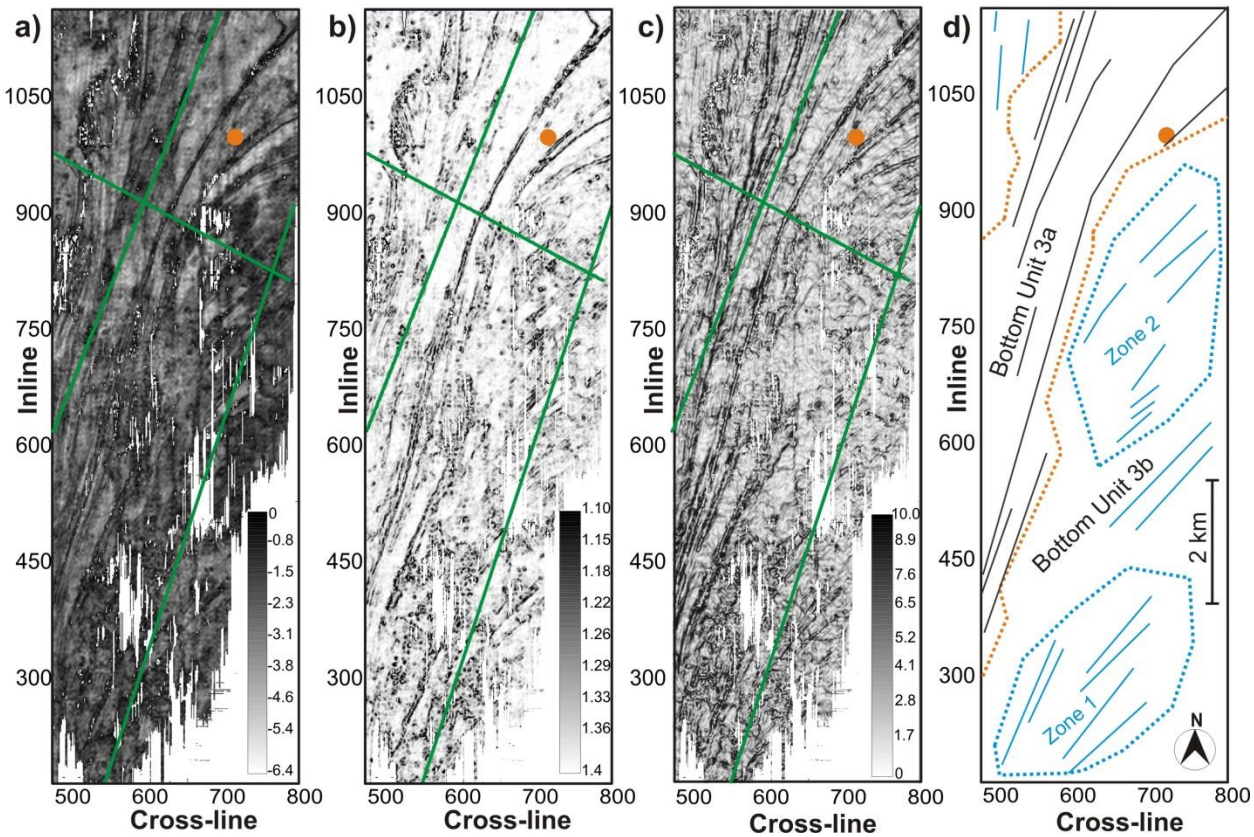


**Fig. 5**: Bottom horizon of MTD, showing (a) amplitude, (b) similarity, and (c) dip of maximum similarity; green lines showing the locations of the arbitrary lines (Figures 2a, 2b, and 2c), orange dot shows the location of drill site UBGH1-4; (d) interpretation of the features found in 5a - 5c: dotted orange line outlines the base of Sub-unit 3a, blue-dotted line outlines two zones of Sub-unit 3b with different character in striations similar to the grooves of Sub-unit 3a, but with different orientation and length

Overall, the amplitude of the bottom reflection (Fig. 5a) is quite homogeneous compared to the top-reflection (Fig. 3). It additionally reveals striations that are low in amplitude. However, the seismic similarity image (Fig. 5b) shows a clearer image of these striations (darker colors represent low seismic similarity). The dip of maximum similarity (Fig. 5c), an attribute representing the rate of change in similarity, increases the sharpness and thus reveals a larger number of these groove-like features compared to amplitude or similarity. The grooves have a distinctive pattern, mainly consisting of elongated closely spaced pairs of bands lower in reflection amplitude and similarity with high dip of maximum similarity values (Fig. 6). The

grooves cross-cut through the study area from the southwest to the northeast, then bend slightly, and finally develop into a fan-like run-out near drill site UBGH1-4.

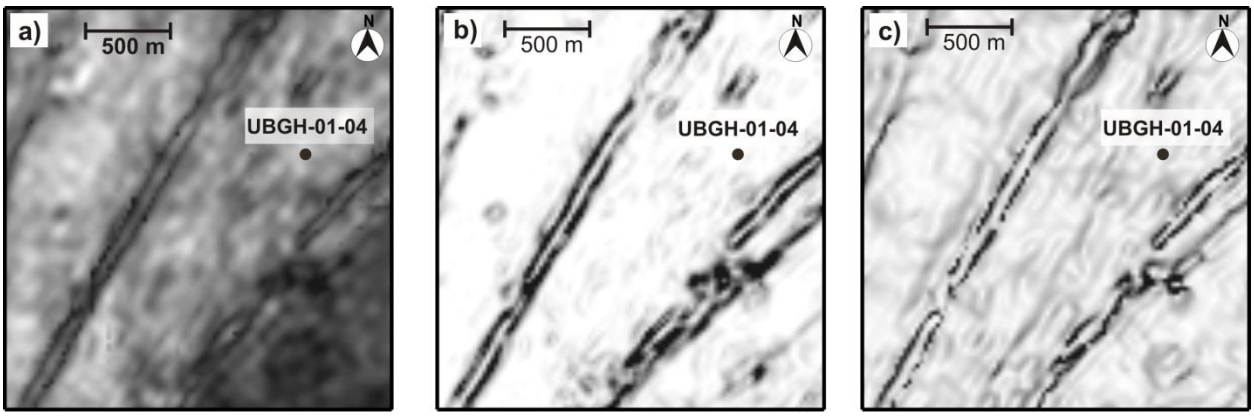


**Figure 6**: Zoom on two prominent grooves near the drill site UBGH1-4 showing (a) amplitude, (b) similarity, and (c) dip of maximum similarity. Same color-bars and scales as in Fig. 5 are used

In contrast to the area covered by Sub-unit 3a, regions in the south and south-east of the bottom-reflection belonging to Sub-unit 3b have a rather chaotic distribution of features with overall low coherence values (area labeled Zone 1 in Fig. 6d). By means of the seismic coherence attribute, those strongly discontinuous features which can't be seen in Fig. 3 now become apparent, thereby revealing a deflection towards the east. This deflection is even stronger than the one seen in the striations of the bottom reflection within Sub-unit 3a. The change in the degree of coherence between the north-western and south-eastern parts is consistent with the change in the internal reflection characteristics as seen in Figs. 2a, 2b, and 2c. This shift in seismic character as well as coherence suggests a different deposition mechanism for the Sub-units 3a and 3b. Furthermore, grooves belonging to Sub-unit 3a strike at angles between 20º and 40 º when measured clockwise from the north. The striations belonging to Unit 3b all show an angle of about 50º, being much shorter in length.

*Comparison to the seismic characteristics of the seafloor*

To be able to reconstruct the depositional history of the MTD Unit 3 and its features, we calculated the same seismic attributes for the seafloor (Fig. 7), which itself is the top of the most recent MTD in the study area.

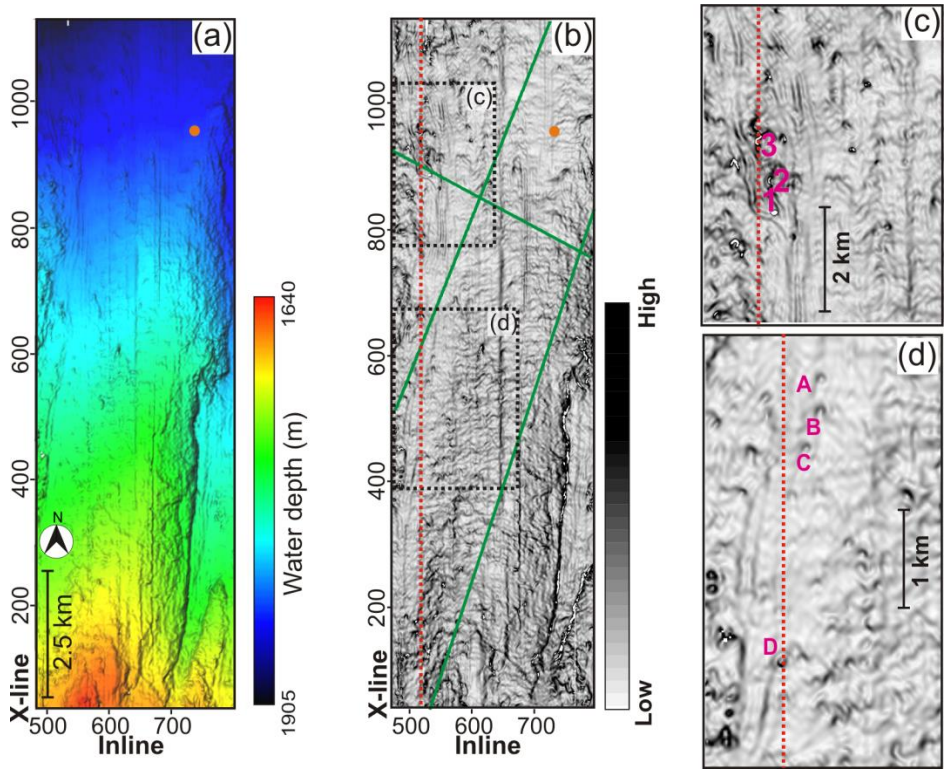


**Fig. 7**: Seismic attributes of the seafloor: a) depth as two-way travel-time (TWT), b) dip of maximum similarity, c) zoom of portion of seafloor with outrunner blocks, and d) zoom of seafloor with distinct flow-pattern (grooves) around a series of outrunner blocks. The red line is inline 521 shown in Fig. 8

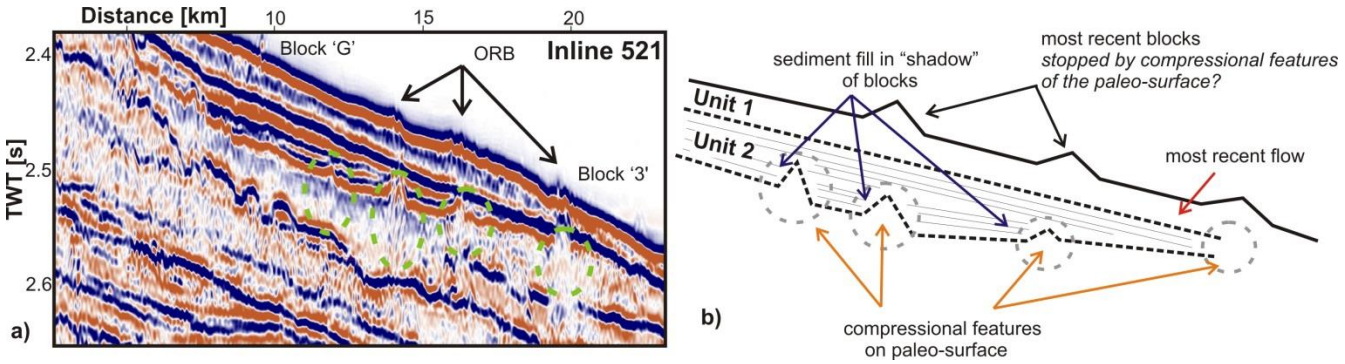


**Fig. 8**: a) seismic amplitude data of inline 521 showing the outrunner blocks (ORBs) on the seafloor with the underlying compressional features as indicated by the green circles; b) interpretation of the geometry in inline 521 (drawing not to scale)

The seafloor reflection shows lower absolute values in the rate of change in similarity compared to the bottom horizon of Unit 3 and a stronger varying topography. A prominent saddle-like structure striking southwest-northeast is seen. The shallower southern portion of the 3-D data coverage has a much rougher character in seafloor-topography than the structural low to the north. Figs, 7c and 7d are detailed views of seafloor-features that are located in the north-western part of the 3-D seismic data coverage. Three small seafloor elevations (labeled A, B, C, and D in Fig. 7c) are associated with short grooves, similar to those seen at the base of the MTD (Sub-unit 3a) initiating in the northwest corner of the present seafloor. Fig. 7d shows several larger blocks that seem to have been passed by other material, as suggested by grooves bending around them. The consistently high values in the dip of maximum similarity in Figs. 7b, 7c, and 7d running straight from north to south are due to acquisition foot-print and insufficient statics correction. The seafloor blocks (labeled A, B, C, and D in Fig. 7d) seem to have travelled past one another on their way down the slope stopping approximately in line with each other. Also, these three blocks are linked to short, a few hundred meter long grooves. The features in Fig. 7c (labeled 1, 2, and 3), however, appear to have been blocking subsequent material that flowed down slope, as seen by the grooves bending around them. This shows that the material of the MTD (Unit 1) did not flow as a single mass, but likely consists of several events and larger blocks of material that slid past each other. It is also worth noting that the outrunner blocks seen on top of the seafloor are influenced by earlier topographic features (Fig. 8). Elevated portions of the top of the MTD (Unit 3) have apparently influenced subsequent deposition up to the current seafloor. Mini-basins have developed in the shadow of the older blocks but must have not been completely filled by the time of the most-recent MTD event, to still influence modern seafloor topography.

**Sedimentology and physical properties**

The identification of the five units within the upper-most 200 mbsf was based on the seismic reflection character (as depicted in the arbitrary lines shown in Fig. 2). At Site UBGH1-4, LWD-data as well as spot-coring with physical property measurements further allow to describe these units in terms of their sedimentology and physical properties.

The top-Unit 1 shows no internal seismic reflectivity. Photographs of the top core acquired at this site reveal sediments of chaotic (blocky) nature as well as strong internal deformation typical for MTDs (Fig. 9a-c).

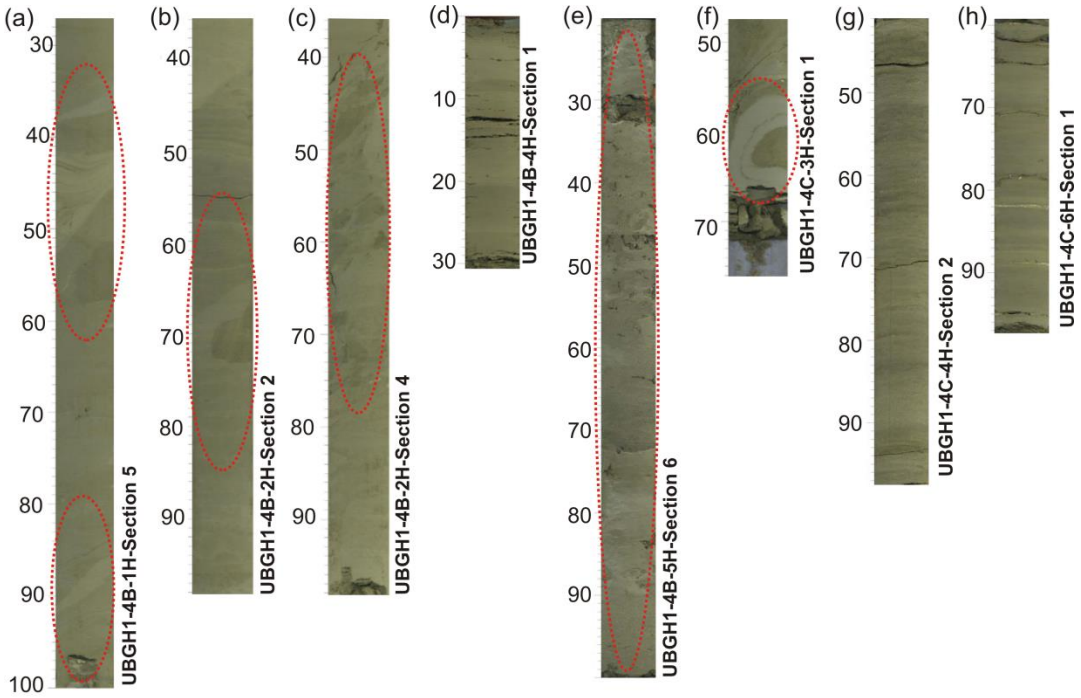


**Fig. 9**: Examples for core images from Site UBGH1-4: a) Core UBGH1-4B-1H, sections 5, b) Core UBGH1-4B-2H section 2, c) and Core UBGH1-4B-2H section 4 showing reworked nature of the top-MTD of Unit-1; d) Core UBGH1-4B-4H section 1 of hemi-pelagic sediment in Unit 2; e) core UBGH1-4B-5H, section 6 from the top of MTD Unit 3; f) core UBGH1-4C-3H section 1; g) core UBGH1-4C-4H section 2 with hemipelagic layered mud; h) Core UBGH1-4C-6H, section 1 with interbedded thin sandy turbidites and hemipelagic mud; red ellipses show parts with reworked, disturbed sediment used to identify this section as a MTD

The sediments show clear signs of stratigraphic disturbance and reworked material. Two cores taken between 60 and 70 mbsf (UBGH1-4B-4H and UBGH1-4B -5H) showing a clear

transition from the hemipelagic sedimentation in Unit 2 (Fig. 9d) to the underlying MTD - Unit 3 (Fig. 9e). Cores taken through the base of Unit 3 (UBGH1-4C-3H) show a transition from strongly reworked sediments (Fig. 9f) to an underlying sequence of predominant low-energy deposition and hemipelagic sediments (Fig. 9g) in core UBGH1-4C-4H. Deeper portion of Unit 4 show a mix of thin, only few centimeter thick sandy turbidites (Fig. 9h) and mud-dominated, un-deformed hemipelagic sediment in core UBGH1-4C-6H. The thin sandy turbidites were gas-hydrate bearing as identified from pore-water chlorinity freshening and infrared core imaging (Kim et al., 2011).

These observations can be tied to the log LWD-data (Fig. 10). A time-depth conversion was obtained from tying the seafloor, and the top, and bottom of the MTD (Unit 3) to the seismic data, followed by integration of the velocity log to increase resolution of the time-depth conversion. Log properties obtained by LWD (Gamma-ray, P-wave velocity, electrical resistivity, density, and neutron porosity) are compared in Fig. 10: the P-wave velocity, electrical resistivity, and density show a marked increase over the interval of the MTD (Unit 3) whereas porosity and gamma-ray values decreased.

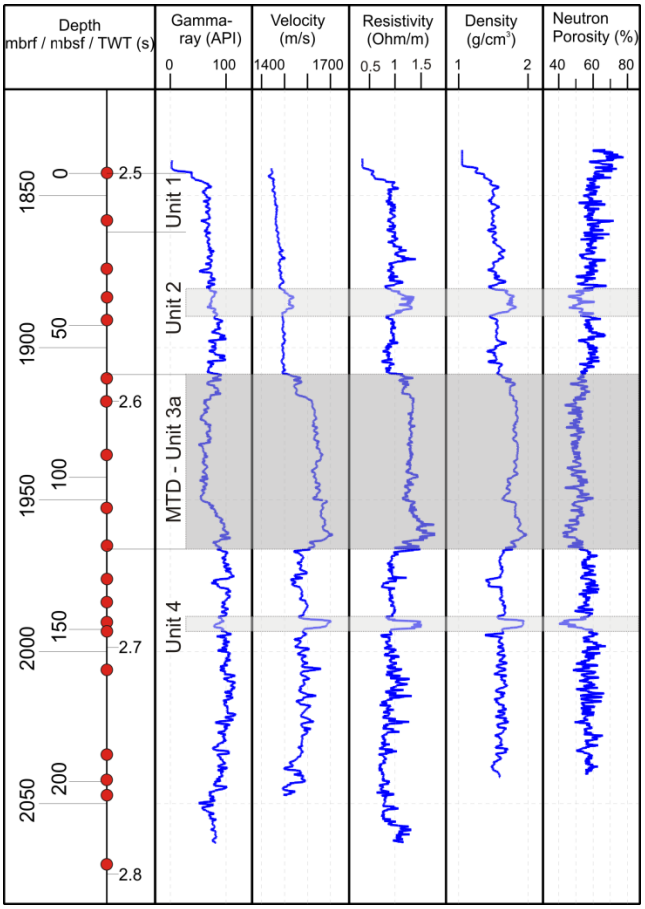


**Fig. 10**: Logging-While-Drilling (LWD) results for drill site UBGH1-4; from left to right: Depth (in meter below rig floor (mbrf), meter below seafloor (mbsf) and two-way time (TWT) in seconds, conversion control points after velocity integration are shown as red dots), Gamma-ray, P-wave velocity, electrical resistivity (ring), bulk density, and neutron porosity; grey box highlights the location of Unit 3a

The synthetic seismogram (Fig. 11) calculated using a wavelet derived from the 3-D seismic data and utilizing the LWD logs of velocity and density show an overall good correlation to the acquired 3-D data, especially for the prominent reflections attributed to the MTD (Unit 3) and base of gas hydrate stability. Changes in physical properties are gradational within the MTD (Unit 3), thus the synthetic seismogram reveals a lack of significant reflections. A tie of the LWD data to the seismic volume is shown in Fig. 12 for the inline and cross-line at Site UBGH1-4.

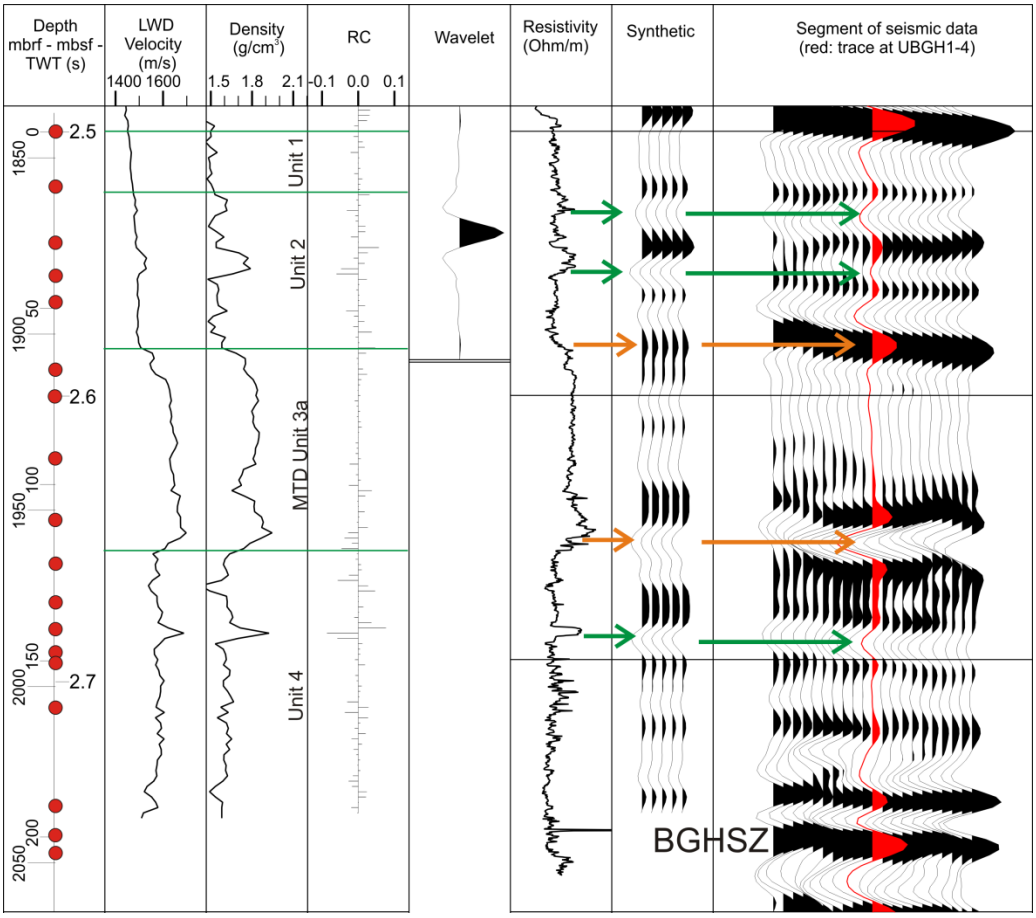


**Fig. 11:** Synthetic seismogram using the Logging-While-Drilling (LWD) P-wave velocity and bulk density logs at Site UBGH1-4 and a seismic wavelet extracted from the 3-D seismic data volume. Top, and base reflection of the MTD units correspond well to the real data (orange arrows). Also, three smaller-MTDs identified in the log do show some correlation to the real data (green arrows)

It is worth to point out two additional although much thinner zones similar to the main MTD (Unit 3) in their log-property trends. The first interval is about 10 m thick and occurs at a depth of 38 to 48 mbsf (2.544 - 2.555 s TWT). This interval is situated within seismic Unit 2, but can't be fully resolved by the frequency range of the seismic data (dominantly 50 Hz, equivalent to a spatial resolution of about 8 m, using a log-derived velocity of 1525 m/s and a resolution limit of 1/4 of the wavelength).

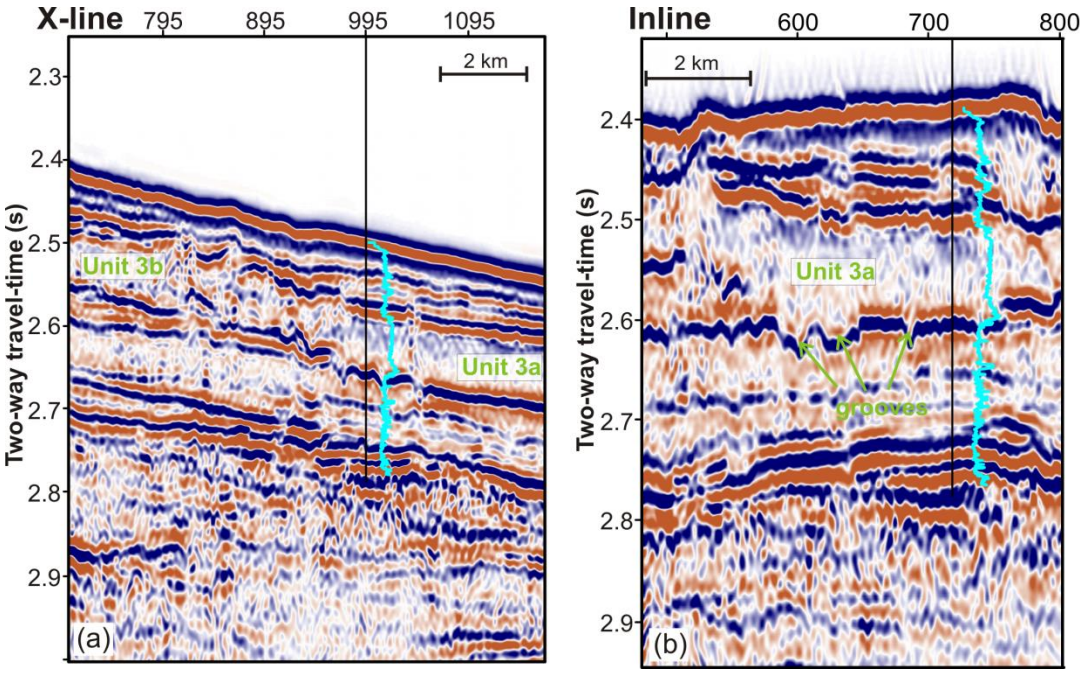


**Fig. 12**: a) seismic line 717 with resistivity-log from borehole UBGH1-4 shown in blue; b) cross-line number 955 with resistivity-log; note the grooves at the bottom of Unit 3a

The second interval is only about 4 m thick (148 - 152 mbsf, 2.680 - 2.685 s TWT). It is located within seismic Unit 5 and coincides with a faint seismic reflection (polarity reversed relative to the seafloor). The fact that this lower zone stands out seismically may be related to the overall lack of other impedance contrasts in the immediate vicinity of this reflection, whereas the shallower MTD (though twice as thick) is within a package of more internal acoustic variability.

The sediment-cores collected at Site UBGH1-4 allowed sedimentological descriptions and detailed physical property measurements (Fig. 13). Porosity and bulk density measured on the top three cores in hole UBGH1-4B as well as the bottom core in Hole UBGH1-4C (UBGH1-4C-6H) match overall fairly well with the LWD data. Larger discrepancies exist around the top and base of the MTD (Unit 3), which may be the result of the complex reworked nature of the sediments, and limited useful zones on the core for physical property measurements due to post-recovery drying and disruption of the sediments. However, marked differences in shear strength, sand-content, and grain density occur around the top and base of Unit 3. The sediments from

core UBGH1-4C-3H situated within the MTD (Unit 3) have higher sand and lower silt content in contrast to sediments from core UBGH1-4C-4H situated below the MTD (Unit 3). These two cores also show a drop in grain density and a marked increase in shear strength across the lower boundary of the MTD (Unit 3).

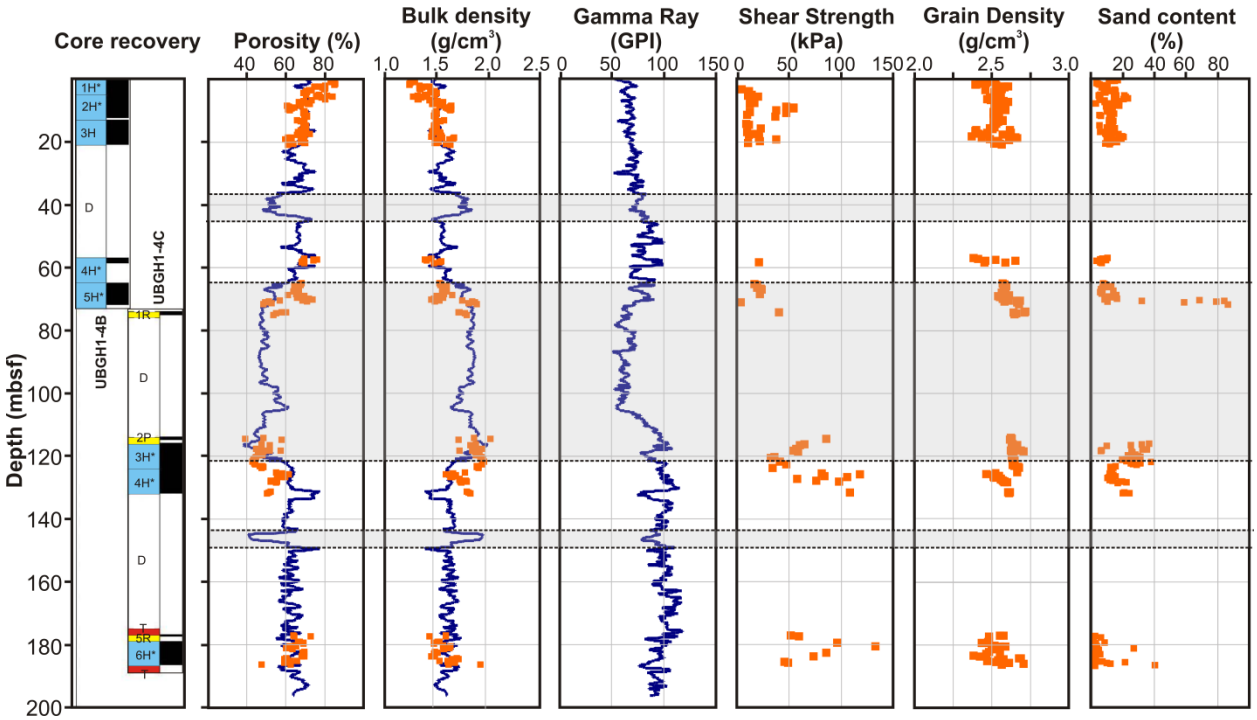


**Fig. 13**: Physical properties of the recovered core (orange squares), compared to LWD-results (blue lines). From left to right: Core recovery in Hole UBGH1-4B and UBGH1-4C (blue boxes indicate intended length of core, black adjacent boxes show actually achieved recovery), porosity, bulk density, gamma-ray, shear strength, grain density, sand content. [Core-naming convention: H: hydraulic piston core, R: rotary pressure core, P: percussion pressure core, T: temperature tool, D: drilled interval; cores annotated by asterisk are shown in Fig. 9]

**Physical dimensions of Unit 3**

Top and bottom of Unit 3 are used to estimate the extent, thickness, and volume of the MTD. Where possible we followed the MTD from inside the 3-D coverage to the overlapping and adjacent 2-D seismic lines to assess its physical dimensions. Using the picked horizons on both, the 3-D volume and 2-D seismic lines, the approximate surface area of the MTD was defined (Fig. 14a). The estimated spatial extent of the mass transport deposit amounts to about 210km$^2$. The thickness of Unit 3 was calculated using velocity from the LWD data and small

regions where picking of the horizons was impossible were interpolated using a gridding-algorithm (Fig. 14b).

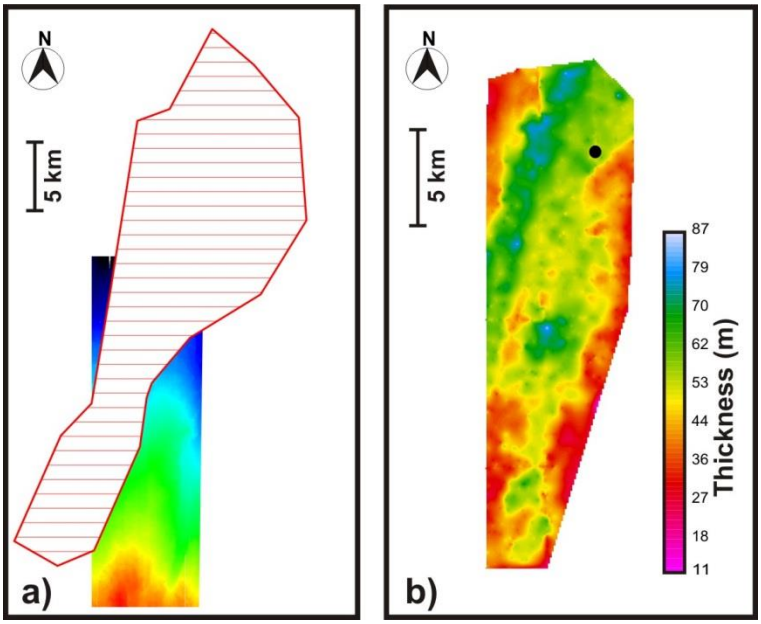


**Fig. 14**: a) Spatial extent and b) thickness of Unit 3; the spatial extent was estimated by including picks of the 3-D volume and adjacent 2-D lines

With an estimated MTD-volume of 1.28 x $10^{10}$ $m^3$ and using the empirical relationship by De Blasio et al (2005) between volume *V* and flow-speed *c* of the form $c = V^{1/6}$, the MTD may have moved down-slope with a speed of about 50 m/s. Where the slope-angle of the paleo-seafloor decreased in the main basin floor the MTD flow started to spread out laterally. The total area covered by the MTD (and thus total volume) cannot be completely calculated as the zone where its thickness is below seismic detection limits cannot be determined. Thus the inferred velocity is probably an approximate lower bound.

Inferring the topography of the paleo-surface and flow direction of the MTD from the seismic attributes shown in Fig. 5, we projected the infill path to a possible source region, which seems to lie somewhere along the southern basin rim about 50km to the south of the 3D data set at current water depths of around 1000m (Fig. 15).

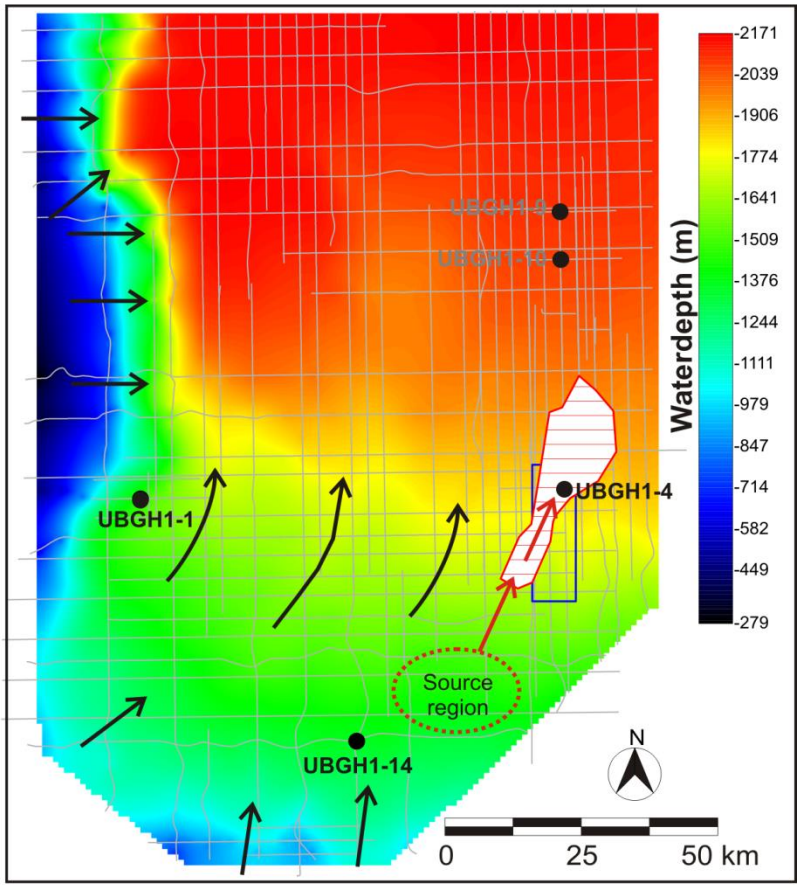


**Fig. 15**: Interpretation of possible flow-direction of recent MTDs (black arrows, perpendicular to bathymetric lines) and mapped paleo-MTD (red arrows) with possible source region (red dotted zone)

The MTD was likely sliding downslope into the northeast direction towards drill-site UBGH1-4, which is slightly rotated further east from inferred modern tracking-paths based on current seafloor topography. The MTD top reflection displays a rather rugged surface topography (e.g. Fig. 2c, and 7b), which could be due to buttressing mechanisms causing sediment accumulation on top of the flow body as described by Garziglia et al. (2008). The compressional features observed in our data-set show similarities to the pressure ridges in Nissen et al. (1999), but are different from those described by Prior et al. (1982), who showed a feature much larger in scale having a terrace-like shape. Compared to the descriptions of Prior et al. (1982), the elevations seen in our data are confined to a smaller area and the undulating character of the pressure ridges is missing.

Arbitrary line 1 (Fig. 2a) is also used to determine the dip-angle of the current seafloor and the base of the MTD. Assuming a water velocity of 1485 m/s, the seafloor dips gently with an angle of ~0.38º. The paleo-seafloor representing the gliding plane of the MTD is dipping at a slope as low as 0.42º to 0.45º and steepens only slightly to a value 2.2 º towards the south-western corner of the 3-D data coverage area. The range in dip-values is obtained by assuming sediment interval-velocities varying between 1500 m/s and 1600 m/s.

**Sliding processes**

The several broad scars (or grooves) which the MTD (Unit 3a) left along the paleo-surface, reach up to ~10 m in depth. Judging from the pattern of scars as seen in Fig. 5 and Fig. 6, the MTD (Unit 3a) seems to have taken a path leading from southwest to northeast, thereby widening slightly towards the north-east to form a fan-like deposition. This widening probably occurred due to the particular topography of the paleo-surface (gliding plane) and may also be associated with a reduction in speed of the flowing sediment mass. Using the dip of maximum similarity attribute it becomes evident that the grooves leading from southwest to northeast have lengths of several kilometers amounting up to more than 10 km. Those tracks have edges with a very large in dip of maximum similarity suggesting steeply inclined sidewalls.

*Bottom scars*

There are two possible explanations for the development of the bottom scars. Comparing Figs. 6b and 6c with the features described by Nissen et al. (1999), the incisions seen in the bottom reflection of the MTD can either be interpreted as gliding tracks of outrunner blocks that separated from the main body of the MTD. Alternatively, they can also be seen as scars caused by sediment clasts that were dragged along with the main MTD-body.

*a) Hypothesis 1: Outrunner blocks*

In the case that the grooves were caused by material that outran the main body, the scars were caused by blocks that would have cut into substrate and left deep, narrow tracks on the paleo-surface. We suggest that the tracks are either part of an older flow-event and have then been filled in by the MTD that makes up Sub-Unit 3a. Or alternatively, they could have been formed by parts of this MTD itself, outrunning the main body which subsequently filled the fresh gliding tracks. The decrease in shear strength and bulk density, which was observed beneath the bottom of the MTD Unit 3 (Fig. 13) supports the latter possibility and could be an explanation for the observation that although the gliding tracks just had formed, they weren't eroded by the sliding material that followed. The length of the gliding tracks as seen in Figs. 5 and 6, which constitutes the major contribution to the inferred extent of the MTD, leads to the assumption that the outrunner blocks traveled at least 10 km. The grooves are exceeding the area of the 3-D seismic data set and there are no individual blocks seen in the reflection of the bottom horizon. According to Nissen et al. (1999) and Prior et al. (1987), outrunner blocks can be formed by an early spill-over of the MTD material, which separates from the main body due to tensional forces. The reason for this complete separation between blocks and main body can be attributed to hydroplaning. Hydroplaning is thought to occur when the front of a MTD pushes through ambient water giving rise to hydrodynamic pressures, which then deform the frontal part of the flow, thus enabling the penetration of a wedge-shaped layer of water underneath the debris. This layer reduces the basal friction and induces tensile stresses farther behind the front, causing a possible detachment and decoupling with respect to the main slide body. Matching with our observations, distances between the outrunner blocks and the main MTD have been reported to amount to several kilometers in many cases (e.g., Ilstad et al., 2004; de Blasio et al., 2005).

De Blasio et al. (2005), who studied the dynamics of subaqueous gravity flows of the Storegga Slide, considered several possible reasons for such long run-out distances. In addition to hydroplaning as a hypothesis, they also see the progressive reduction in yield strength under a high shear rate as a possible contributing factor to long run-out distances. This is a consequence of a collapsing soil structure and the accompanying increase in pore pressure. The decrease in yield strength may be caused by the mixing with seawater and/or water-rich hemipelagic sediments. De Blasio et al. (2005) also consider the increased mobility of the outrunner blocks in respect to the main body as a result of a combination of the two mechanisms, which they called 'shear wetting'. According to their results, the flow-velocity of MTDs is largely the consequence of an equilibrium between the component of the gravity force parallel to the ground-surface and the drag force caused by water. Another contributing factor is the internal friction at the base of the MTD body. De Blasio et al (2005) state that the maximum flow-velocity for hydroplaning scales with $V^{1/6}$, where V is the volume of the MTD and that the flow-velocity of the front is the highest velocity throughout the flow-unit.

*b) Hypothesis 2: Embedded sediment clasts*

Alternatively, the scars or striations could be interpreted as erosional features formed by embedded clasts at the base of the MTD (e.g. Posamentier and Walker, 2006). Such embedded clasts within a MTD would be seismically visible, likely in form of chaotic reflections, or short reflector-elements, such as seen within Sub-Unit 3b. Iverson (1997) states that surge heads carry the greatest concentration of large sediment clasts within a MTD. He describes the head as relatively dry and as restraining the subsequent more fluid, water-saturated debris. There are two mechanisms by which large clasts accumulate at the head: Either they are acquired in transit of the flow and subsequently retained, or they migrate through the flow-body to the head. The

mechanisms can be attributed to kinetic sieving, selective entrainment or because gravity and boundary drag do not suffice to force the clasts through the small voids, which repeatedly open and close during deformation of the MTD, leaving them as a kind of residue near the front. The grain size segregation mechanisms within MTDs are complicated and probably include more than one process.

**Discussion**

Seismic coherency such as similarity and dip of maximum similarity were used as effective tools to map MTDs in the southern part of the Ulleung Basin, East Sea, offshore Korea. Generally, features of a MTD can be discerned from the seismic data by means of their reflection and attribute characteristics. Guided by results of the study of Nissen et al. (1999), we also calculated seismic attributes coherency (similarity) and dip of maximum similarity and retrieved a clearer image of the components of the main MTD (Unit 3) and seafloor (top of MTD Unit 1). The interior body of the MTD Unit 3 has a fairly homogenous seismic character (i.e. acoustic blanking), previously proposed as indicator for the presence of gas hydrate especially when occurring in conjunction with elevated P-wave velocities. The log- and core-derived physical properties show an elevated electrical resistivity and P-wave velocity, but no gas hydrate was recovered from this unit. The increase in resistivity and P-wave velocity is the result of coinciding reduced porosity and increased bulk-density. The MTD is framed by a strong upper and lower seismic reflection, suggesting large contrasts in physical properties between the MTD and the surrounding sediments. The base of the MTD shows a polarity reversal relative to the seafloor reflection (reduction in impedance) identical to the BSR, commonly interpreted as the base of the GHSZ.

The Sub-Unit 3a is characterized by the absence of internal reflectivity and the base of the unit shows long grooves exceeding the dimension of the 3-D seismic data coverage, without visible outrunner blocks. In contrast, the base of Sub-Unit 3b shows short-lived striations and the body of this Sub-Unit is characterized by short-lived, chaotic reflection elements. Therefore, we propose that the striations of sub-Unit 3a are left by out-runner blocks, which traveled ahead of the main MTD body (likely as a result of hydroplaning) and that striations of Sub-unit 3b are the result of embedded clasts.

Using the seismic character of sub-Units 3a and 3b one can propose two alternate scenarios for deposition of the MTD Unit 3: One option is that sediments of Sub-Unit 3b were less fluidized and more consolidated than those of Sub-Unit 3a, which resulted in separate depositional characters: deeper and longer striations associated with Sub-Unit 3a, and shorter striations with Sub-Unit 3b. In this scenario, both sub-Units were deposited at the same time. Alternatively, Sub-Unit 3a could have been deposited later than Sub-Unit 3b, and thus may have cut through the deposits of the older MTD Sub-Unit 3b, eroding and incorporating substrate. Sub-Unit 3a was more fluidized allowing longer grooves to develop than what is seen at the base of Unit 3b (that was not eroded).

With a previously established empirical relation between volume and flow-velocity, we inferred a velocity of at least 50 m/s for the main MTD body despite the shallow basin slope angle. Velocities of this magnitude have been reported elsewhere such as in the case of the Storegga (De Blasio et al., 2005) and the Currituck slides (Locat et al., 2009) but our result rather poses an upper limit of the possible flow speed. Additionally, run-out distances are found to amount to at least 10 km. Large traveling distances in low slope angle environments have been studied before (e.g. Hampton and Locat, 1996; Mohrig et al., 1999; Locat and Lee, 2002) As an

example, the Amazon and the Mississippi Fan both reveal equally long run-out distances despite a smoothly dipping seafloor topography (e.g. Hampton and Locat, 1996; Maslin et al., 2005).

**Conclusions**

Seismic coherency has proven to be an effective tool for the study of flow behaviour of MTDs. The dip of maximum similarity is especially capable of enhancing the contrast of the MTD and seafloor traits. Gliding tracks are depicted as two narrow, parallel lines thus making it possible to discern them from other features such as faults which would be visible as only one line of discontinuity in the seismic coherency attribute.

With the help of seismic coherency we were able to infer the physical dimensions of the MTD (Unit 3), its maximum velocity, and the extent of its run-out. The entire MTD (Unit 3) is assumed to have followed a slightly slanted path to the northeast cutting through an older MTD complex. The estimated spatial extent and approximate volume of the MTD derived from the 3-D and adjacent 2-D seismic data amounts to 210 $km^2$ and 1.28 x $10^{10}$ $m^3$, respectively. The possible source-region lies ~50 km upslope from Site UBGH1-4 as inferred by following the MTD top and bottom reflections from the 3-D seismic data coverage to adjacent 2-D seismic lines further south of the 3D data volume. The main body could have traveled with a velocity as high as 50 m/s and its outrunner blocks have covered a distance of at least 10km.

Since the 3D data does not capture the total extent which the outrunner blocks traveled and since mass failure and the occurrence of outrunner blocks still are ongoing phenomena in the Ulleung Basin, further studies of slope failure and outrunner blocks are necessary. Long distance run-out, high flow velocities, and the large, fast traveling outrunner blocks all present risk factors for offshore infrastructure and the impact of a collision with a production facility could lead to

significant damage that would pose a threat to human life and could cause possible widespread pollution.

**Acknowledgments**

We would like to thank all scientists involved in the first scientific drilling expedition in the Ulleung Basin in 2007 as well as all crew and technical staff onboard the vessel *Rem-Etive*. We also want to thank KIGAM for allowing data distribution, especially the 3-D seismic data volume at drill site UBGH1-4. This is Earth-Science-Sector (ESS) contribution number: 20100042.

***Bibliography***

Bahk J.J., Han S.-J., Khim B.-K., 2004, *Variations of terrigenous sediment supply to the southern slope of the Ulleung Basin, East / Japan Sea since the Last Glacial Maximum*, Geosciences Journal, **8**(4), 381-390

Bahk J.-J., Kim D.-H., Chun J.-H., Son B.K., Kim J.-H., Ryu B.-J., Torres M., Schultheiss P., Collett T., Riedel M., 2011a, *Gas hydrate occurrences and their relation to hosting sediment properties: results from UBGH2, East Sea*, In: Proceedings of the 7th International Conference on Gas Hydrates (ICGH 2011)

Bahk J.-J., Um I.-K., M. Holland, 2011b, *Core lithologies and their constraints on gas-hydrate occurrence in the East Sea, offshore Korea: Results from the site UBGH1-9*, Journal of Marine and Petroleum Geology (in press)

Bahorich M., Farmer S., 1995, *The coherence cube*, The Leading Edge, 1053-1058

Bouriak S., Vanneste M., Saoutkine A., *2000, Inferred gas hydrates and clay diapirs near the Storegga Slide on the southern edge of the Vøring plateau, offshore Norway*, Marine Geology, **163**, 125–148

Bünz S., Mienert J., Vanneste M., Andreassen K., 2005, *Gas hydrates at the Storegga Slide: Constraints from an analysis of multicomponent, wide-angle seismic data*, Geophysics, **70**(5), B19-B34, doi:10.1190/1.2073887

Chopra S.,2002, *Coherence Cube and beyond*, First Break, **20**, 27-33

Chopra S., Marfurt K., 2006, *Seismic Attributes – a promising aid for geologic interpretation*, CSEG Recorder, Special Edition

Chough S.K., Barg E., 1987, *Tectonic history of the Ulleung Basin Margin, East Sea (Japan Sea)*, Geology, **15**, 45-48

Chun J.H., Kwon Y.I., Lee H.Y., Kim H.J., Kim J.H., Park Y.S., Jeon C.W., Lee J.W., An G.O., Son B.K., Ko J.H., Ryu B.J., Sunwoo D., Oh J.H., Lee Y.J., Cheong T.J., Lee J.Y., Kang N.K., 2008, *Shallow gas hydrate in deep sea sediments in the Ulleung back-arc basin, offshore Korea*, In: 6th International Conference on Gas Hydrates (ICGH 2008), Vancouver, Canada, pp. 86

Clennell M.B., Hovland M., Booth J.S., Henry P., Winters W.J., 1999, *Formation of natural gas hydrates in marine sediments 1. Conceptual model of gas hydrate growth conditioned by host sediment properties*, Journal of Geophysical Research, **104**, 22,985-23,003

Coleman J.M., Prior D.B., 1978, *Submarine landslides in the Mississippi River Delta*, Offshore Technology Conference

De Blasio F.V., Elverhøi A., Issler D., Harbitz C.B., Bryn P., Lien R., 2005, *On the dynamics of subaqueous clay rich gravity mass flows – the giant Storegga slide, Norway*, Marine and Petroleum Geology, **22**, 179-186

Garziglia S., Migeon S., Ducassou E., Loncke L., Mascle J., 2008, *Mass-transport deposits on the Rosetta province (NW Nile deep-sea turbidite system, Egyptian margin): Characteristics, distribution, and potential causal processes*, Marine Geology, **250**, 180-198

Gauer P., Kvalstad T.J., Forsberg C. F., Bryn P., Berg K., 2005, *The last phase of the Storegga Slide: simulation of retrogressive slide dynamics and comparison with slide-scar morphology*, Journal of Marine and Petroleum Geology, **22**, 171-178

Hampton M.A., Locat J., 1996, *Submarine Landslides*, Review of Geophysics, **34**(1), 33-59

Ilstadt T., De Blasio F.V., Elverhoi A., Harbitz C.B., Engvik L., Longva O., Marr J.G., 2004, *On the frontal dynamics and morphology of submarine debris flows*, Journal of Marine Geology, **213**, 481-497

Iverson R.M., 1997, *The Physics of Debris Flows*, Reviews of Geophysics, **35**, 245-296

Kim G.Y., Yi B.Y., Yoo D.G., Ryu B.J., Riedel M., 2011, *Evidence of gas hydrate from downhole logging data in the Ulleung Basin, East Sea*, Journal of Marine and Petroleum Geology, **28**(10), 1979-1985

Kvalstad T.J., Andresen L., Forsberg C.F., Berg K., Bryn P., Wangen M., 2005, *The Storegga Slide: evaluation of triggering sources and slide mechanics*, Journal of Marine and Petroleum Geology, **122**(7), 245-256

Lee G.H., Suk B.-C., 1998, *Latest Neogene-Quaternary seismic stratigraphy of the Ulleung Basin, East Sea (Sea of Japan)*, Journal of Marine Geology, **146**, 205-224

Lee G.H., Kim, J.H., Han, S.J., Kim, D.C., 2001, *Seismic stratigraphy of the deep Ulleung Basin in the East Sea (Japan Sea) back-arc basin*, Journal of Marine and Petroleum Geology, **18**, 615-634

Lee G.H., Kim B., 2002, *Infill history of the Ulleung Basin, East Sea (Japan Sea) and implications on source rocks and hydrocarbons*, Journal of Marine and Petroleum Geology, **19**, 829-845

Lee H.J., Chough S.K., Yoon S.H., 1996, *Slope-stability change from late Pleistocene to Holocene in the Ulleung Basin, East Sea (Japan Sea)*, Sedimentary Geology, **104**, 39-51

Lee J.H., Baek Y.S., Ryu B.J., Riedel M., Hyndman R.D., 2005, *A seismic survey to detect natural gas hydrate in the East Sea of Korea*, Marine Geophysics Research, **26**, 51-59

Lee M.W., Dillon W.P., 2001, *Amplitude blanking related to gas hydrate concentration*, Marine Geophysical Researches, **22**(2), 101-109

Locat J., Lee H.J., 2002, *Submarine landslides: advances and challenges*, Can. Geotech. J., **39**, 193-212

Locat J., Lee H., ten Brink U.S., Twitchell D., Geist E., Sansoucy M., 2009, *Geomorphology stability and mobility of the Currituck slide*, Journal of Marine Geology, **264**, 28-40

Marfurt K.J., Kirlin R.L., Farmer S.L., Bahorich M.S., 1998, *3-D seismic attributes using a semblance based coherency algorithm*, Geophysics, **63**(4), 1150-1165

Maslin M., Vilela C., Mikkelsen N., Grootes P., 2005, *Causes of catastrophic sediment failures of the Amazon Fan*, Quaternary Science Reviews, **24**, 2180-2193

Mienert J., Posewang J., Baumann M., 1998, *Gas hydrates along the northeastern Atlantic Margin: Possible hydrate-bound margin instabilities and possible release of methane*, In: J. P. Henriet, and J. Mienert, eds., Gas hydrates: Relevance to world margin stability and climate change: Geological Society of London Special Publication **137**, 275–291

Mienert J., Vanneste M., Buenz S., Andreassen K., Haflidason H., Sejrup H.P., 2005, *Ocean warming and gas hydrate stability on the mid-Norwegian margin at the Storegga Slide*, Journal of Marine and Petroleum Geology, **22** (1-2), 233-244

Mohrig D., Ellis C., Parker G., Whipple K.X., Hondzo M., 1998, *Hydroplaning of subaqueous debris flows*, Geological Society of America Bulletin, **110**, 387-394

Mohrig D., Elverhøi A., Parker G., 1999, *Experiments on the relative mobility of muddy subaqueous and subaerial debris flows and their capacity to remobilize antedecent deposits*, Journal of Marine Geology, **154**, 117-129

Nissen S.E., Haskell N.L., Steiner C.T., Coterill K.L.,1999, *Debris flow outrunner blocks, glide tracks, pressure ridges identified on the Nigerian continental slope using 3-D seismic coherency*, The Leading Edge, 595-599

Park C.H., 2007, *Hydrography of the East Sea*, In: Lee, K.-S., Kim, W.-S. (Eds.), Ocean Atlas of Korea - East Sea -, National Oceanographic Research Institute, Incheon, pp. 66-75

Park K.P., 2008, *Gas hydrate exploration activities in Korea*, In: Proceedings of the 6th International Conference on Gas Hydrates, ICGH 2008, Vancouver 2008, pp. 7

Park K.-P., Bahk J.-J., Kwon Y., Kim G.-Y., Riedel M., Holland M., Schultheiss P., Rose K., and the UBGH-1 Scientific Party, 2008, *Korean national program expedition confirm rich gas hydrate deposits in the Ulleung Basin, East Sea*, DOE-National Energy Technology Laboratory (NETL) Fire in the Ice Methane Hydrate Newsletter, p. 6–9: http://www.netl.doe.gov/technologies/oilgas/publications/Hydrates/Newsletter/HMNewsSpring08.pdf (last access September 2, 2011)

Posamentier H.W., Walker R.G., 2006, *Deep-water turbidites and submarine fans*. In: Facies Models Revisited, SEPM Spec. Publ., **84**, 397-520

Prior D.B., Bornhold B.C., Coleman J.M., Bryant W.R., 1982, *Morphology of a submarine slide, Kitimat arm*, British Columbia, Geology, **10**, 588-592

Riedel M., Hyndman R.D., Spence G.D., Chapman N.R., 2002, *Seismic Investigations of a Vent Field Associated with Gas Hydrates, Offshore Vancouver Island*, Journal of Geophysical Research, **107**(B9), 2200, doi:10.1029/2001

Ryu B.-J., Riedel M., Kim J.-H., Hyndman R.D., Lee Y.-J., Chung B.-H., Kim I.-S., 2009, *Gas hydrates in the western deep-water Ulleung Basin, East Sea of Korea*, Journal of Marine and Petroleum Geology, **26** (8), 1483-1498

Sohn Y.K., 2000, *Depositional processes of submarine debris flows in the Miocene fan deltas, Pohang Basin, Korea with special reference to flow transformation*, Journal of Sedimentary Research, **70**(3), 491-503

Taner M.T., Koehler F., 1969, *Velocity spectra – digital computer derivation and applications of velocity functions*, Geophysics, **34**, 859-881

Torres M.E., Tréhu A.M., Cespedes N., Kastner M., Wortmann U.G., Kim J.-H., Long P., Malinverno A., Pohlman J.W., Riedel M., Collett T., 2008, *Methane hydrate formation in turbidite sediments of northern Cascadia*, IODP Expedition 311, Earth and Planetary Science Letters, **271**, 170-180

Vogt P. R., Jung W. Y., 2002, *Holocene mass wasting on upper non-polar continental slopes — Due to post-glacial ocean warming and hydrate dissociation?*, Geophysical Research Letters, **29**, doi:10.1029/2001GL013488

# Mass-transport deposits and gas hydrate occurrences in the Ulleung Basin, East Sea - Part 2:

# Gas hydrate content and fracture-induced anisotropy

**Abstract**

Mass transport deposits (MTDs) and hemipelagic mud, interbedded with sandy turbidites are the main sedimentary facies in the Ulleung Basin, East Sea, offshore Korea. The MTDs show similar seismic reflection characteristics to gas-hydrate-bearing sediments such as regional seismic blanking (absence of internal reflectivity) and a polarity reversed base-reflection identical to the bottom-simulating reflector (BSR). Drilling in 2007 in the Ulleung Basin recovered sediments within the MTDs that exhibit elevated electrical resistivity and P-wave velocity, similar to gas hydrate-bearing sediments. In contrast, hemipelagic mud intercalated with sandy turbidites have much higher porosity and correspondingly lower electrical resistivity and P-wave velocity.

At drill-site UBGH1-4 the bottom half of one prominent MTD unit shows two bands of parallel fractures on the resistivity log-images indicating a common dip-azimuth direction of about ~230º (strike of ~140º). This strike-direction is perpendicular to the seismically defined flow-path of the MTD to the north-east. At Site UBGH1-14, the log-data suggest two zones with preferred fracture orientations (top: ~250º, bottom: ~130º), indicating flow-directions to the north-east for the top zone, and north-west for the bottom zone. The fracture-patterns may indicate post-depositional sedimentation that gave rise to a preferred fracturing possibly linked to

dewatering pathways. Alternatively, fractures may be related to the formation of pressure-ridges common within MTD units.

For the interval of observed MTD units, the resistivity and P-wave velocity log-data yield gas hydrate concentrations up to ~10% at Site UBGH1-4 and ~25% at Site UBGH1-14 calculated using traditional isotropic theories such as Archie's law or effective medium modeling. However, accounting for anisotropic effects in the calculation to honour observed fracture patterns, the gas hydrate concentration is overall reduced to less than 5%. In contrast, gas hydrate was recovered at Site UBGH1-4 near the base of gas hydrate stability zone (GHSZ). Log-data predict gas hydrate concentrations of 10 - 15% over an interval of 25 m above the base of GHSZ. The sediments of this interval are comprised of the hemipelagic mud and interbedded thin sandy turbidites, which did contain pore-filling gas hydrate as identified from pore-water freshening and core infra-red imaging. Seismically, this unit reveals a coherent parallel bedding character but has overall faint reflection amplitude. This gas-hydrate-bearing interval can be best mapped using a combination of regular seismic amplitude and seismic attributes such as Shale indicator, Parallel-bedding indicator, and Thin-bed indicator.

**Introduction**

As part of the Korean gas hydrate program, systematic regional 2-D reflection seismic data were acquired across the Ulleung Basin, East Sea (Fig. 1) to characterize the depositional environment and to map gas hydrate accumulations mainly by identifying the bottom-simulating reflector (BSR) (e.g. Ryu et al., 2009; Lee et al., 2005; Park et al., 2008). Additionally, a 3-D seismic data set was acquired in the south-eastern region of the Ulleung Basin thought to potentially contain gas hydrate based on initial interpretations of the BSR occurrence and wide-spread seismic characteristics including seismic blanking and elevated interval velocities. The

Ulleung Basin Gas Hydrate Drilling Expedition 1 (UBGH1) in 2007 (see Fig. 1 for location of drill sites) was conducted to verify the presence of gas hydrate in the basin and consisted of a logging-while-drilling (LWD) operation at five sites (UBGH1-1, UBGH1-4, UBGH1-9, UBGH1-10, and UBGH1-14) followed by a coring operation at three of those sites (UBGH1-4, UBGH1-9, and UBGH1-10). Additional wire-line logging and vertical seismic profiling was conducted at Site UBGH1-9. Drilling and coring at Site UBGH1-4 encountered gas hydrates within sandy turbidites near the base of the gas hydrate stability zone (GHSZ). The other two sites of UBGH1 with coring operations were located within prominent cold-vent features (also referred to as seismic chimneys), and gas hydrate was recovered in massive form as vein- and fracture-fill (Kim et al., 2011; Bahk et al., 2011). Linkages between fracture-formation and gas hydrate occurrences within these type of chimney-structures have been investigated also as part of other drilling campaigns off India (e.g. Riedel et al., 2010; Holland et al., 2008), the northern Cascadia margin (Riedel et al., 2006a), as well as in the Gulf of Mexico (e.g. Cook et al., 2008). Especially in the fracture systems drilled offshore India, a high degree of anisotropy has been found to alter the log-measurements of electrical resistivity and P-wave velocity (e.g. Cook and Goldberg, 2008) due to the alignment of the logging tools in the borehole with the almost vertical fracture-planes. As a result, the gas hydrate concentrations inferred from traditional techniques such as Archie's-law (Archie, 1942; Collett and Ladd, 2000) are skewed to unrealistically high values when compared to results from pressure-coring or pore-water freshening (Lee and Collett, 2009).

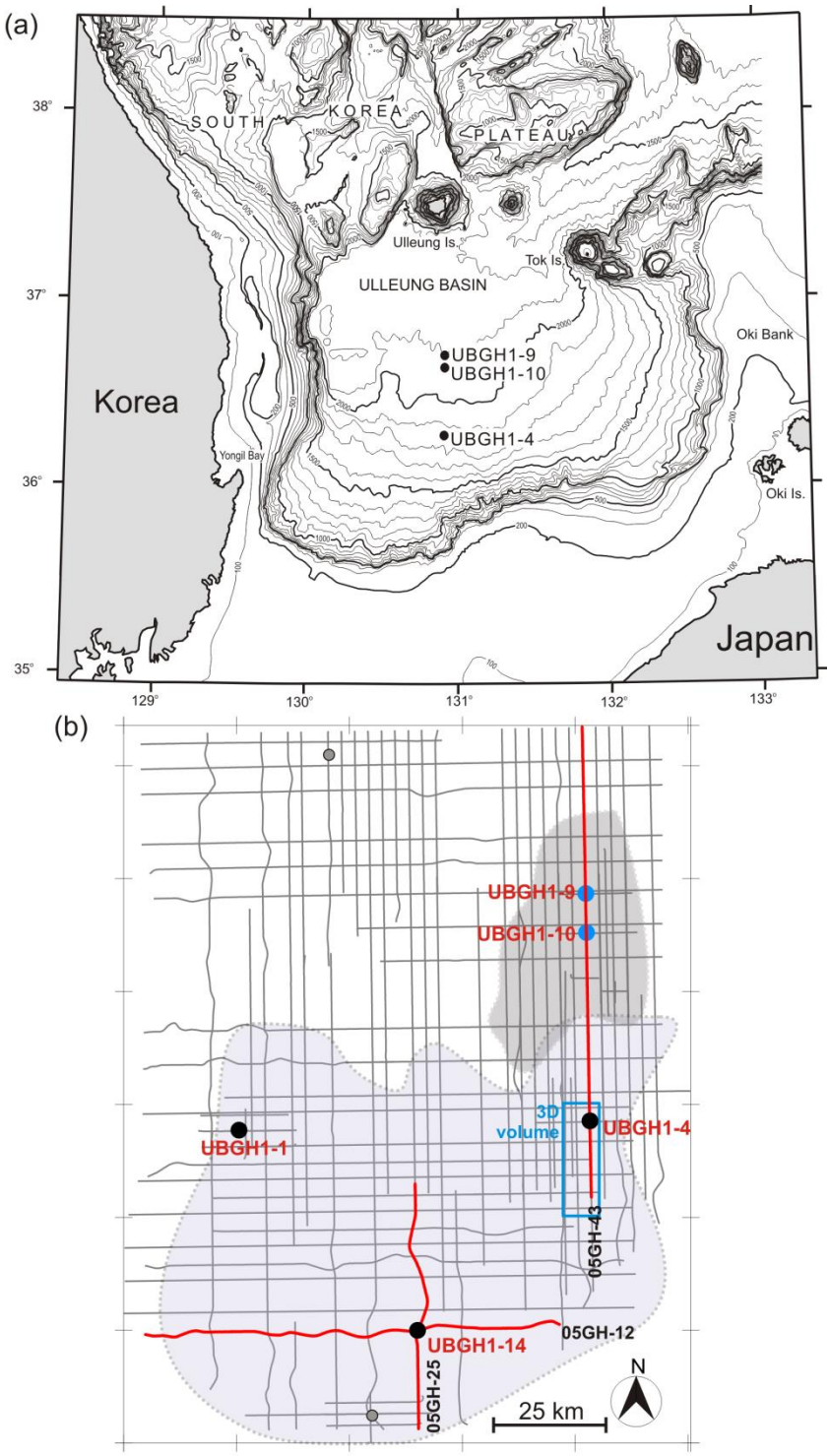


**Fig. 1:** a) Location of the Ulleung Basin in the East Sea/Sea of Japan. b) Detailed map of the seismic data coverage, water depth, BSR-distribution (violet-shaded zone), and occurrence of chimney-like features (grey-shaded zone). Additional, isolated chimney-like features were seen in two locations, shown as grey dots. The area of the 3-D seismic data set is outlined in a blue box (details see companion paper by Scholz et al). Drill sites visited during UBGH1 are shown as dots

At Sites UBGH1-4 and UBGH1-14 the LWD data show several depth intervals with prominent strata-bound fractures, but these sites are not within chimney structures. In this study, we use the LWD borehole images of resistivity to delineate fracture-orientation and combine these results with seismic data to understand linkages between the depositional environments of mass-transport deposits (MTDs) and gas hydrate formation. This study is linked to the companion paper by Scholz et al. who used seismic attributes to define seismic characteristics and flow-direction of a MTD encountered at Site UBGH1-4. Understanding the sedimentary processes (e.g. deposition of MTDs, hemipelagites, and turbidites) in the Ulleung Basin and associated sediment types (sand or clay) is an important component of the gas hydrate petroleum system and helps in the prediction of appropriate porous media that are known as preferred hosts for gas hydrates.

**Geologic setting, sedimentation patterns and general gas hydrate occurrence-regimes**

The Ulleung Basin is a continental back-arc basin and lies on the eastern margin of the Eurasian Plate, separated from the Pacific by the Japanese Islands. The East Sea containing the Ulleung, Japan, and Yamato basins originates in the Oligocene with an extensional phase extending to the middle Miocene (32 – 10 Ma). Crustal thinning and seafloor spreading was followed by convergence linked to a change of the direction of plate motion in the late Miocene as part of the subduction along the Japanese Island arc as well as back-arc closure and crustal shortening (Lee and Suk, 1998). The East Sea is still in the state of compressive deformation today. Lee et al. (2001) mention two distinct phases of different sedimentation patterns consisting of mainly MTDs during the late Neogene and extensive turbidite and hemipelagic sedimentation since the Pleistocene. Uplift and deformation in the south and southeast of the

basin due to back-arc closure are seen as causes for the enormous volumes of sediments found in the basin (Lee et al., 2001).

The seafloor of the Ulleung Basin is fairly smooth in the centre and dips gently from 2000 m water depth to 2500 m in the northeast (Park et al., 2008). Slide and slump deposits occur mainly on the upper steeper slopes of the southern part of the basin whereas debris flows are found at the lower slopes of the basin. As the depositional energy of the mass transport processes decreases with increasing distance from the source, interbedded turbidites and hemipelagic sediments were deposited further to the northeast of the basin. As the number of mass transport flows retreated since the late Miocene, a prominent change in sedimentary facies occurred in the central basin, with a transition from high energy MTDs to low energy turbidites and hemipelagic sediments. The occurrence of clustered chimney-like features with their massive gas hydrate occurrences (as seen e.g. in Site UBGH1-9 and UBGH1-10) in form of vein- and fracture fill is constrained to the northern part of the basin where the upper-most 200-300 m of sediments are mostly comprised of interbedded turbidites and hemipelagic sediments (Horozal et al., 2009; Ryu et al., 2009). More isolated chimney-like features, associated with faults were also found in other parts on the basin (Fig. 1).

Sediments within the gas hydrate stability zone at the southern portion of the basin are dominated by MTDs with some minor events containing hemipelagic and interbedded turbidite sediments. Gas hydrate was encountered here at Site UBGH1-4 within the thin sandy turbidite intercalated with hemipelagic mud. As an example of this change in sedimentation pattern across the basin, seismic line 05GH-43 is shown in Fig. 2 crossing the three coring sites UBGH1-4, UBGH1-10, and UBGH1-9 (from south to north).

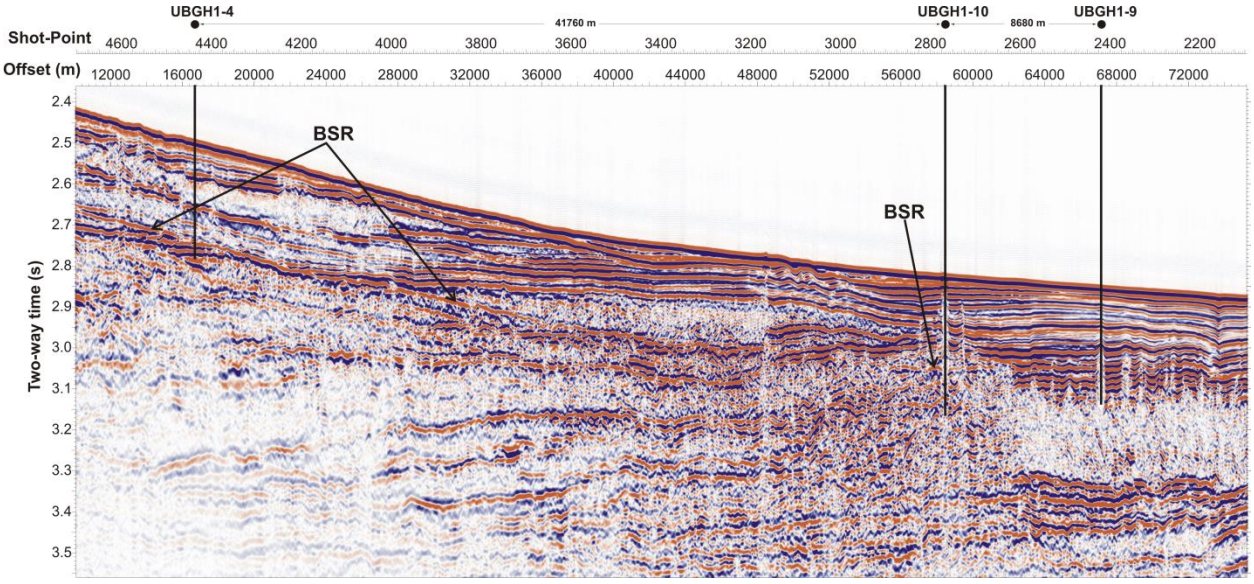


**Fig. 2:** Seismic line 05GH-43 crossing the three core-sites UBGH1-4, UBGH1-10, and UBGH1-9 (south to north). The prominent change in sedimentation pattern from MTDs in the south at Site UBGH1-4 to dominantly seafloor-parallel deposition of hemipelagic and thin turbidites in the north is evident. Site UBGH1-9 and UBGH1-10 are within cold vents, also referred to as chimney-like features

The occurrence of a prominent BSR is apparently limited to the southern portion of the basin. It is difficult to discern it in the northern basin around the chimney features because sedimentary layers of the area are mostly developed parallel to the seafloor. In this northern basin, the depth of BSR is possibly much shallower due to the regional increase in heat flow (Horozal et al., 2009).

## Data and methods

The seismic data used for this study are explained in the companion paper (Scholz et al). Here, we use the 3-D seismic attributes related to similarity (also referred to as seismic coherence) to define the flow-direction of the MTD intersected at Site UBGH1-4. We also use two crossing 2-D seismic lines at Site UBGH1-14 (~60 km southwest from UBGH1-4) to link observations from log-data to seismic reflections. LWD-data (gamma-ray, bulk-density, porosity, P-wave velocity, as well as electrical resistivity) from Sites UBGH1-04 and UBGH1-14 are shown in Fig. 3.

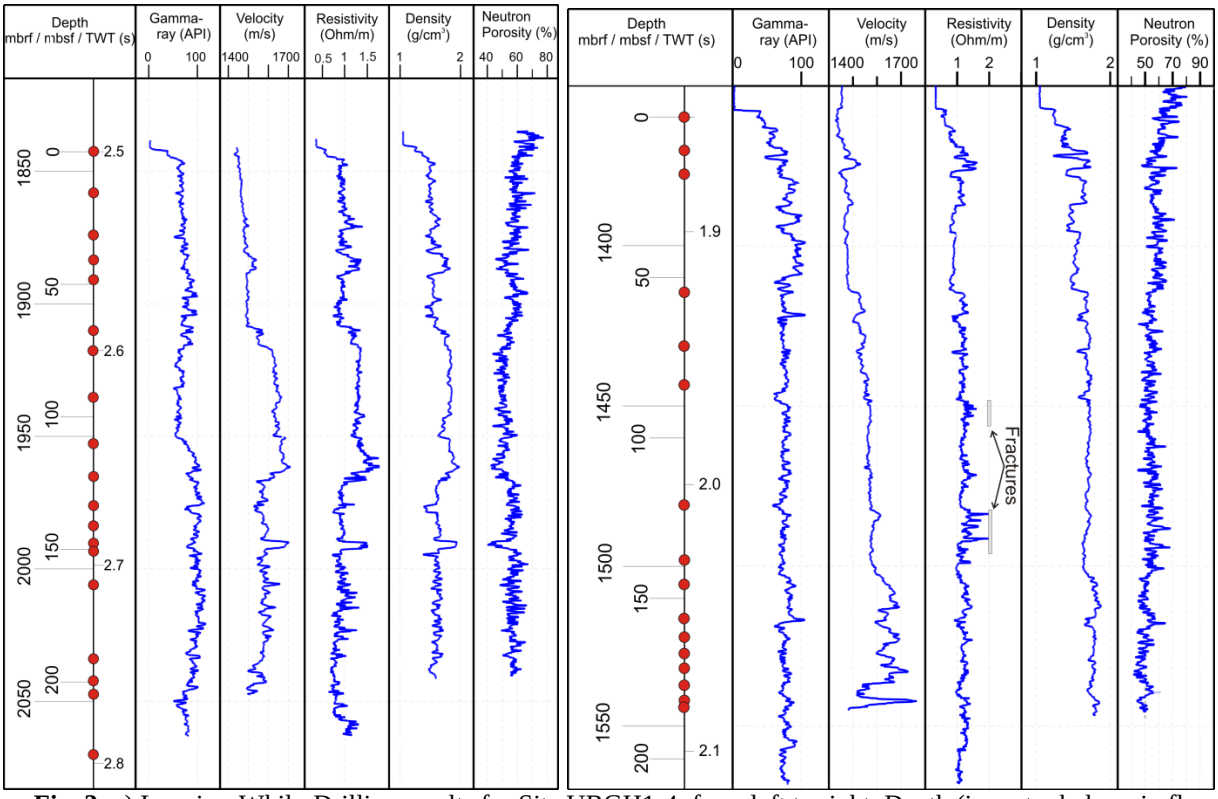


**Fig. 3:** a) Logging-While-Drilling results for Site UBGH1-4; from left to right: Depth (in meter below rig floor (mbrf), meter below seafloor (mbsf) or two-way time (TWT) in seconds, conversion control points after velocity integration are shown as red dots), Gamma-ray, P-wave velocity, electrical resistivity (ring), bulk density, and neutron porosity. b) Logging-While-Drilling results for Site UBGH1-14; from left to right: Depth (in meter below rig floor (mbrf), meter below seafloor (mbsf) and two-way time (TWT) in seconds), conversion control points after velocity integration are shown as red dots), Gamma-ray, P-wave velocity, electrical resistivity (button-deep), bulk density, and neutron porosity. Two zones of apparent fractures are shown as grey bars

Matching characteristic log-trends to seismic reflections was achieved by calculating synthetic seismograms (Fig. 4) from the LWD P-wave velocity and density log and estimating representative wavelets from the seismic data crossing the boreholes. A time-depth curve was defined by tying key-horizons (seafloor, BSR) and integrating over the LWD P-wave velocity log.

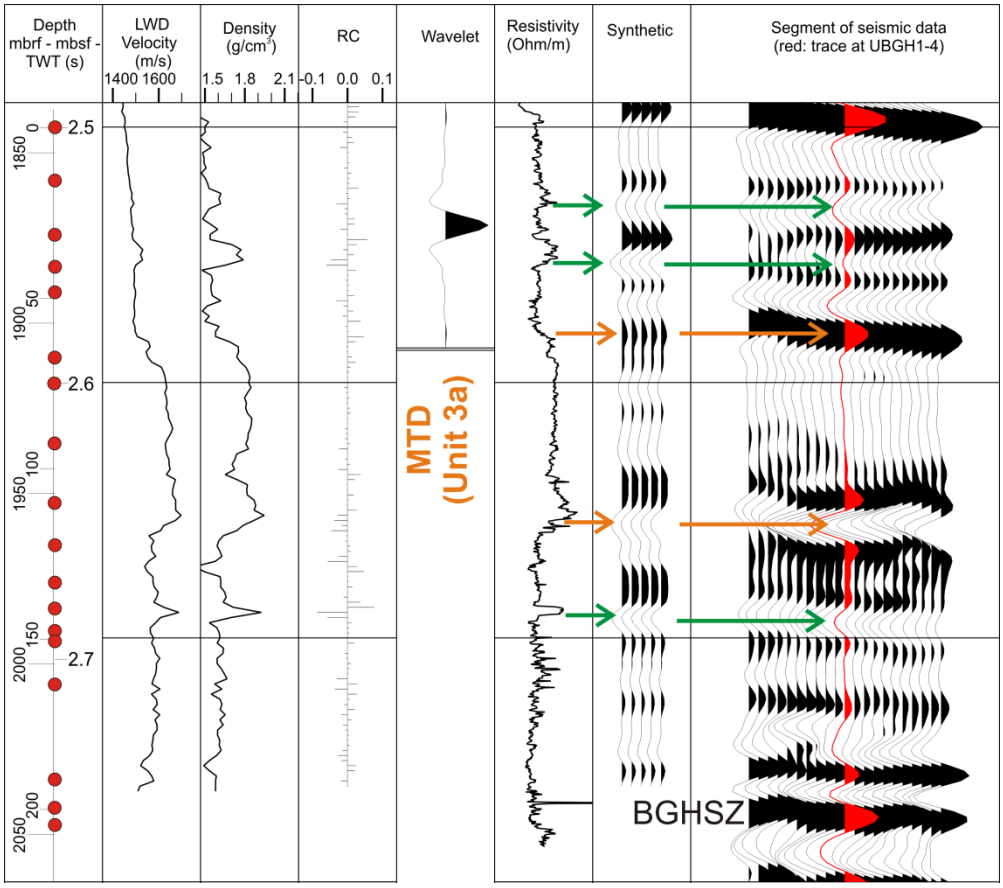


**Fig. 4:** a) Synthetic seismogram using the Logging-While-Drilling (LWD) P-wave velocity and bulk density logs at Site UBGH1-4 and a seismic wavelet extracted from the 3-D seismic data volume. Top and base reflection of the MTD (Unit 3a) correspond well to the seismic data (orange arrows). Also, three smaller-MTDs identified in the log do show good correlation to the seismic data (green arrows)

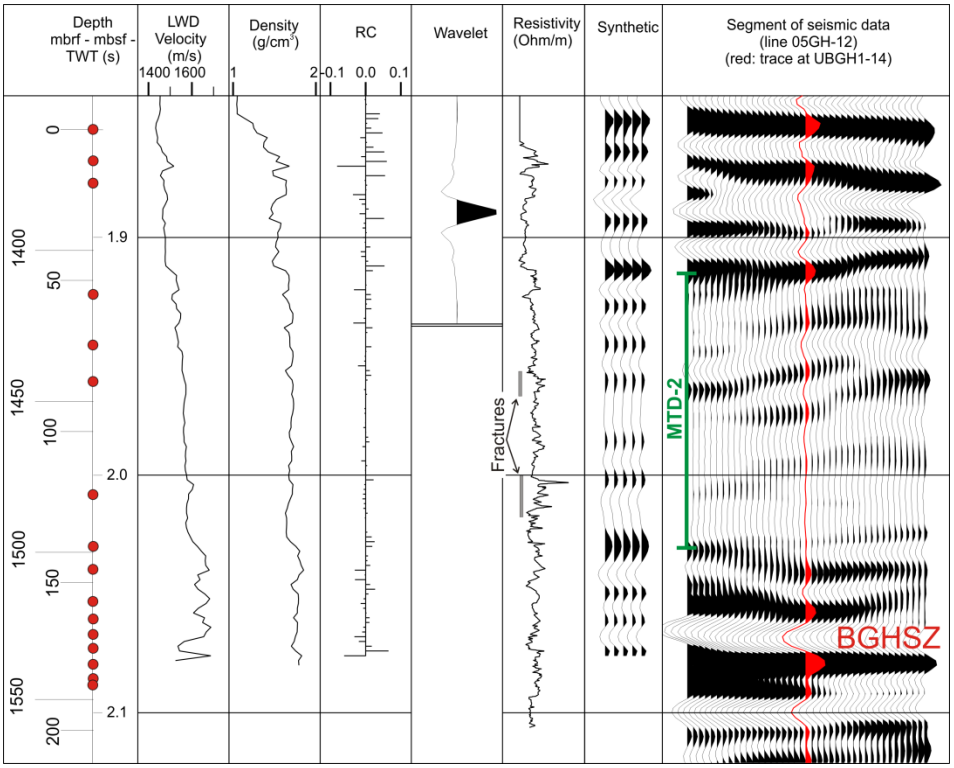


**Fig. 4:** b) Synthetic seismogram using the Logging-While-Drilling (LWD) P-wave velocity and bulk density data at Site UBGH1-14 and a seismic wavelet extracted from the 2-D seismic data crossing this site (05GH-12, Figure 5b). Top, and base reflection of the MTD units correspond well to the real data

We calculate gas hydrate concentrations from electrical resistivity log using the empirical Archie (1942) relation, which assumes that gas hydrate forms within the pore-space of the sediment. The cross-plot between formation factor (measured resistivity normalized by the in situ pore-water resistivity) and porosity defines the required empirical constants in the Archie-calculations as listed in Table 1.

| Site | Neutron Porosity | | Density Porosity | |
|---|---|---|---|---|
| | a | m | a | m |
| UBGH1-4 | 1.751 | 1.537 | 1.943 | 1.451 |
| UBGH1-14 | 1.407 | 1.664 | n.d. | |

**Table 1**: Estimated Archie-Parameters from Sites UBGH1-4 and UBGH1-14 for neutron- and density porosity

Only the assumed non-gas hydrate-bearing zones are used in this analysis (upper 70 mbsf and all data below the GHSZ). At Site UBGH1-4 it is possible to use measured in situ pore-water salinity (which varies from 34 ppt at the seafloor to a slightly increased value around 37 ppt at 125 mbsf before decreasing to 35 ppt) and a measured temperature gradient (~90ºC/km) to define the in situ pore water resistivity. At Site UBGH1-14, we only have log-data but no core. Thus, we assumed uniform pore-water salinity (seawater-values of ~34 ppt) and a reduced geothermal gradient (~65ºC/km) reflecting the regional trends in the basin (as defined by Horozal et al., 2009). For both sites, two sets of porosity-values are available (neutron-porosity and density-porosity) and separate Archie-parameters are estimated from the Pickett-plots (Table 1). Neutron- and density porosity are not easily comparable as the assumption of uniform grain-density for the complete logged interval is not necessarily valid. At Site UBGH1-4, few cores were recovered. Grain density appears to be ~2.55 g/cm$^3$ for most cored parts, with a notable exception found in cores from within the main MTD, where values are characteristically higher at 2.65 g/cm$^3$. Due to the lack of recovered core, we did not attempt calculating density-porosity for Site UBGH1-14. In all subsequent calculations for gas hydrate content the exponent *n* is set constant (*n*=1.96), following the suggestion of Collett and Ladd (2000) defining *n* from an assumed mix of sediments. All values of gas hydrate concentrations reported later are defined as fraction of the pore space (not rock-volume).

Utilizing P-wave velocity as an additional indicator for gas hydrate concentration we use the effective medium modeling (EFM) theory for marine sediments (Helgerud, 1999). A mineralogy-mixture of 90% clay with 10% quartz is assumed uniformly for the entire depth interval of the gas hydrate stability zone at both drill sites. Additional constants required for the modeling are defined in Table 2.

| | |
|---|---|
| Number of grain contacts | 8 |
| Critical porosity | 0.38 |
| Pore-water bulk modulus | $2.4 \times 10^9$ Pa |
| Pore-water density | 1030 kg/m$^3$ |
| Clay bulk modulus | $20.9\times 10^9$ Pa |
| Clay shear modulus | $6.85\times 10^9$ Pa |
| Clay density | 2580 kg/m$^3$ |
| Quartz bulk modulus | $36.6\times 10^9$ Pa |
| Quartz shear modulus | $45\times 10^9$ Pa |
| Quartz density | 2650 kg/m$^3$ |
| Hydrate bulk modulus | $7.9\times 10^9$ Pa |
| Hydrate shear modulus | $3.3\times 10^9$ Pa |
| Hydrate density | 920 kg/m$^3$ |

**Table 2**: Required parameters for the effective medium model (EFM) calculations following the approach by Helgerud (1999)

We further use the LWD resistivity borehole images from three measurements reflecting different penetration depths (button-deep (BD), button-medium (BM), and button-shallow (BS)) to measure fracture parameters (dip-magnitude, dip-direction, and azimuth- and strike-orientation) following procedures described in Cook and Goldberg (2008) and Cook et al. (2008). Fractures present in the data are seen as sinusoidal patterns in the unwrapped borehole image data. The process of defining fracture orientation was done by selecting a best-fit sinusoidal line representing the fracture to the observations. The image data were first oriented to north (0 º or 360 º) and corrected for the local magnetic declination (~7.7º). Borehole-calliper information was also used to constrain the width of the data image used but the borehole

diameter is mostly stable and on average 9 inch wide. A few noticeable enlarged sections in the upper 50 mbsf exist, especially in the top 10-20 mbsf interval where sediment is soft. Borehole resistivity-images were used in static (for a fixed range of resistivity values) and dynamic (for depth-interval of 0.5m) normalization mode for comparison purposes.

**Results**

*UBGH1-4 seismic and log-data*

The sediments at Site UBGH1-04 are dominated by MTD units and thin interbeds of hemipelagites and turbidites. As seen in Fig. 2 (line 05GH-43), the upper-most MTD units reach northward into the deeper basin to the drill site UBGH1-10. A closer comparison of the seismic data (Fig. 5a) with the synthetic seismogram (Fig. 4a) shows a direct correlation between the three MTD units and seismic reflection events (correlation between synthetic and real data is ~75% for the entire interval of log-data availability).

The MTDs are seismically transparent but intervals composed of hemipelagites and turbidites are identified by coherent and extensive reflection-packages. The overlay of the resistivity-log (BD) with the seismic data shows that the zone of gas hydrate recovery (160-185 mbsf) in thin sandy turbidites is located just above the BSR, a zone with faint reflection amplitude but an overall well-defined package of coherent, extensive seismic reflectivity. The log-data (Fig. 3a) show synchronous trends of elevated resistivity, P-wave velocity, and density with a related reduction in porosity over the interval of the main unit (MTD-2, 77 - 127 mbsf). The top 35 mbsf are showing almost constant values in these physical properties, with a pronounced lower section (110-127 mbsf) where again resistivity, P-wave velocity, and density increase until the MTD is sharply truncated at the bottom. Below this MTD the log-values are again almost constant, with

the exception of a thin unit (MTD-3, 149 - 152 mbsf) with identical trends in resistivity, P-wave velocity, density, and porosity as the overlying unit (MTD-2).

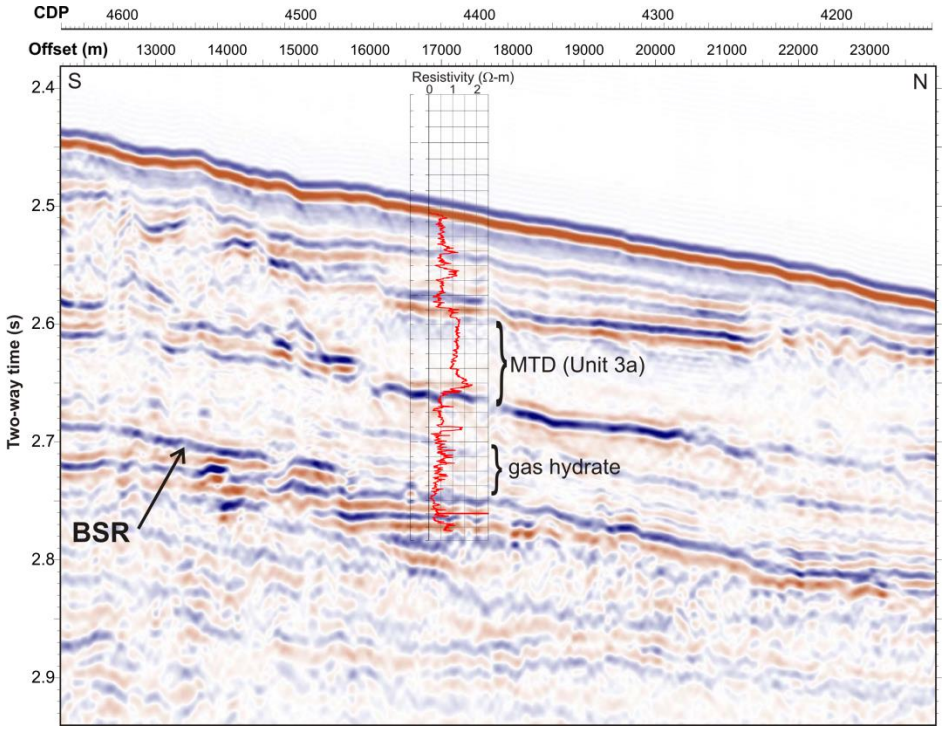


**Fig. 5:** a) Section of seismic line 05GH-43 through Site UBGH1-4. A BSR is present but weak in amplitude. One mass-transport unit (MTD-2) dominates the depositional environment at this site. The LWD-resistivity log (red) is superimposed highlighting the individual intervals of the borehole through MTDs or hemipelagic mud with thin turbidites

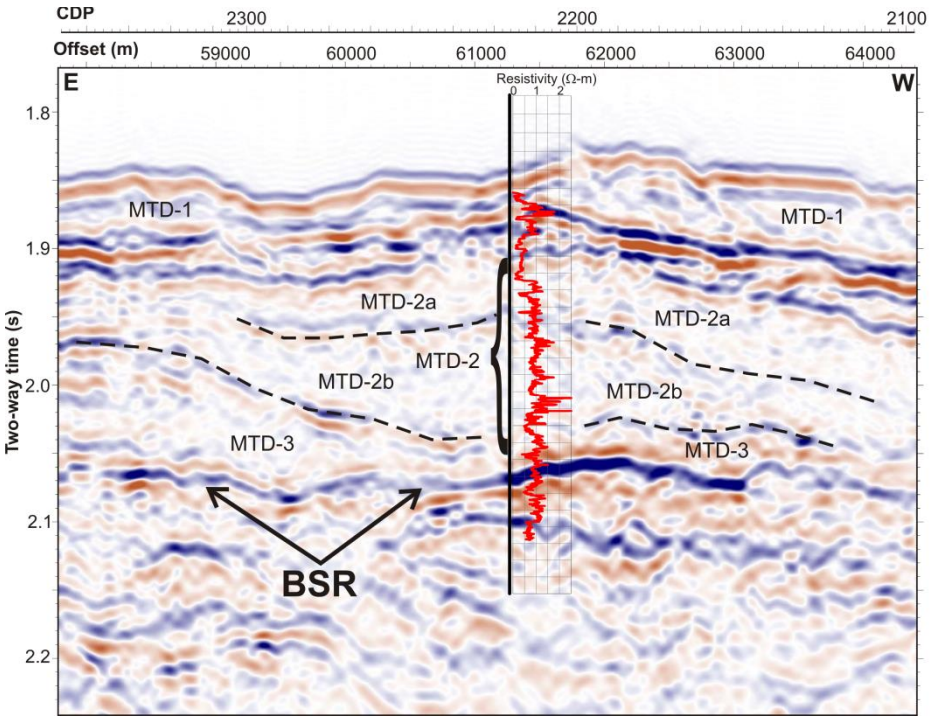


**Fig. 5:** b) Section of seismic line 05GH-12 (E-W) through Site UBGH1-14. Note the presence of a strong BSR with reflection-amplitudes enhanced below. Most sediments between the seafloor and BSR are comprised of MTDs with some faint reflections showing sub-layering within the main flow unit.
The LWD-resistivity log (red) is superimposed

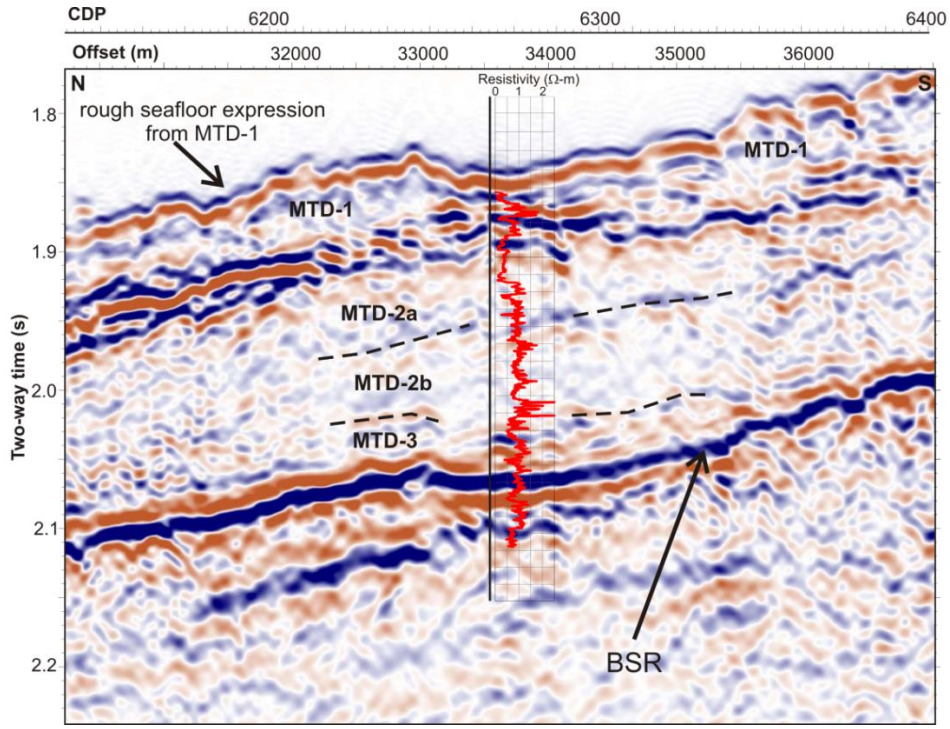


**Fig. 5:** c) Section of seismic line 05GH-25 (N-S) through Site UBGH1-14. Note the presence of a strong BSR with reflection-amplitudes enhanced below. Most sediments between the seafloor and BSR are comprised of MTDs with some faint reflections showing sub-layering within the main flow unit.
The LWD-resistivity log (red) is superimposed

*UBGH1-14 seismic and log-data*

Two 2-D seismic lines are crossing at the drill site UBGH1-14 (Fig. 5b, c) and in both cases the resistivity curve (BD) is overlaid on the seismic image. The correlation between individual MTD units and seismic events is less well developed at this site as it is at UBGH1-4. However, a time-depth conversion with the integrated LWD velocity-log and two key horizons (seafloor, BSR) allows to link features seen in the log-data to seismic events, although correlation is only ~45% for the entire interval of log-data availability. The top ~25 mbsf show strong seismic reflection events and represent the base of the upper-most MTD unit, which has a very rough reflection surface (i.e. the seafloor). Beneath this event, almost all of the sedimentary package down to (and slightly below) the BSR appears as one larger MTD event. However, some faint reflection events within this interval (25 - 160 mbsf) are visible and suggest two sub-flows within the main MTD body, but they do not correlate well to a log-response in density and velocity (Fig. 4b). Log-data of density, porosity, and gamma-ray are almost constant throughout the MTD unit with a slight increase in P-wave velocity (Fig. 3b). However, resistivity values show several shorter intervals with increased values (e.g. 91-101 mbsf, 125-137 mbsf) characterized by small spikes. These two zones of higher resistivity are also preceded by a decrease in gamma-ray values (sand) over a thickness of 3-5 m each, which may be an indication of the base of the overlying flow-unit.

*LWD-RAB images for fracture-analysis*

Two bands of prominent fractures were identified on the resistivity borehole images at site UBGH1-4 (Fig. 6a).

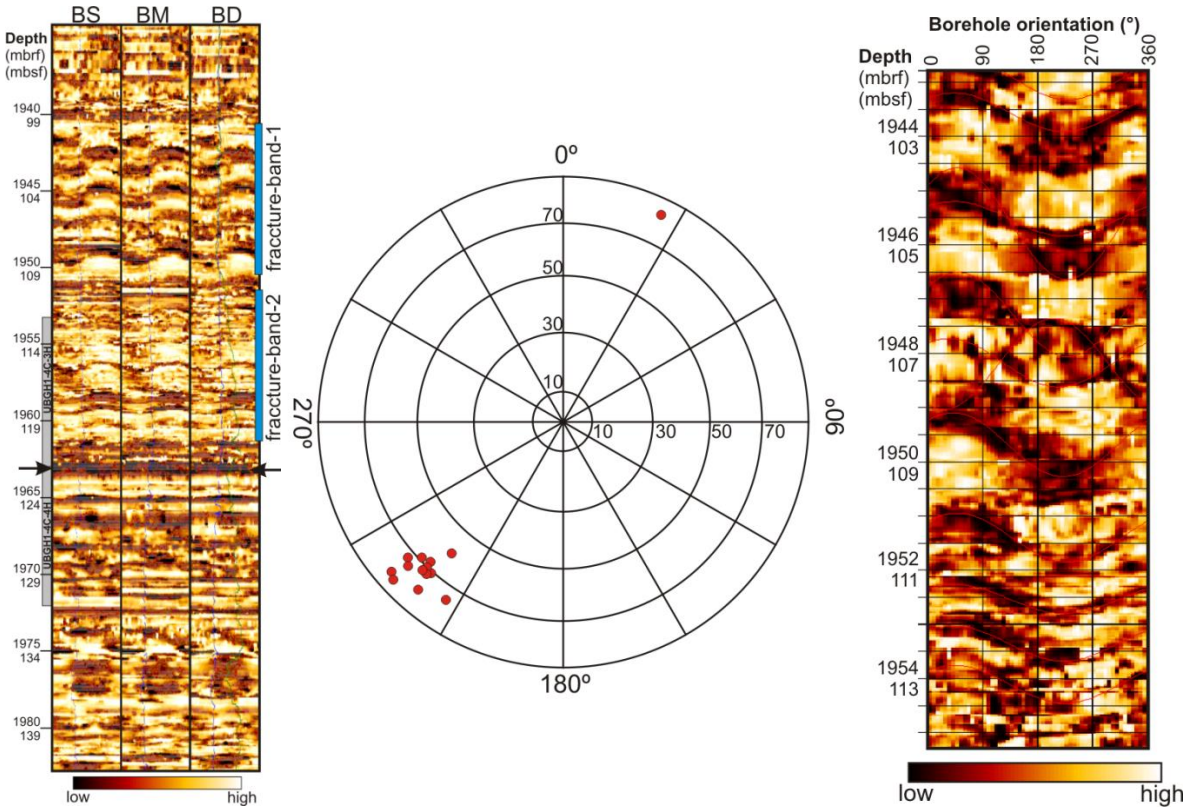


**Fig. 6:** a) Overview of the fracture-bands seen in the LWD-resistivity images at Site UBGH1-4; panels are the individual resistivity images (button-shallow: BS, button-medium: BM, button-deep: BD). Additionally the average BS, BM, and BD-resistivity logs and gamma-ray curve (green) is overlain on the individual images. Resistivity-image data were normalized dynamically over a depth interval of 0.25m, and thus the images are highly accentuated with the actual difference between the high (yellow to white colors) and low resistivity values (brown to black) are ~0.5 Ωm. Arrows indicate the base of the main MTD unit. b) Fracture-orientation analyses for Site UBGH1-4 (depth interval of 101 - 113 mbsf). On the left is the plot of azimuth orientation for 14 analysed fractures (Schmidt-Plot, concentric circles represent dip-degree 0 - 90º), which are overlain as thin lines on the resistivity image on the right (button-deep, dynamic normalization over 0.25m). With the exception of one fracture centred at 107 mbsf, all others show an azimuth of ~230º

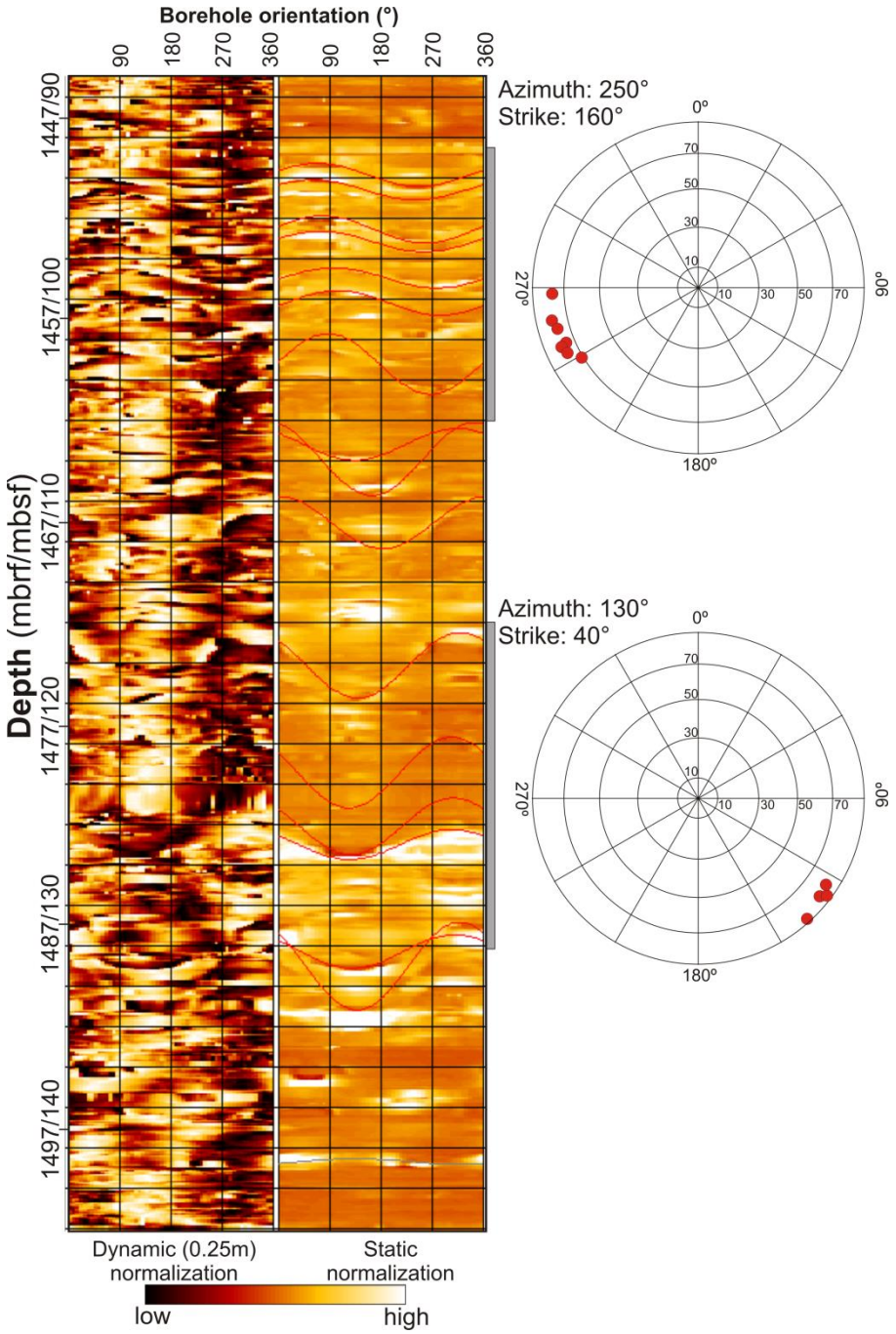


**Fig. 6:** c) Fracture-bands seen at Site UBGH1-14. Shown is the button-deep borehole image in dynamic (0.25 cm) and static normalization. Superimposed on the static-normalization resistivity image are the matched lines of individual fractures. Plots on the right (Schmidt-Plot, concentric circles represent dip-degree 0 - 90º) for the upper interval (91 - 106 mbsf) and lower interval (115 - 131 mbsf) do show the alignment of the fracture in common azimuth directions of 250º and 130º, respectively

The upper band extends from 100 mbsf to 110 mbsf and shows alternating bands of high - low resistivity. The thickness of these individual fractures is about 1.5m. Beneath this upper fracture-

band a second interval with fractures can be seen between 111 and 125 mbsf; however, these are thinner and only about ~0.5m wide. Results of the orientation analyses are listed in Table 3a and an example is shown in Fig. 6b. In general the average dip azimuth is ~230º (223º - 239º) in both fracture bands but the dip-degree is varying between shallow dips of around 60º in the lower band to over 80º in the upper band. Comparing the resistivity with the density image shows that areas of low resistivity correspond to areas of low density (Fig. 7).

| Depth (mbrf) | Depth (mbsf) | Azimuth (º) | Dip (º) |
|---|---|---|---|
| 1943.15 | 102.15 | 231.1 | 78.4 |
| 1943.98 | 102.98 | 222.8 | 79.5 |
| 1945.28 | 104.28 | 230.1 | 79.3 |
| 1945.84 | 104.84 | 233.3 | 50.8 |
| 1947.33 | 106.33 | 233.1 | 80.7 |
| 1948.20 | 107.20 | 25.7 | 84.5 |
| 1948.22 | 107.22 | 224.3 | 75.0 |
| 1949.98 | 109.98 | 238.9 | 80.0 |
| 1951.49 | 110.49 | 229.6 | 74.3 |
| 1952.51 | 111.51 | 232.1 | 70.2 |
| 1953.29 | 112.29 | 235.5 | 75.7 |
| 1954.22 | 113.22 | 232.1 | 79.9 |
| 1956.96 | 115.96 | 228.2 | 752.6 |
| 1958.96 | 117.96 | 233.5 | 71.9 |
| 1959.81 | 118.81 | 238.9 | 65.5 |

**Table 3a:** Derived dip-degree and azimuth orientations for Sites UBGH1-4

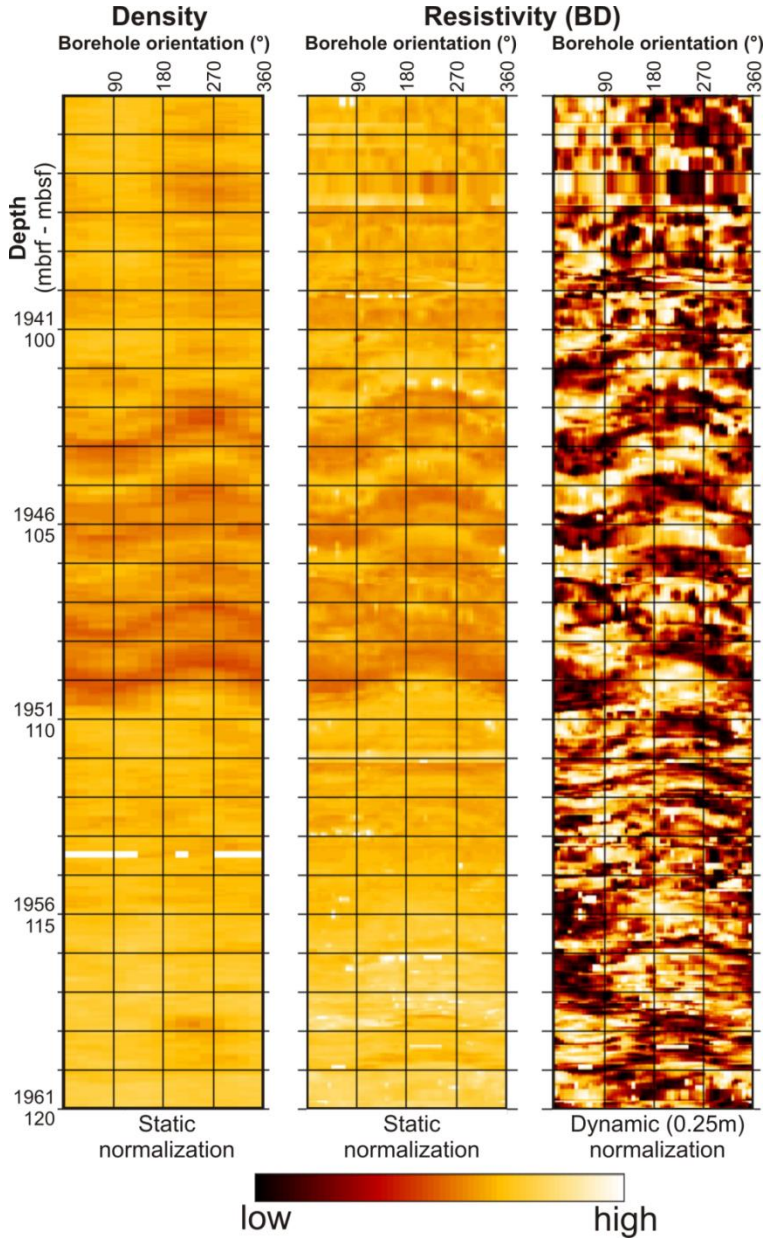


**Fig. 7:** Comparison of density and resistivity borehole images for the fracture bands at Site UBGH1-4. The zone from 102 - 110 mbsf shows sinusoidal patterns in density and resistivity, with low density values corresponding to low resistivity. The zone from 110 - 120 mbsf shows sinusoidal patterns only in the resistivity data

At Site UBGH1-14, fractures are in general more abundant and show a wider range of distributions (Table 3b).

| Depth (mbrf) | Depth (mbsf) | Azimuth (º) | Dip (º) |
|---|---|---|---|
| 1943.15 | 102.15 | 231.1 | 78.4 |
| 1943.98 | 102.98 | 222.8 | 79.5 |
| 1945.28 | 104.28 | 230.1 | 79.3 |
| 1945.84 | 104.84 | 233.3 | 50.8 |
| 1947.33 | 106.33 | 233.1 | 80.7 |
| 1948.20 | 107.20 | 25.7 | 84.5 |
| 1948.22 | 107.22 | 224.3 | 75.0 |
| 1949.98 | 109.98 | 238.9 | 80.0 |
| 1951.49 | 110.49 | 229.6 | 74.3 |
| 1952.51 | 111.51 | 232.1 | 70.2 |
| 1953.29 | 112.29 | 235.5 | 75.7 |
| 1954.22 | 113.22 | 232.1 | 79.9 |
| 1956.96 | 115.96 | 228.2 | 752.6 |
| 1958.96 | 117.96 | 233.5 | 71.9 |
| 1959.81 | 118.81 | 238.9 | 65.5 |

**Table 3b:** Derived dip-degree and azimuth orientations for Sites UBGH1-14

However, the two intervals of slightly elevated electrical resistivity values show fractures with a preferred orientation (Fig. 6c). The upper zone (90-98 mbsf) shows azimuth-values of ~250º (dip-degree ~80º) and the lower zone (127 - 135 mbsf) shows azimuth-values of ~130º (dip-degree ~80º).

*Gas hydrate concentrations at UBGH1-4*

Using the standard Archie-technique with empirical values as defined above, gas hydrate concentrations were calculated from the LWD BD-resistivity (same as used for the fracture-orientation analysis) and the density-porosity and neutron-porosity logs. The BD-resistivity log itself represents the average resistivity value at each depth-point across the borehole wall and as

such smears out the detailed information seen in the RAB images. At Site UBGH1-4, the estimated gas hydrate saturation is on average zero within the top 70 mbsf (Fig. 8a).

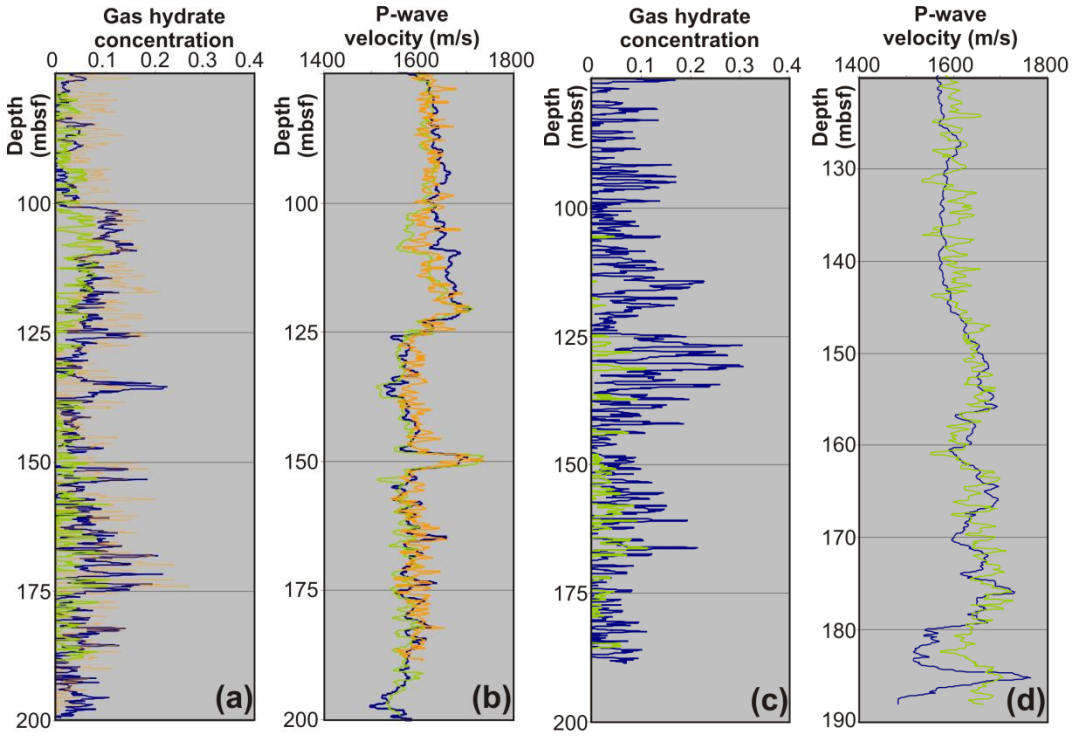


**Fig. 8:** a) UBGH1-4: Apparent gas hydrate concentrations from Archie analysis using density-porosity (blue) and neutron porosity (orange). Using the effective medium model gas hydrate concentrations (green) are overall lower then resistivity-based estimates but mimic the same depth-trend. b) Comparison of measured LWD velocity (blue) with two predictions of the 0%-gas hydrate baseline velocity based on density-porosity (green) and neutron-porosity (orange). For most of the borehole the predicted baseline agrees with the measurements (which yields no effective gas hydrate content), with the notable exception of the lower part of the MTD unit (100 - 120 mbsf), where the LWD-velocity is consistently higher than the predictions. c) UBGH1-14: Archie-based gas concentration estimates (blue) with basic assumptions on background values of constant salinity and temperature gradient and velocity-based calculations (green for lower section of the borehole). d) LWD P-wave velocity measurements (blue) compared to prediction of baseline velocity-trend with 0% gas hydrate (green) using neutron-porosity

For the interval of the main MTD, gas hydrate concentrations average ~5% for the interval of 70-100 mbsf and 10% for the remainder interval of 100-125 mbsf. The pronounced zone between 100 mbsf and 110 mbsf with concentration values around 10% coincides with an interval of prominent fractures as seen in the resistivity images. The interval of 150-175 mbsf shows pronounced spikes in resistivity corresponding to higher gas hydrate concentrations up to 20%. In this interval, the cored sediments were composed of a mix of hemipelagic mud with thin

interbedded sandy turbidites. The turbidites were gas-hydrate bearing as seen in pronounced pore-water chlorinity freshening and infra-red cold spots (Fig. 9).

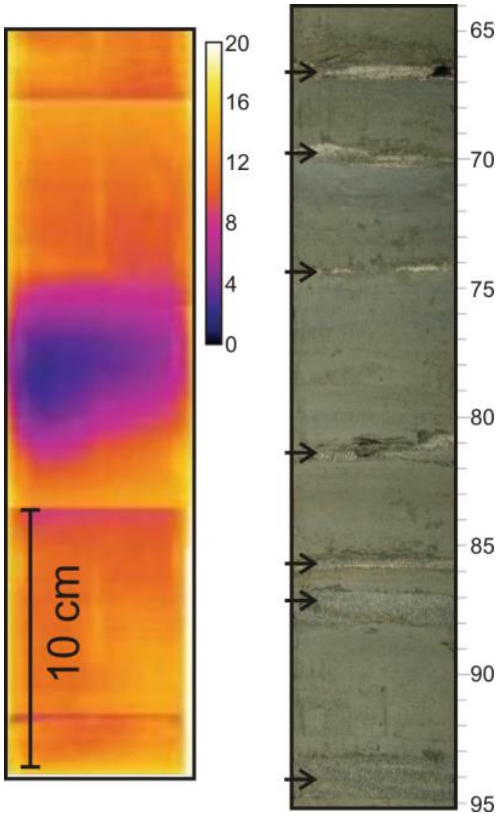


**Fig. 9:** a) Example of an IR cold-spot from core UBGH1-4C-6H (sample was taken for pore-water analyses), b) Example of thin sandy turbidites (arrows) within hemipelagic mud (from same core, but different section)

Using the effective-medium theory we estimated gas hydrate concentration from the LWD P-wave velocity data and the results yield slightly lower values than the resistivity-based estimates (Fig. 8a). The prediction of the zero-gas-hydrate background trend is crucial for the velocity-based estimates and we assumed two baselines based on neutron- and density-porosity (Fig. 8b), respectively. For the most part of the borehole, the measurements agree with the base-line predictions, with the notable exception of some parts of the MTD unit where fractures were developed (100 - 125 mbsf).

*Gas hydrate concentrations at UBGH1-14*

At Site UBGH1-14 the required assumptions on baseline parameters result in an overall higher uncertainty in the calculated gas hydrate concentrations. Gas hydrate concentration estimates are around zero for the top 70 mbsf using the resistivity-log (Fig. 8c). Values reach up to 25% around 125-130 mbsf where also preferred fracture-orientations were found in the borehole resistivity images. The general smooth trend in the downhole P-wave velocity log suggests very small gas hydrate concentrations. Deviations from the smooth trend can only be seen within the interval of 120 - 180 mbsf above the BSR. We therefore focus the velocity modeling and analysis onto this interval (Figs. 8c, 8d). Resulting concentration estimates from the velocity-data are much lower than resistivity-based values and are on average ~5%. However, most of the non-zero gas hydrate concentration values are due to the relatively noisy and undulating nature of the neutron-porosity measurements. Comparing the predicted with the measured velocity log shows that on average the non-hydrate-bearing background velocity trend follows the LWD velocity data.

**Interpretation of log-data**

*Linkages between MTD and fracture orientation*

The presence of fractures and their preferred orientations were unexpected at Sites UBGH1-4 and UBGH1-14 as pre-drilling seismic analyses did not show any nearby cold-vent-like features, in which typically fractured-systems were encountered in the past drilling operations off India and the Cascadia margin (Riedel et al., 2006; Collett et al., 2008). Close inspection of the 3-D seismic data around Site UBGH1-4 showed a prominent MTD, and seismic attribute analyses allowed to define the reconstruction of the flow-direction, especially by

mapping extensive grooves in the bottom-reflection event (see companion paper by Scholz et al.). The two bands of fractures within the bottom-half of the MTD show a set of fractures with the strike orientation being perpendicular to the flow-direction of the main MTD (Fig. 10). The MTD did flow towards an overall NE-direction (~40º) with the fracture-strike orientation being ~140º. The fractures do, however, dip to the opposite of the MTD flow direction, i.e. towards the SW (dip azimuth is ~230º). Closer to Site UBGH1-4, the grooves at the base of the MTD indicate a lateral spreading of the flow itself, probably indicating a reduction in flow-speed in that region.

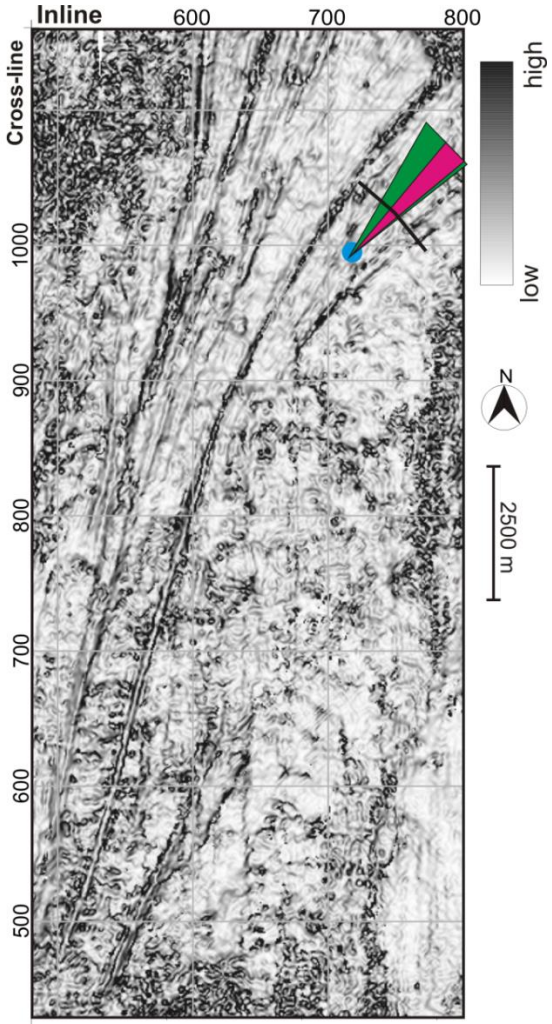


**Fig. 10:** Comparison of flow-direction as defined by seismic attribute dip-of-maximum similarity (green cone) and from fractures seen in the resistivity image logs (red cone). Also shown are strike-orientations (black-lines) of the aligned fractures

If the fracture orientation is reflecting the overall flow-direction of the accompanying MTD, one could similarly reconstruct flow-directions for the MTDs seen at Site UBGH1-14. Here no 3-D seismic data exist to aid in the analyses but the proximity of the site on the southern slope of the basin may result in flow directions similar to that seen at Site UBGH1-4. The fracture band in the depth interval of 125 - 135 mbsf shows preferred dip-azimuth orientations of ~130º (strike ~40º), and the upper band in the depth interval of 85 - 100 mbsf shows preferred dip-azimuth orientations of ~250º (strike 160º). These directions would suggest two different flow-directions: the upper band would reflect a mass flowing towards the NE almost like that seen at Site UBGH1-4, but the lower band would reflect a flow-direction to the NW. Overall these orientations are not inconceivable but somewhat surprising as being rotated considerably relative to each other. However, the seismic and log-data overall suggest a multi-layered flow that comprises most of the depth interval within the gas hydrate stability zone at Site UBGH1-14 and a more complex fracture-pattern is thus possible.

The fractures and their strike are oriented in a similar direction as pressure-ridges described by Nissen et al. (1999) or Prior et al. (1982). The formation of pressure-ridges may be understood as a result of differential flow-speeds and along-flow compression within the flowing mass of sediments itself or as a result of outrunner blocks displacing sediment by scraping through the underlying sediment package thereby creating the prominent grooves seen in the seismic coherency attribute. The first process would result in more wide-spread, parallel bands of ridges, whereas the second process would result in more isolated ridges directly associated with individual blocks.

Alternatively, the fracture patterns may not necessarily reflect the MTD flow-direction and the similarity in seismically-defined flow-direction and fracture-strike orientation could be

coincidental. Overall the MTDs encountered during the logging and coring show higher resistivity, density and P-wave velocity values within the flow as compared to the section above and below it. In all MTDs intersected these increases are associated with porosity-reduction (see Fig. 3). The fractures are superimposed on this trend and increase resistivity and velocity even further. However, the significantly different physical properties of the MTD sediments may represent a post-slump reconsolidation of the sediments that have been entirely re-mixed and possibly sorted as a result of the gravitationally driven flow down-slope. This apparent over-compaction reflects that sediments in the MTD flow got re-distributed against their original layering and "normal" compaction. The post-depositional settling of the sediments results possibly in a preferred alignment of the sediments that are seen as a fracture-pattern in the resistivity images. The fractures may also represent dewatering pathways.

*Gas hydrate concentrations and anisotropy*

Using isotropic models such as Archie or EFM for gas hydrate concentration estimates is a standard approach to analysing log-data. The Archie-based analysis assumes that gas hydrate occupies the sediment pore-space evenly and thus effectively reduces the pore-space with the predicted increase in electrical resistivity measurements. EFM equally assumes gas hydrate is distributed evenly, and gas hydrate content increases velocity (and effectively reduces porosity). The fracture-analyses at both drill sites demonstrate that fractures are present over some intervals and are oriented in a preferred direction. Coring at Site UBGH1-4 through an interval with fractures did, however, not recover any gas hydrate and no pore-water freshening or IR cold spots were recognized. The log-resistivity and P-wave velocity values are increased relative to an assumed baseline and isotropic model, and predict ~10% of gas hydrate on average within these zones. Independent on the origin of the fractures discussed above, they do impact the log-

measurements and related gas hydrate concentration calculations. This has been noticed previously during gas hydrate drilling campaigns, but mainly when associated with cold vents, or seismic chimney structures (e.g., Lee and Collett, 2009; Cook and Goldberg, 2008). In general, fractures induce some degree of anisotropy to the measurements within the borehole where the tool and plane of measurement are more or less aligned parallel to the fracture-planes.

As an example to investigate the effect of anisotropy we use the resistivity log from Site UBGH1-14 in the lower fracture-band. The resistivity values of individual spikes in the resistivity-log are as high as 2 Ωm. Average resistivity values calculated using the above-defined Archie-parameters with an average porosity of 50% result in a "background" sediment resistivity of ~1.15 Ωm for this interval. This results in an apparent gas hydrate concentration of ~30% (Fig. 8c). In comparison, electrical resistivity values exceeding 200 Ωm over an assumed no-gas hydrate background resistivity of ~1.5 Ωm were noted at drill sites UBGH1-9 and UBGH1-10 (Kim et al., 2011) where massive forms of gas hydrate as fracture-fill were recovered. Archie-based calculations do result in extremely high gas hydrate concentrations of 90% or higher, although pressure-coring analyses predict lower gas hydrate concentrations of around 25-30%. As shown by Lee and Collett (2009) already a few percent of gas-hydrate-filled fractures oriented parallel to the borehole increase the measurement of sediment-resistivity. According to their modeling result, the presence of 10% gas hydrate-filled fractures increases resistivity by a factor ~5. Thus, a very small bulk-volume of gas hydrate within a few fractures may have artificially increased the resistivity measurements and Archie-based gas hydrate concentration estimate at the two sites UBGH1-4 and UBGH1-14. Overall the degree of anisotropy is relatively low at the two drill sites UBGH1-4 and UBGH1-14 due to the small number of fractures present.

The effect is stronger on the resistivity measurements than on P-wave velocity, as previously noted by Lee and Collett (2009).

Although the one core recovered from an interval containing fractures at Site UBGH1-4 did not reveal any detectable gas hydrate it is not inconceivable that the fractures seen do represent some minor amount of gas hydrate. The LWD borehole in which the resistivity image data were collected has a lateral offset of ~10 meter from the first cored hole and two penetrations were required to complete coring-operations at Site UBGH1-4, with an additional offset of the second cored hole relative to the first cored hole. Fractures that are steeply dipping cannot necessarily be expected to occur within the exact same depth interval between adjacent boreholes.

**Using advanced seismic attributes to map gas hydrate within thin turbidite sands**

The log-analyses and fracture-detection showed that gas hydrate at Site UBGH1-4 is only found within thin sandy turbidites in the lower portion of the borehole near the BSR and not within apparently high-resistivity zones found within MTDs. It is challenging to identify these thin turbidite layers seismically as they are too thin to be detectable with common seismic data. However, the close association of the sandy turbidites with the hemipelagic sediment facies and a depositional environment in the Ulleung Basin of overall low-energy (in contrast to high energy MTDs) reflected in parallel and continuous bedding, can be exploited to define the extent of this gas-hydrate-bearing layer. The seismic image shown in Fig. 2 and Fig. 5a illustrates how this sedimentary sequence is imaged by seismic data. Sediment packages closer to the seafloor are laterally extensive and strong in reflection amplitude in comparison to packages near the BSR, which are seen as laterally continuous but overall faint reflections. The fact that the lower unit of laterally continuous hemipelagic sediments with sandy turbidites is much reduced in

amplitude compared to the analogous sediments shallower in the section could be the result of the presence of some gas hydrate that reduces the impedance contrast between the sandy turbidite and surrounding mud (as suggested by Lee and Dillon, 2001). However, if the gas hydrate concentration is high and the sand-thickness is large compared to the seismic frequency content used for imaging the reflection amplitude could be much enhanced, as e.g. seen in the Gulf of Mexico (Frye et al., 2010) or Arctic deposits (Bellefleur et al., 2006).

A combination of geometrical seismic attributes involving basic reflection amplitude, instantaneous frequency, and similarity (e.g., Taner et al., 1994) may help to delineate this particular interval. The aim is to highlight the sediments as laterally continuous and simultaneously overcome the faint reflection amplitude character to aid in detection and mapping of these types of sediment-packages. Three seismic attributes are known to help delineate clay-rich thin beds that occur laterally continuous: "Parallel Bedding Indicator", "Thin Bed Indicator" and "Shale Indicator" (e.g. Meyer et al., 2001). The seismic attribute referred to as "Parallel Bedding Indicator" is defined as the variance of the attribute "Dip of maximum similarity". The attribute represents the standard deviation of the instantaneous dips computed over the user-defined average dip computation window. Zones with parallel bedding will therefore show close to zero variance values. The attribute "Shale Indicator" is a hybrid attribute combining several attributes that have been assembled to detect possible shale in the depositional environment. Shales may be identified by their geometrical configuration as thin, parallel laminations with high lateral continuity. This attribute uses instantaneous frequency for thin bed detection, parallel bedding indicator (as defined above), and similarity (coherency) and coherency-variance for better lateral continuity detection. Highest output values of this attribute are therefore indicative of the highest possibility of shale occurrence. The attribute "Thin Bed Indicator" is computed as

the difference between instantaneous and time averaged frequencies. This attribute indicates thin beds, when laterally continuous. It further highlights non-reflecting zones (e.g. the MTDs), when it appears laterally at random.

At Site UBGH1-4, coring indicated a depositional environment of interbedded hemipelagic mud and sandy turbidites within the top 60 mbsf. The depth of 0.046 s TWT below seafloor (~40 mbsf) was chosen for attribute analyses. Fig. 11a shows the three above-mentioned attributes in comparison to regular reflection amplitude computed in a horizon-slice parallel to the seafloor.

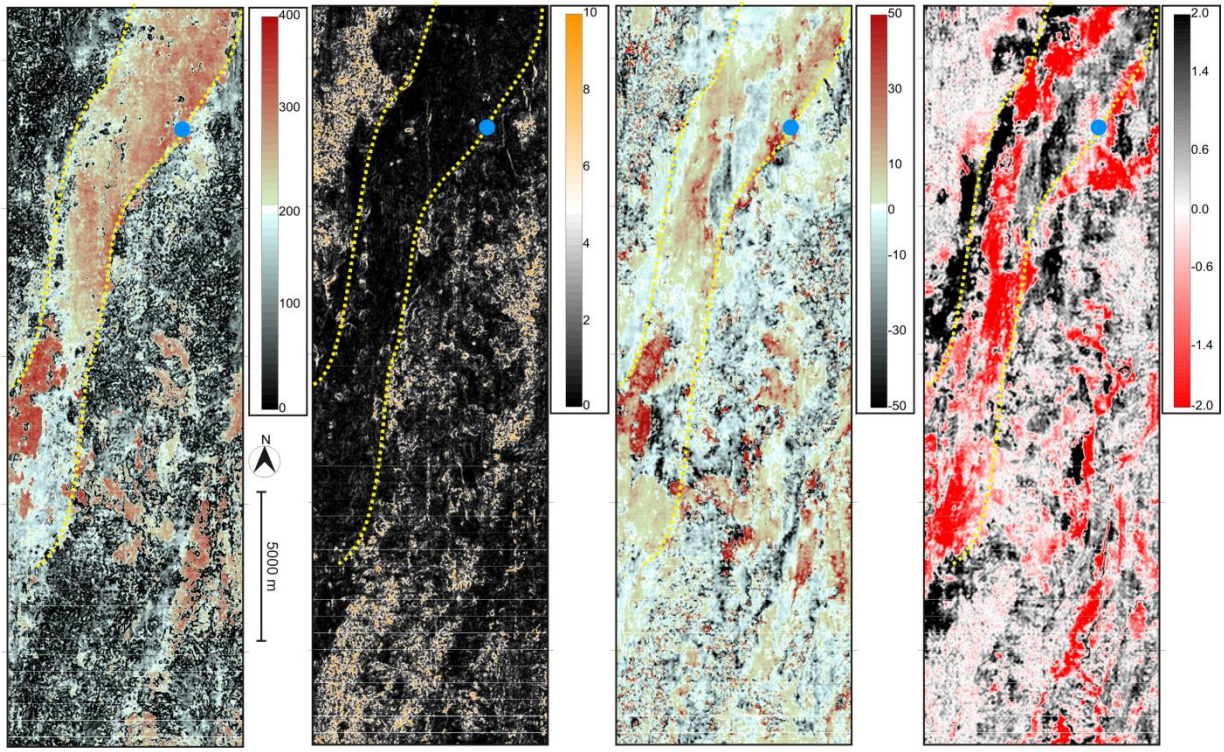


**Fig. 11:** a) Slices of seismic attributes for definition of sediment-depositional environments taken at 0.046 s two-way time below seafloor from 3-D seismic volume. The slices highlight the sequence that is on top of the main MTD at Site UBGH1-4 and cores show a mix of sand with hemipelagic mud (outlined by yellow dotted lines). From left to right: Shale indicator, Parallel-bedding indicator, Thin bed indicator, reflection amplitude. Site UBGH1-4 is shown as blue dot. Note the sharpness in defining the edges of the highlighted zones in the attributes relative to reflection amplitude

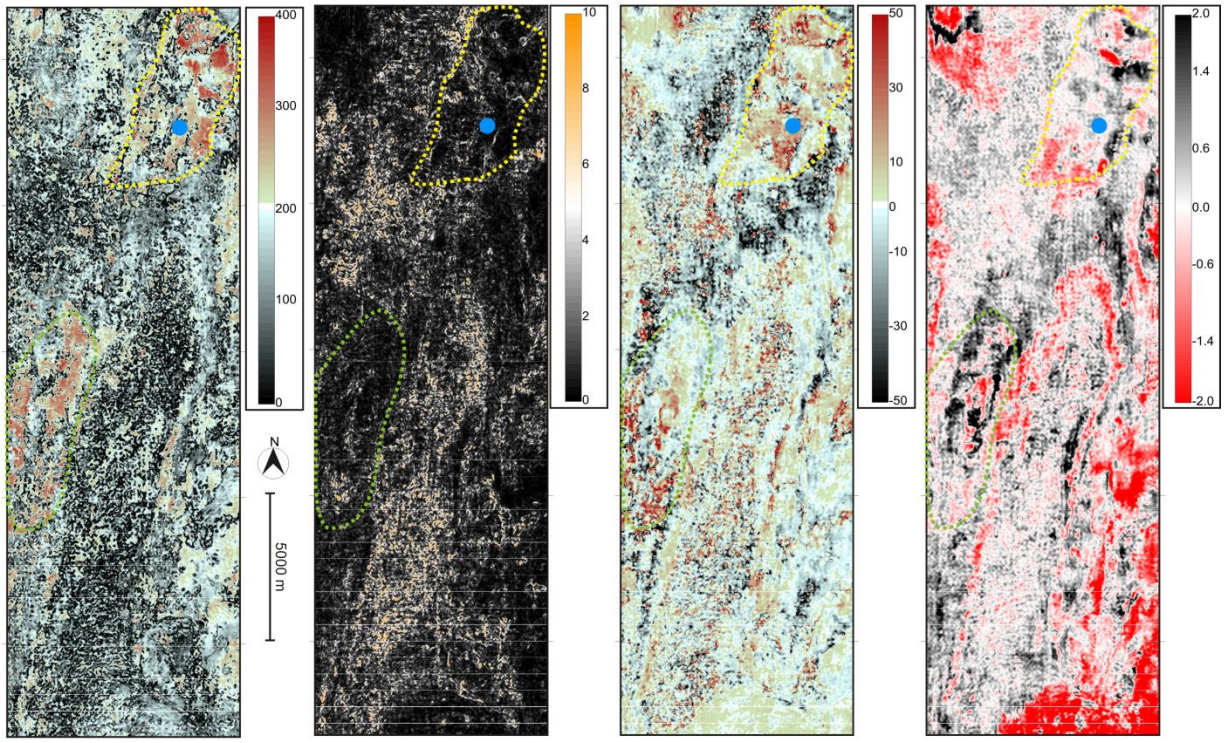


**Fig. 11:** b) Slices of seismic attributes taken at 0.224 s two-way time below seafloor from 3-D seismic volume, highlighting the zones that are comprised of gas-hydrate-bearing sands within hemipelagic mud (identical in sediment-depositional environment as above MTD), shown here outlined by the yellow dotted line. Also shown is a potential gas-hydrate bearing sand/hemipelagic zone (outlined by a green dotted line) of similar seismic character as the zone intersected at Site UBGH1-4 (blue dot). From left to right: Shale indicator, Parallel-bedding indicator, Thin bed indicator, reflection amplitude

The reflection seismic data show zones of higher amplitude values within the outlined zone of hemipelagic sediments; however the edges of this unit are not well constrained by the amplitude values. A much sharper image appears in the derived attributes, especially using the Shale indicator. Also, subtle differences within the outlined zone reflecting depositional variations within the hemipelagic sediment sequences, are not as easily discernible in the amplitude data alone, but appear accentuated in the various attributes. The zone of continuous high values in Shale indicator for the sediment sequence mostly coincides with the location of the underlying MTD unit and indicates that the thin turbidites interbedded with hemipelagic sediments followed a flow-direction similar to the MTD. For comparison, Fig. 11b shows an example of the three attributes on a horizon-slice computed parallel to the seafloor at a depth of the gas hydrate

occurrence at Site UBGH1-4 (0.224 s TWT below seafloor, ~180 mbsf). The comparison of the three attributes with regular reflection amplitude shows that the sequence of turbidite sands embedded within the hemipelagic mud (outline din yellow) can be detected and mapped around the drill-site much easier using a combination of the Shale indicator and other attributes, than using the reflection amplitude alone. The extent, especially the edges of the layer become much better defined, and subtle nuances within the interval itself are also accentuated.

The advantage of the definition of an attribute that is sensitive to reflect a specific sedimentary facies is in 3-D volume rendering applications. We defined a derivative-attribute from the "Shale Indicator" first by subtracting a constant from the total attribute representing a cut-off value above which we think the sedimentary facies of interbedded hemipelagic mud and sandy turbidites is dominant. The cut-off was chosen from visual inspection and comparison of values in the attribute data around the drill site UBGH1-4. Afterwards, the attribute was further modified by clipping all values below the cut-off to zero. Fig. 12 shows a perspective-view of the modified attribute with all values below the cut-off being made transparent, leaving the actual remaining data as a 3-D volume visible.

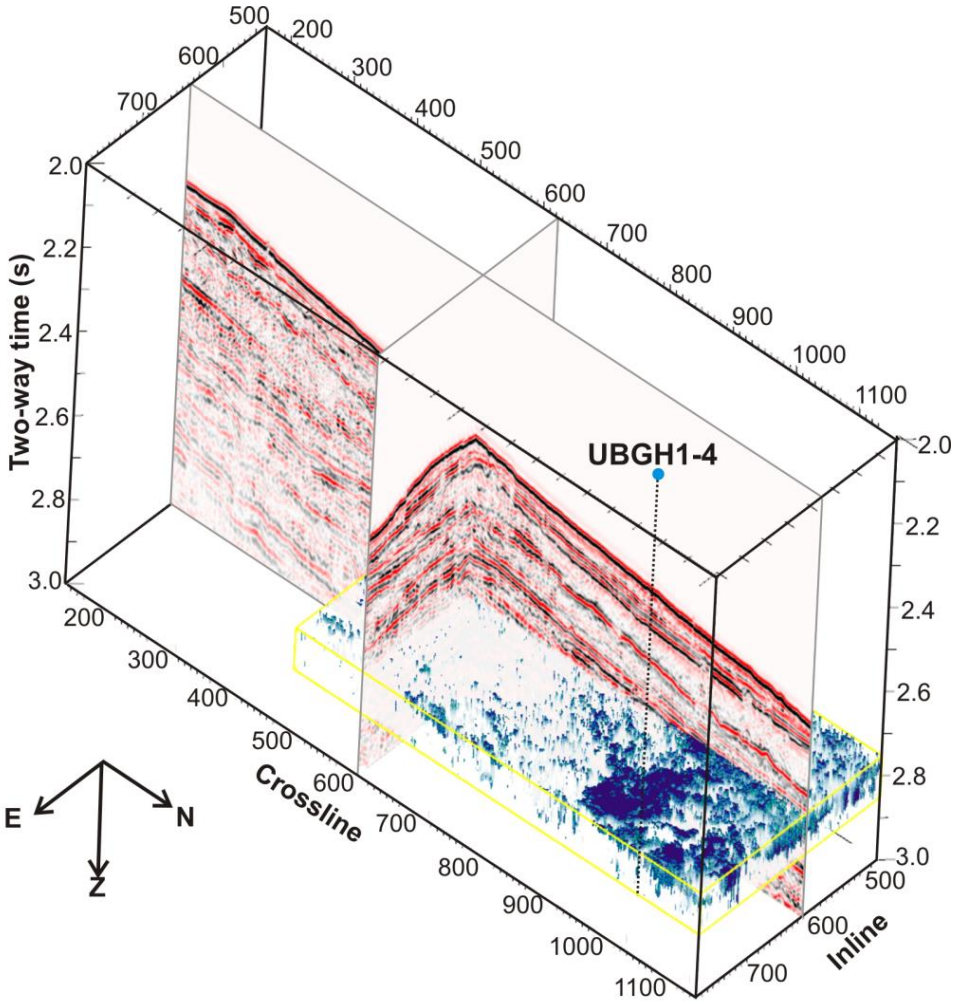


**Fig. 12:** perspective view of lower facies after clipping of shale-indicator attribute and opacity definition of volume to show only the continuous sequence that is gas hydrate bearing

Two seismic sections from the 3-D volume are shown to help visualise the extent of the sediment-body highlighted, which now can be better identified not only in areal extent, but also thickness. A last step in using the 3-D rendering capability is to assign this sediment volume gas hydrate concentration values. We have only few cores and one LWD-data set to define an average concentration. Using the above gas hydrate calculations from P-wave velocity and resistivity, an average concentration of 10% may be appropriate. However, the lack of a well-defined reservoir (i.e. thick sands), limited core and log-data and lack of definitive a seismic signal (bright-spot) make it impossible to calculate a realistic gas hydrate concentration within

this sedimentary facies as e.g. done at other locations in the Arctic at the Mt. Elbert site, (Inks et al., 2009), Mallik (Riedel et al., 2010, Bellefleur et al., 2006), or in the Gulf of Mexico (Dai et al., 2008).

**Summary and Conclusions**

The sediment depositional environment in the southern Ulleung Basin is dominated by MTDs. Logging and coring in the Ulleung Basin showed that sediments within the MTD unit exhibit unusually high density, P-wave velocity, and resistivity, as well as a reduced porosity compared to sediments above and below. The physical properties as well as core images reflect that the sediments of the MTD unit were redistributed, sheared, and disturbed and are overall more compacted. The MTDs are seismically transparent with a bottom reflection that looks identical to the BSR that usually marks the base of the gas hydrate stability zone. Gas hydrate concentrations at Sites UBGH1-4 and UBGH1-14 were estimated utilizing the LWD P-wave velocity and electrical resistivity data. Apparent gas hydrate concentrations range at Site UBGH1-4 from 5% to 10% within the MTD unit and reach up to 20% in the sandy turbidite zone near the base of gas hydrate stability zone. However, a set of fractures were seen within the MTD unit at Site UBGH1-4 that results in an overestimation of gas hydrate content due to anisotropic effect on the log-measurements. Cores recovered from the lower interval of the MTD where the resistivity and velocity log-data predict some gas hydrate to exist did not recover any gas hydrate (no pore-water freshening or IR cold-spots). However, we conclude that the more resistivity fractures do represent some minor component (less than 1% by volume) of bulk gas hydrate.

Comparing the fracture-strike orientation with seismically defined flow-patterns of the MTD at Site UBGH1-4 suggests that the fractures represent post-depositional re-alignment of the

sediments that result in an overall lower porosity (and thus higher velocity and base-resistivity than the surrounding sediment). The fractures may either originate from gravitational compaction of the sediments after deposition associated with dewatering, or from internal compressive forces due to differential flow-speeds in the MTD itself leading to the formation of pressure-ridges.

Although no cores were recovered at Site UBGH1-14 the LWD log data were also used to estimate gas hydrate concentrations based on simple assumptions of the baseline pore-fluid salinity and geothermal gradient. The LWD-resistivity images were used for a fracture analysis and two zones of fractures were identified. Using the standard resistivity Archie-analyses, concentrations from resistivity show average values of 5-15% with two pronounced intervals of higher concentrations up to 30% where fractures were identified. Estimates using P-wave velocity show almost no gas hydrate content at Site UBGH1-14. The fractures again appear closely linked to seismically defined sub-layers within a larger MTD mass. We conclude that the resistivity data are again biased by anisotropic effects from the fractures and that this site likely has very little gas hydrate by volume, despite the fact that a strong BSR is present.

In contrast, gas hydrate was recovered at Site UBGH1-4 within sandy turbidites interbedded within hemipelagic mud. This sedimentary facies regularly alternates with the MTDs in the Ulleung Basin and is very common, especially in the northern part of the basin. We therefore attempted to develop a mapping technique that utilizes a combination of seismic attributes that are based on the basic seismic similarity attribute (coherence). The attribute referred to as "Shale Indicator" is especially useful to highlight the laterally continuous hemipelagic mud with interbedded sandy turbidites. By clipping the calculated attribute values to a defined threshold and using 3-D-volume rendering algorithms to show only values above the threshold with the remaining volume being transparent, the gas-hydrate bearing unit can be

mapped and visualized in 3-D. Although the lack of multiple penetrations of this unit with log-data for further improved gas hydrate concentration estimates, the use of seismic attributes and 3-D visualization improves gas hydrate resource assessments in the Ulleung Basin.

**Acknowledgments**

We would like to thank all scientists involved in the first scientific drilling expedition in the Ulleung Basin in 2007 as well as all crew and technical staff onboard the vessel Rem-Etive. We also want to thank KIGAM for allowing data distribution, especially the 3-D seismic data volume at Site UBGH1-4. This is Earth-Science Sector (ESS) contribution number: 20100042.

***Bibliography***

Archie G. E., 1942, *The electrical resistivity log as an aid in determining some reservoir characteristics*, Trans. AIME, **146**, 54-62

Bahk J.-J., Um I.-K., Holland M., 2011, *Core lithologies and their constraints on gas-hydrate occurrence in the East Sea, offshore Korea: Results from the site UBGH1-9*, Journal of Marine and Petroleum Geology (in press)

Bellefleur G., Riedel M., Brent T., 2006, *Seismic characterization and continuity analysis of gas-hydrate horizons near Mallik research wells, Mackenzie Delta, Canada*, The Leading Edge, **25**(5), 599-604

Collett T. S., Ladd J., 2000, *Detection of gas hydrate with downhole logs and assessment of gas hydrate concentrations (saturations) and gas volumes on the Blake Ridge with electrical resistivity log data*, In: Paull, C.K., Matsumoto, R., Wallace, P.J., and Dillon, W.P., eds., Proceedings of the Ocean Drilling Program, Scientific Results, **164**, p. 179 – 191

Collett T.S., Riedel M., Cochran J., Boswell R., Presley J., Kumar P., Sathe A.V., Sethi A., Lall M., Sibal V., and the NGHP Expedition 01 Scientists, 2008, *Indian National Gas Hydrate Program (NGHP) Expedition 01, Initial Report*, Directorate General of Hydrocarbons, Ministry of Petroleum and Natural Gas, India

Cook A.E., Goldberg D., Kleinberg R.L., 2008, *Fracture-controlled gas hydrate systems in the northern Gulf of Mexico*, Marine and Petroleum Geology, **25**, 932–941

Cook A. E., Goldberg D., 2008, *Extent of gas hydrate filled fracture planes: Implication for in situ methanogenesis and resource potential*, Geophysical Research Letters, **35**, L15302, doi:10.1029/2008GL034587

Dai J., Snyder F., Gillespie D., Koesoemadinata A., Dutta N., 2008, *Exploration for gas hydrates in the deepwater, northern Gulf of Mexico: Part I. A seismic approach based on geologic model, inversion, and rock physics principles*, Marine and Petroleum Geology, **25**, 830-844

Frye M.C., Shedd W.W., Godfriaux P.D., Dufrene R., Collett T.S., Lee. M.W., Boswell R., Jones E., McConnell D.R., Mrozewski S., Guerin G., , Cook A., 2010, *Gulf of Mexico Gas Hydrate Joint Industry Project Leg II: Results from the Alaminos Canyon 21 Site*, Offshore Technology Conference paper 20552, Offshore Technology Conference, Houston, 3-6 May, 2010

Helgerud M. B., Dvorkin J., Nur A., 1999, *Elastic-wave velocity in marine sediments with gas hydrates: effective medium modeling*, Geophysical Research Letters, **26**, 2021–2024

Holland M., Schultheiss P., Roberts J., Druce M., 2008, *Observed Gas Hydrate Morphologies in Marine Sediments*, In: Proceedings of the 6th International Conference on Gas Hydrates (ICGH 2008), Vancouver, BC, Canada, July 6-10, 2008, https://circle.ubc.ca/handle/2429/1201

Horozal S., Lee G.H., Yi B.Y., Yoo, D.G., Park K.P., Lee H.Y., Kim W.S., Kim H.J., Lee K.S., 2009, *Seismic indicators of gas hydrate and associated gas in the Ulleung Basin, East Sea (Japan Sea) and implications of heat flows derived from depths of the bottom-simulating reflector*, Marine Geology, **258**, 126-138

Inks T., Lee M., Agena W., Taylor D., Collett T.S., Hunter R., Zyrianova M., 2009, *Prospecting for gas hydrate accumulations using 2-D and 3-D seismic data, Milne Point, North Slope, Alaska*, In: Natural Gas Hydrates—Energy Resource Potential and Associated Geologic Hazards, T.S. Collett, A. Johnson, C. Knapp, and R. Boswell, eds., AAPG Memoir **89**, 1-29

Kim G.Y., Yoo D.G., Ryu B.J., Riedel M., 2011, *Evidence of gas hydrate from downhole logging data in the Ulleung Basin, East Sea*, Journal of Marine Petroleum Geology (in press)

Lee M.W. Collett T.S., 2009, *Gas hydrate saturation estimated from fracture reservoir at Site NGHP-01-10, Krishna-Godavari Basin, India*, Journal of Geophysical Research, **114**, B07102, doi:10.1029/2008JB006237

Lee M. W., Dillon W.P., 2001, *Amplitude blanking related to gas hydrate concentration*, Marine Geophysical Researches, **22**(2), 101-109

Lee G.H., Suk B.-C., 1998, *Latest Neogene-Quaternary seismic stratigraphy of the Ulleung Basin, East Sea (Sea of Japan)*, Journal of Marine Geology, **146**, 205-224

Lee G.H., Kim J.H., Han S.J., Kim D.C., 2001, *Seismic stratigraphy of the deep Ulleung Basin in the East Sea (Japan Sea) back-arc basin*, Journal of Marine and Petroleum Geology, **18**, 615-634

Lee J.H., Baek Y.S., Ryu B.J., Riedel M., Hyndman R.D., 2005, *A seismic survey to detect natural gas hydrate in the East Sea of Korea*, Journal of Marine Geophysical Research, **26**, 51-59

Meyer D.E., Harvey E.L., Bulloch T.E., Voncannon J.C.,Sheffield T.M., 2001, *Use of seismic attributes in 3-D geovolume interpretation*, The Leading Edge, **20**(1377 ), doi:10.1190/1.1486768

Nissen S.E., Haskell N.L., Steiner C.T., Coterill K.L., 1999, *Debris flow outrunner blocks, glide tracks, pressure ridges identified on the Nigerian continental slope using 3-D seismic coherency*, The Leading Edge, 595-599

Park K.-P., Bahk J.-J., Kwon Y., Kim G.-Y., Riedel M., Holland M., Schultheiss P., Rose K., and the UBGH-1 Scientific Party, 2008, *Korean national program expedition confirm rich gas hydrate deposits in the Ulleung Basin, East Sea*, DOE-National Energy Technology Laboratory (NETL) Fire in the Ice Methane Hydrate Newsletter, 6–9:

http://www.netl.doe.gov/technologies/oilgas/publications/Hydrates/Newsletter/HMNewsSpring08.pdf

Prior D.B., Bornhold B.C., Coleman J.M., Bryant W.R., 1982, *Morphology of a submarine slide, Kitimat arm, British Columbia*, Geology, **10**, 588-592

Riedel M., Collett T.S., Kumar P., Sathe A.V., Cook A., 2010, *Seismic imaging of a fractured gas hydrate system in the Krishna-Godavari Basin offshore India*, Journal of Marine and Petroleum Geology, **27**, 1476–1493

Riedel M., Collett T.S., Malone M. J., and the Expedition 311 Scientists, 2006, Proc. IODP, 311: Washington, DC (Integrated Ocean Drilling Program Management International, Inc.), doi:10.2204/iodp.proc.311.2006

Riedel M., Collett T.S., Kumar P., Sathe A.V., Cook A, 2010, *Seismic imaging of a fractured gas hydrate system in the Krishna-Godavari Basin offshore India*, Journal of Marine Petroleum Geology, **27**, 1476-1493

Ryu B.-J., Riedel M., Kim J.-H., Hyndman R.D., Lee Y.-J., Chung B.-H., Kim I.-S., 2009, *Gas hydrates in the western deep-water Ulleung Basin, East Sea of Korea*, Journal of Marine and Petroleum Geology, **26** (8), 1483-1498

Taner M. T., Schuelke James S., O'Doherty R., Baysal E., 1994, *Seismic attributes revisited*, 64th Annual Internat. Mtg., Soc. Expl. Geophys., Expanded Abstracts, **94**, 1104-1106